Imaging polarimetry for the characterisation of exoplanets and protoplanetary discs.

Scientific and technical challenges.

Cover image: Synthetic R-band VLT/SPHERE-ZIMPOL polarised intensity image of a transitional disc generated by the presence of a 9 M_{Jup} planet.

Imaging polarimetry for the characterisation of exoplanets and protoplanetary discs.

Scientific and technical challenges

Proefschrift

ter verkrijging van de graad van doctor aan de Universiteit Leiden, op gezag van de Rector Magnificus prof. mr. C. J. J. M. Stolker, volgens het besluit van het College Voor Promoties te verdedigen op donderdag 12 december 2013 te 8.45 uur.

door

Maria de Juan Ovelar

geboren op 27 July 1981 te Madrid, Spanje

Promotor: Prof. dr. C. U. Keller

Co-promotor: Dr. ir. F. Snik

Overige leden: Prof. dr. Huub Röttgering

Prof. dr. Ignas Snellen

Prof. dr. Carsten Dominik (University of Amsterdam)

Prof. dr. Malcolm Fridlund (ESTEC, Sterrewacht Leiden)

Dr. Hans Martin Schmid (ETH Zurich, Switzerland)

The best way out is often through.

— adapted from Robert Frost, *1874 – 1963*

Contents

Chapter 1

Introduction

As the 19th century Pulitzer Prize-winning American novelist Edith Warton once wrote, *"there are two ways of spreading light: to be the candle or the mirror that reflects it"*. It turns out that study of the light spread by the mirror not only tells us about the candle, but also about the mirror itself. As humans, light moves through space and time keeping accounts of all the interactions it undergoes in its way and, as humans, it can tell a lot about it if one asks the right questions.

When we look at a star and its circumstellar matter, we are looking at the light that comes from both the candle and the mirror. The candle is the central source and the mirror the surrounding matter by which a fraction of the starlight is reflected/scattered towards us. Whether that surrounding matter is in the form of particles in a circumstellar disc or in the atmosphere of a planet is only relevant for the context of the posterior analysis. The physical process by which that light is spread towards us is the same in any of those cases: scattering. Scattered light becomes linearly polarised, and the characteristics of this linear polarisation depend on the scatterers, in other words, the polarisation state of scattered light carries information about the medium by which it was scattered. Polarimetry is therefore one of the few tools we count on to ask light the right question.

Humans have always wondered about the existence of other worlds and other forms of life, but it was only very recently, with the discovery of the first planets outside of our Solar System (Wolszczan & Frail 1992, Mayor & Queloz 1995), when the real chance to answer these questions materialised. Since then, and mainly thanks to ground-based instruments like HARPS (Mayor et al. 2003) and space missions like Kepler (Koch et al. 1998) and COROT (Baglin et al. 2006), more than 800 planets have been confirmed (see Figure 1.1) and more than 3000 candidates are awaiting confirmation. Unfortunately, most of these planets have been detected with what we call *"indirect"* methods, which means that we have inferred their existence, and some of their basic properties, from the analysis of their parent stars' light. Ideally, we would like to be able to directly register and analyse the light coming from these planets but there is a major challenge we have to overcome: the contrast ratio between the planet and the star. The light from the planet is about nine orders of magnitude fainter than
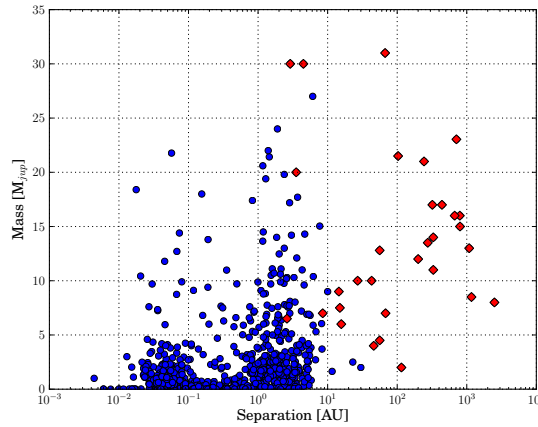
Figure 1.1: Mass vs. separation plot of the currently confirmed substellar companions. Red diamonds denote those that have been detected by direct imaging. *Source:* exoplanet.eu.

the light of its parent star when observing at visible wavelengths, and this is for a Jupiter-like planet orbiting at $1\,\mathrm{AU}$ from its parent star and seen from a distance of $4\,\mathrm{pc}$. In the case of a terrestrial planet this difference can increase up to about eleven orders of magnitude. So it is challenging.

In the past five years, considerable development of imaging instruments and techniques such as choronagraphy, adaptive optics and optimised data reduction, have allowed astronomers to obtain images of about 30 exoplanets. Figure 1.1 shows the mass vs. separation plot of all currently confirmed exoplanets where red diamonds mark those that have been discovered through direct imaging. These are, with a few exceptions, quite massive ($3-10\,\mathrm{M_{jup}}$), young ($\sim 1-90\,\mathrm{Myr}$) and hot ($\sim 1000\,\mathrm{K}$) planets orbiting at considerable distances from their parent star ($\sim 3-2000\,\mathrm{AU}$), characteristics that make them ideal targets for direct imaging at infrared wavelengths. Figure 1.2 shows the images of four of them: Fomalhaut b (which was detected at visible wavelengths), HR 8799 system (b,c,d,e), beta Pictoris b and kappa Andromedae b (Kalas et al. 2008, Marois et al. 2008, Marois et al. 2010, Lagrange et al. 2010). Looking at the position of the red diamonds in Fig. 1.1, we see that this technique covers a region of the mass-separation plane that is not available to indirect methods. This together with the fact that directly detected light allows for direct atmospheric characterisation (see e.g. Bowler et al. 2010, Barman et al. 2011, for the first direct spectroscopic results on the HR 8799 planets), is helping us greatly to expand our knowledge of currently known exoplanets.

But these planets have very little in common with our Earth and the planets we share the Solar System with. The radius of the orbit of our outermost planet, Neptune, is about $30\,\mathrm{AU}$, and its mass is $\sim 0.05\,\mathrm{M_{jup}}$,while our most massive planet is Jupiter, which orbits at $\sim 5\,\mathrm{AU}$

from the Sun. The age of our Solar System is about $4.5\,\text{Gyr}$. If we want to directly image anything like our Solar System, and in particular an Earth-like planet, we simply need to make our telescopes as big as possible, to be able to resolve features as close to the star as possible, and put together every "smart trick" we can think of to increase the contrast achievable with our instruments to distiguish the feature (hopefully a planet) and the starlight. And this is where polarimetry comes into play.
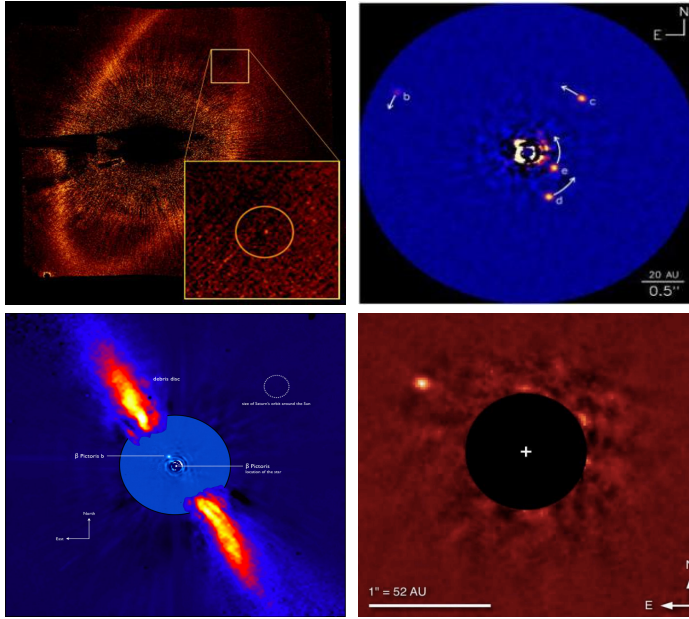
Figure 1.2: Some examples of directly imaged exoplanets. *Upper left:* Fomalhaut b (Kalas et al. 2008). *Upper right:* HR8799 b,c,d and e (Marois et al. 2008, Marois et al. 2010). *Lower left:* beta Pic b (Lagrange et al. 2010) *Lower right:* κ Andromedae b (Carson et al. 2013). *Images credit*: (from left to right and top to bottom) Paul Kalas/UC Berkeley, NASA, ESA; NRC-HIA, C. Marois, and Keck Observatory; ESO/A.-M. Lagrange et al.; NAOJ/Subaru/J. Carson (College of Charleston)

Light emitted by a star is generally unpolarised[1] and the particles in the atmosphere of a planet, or the dust grains in a circumstellar disc polarise the starlight as they scatter it towards us. This means that if we can observe a star/planet or star/disc system in polarised light, theoretically, only the planet/disc will show up in the image, provided that we can spatially resolve them. In reality the measurement of polarisation is not straightforward and often instrumental effects get in the way adding polarisation and/or modifying the polarisation state of the signal we want to measure (see Chapters 6 and 7). In addition, polarimetry is

---

[1]Starlight can get polarised due to e.g. magnetic fields or scattering processes in its own atmosphere but, in general, the contribution of these effects is negligible (Kemp et al. 1987)

a differential technique. We need to subtract orthogonally polarised images to distinguish polarised from unpolarised light, i.e. subtract signal. This translates to the need for a large amount of photons to detect small differences. But we shouldn't be discouraged by these issues. The current state of the art polarimetric techniques can already achieve contrasts between the star and its circumstellar regions of 10^{-6} (e.g. Rodenhuis et al. 2012, Milli et al. 2013) which means that we are doing pretty well in dealing with the challenges polarimetry encompass.

To add to the good news, the astronomical community is looking forward to the upcoming European Extremely Large Telescope (E-ELT) (Delabre 2008, McPherson et al. 2012). This telescope will have a primary mirror with a diameter of $D \sim 39\,\mathrm{m}$, which translates into more than $970\,\mathrm{m}^2$ of collecting area. Working at the diffraction limit, the spatial resolution delivered by this telescope will go from about 3 to $10\,\mathrm{mas}$ (at 0.6 and $1.6\,\mu\mathrm{m}$, respectively) which, when observing a star at $40\,\mathrm{pc}$ from our Sun, means that we could resolve features located at a tenth of an astronomical unit (AU) form the central star. These collecting and resolution capabilities make it ideal for performing highly sensitive and accurate polarimetry (see, e.g., Strassmeier & Others 2009, Keller et al. 2010).

What is the mechanism through which planets form? Is it the same for all planets and environments? What sets their final characteristics? Can planet formation be affected and even prevented by the environment? Can planets other then the Earth host life? To be able to answer such questions it is key to advance our knowledge on the characteristics of exoplanets and their cradles: protoplanetary discs.

This thesis is composed of a collection of studies focused on developing new observational and instrumental polarimetric imaging techniques that could serve in this quest: the characterisation of exoplanets and their birth environment. However, in favour of this ultimate goal, other techniques are explored in some of the studies.

1.1 Scattering and polarisation

Scattering takes place when an electromagnetic wave encounters matter. As described in the excellent book *"Absorption and scattering of light by small particles"* by Bohren & Huffman (1983), one could, very basically, picture this process as follows. The oscillatory electric field of the wave induces a dipole moment in the discrete electric charges that compose matter. These dipoles oscillate and re-radiate in all directions giving rise to the scattered radiation, which, in the case of elastic scattering (the type we consider in this thesis), has the same frequency as the incident radiation.

In any case, the scattered radiation becomes linearly polarised due to the geometry of the process. We can, again, try to picture the underlying physics in a very basic manner. Electromagnetic radiation is carried by waves that are composed of mutually perpendicular oscillations of the electric and magnetic fields. These oscillations, in isotropic media, are also perpendicular to the direction of propagation. If the two orthogonal components (e.g. x- and y-) of the electromagnetic field have a fixed phase difference, then we say that the light is polarised. In particular, if this fixed difference is zero (i.e. the x- and y-components are
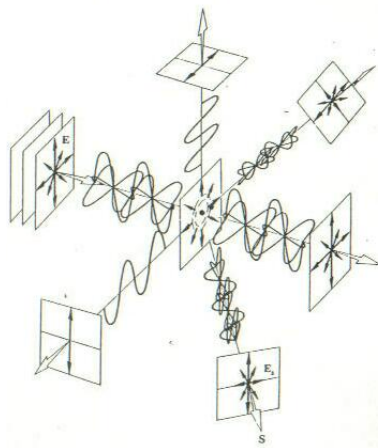
Figure 1.3: Schematic view of polarization of light by scattering off a single particle. The electric field of the unpolarized incoming light, vibrating in all directions contained in the perpendicular plane to the direction of propagation, sets the electric charges in the particle (black dot) into vibration emitting the scattered radiation. The scattered light is therefore fully polarised in any direction contained in that plane. In other directions, the scattered light will be partially polarised, with the exception of the direction of the original propagation, in which light will be unpolarised. *Image credit*: Hecht, Eugene, Optics 4th Edition, © 2002. Reproduced by permission of Pearsons Education, Inc., Upper Saddle River, NJ.

in phase) we say that light is linearly polarised and, in this case, the direction of vibration of the electric (and, therefore, magnetic) field is unique. Now, when unpolarised radiation encounters a particle, as explained before, the dipoles in the particle are set into oscillation. These induced oscillations occur in random directions because there is no preferred direction of the electric field, but all these random directions are contained in the plane perpendicular to the direction of propagation, i.e. there is no oscillation parallel to the propagation. Light scattered in any direction contained in that plane, will be linearly polarised because the oscillations that generated it are all contained in the plane. Figure 1.3 shows a schematic view of this process.

Reflection and refraction can be seen as a particular scattering processes where the medium encountered by the light is optically dense (separation between scatterers is small compared to the wavenegth of the incident radiation) and there is an infinite (compared to the wavelength) and continuous boundary separating the two media (a surface) (Bohren & Huffman 1983). Light reflected off a surface like a mirror or the surface of a planet, becomes therefore polarised in a similar fashion. This, as we shall see in Chapters 6 and 7, turns to be a big problem in astronomical polarimetry since light undergoes multiple reflections and refractions in the optical path of telescopes and optical instruments.

1.1.1　Stokes formalism and Mueller matrices

In dealing with the interactions between optical elements and polarised light, the chapters in Part II of this thesis adopt the mathematical framework of the Stokes formalism (Stokes 1852). In this formalism light is described by a four component vector $\mathbf{S} = (I, Q, U, V)^T$ where I is the intensity, Q and U are linear polarisations in the $0/90°$ and $\pm 45°$ directions[2] and V is circular polarisation. The effect a medium has on light as it passes through can be described by a transformation of its Stokes vector. Therefore, we can mathematically describe the interaction by a matrix multiplication between the incoming Stokes vector ($\mathbf{S}_{\mathrm{in}}$) and a 4×4 matrix ($\mathbf{M}_{\mathrm{medium}}$) that describes the characteristic of the medium, the so called Mueller matrix (Mueller 1948). The transformed Stokes vector ($\mathbf{S}_{\mathrm{out}}$) is then obtained as:

$$\mathbf{S_{out}} = \mathbf{M_{medium}}\mathbf{S_{in}} \,. \tag{1.1}$$

If one knows the Muller matrices of individual elements in an optical system, the total Muller matrix of the system ($\mathbf{M}_{\mathrm{total}}$) can be obtained as

$$\mathbf{M}_{\mathrm{total}} = \mathbf{M_n} \cdot ...\mathbf{M_2} \cdot \mathbf{M_1} \,, \tag{1.2}$$

where $\mathbf{M_n}...\mathbf{M_1}$ represent the Mueller matrices of the n elements of the optical system with 1 being the first element in the optical path and n being the last. Equation ?? below shows how each element of the Mueller matrix describes the relationship between a component of the incoming Stokes vector and a component of the outgoing Stokes vector.

$$\mathbf{M} = \begin{pmatrix} I_{\mathrm{in}} \to I_{\mathrm{out}} & Q_{\mathrm{in}} \to I_{\mathrm{out}} & U_{\mathrm{in}} \to I_{\mathrm{out}} & V_{\mathrm{in}} \to I_{\mathrm{out}} \\ I_{\mathrm{in}} \to Q_{\mathrm{out}} & Q_{\mathrm{in}} \to Q_{\mathrm{out}} & U_{\mathrm{in}} \to Q_{\mathrm{out}} & V_{\mathrm{in}} \to Q_{\mathrm{out}} \\ I_{\mathrm{in}} \to U_{\mathrm{out}} & Q_{\mathrm{in}} \to U_{\mathrm{out}} & U_{\mathrm{in}} \to U_{\mathrm{out}} & V_{\mathrm{in}} \to U_{\mathrm{out}} \\ I_{\mathrm{in}} \to V_{\mathrm{out}} & Q_{\mathrm{in}} \to V_{\mathrm{out}} & U_{\mathrm{in}} \to V_{\mathrm{out}} & V_{\mathrm{in}} \to V_{\mathrm{out}} \end{pmatrix} \,, \tag{1.3}$$

where the subscripts in and out refer to incoming and outgoing Stokes vector components, respectively.

The four Stokes components have to fulfill some requirements to constitute a physically meaningful Stokes vector, i.e.

$$I^2 + Q^2 + U^2 + V^2 \geq 0 \quad \text{and} \quad I \geq 0 \,. \tag{1.4}$$

In order to retain the physical meaning of the Stokes vector through the transformation, a 4×4 matrix must as well meet some requirements to be a Mueller matrix, e.g. element $I_{\mathrm{in}} \to$

---

[2]$+$ and $-Q$ and U denote orthogonal polarisation directions, i.e. $+Q$ corresponds to linear polarisation in the e.g. $0°$ direction while $-Q$ corresponds to $90°$. $+V$ or $-V$ correspond to right or left-handed circular polarisation, respectively, depending on the reference system chosen.

I_{out} must be positive ($M_{00} \geq 0$) and first row and columns must be physically meaningful Stokes vectors, i.e. they have to fulfill the conditions in Eq. 1.4 (see del Toro Iniesta 2003, and references therein). Mueller matrices can be defined for most types of medium, optical element and, as we said, complex optical system and they are the key element we will be using for the analysis of the polarimetric performance of optical telescopes in Part II of this thesis.

1.1.2 Measuring polarisation

As we have noted before, polarimetry is is a differential technique. Unless we can directly measure the amplitude and phase of the electromagnetic field (which is the case for waves in the radio domain), to measure the amount of polarisation light carries in a certain direction we need to take two intensity measurements: one *filtering* polarised light in that particular direction and another one filtering polarisation in the orthogonal direction. As a very basic example, we can think of a detector placed after a linear polariser, which only lets through light polarised in a certain direction. If we orient the polariser to let light polarised in the $0°$ direction pass (we define this to be the $+Q$ direction), the intensity recorded by our detector is

$$I_{0°} = 0.5 \cdot (I + Q).$$ (1.5)

If we now rotate the polariser to the $90°$ position ($-Q$ direction), we measure

$$I_{90°} = 0.5 \cdot (I - Q).$$ (1.6)

Now,

$$Q = (I_{0°} - I_{90°}).$$ (1.7)

In the same way, rotating our polariser between $\pm 45°$ we can obtain U as

$$U = (I_{45°} - I_{-45°}),$$ (1.8)

and, if we place an optical element capable of transforming circularly polarised light into linearly polarised light before our linear polariser in the optical path, we obtain a circular polariser with which we can also measure circularly polarised light as

$$V = (I_{\text{RHcircpol}} - I_{\text{LHcircpol}}).$$ (1.9)

The different positions of the polariser define a particular state of the measuring device (polariser+detector) that we call modulation states. Our example pictured the simplest possible
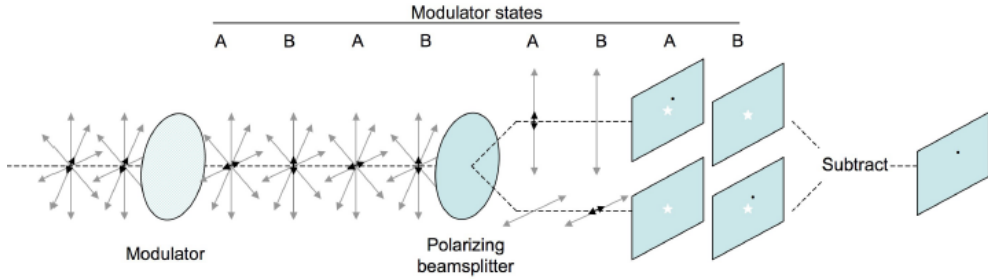
Figure 1.4: Schematic view of the polarization measurement process using temporal and spatial modulation used by ExPo. The modulator switches between orthogonal directions of the polarisation to be measured, defining states A and B. The polarising beamsplitter then separates the two orthogonal polarisation states into left (L) and right (R) beams. Double subtraction of (AL-AR)-(BL-BR) minimises (systematic) spatial and temporal differences (Canovas et al. 2012a). *Image credit:* M. Rodenhuis

way of modulating but one can design, and optimise, many different modulation schemes depending on what Stokes component (or cobination of them) one is interested in measuring. More generally, instead of using a rotating polariser, the modulation is achieved by means of a retarding element (i.e. *modulator*) and a fixed polariser (i.e. *analyser*). A retarding element imparts a phase lag to one of the orthognal components of the electric field, thus, modifying the polarisation state of the wave passing through. by carefully orienting the retarder in the required direction we can *transform* the polarisation state we want to measure in the direction the fixed polariser would filter to the detector.

However, one has to be very careful when using this technique since, even though this subtraction can eliminate many systematic errors, any differences between the two states being subtracted will appear as polarisation signal. To minimise these effects, the two orthogonally polarised intensity measurements should be as equal as possible, temporally and spatially. Ideally, one takes the two intensity measurements instantaneously assuring that the optical paths of the two orthogonal beams are exactly the same. This is, of course, not possible and either we take measurements of the orthogonal states instantaneously spatially separating the two beams (i.e. *spatial modulation*) or we measure the beams through the same optical path at separated times (i.e. *temporal modulation*). Most night-time polarimeters operating today combine these two types of modulation that allow to apply techniques such as the double difference (Bagnulo et al. 2009, Hinkley et al. 2009) or the double ratio (Semel et al. 1993, Tinbergen 1996, Schmid et al. 2006b) which minimise systematic errors and atmospheric effects. Fig. 1.4 shows a schematic example of the temporal and spatial modulation combination used designed for the Extreme Polarimeter, ExPo (Rodenhuis et al. 2012). Other types of modulation such as the *spectral modulation* (Nordsieck 1974, Snik et al. 2009) provide very interesting prospects for improvement.

Mathematically, at each modulation state m, the polarimetric system (in our example simply composed of $modulator + analyser + detector$) will be represented by its Mueller matrix $\mathbf{M}_\mathrm{m}$. The first row of that Mueller matrix describes how each incoming Stokes component is transformed into the intensity that the detector will register (see Eq. 5.2), thus describing the modulation state. If we build a matrix out of all m first rows of the Mueller matrices at each modulation state, we have what is known as the *modulation* matrix, normally denoted as $\mathbf{O}$. This matrix relates the incoming Stokes vector with the $1 \times m$ vector composed by all the consecutive intensity measurements (I_m), as follows:

$$\mathbf{I}_\mathrm{meas} = \mathbf{O}\mathbf{S}_\mathrm{in}\,, \tag{1.10}$$

where $\mathbf{I}_\mathrm{meas} = (I_1, I_2, \ldots, I_m)^T$, and describes the modulation scheme of our polarimetric system. In the end, the polarimetric problem consists of obtaining the incoming Stokes vector, $\mathbf{S}_\mathrm{in}$, from the m intensity measurements. If the $4 \times m$ matrix $\mathbf{D}$ is an inverse of $\mathbf{O}$ (i.e. $\mathbf{D}\mathbf{O} = \mathbb{1}$), then,

$$\mathbf{S}_\mathrm{meas} = \mathbf{D}\mathbf{I}_\mathrm{meas}\,, \tag{1.11}$$

and $\mathbf{D}$ is known as the *demodulation* matrix (del Toro Iniesta & Collados 2000). Note that we denote the vector resultant from this operation as $\mathbf{S}_\mathrm{meas}$ and not $\mathbf{S}_\mathrm{in}$ because the measurement process is never perfect and therefore the original $\mathbf{S}_\mathrm{in}$ cannot be perfectly recovered.

The transformation undergone by a Stokes vector that goes through the measurement process defined by our polarimetric elements and our modulation/demodulation process can be mathematically represented by the *response* matrix $\mathbf{X}$ (Ichimoto et al. 2008), which is defined as,

$$\mathbf{X} = \mathbf{D}\mathbf{O}\,, \tag{1.12}$$

and therefore,

$$\mathbf{S}_\mathrm{meas} = \mathbf{X}\mathbf{S}_\mathrm{in}\,, \tag{1.13}$$

where $\mathbf{S}_\mathrm{meas}$ is the Stokes vector we obtain as a result of the polarimetric process. Ideally, and almost by definition, $\mathbf{X} = \mathbb{1}$, but in reality, our polarimetric instruments and modulation-demodulation schemes are never completely efficient. The response matrix becomes then an important tool to evaluate the efficiency or "goodness" of our polarimetric system and to help in its optimisation. The usefulness of the response matrix as a diagnostic tool is particularly exploited in Chapter 7 for the analysis of the limitations the different Nasmyth configurations of the E-ELT telescope impose on polarimeters working at that position.

For a much deeper description of the mathematical process outlined here, I recommend the excellent book *"Introduction to Spectropolarimetry"* (Chapters 4 and 5 in particular) by del Toro Iniesta (2003) and references therein.

1.2   Some open questions on planet formation

Despite the amount of exoplanets found and the great effort that is being put into the field, we currently do not fully understand how planets form. We know they form out of the dust and gas that remains from the star formation process, and that orbits the star forming what we call a *protoplanetary* disc. We also know, to some degree, what is the result of the process, i.e. planet formation and evolution theories should be able to reproduce the characteristics and frequencies of the planets we know from observations. This is not the case yet (e.g. Ida & Lin 2004, Mordasini et al. 2009). The problem of evolving discs into planetary systems is complex and involves physical processes related to e.g. hydro and magnetodynamics, radiative transfer, high energy physics and physics of collisions, and they all interact to affect the formation of planets and their evolution through disc-environment, planet-disc, planet-planet and planet(s)-environment interactions.

1.2.1   Planet formation and migration

There are two currently accepted theories of planet formation: *core accretion* (e.g. Safronov 1969, Pollack et al. 1996, Ida & Lin 2004) and *gravitational instability* (e.g. Cameron 1978, Boss 1997). The first one proposes the scenario where planets form by first growing micronsized dust grains all the way up to kilometer sizes, in principle, through coagulation of particles driven by collision. These kilometer-sized *planetesimals* are now enough massive to grow through gravitational interactions reaching thousands of kilometers, point at which they start to accrete gas. Depending on their mass and the available amount of gas, they can form terrestrial planets or gas giants (see Alexander 2013, for a recent review). This mechanism is the preferred one to explain the formation of rocky and up to Jupiter-mass planets at radial separations lower than $< 10\,\mathrm{AU}$ (Ida & Lin 2004, Pollack et al. 1996).

In turn, the second theory puts forward the idea that a gaseous disc, if massive and turbulent enough, can become gravitationally unstable, quickly fragmenting into self-gravitating structures, which then collapse to become giant planets. This mechanism could form very massive planets and operates at distances of about $30 - 50\,\mathrm{AU}$ from its parent star (Rafikov 2005, Matzner & Levin 2005, Stamatellos & Whitworth 2008).

Neither of these theories is, however, free from caveats. For example, as explained above, planets formed by gravitational instability can be very massive and form far away from the star. This could explain the existence of the population of massive giant planets located far from their star that we see. The problem is that, once they form, they are very unlikely to remain at such distances. Migration processes are likely to rapidly bring the planet closer to the star due to the interaction with the gravito-turbulent disc (Baruteau et al. 2011, Zhu et al. 2012). Some other migration mechanisms, as well as planet-planet interactions, have been proposed to become active when the planet reaches the inner regions and have the potential to slow down, stop or even reverse the inward drift, but they are still under study (see Baruteau & Masset 2013, for a great review on planet migration).

Also, the story of the core accretion scenario is one full of *"barriers"* (Weidenschilling 1977, Brauer et al. 2008, Okuzumi 2009, Zsom et al. 2010). One of the most important is
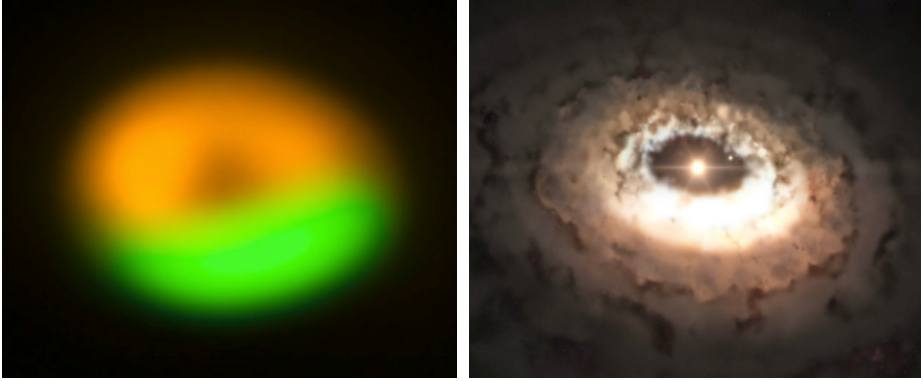
Figure 1.5: ALMA Cycle 1 image (*left*) and artist impression (*right*) of a *"dust trap"* (van der Marel et al. 2013). The color scale in the ALMA image corrresponds to density. The data shows how mass is accumulating at a particular position in the disc generating a large density asymmetry. *Image credit*: www.eso.org

the so-called *1-meter barrier* (Weidenschilling 1977, Brauer et al. 2008), where 1-m sized particles should be depleted from the disc due to *"radial drift"*. This mechanism is caused by the difference in velocity between the gas and dust particles in the disc which generates a drag force that causes the dust particles to lose momentum and spiral inwards. When the dust particles reach the $\sim 1\,\mathrm{m}$ size scale, the radial drift makes them flow to the star in timescales shorter than those needed to grow to larger sizes. Also in this case some mechanisms have been proposed to overcome the problem. Studies such as Rice et al. (2006), Alexander & Armitage (2007), Brauer et al. (2008), Zhu et al. (2011, 2012), Pinilla et al. (2012a), Regály et al. (2012), Birnstiel et al. (2013) have explored the concept of *"particle traps"* where dust can accumulate and grow *"protected"* from the radial drift (see next subsection and Chapter 3 for more details). These theories are currently gaining weight as recent millimeter and sub-millimeter observations of protoplanetary discs have revealed structures matching their predictions (e.g. Ohashi 2008, Mayama et al. 2012, Casassus et al. 2013, van der Marel et al. 2013)

1.2.2 Disc evolution: Transitional discs

It is obvious from the description of the previous section that the characteristics of the disc where planets form strongly influence the planet formation process, which in turn sets the initial characteristics of the planet(s), as well as the conditions for their posterior evolution. This means that the study of protoplanetary discs can provide important information to constrain planet formation and evolution processes.

Protoplanetary discs have a median lifetime of 2-3 Myr, although the span goes from 1 to $10\,\mathrm{Myr}$, approximately (e.g.Sicilia-Aguilar et al. 2008, Mamajek 2009, Luhman et al. 2010,

Ercolano et al. 2011, see Williams & Cieza 2011, for an extended review and Bell et al. 2013 for a recent study suggesting longer lifetimes of up to $12\,\mathrm{Myr}$). This is an important constraint for planet formation and evolution since both formation and migration processes require the disc to be present in order to operate[3]. Processes such as accretion onto and photoevaporation from the central star are thought to dominate the evolution of the disc and eventually cause its dissipation (e.g. Hartmann et al. 1998, Muzerolle et al. 1998, Clarke et al. 2001, Alexander et al. 2006, Gorti et al. 2009a). At the same time, mechanisms such as coagulation, fragmentation, settling and the previously mentioned radial drift operate together to define the radial, azimuthal and vertical distribution of dust in the disc at different times (e.g. Dullemond & Dominik 2004, 2005, Dullemond et al. 2008, Weidenschilling 2008, Brauer et al. 2008, Birnstiel et al. 2010).

A particularly interesting sub-category of protoplanetary discs is that of *"transitional discs"*. These discs were first detected when spectroscopic analyses of some protoplanetary discs showed a lack of the typical 10-20 μm silicate feature in the spectral energy distribution (SED) (Strom et al. 1989, Calvet et al. 2002, 2005). Because emission at those wavelengths is dominated by small (on the order of microns and less) warm dust, this was interpreted at first as a signature of disc *clearance* localised in regions of the disc close to the star. Indeed, images of these discs at sub-millimeter wavelengths revealed inner holes of a few tens of AUs in most of the targets with transitional SEDs (e.g. Andrews et al. 2011). Because they seem to represent the transition between a full (i.e. an evolutionary stage named Class II) and dissipated (i.e. evolutionary stage Class III) disc they were eventually referred to as transitional discs (e.g. Calvet et al. 2002). Recently, another sub-category called *"pre-transitional discs"* (Espaillat et al. 2007) has been proposed to group those discs which do present emission from an inner disc and a separated outer disc, in other words, a *"gap"* instead of an inner hole.

Transitional and pre-transitional discs present a considerable variety of gap/hole sizes, accretion rates, SED shapes and imaged structures, which could be indicative of different processes dominating the depletion of mass (e.g. Najita et al. 2007, Espaillat et al. 2007). The main candidates to be the responsible mechanism are grain growth, photoevaporation and dynamical interactions between the disc and a planet (see Williams & Cieza 2011, Alexander 2013, and references therein) or a combination of them (Rosotti et al. 2013). All of them have the potential to reproduce the type of SEDs and sub-millimeter and millimeter images transitional discs show, but they affect the distribution of gas and dust very differently. For example, the process of photoevaporation depletes the affected region of both gas and dust (e.g. Clarke et al. 2001), whereas grain growth only produces a depletion on the distribution of dust in the region, leaving the gas distribution unaffected (e.g. Dullemond & Dominik 2005).

The interaction between the disc and a planet is, for obvious reasons, one of the most exciting processes to be considered as the cause of this transitional morphology. As we mentioned in the previous section, the presence of a planet modifies the distribution of gas in the disc triggering accumulation and filtering processes. These are interesting because 1) they

---

[3]Of course, after dissipation of the disc, processes such as dynamical interactions can still take place and play an important role in shaping the planetary system (e.g. Brasser et al. 2009, Morbidelli et al. 2009)

generate particular structures in the disc that could not be reproduced by photoevaporation or grain growth and 2) because they provide a shelter for dust particles to grow overcoming the 1-meter barrier and therefore providing the potential for planet formation. Figure 1.5 shows the recent astonishing observations presented by van der Marel et al. (2013) along with an artist's impression. In this work, the authors used ALMA Cycle 1 to look for signatures of planet formation in the gap of the transition disc orbiting Oph IRS 48. Observations of the disc probing micron-sized dust grains and gas suggested a structure of rings centered on the star whereas the emission detected from millimeter-sized grains showed an asymmetry, hinting the accumulation of this type of grains at a particular position in the gap.

This work, along with other observational studies such as e.g. Casassus et al. (2013), Dong et al. (2012), Quanz et al. (2013a), Maaskant et al. (2013) where multi-wavelength imaging techniques are applied to transitional discs to probe different parts of the gas and dust distribution, are starting to highlight the importance of defining a set of imaging diagnostics to understand the origin of these targets and constrain the properties of any companions that may be responsible for their observational signatures. In Chapter 3 of this thesis (de Juan Ovelar et al. 2013) we present a study on this particular issue. Based on hydrodynamical and dust evolution models we simulate imaging observations of transitional discs to explore the different observational signatures generated by the presence of the planet.

1.2.3 Environmental effects

So far, we have only considered the parameters that influence planet formation and evolution in disc-planet systems that are *"isolated"*. But most stars form in groups that may be gravitationally bound for enough time to have an impact on the evolution of the disc and/or planetary systems (e.g. Lada & Lada 2003, Kruijssen 2012). There are two main mechanisms through which the environment can act upon the evolution of a disc and/or a planetary system: photoevaporation from nearby massive stars (Scally & Clarke 2001, Adams et al. 2004, 2006, Fatuzzo & Adams 2008) and dynamical interactions between stars (e.g. Bonnell et al. 2001, Olczak et al. 2006, 2010, Spurzem et al. 2009, Dukes & Krumholz 2012, Parker & Quanz 2012).

The most visual example we have of these type of interactions are the beautiful Hubble Space Telescope images of the Orion propyds. Figure 1.6 shows a few images of these targets where we can see how the ultra-violet field generated by the group of O stars in the center of the cluster is eroding, through photoevaporation, the outer part of the discs surrounding these young stars. To what degree is this process affecting the potential of discs to form planets? Is external photoevaporation or dynamical interactions the dominant process for disc truncation in high stellar density environments? Does this depend on the characteristics of the environment? How does this affect the habitability of planets, if formed?

From the observational point of view several studies have been carried out in nearby star forming regions (SFRs) aiming to answer some of these questions (e.g. Eisner & Carpenter 2006, Mann & Williams 2010, Furlan et al. 2011, Luhman & Mamajek 2012). However, these either probe low density environments or lack the number of sources required to provide

Figure 1.6: Hubble Space Telescope images of some Orion *"proplyds"*. *Credit*: NASA, ESA

statistically conclusive evidence for the environmental impact. So far, no planets have been
found in dense globular clusters (Gilliland et al. 2000, Nascimbeni et al. 2012). Is this related
to the old age and high density of these environments? Is there a value for the ambient stellar
density in a SFR above which planets cannot form or evolve in the way our Solar System
did? In Chapter 4 of this thesis (de Juan Ovelar et al. 2012b), we present a statistical analysis
of the distribution of radii of resolved discs with respect to the ambient surface stellar density
(Σ) of their SFR. As a result, we provided tentative evidence for the truncation of discs in
environments with $\Sigma > 10^{3.5}\mathrm{pc}^{-2}$. However, to confirm the relation with ambient stellar
density, we still need to probe denser environments and although the observed truncation is
consistent with our estimate for that generated by dynamical interactions, we cannot assure
that photoevaporation is not the cause. Moreover, even if we manage to constrain the relation
between truncation and environment, we still lack a complete theoretical model to predict the
impact on planet formation and evolution.

1.2.4 Planet characteristics. Life?

The field of characterisation of exoplanets is rapidly advancing thanks to the improvement of
instrumentation and data reduction techniques. Through indirect methods (i.e. radial velocity,
microlensing and transit) it is possible to obtain an estimate of the physical characteristics of
exoplanets such as their mass, period, size and density. However, without multi-wavelength
photomoetry or spectroscopy of some kind, it is not possible to obtain information about their
chemistry and composition. Only recently, the use of *"transit spectroscopy"*[4] has allowed for

---

[4]This technique consists of measuring the spectrum of the stellar light during an eclipse with its orbiting planet.
The analysis of the absorption features in the spectrum provides information about the chemical composition of the
atmosphere of the planets.

such studies (see e.g. Tinetti et al. 2007, Snellen et al. 2010, Huitson et al. 2012 and Seager & Deming 2010, for an extensive review on the field).

Regarding directly imaged exoplanets also a number of studies have been published so far with measured spectra (e.g. Chauvin et al. 2004, Mohanty et al. 2007, Patience et al. 2010, Bowler et al. 2010, Barman et al. 2011, Oppenheimer et al. 2013). The analysis of these spectra and comparison with theoretical atmospheric models has provided important constraints on the physical and chemical properties of these bodies as well as the opportunity to improve these models.

Despite these advances, we still don't have enough data to draw strong conclusions on how these planets have formed and evolved. Moreover, no photometric or spectroscopic data can provide information about the structure of the atmosphere/surface of the planets because we cannot resolve them. Instead, we just detect the light integrated over the area occupied by the planet in our detector (i.e. the *"disc integrated"* light). Do these planets have oceans and continents distributed in an inhomogeneous manner? Are they covered by haze? Are their clouds distributed in bands or patches?

For a planet to be able to host life (as we know it) it has to allow the existence of liquid water. The radial separations from a star where the temperature allows for a planet with an Earth-like atmosphere to meet this requirement is known as the *habitable zone*. By measuring planet transits, the Kepler (Koch et al. 1998) instrument has been able to identify about ~ 50 exoplanet candidates with sizes comparable to the planets in our solar system (the ones more massive than Earth) lying in the habitable zone of their host stars (see Borucki et al. 2011, for an overview on the characteristics of planets found by Kepler). Undoubtedly, the next big step is to find out whether these planets host any liquid water that would allow life to potentially develop.

1.3   Using imaging polarimetry

1.3.1   Protoplanetary discs

High contrast imaging polarimetry is a relatively young field in night-time astronomy, but in its short life it has proved to be very valuable. In 1997 Close et al. published polarimetric images of the Herbig Ae/Be star R Monocerotis obtained with an AO system, which made them the first high-contrast polarimetric images ever obtained from a star other than the Sun. Since then, observers have successfully applied this technique to image circumstellar environments of both young and old stars (Quanz et al. 2011, Hashimoto et al. 2011, Quanz et al. 2012, Canovas et al. 2012b, Jeffers et al. 2012, Dong et al. 2012, Thalmann et al. 2013, Quanz et al. 2013b, Canovas et al. 2013).

As we pointed out before in this introduction, the main characteristics that make polarimetry a very powerful technique are 1) it reduces the contrast between the central starlight and the surrounding (scatering) matter (Keller et al. 2010), and 2) it provides important information about the structure and composition of the scattering environment that cannot be obtained by only measuring intensity (see Min et al. 2012, for an example on the effects dust structure
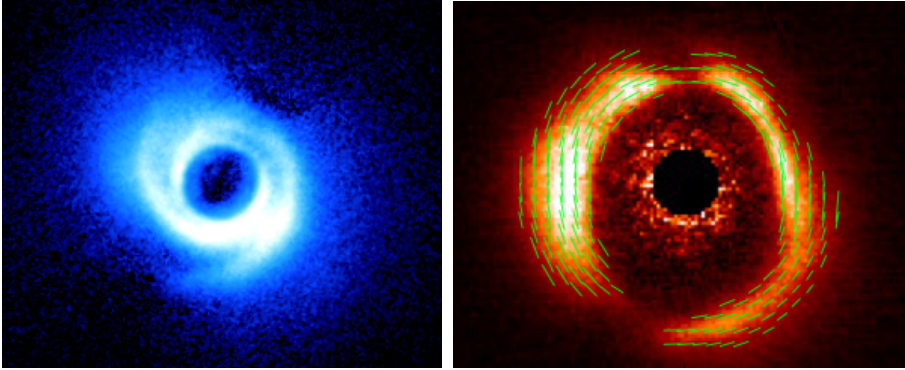
Figure 1.7: Polarimetric images of the polarised intensity flux of the transition discs around SAO 206462 (left) and HD 142527 (right) obtained with Subaru/HiCIAO and VLT/NACO, respectively (Muto et al. 2012, Canovas et al. 2013). *Image credit*: NAOJ/Subaru and Canovas, A&A, 556, A123, 2013, reproduced with permission ©ESO.

has on polarimetric measurements of circumstellar discs).

One interesting polarimeter working at the $4.2\,$m William Herschel Telescope in La Palma is the *Extreme Polarimeter* (ExPo, Rodenhuis et al. 2012). Operating as visiting instrument, it can provide a contrast between the star and its surrounding of five orders of magnitude without the use of any AO or choronagraphic systems. The instrument has undergone recently an upgrade that has resulted in the addition of an AO system and the design of an integral field unit (Rodenhuis et al. 2012).

If ExPo is a clear example of the application of the first quality of polarimetry we listed, instruments like VLT/NACO (Lenzen et al. 2003, Rousset et al. 2003) or Subaru/HiCIAO (Hodapp et al. 2008) are the flagship examples of usage of the second. These instruments work with as much as four times the collecting area delivering to ExPo (primary mirror diameters of about $\sim 8\,$m) and they operate with the assistance of advanced AO and choronagraphic systems. This means that the contrast performance is already high and polarimetry can take the next step and explore the details of the (already detectable in intensity) structures in the disc. The left panel of Fig. 1.7 shows a polarimetric image of the transition disc around SAO 206462 obtained with Subaru/HiCIAO (Muto et al. 2012). The authors detected, for the first time, dust in the (previously thought empty) hole of the transition disc (at about $\sim 30\,$AU) and spiral features at about $\sim 70\,$AU. By modeling these spiral features the authors showed that they are consistent with the presence of embedded planets. The right panel shows a polarimetric image of the transition disc around HD 142527 obtained by Canovas et al. (2013) with VLT/NACO. In this study, polarimetric measurements were used to constrain the characteristics of the dust particles in the disc and detect new spiral features and regions depleted of small dust grains that are in agreement with the position of dust traps in the disc previously reported by Casassus et al. (2013) and predicted by the theories we

mentioned in Section 1.2.2.

The interpretation of observational results like these is in itself a challenge that requires combination of state of the art hydro-dynamical, dust evolution models and radiative transfer codes (e.g. Masset 2000, Birnstiel et al. 2010, Pinilla et al. 2012a, Min et al. 2009).

As these observations prove, polarimetric images are very powerful by themselves but that is far from being the end of the story. As mentioned before, in Chapter 3 of this thesis we present synthetic observations of transition discs where we show that combining visible and near-infrared polarimetry with mid-infrared and sub-mm images of transitional discs is a very promising strategy to constrain characteristics of the companion that is potentially causing these impressive structures in the discs.

1.3.2   Exoplanets

The main success of planet direct imaging has come with the development of techniques such as Angular Differential Imaging (ADI, Marois et al. 2006) that make possible to differentiate (planetary) point-like sources from the remnants of the star halo after subtracting the stellar point spread function (PSF), i.e. the *"speckles"*. This technique however requires the field of view to rotate with respect to the detector which is counterproductive for polarimetric purposes. If the sky rotates in between orthogonally polarised frames, as is the case when using pupil-stabilised observing modes for ADI, the position of the planet will not be the same in the detector, and the subtraction we perform to obtain the polarised intensity image will introduce spurious polarimetric signals. It is therefore not trivial to combine these two techniques. In Chapter 2, we present the first results of an ongoing study we are performing to develop an optimal combination of these techniques (polarimetric and angular differential imaging, PADI) that allows to measure the polarisation signal of giant exoplanets using VLT/NACO observations of the HR 8799 planetary system.

Hot giant planets that orbit far away from their parent star such as the HR 8799 planets, are not likely to show polarisation due to scattered starlight due to the distance. However, in 2011 de Kok et al. published a study where they show how hot giant planets are likely to polarise their own infrared emission due to scattering in their atmosphere, an effect that has been measured in brown dwarfs (Ménard et al. 2002, Tata et al. 2009). The atmosphere of these bodies scatter the infrared emission that comes from the interior of the planet. If the atmosphere has a spherical symmetry, the different directions of this polarisation cancel each other when integrated over the disc. But if the atmosphere features asymmetries caused by e.g. patches of clouds, bands, flattening due to rotation or night-day side effects, some polarisation signal remains in the disc-integrated signal we detect from Earth (see Fig. 1.8). Mere detection of polarisation would prove the existence of clouds, and the degree and direction of polarisation would provide information about the atmosphere structure that would be unobtainable by other means.

For a direct polarimetric detection of a low mass exoplanet, we need to wait for future instruments. In a recently published study Milli et al. (2013) have shown that the prospects of achieving this with the upcoming VLT/SPHERE-ZIMPOL instrument (see Section 1.4) are
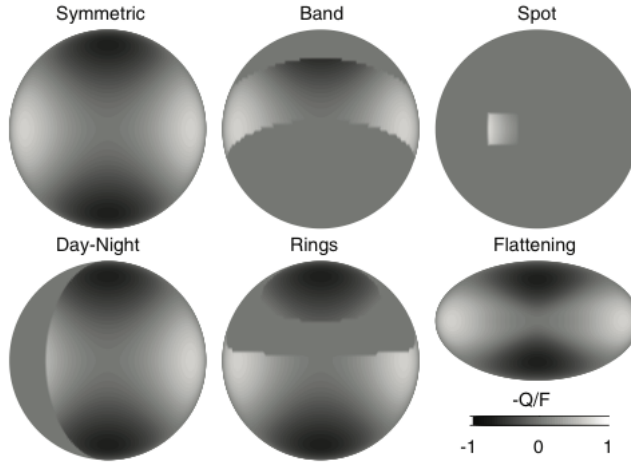
Figure 1.8: Simulated images of the structure generated by different atmospheric features in the fractional polarisation signal of a planet. When integrated over the disc, if the structure presents asymmetries, the polarisation signal remains (de Kok et al. 2011). *Image credit: R. de Kok*

considerable.

Looking farther on the horizon, theoretical work developed to model the polarimetric signatures of low-mass (Earth-like) planets has shown that polarimetry will not only be needed to perform characterisation of the structure and composition of these planets and their potential to host life (Karalidi et al. 2011, Karalidi & Stam 2012, Karalidi et al. 2012, 2013) but also that neglecting its effect in the measured disc-integrated signals will lead to errors in the interpretations of the data (Stam & Hovenier 2005).

1.4   Polarimetry with the E-ELT and VLT telescopes. Instrumental Polarisation

The Very Large Telescope (VLT) and European Extremely Large Telescope (E-ELT) are ideal facilities to exploit the powerful capabilities of polarimetry. Up until September 2013, when it was removed from the $8.2\,\mathrm{m}$ VLT's unit telescope 4 (UT4) to be further relocated, NACO was one of the most successful instruments when it comes to direct imaging of exoplanets and polarimetric imaging of circumstellar environments. And that is despite the fact that it was not optimised for polarimetric measurements. An instrument like the upcoming VLT/SPHERE (see following subsections), which features advanced polarimetric and adaptive optics systems, could resolve faint features about $\sim 4\,\mathrm{AU}$ across at $140\,pc$. With such an instrument the prospects for exoplanetary research will be greatly expanded.

Now, in terms of collecting power and advanced technology, a telescope like the E-ELT

simply does not have competition. The planet finder EPICS designed to work on it and featuring extreme AO, spectrographic and polarimetric systems, will, without a doubt, revolutionise the field.

However, these two instruments (i.e. VLT/SPHERE and E-ELT/EPICS) will be located at the Nasmyth focus of their respective telescopes. As we explain in Section 1.4.2 below, this focus is not optimal for polarimetry since instrumental effects are likely to considerably affect the polarimetric performance of the instrument. Moreover, apart from their dependecy on the particular design and quality of the optical elements, these effects vary with conditions of the observations such as e.g. wavelength and pointing. It is therefore crucial to characterise in detail the polarimetric performance of these telescopes and come up with strategies and clever designs to fight the instrumental *"pollution"* of our precious signal.

It is with this aim that we developed the M&m's code.

1.4.1   The M&m's code

Polarimeters are rarely built following the systems engineering approach to design, as is the case for almost all other (optical) instruments. There is currently no code available that can serve as a performance simulator and error budgeting tool for polarimetric systems. But in the era of instruments for telescopes such as the VLT or E-ELT, the scales do not allow for trial-and-error, and an accurate analysis of the error and performance budget is imperative.

The main reason why a systems engineering approach has not been formalised in polarimetry is the complexity of the error propagation in such systems. As described in Section 1.1, we model polarisation using vectors, and therefore errors have to be described (and propagated) as such. This poses the challenge of propagating errors throughout the optical system (and measurement process) using error propagation frameworks that differ considerably from the ones applied to scalar errors. In 2009 Keller & Snik developed such a mathematical framework to estimate the contribution of each physical parameter to the response

Figure 1.9: Artists impression of the E-ELT and VLT telescopes in comparison with the Colosseum in Rome. *Image credit: www.eso.org*
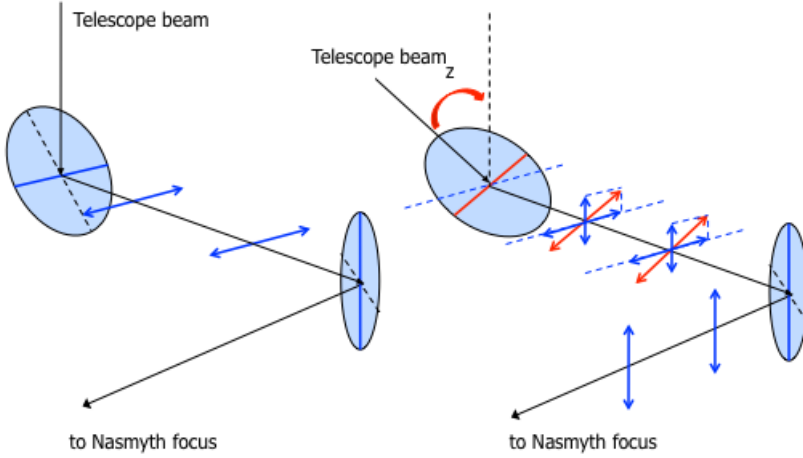
Figure 1.10: Schematic view of how instrumental polarisation (IP) is only corrected for the zenith position with the *"crossed"*-twin mirrors technique. Reflection on mirrors polarises light in the direction perpendicular to the reflection plane (i.e. the plane defined by the directions of propagation of incident and reflected light). When the telescope is pointing to zenith, the IP generated by reflection on the Nasmyth mirror gets compensated by the IP generated by the crossed mirror, of the same amount but opposite sign. However, when the telescope departs from the zenith position, the direction of the IP generated has a component that adds up and therefore some IP remains.

matrix of the polarimetric system.

Based on this framework we developed the M&m's code that is used in Part II of this thesis to evaluate the polarimetric capabilities of instruments located at the Nasmyth port of the VLT and E-ELT telescopes and provide insight on the polarimetric behaviour of these systems. In Chapter 5 we present the details of the code.

1.4.2 Instrumental polarisation at the Nasmyth focus of telescopes

Light reflected off the surface of a mirror is linearly polarised. The most frequantly used approach to direct the beam to the Nasmyth focus of a telescope, makes use of a $45°$ mirror placed after the primary and secondary ones. Light undergoes a $90°$ reflection on this mirror, a process that has been shown to linearly polarise up to 5% at visible wavelengths of the incoming light Gehrels 1960, Cox 1976, Joos et al. 2008, van Harten et al. 2009, Perrin et al. 2010). Additionally, a fraction of the incoming linear polarisation (if present) is lost due to conversion into circular polarisation. This is known as the *cross-talk* effect. It is known that these instrumental effects can be corrected by the *crossed-twin* mirrors technique (Cox 1976) which consists on placing a second mirror after the one that is causing the effect with a particular orientation. The drawing placed on the left side of Figure 1.10 shows how this technique works. Since the reflection process polarises light in the direction perpendicular to

the reflection plane, defined by the directions of propagation of incident and reflected beams, if a second mirror with the same characteristics is positioned such that it reflects light in the same plane that contains the direction of this IP, the polarisation generated by this second mirror, which is of the same value and opposite sign, compensates the original IP.

The main problem when applying this solution to Nasmyth focus instruments is illustrated in the second drawing of 1.10 (to the right). The mirror used to deflect the light to the Nasmyth focus rotates together with the telescope as it points. Since the "crossed twin" remains fixed at the Nasmyth port this crossed configuration is only achieved when the telescope points to zenith.

1.4.3   SPHERE-ZIMPOL

SPHERE (Spectro-Polarimetric High-contrast Exoplanets Research) is an instrument specifically designed for the detection and characterisation of exoplanets at the VLT (Beuzit et al. 2006). The imaging polarimeter designed for this instrument is ZIMPOL (Zurich IMaging POLarimeter), a single-beam polarimeter that makes use of a fast modulation-demodulation technique to achieve very high polarimetric sensitivity (Gisler et al. 2004, Schmid et al. 2006a, Thalmann et al. 2008, Roelfsema et al. 2010, Schmid et al. 2010, 2012). On top of this, SPHERE has two more instruments providing dual-beam and integral-field spectrographic capabilities. The instrument will work in the $\sim [0.6\text{-}0.95]\,\mu\mathrm{m}$ wavelength range and is planned to see light in early 2014.

SPHERE is located at the Nasmyth focus of one of the VLT's four UTs. The folding of the light to that focus is achieved by a $90°$ reflection on a mirror, after the primary and secondary ones. As explained in the previous section, this reflection generates IP which ZIMPOL deals with combining the crossed mirrors technique with a clever solution for compensating at zenith angles other than zero (Stuik et al. 2005). This solution, consists on placing a half wave plate (HWP) between the Nasmyth and crossed mirrors that rotates the direction of the IP stabilising it to the direction the crossed mirror can compensate for. Figure 1.11 shows a schematic view of this process. In Chapter 6 we analyse this system through simulations with the M&m's code and laboratory data from ZIMPOL tests confirming that this correction indeed reduces the IP to the required values.

1.4.4   EPICS-EPOL

The Exoplanet POLarimeter (EPOL, Keller et al. 2010) is the imaging polarimeter designed for the Exoplanet Imaging Camara and Spectrograph (EPICS, Kasper et al. 2010) instrument on the future $39\,\mathrm{m}$ E-ELT. This advanced polarimeter aims to not only detect but also characterise the atmospheres of exoplanets with unprecedented sensitivity and accuracy in the $\sim [0.5\text{-}0.9]\,\mu\mathrm{m}$ wavelength range. EPICS will be located at the Nasmyth focus of the E-ELT. In this telescope there will be at least five mirrors before the polarimeter.

Figure 1.12 shows a drawing of the mirror configuration of the E-ELT up to the Nasmyth port. In this telescope, light undergoes five reflections before reaching the Nasmyth port. The primary, secondary and tertiary mirrors (M1,M2 and M3) are rotationally symmetric and are
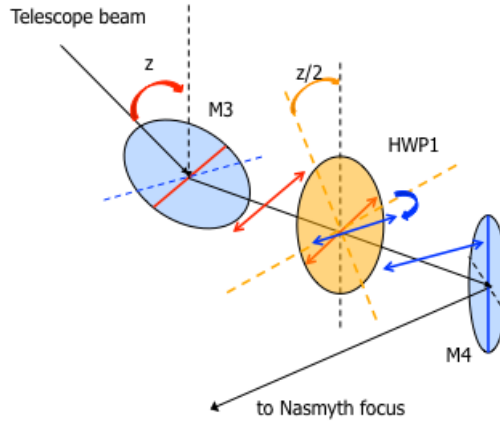
Figure 1.11: Schematic drawing of the correction achieved combining the *crossed*-twin mirror technique and a half wave plate (HWP) that rotates the instrumental polarisation generated by the reflection on the Nasmyth mirror to the position where the crossed mirror can correct for it (Stuik et al. 2005).

perpendicular to the direction of the beam, which makes the IP generated negligible. To fold the light to the Nasmyth port the E-ELT has two mirrors that are also part of the adaptive optics (AO) system of the telescope: the fourth and fifth mirrors (M4 and M5). M4 has an inclination of $8.5°$ and is a deformable mirror (DM), and M5 is inclined $36.5°$ and has tip-tilt capabilities.

At the moment, two designs are being considered to take the beam to the instrument at the Nasmyth focus: the *straight-through* and *bent* configurations. In the first the instrument is located at the point indicated in Fig. 1.12 as "Nasmyth focal surface". At this same location, in the second (*bent*) arrangement, a sixth $45°$ inclined mirror folds the Nasmyth focus by $90°$. This sixth mirror is fixed at the Nasmyth port, which complicates the behaviour of the instrumental polarisation effects as we show in Chapters 6 and 7 of this thesis.

A solution like the one adopted for SPHERE-ZIMPOL to compensate for the instrumental polarisation is not feasible in the case of the E-ELT because after M4 the diameter of beam is too large for the size of currently available high-quality achromatic HWPs. However, in Chapter 7 we present a solution consisting in performing the modulation in two steps. The first step of the modulation is achieved by a retarding element placed at the intermediate focus of the telescope (located at the hole in the centre of M4). The second step is performed at the polarimeter's location. Through simulations of this *"two-stage"* modulation scheme applied to both *"straight-through"* and *"lateral"* configurations, we show that almost perfect cancellation of all instrumentally-generated polarisation effects can be achieved.
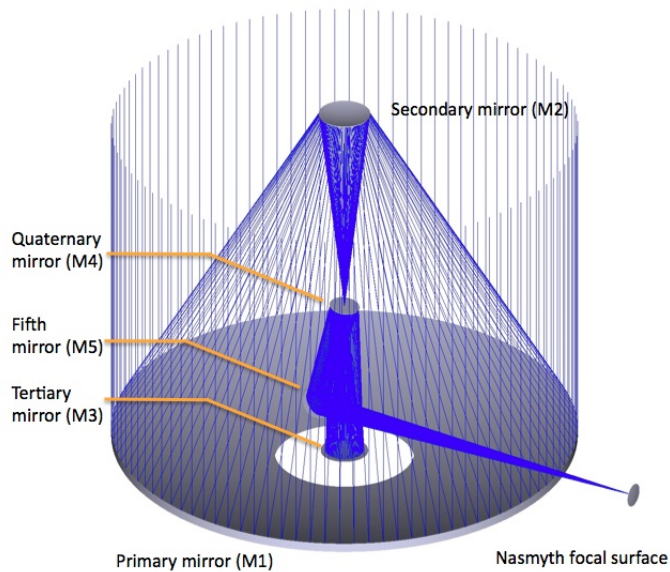
Figure 1.12: Drawing of the mirror configuration of the E-ELT up to the Nasmyth port. In the *straight-through* configuration, the instrument will be located at the Nasmyth focal surface indicated in the figure. In the *"Lateral"* configuration, at this same position a sixth (fixed) mirror is placed to fold the beam again by $90°$. *Image credit: www.eso.org*

This thesis

As mentioned in the first section of this introduction, the main goal of this thesis is to contribute to the achievement of the scientific and technical challenges that the polarimetric characterisation of exoplanets and protoplanetary discs encompass. We present studies focused on evaluating and solving technical difficulties as well as observational and modeling studies addressing some scientific questions.

The thesis is therefore divided into two parts. Part I gathers studies corresponding to the latter group (Chapters 2, 3 and 4), while Part II, developed in the context of the E-ELT/EPICS-EPOL instrument, comprises studies related to technical developments (Chapters 5, 6 and 7). Although the content of some studies has been already discussed, we present now a short summary of every chapter highlighting main findings and future avenues.

In Chapter 2 we present the first attempt to measure polarisation from the exoplanets orbiting around HR 8799. As explained before, such measurements could provide important information on the structure of the planet's atmospehrs and physical parameters such as their spin axis. We observe the system with with VLT/NACO in H and Ks bands combining, for the first time, pupil-stabilised and polarimetric modes. The aim is to 1) detect polarisation at the position of planets HR 8799 b and/or c and 2) explore the potential and current limitations of the technique. Our first results do not show polarisation signal at the position of any of the planets. However, our upper limits for detection are high and there is still room for improvement. We do see that the technique holds potential to improve the speckle suppression in regions close to the central star and we present details on the ideas for improvement we plant to investigate in the future.

In Chapter 3 we combine state of the art hydrodynamical, dust evolution, radiative transfer and instrumental simulators to produce synthetic imaging observations of transitional discs with VLT/SPHERE-ZIMPOL, Subaru/HiCIAO, VLT/VISIR and ALMA. Assuming that the morphology of these discs is caused by the presence of a planet, the goal is to provide observers with a set of imaging diagnostics at different wavelengths, focusing on the potential to constrain properties of the planet they host. An important conclusion of our study is that, in particular, combination of high resolution polarimetric images at short wavelengths with sub-mm images can tightly constrain the mass and position of the (unseen) planet as well as the characteristics of the dust distribution. Such observations will be possible with the upcoming VLT/SPHERE-ZIMPOL and ALMA Full Array instruments, and are likely to provide new insights on transitional discs and their relation to planet formation.

Chapter 4 presents a study on the observational signatures of environmental effects on protoplanetary discs. Our aim is to ultimately understand if there is a limit for the ambient stellar density of the region in which a protoplanetary disc evolves that prevents the evolution of planetary systems such as ours. Focusing on dynamical interactions, we estimate the radial truncation of protoplanetary discs as a function of the ambient stellar density of their environment and compare it with imaging measurements of disc radii in nearby star forming regions. We find that the distribution of of measured radii of circumstellar discs appears truncated in environments with high ambient stellar surface densities and that this truncation is consistent

with our predictions for the dynamical interactions. However, the highest density region in our resolved discs population (i.e. the Orion Nebula Cluster) is still not very high compared to more massive environments and to confirm our detection of the truncation signature we propose to carry out observations to measure the disc mass function in higher density environments. These observations could be carried out currently with ALMA and could also help distinguishing the origin of the truncation (i.e. dynamical encounters vs. photoevaporation from nearby massive stars).

Chapter 5 presents the error budgeting and polarimetric performance code we have built to simulate the polarimetric response of any optical arrangement and assess the design of new polarimetric instruments. The mathematical and physical frameworks of the code are presented as well as the basic functions and modes available. The code has evolved much since we presented this study although still some features need to be implemented. M&m's are central to the studies presented in Chapter 6 and 7 in which we aim to characterise (and correct) instrumental polarisation issues.

In Chapter 6 we use the code to simulate the instrumental polarisation effects generated in the optical path of the VLT and E-ELT telescopes up to their Nasmyth focii. We focus on reproducing laboratory data obtained with ZIMPOL using a dedicated laboratory set up to simulate the VLT mirrors' arrangement and to predict instrumental effects in the optical path of the E-ELT. We are able to reproduce the ZIMPOL data and provide, based on our simulations, some insight on the wavelength-dependent behaviour of the modulation system of the instrument. We also present the analysis of the correction of these effects that is carried out for ZIMPOL confirming that the instrumental polarisation is reduced to acceptable levels. We present as well a preliminary analysis of the E-ELT (to be expanded in Chapter 7) showing that the levels of instrumental polarisation generated are large and explore some ideas for their correction.

Finally, in Chapter 7 we expand the previous study analysing in detail the instrumental polarisation effects generated at the Nasmyth focus of the E-ELT. We use the M&m's code to estimate these effects for the different mirror configurations being currently considered for this focus. We find that instrumental effects are outside of the requirements for the level of sensitivity and accuracy needed. We then propose and analyse two strategies to suppress these instrumental effects based on the introduction of a retarding element in the intermediate focus of the telescope. Modifying the modulation schemes of the polarimeter to include this element it is possible to reduce (and even cancel) some of the effects to levels that ensure sufficient accuracy in the polarimetric performance of instruments aiming to operate at this facility. Based on these results we conclude that polarimetric characterisation of exoplanets can be achieved with the E-ELT provided that the instrumental effects are either corrected or calibrated out.

Part I

Chapter **2**

Polarimetric Angular Differential Imaging of the HR 8799 b and c exoplanets

M. de Juan Ovelar, F. Snik, R. de Kok, T. Meshkat, C. Thalmann, M. Kenworthy, J. Girard, D. Mawet and C. U. Keller
to be submitted

> *Bad times have a scientific value.*
> *These are occasions a good learner should not miss.*
> – Ralph Waldo Emerson

Abstract

We present H and K_s band observations of the HR 8799 exo-planetary system using a new approach, polarimetric angular differential imaging (PADI), to measure a polarisation signal from the planets. We focus on planets b and c in this system, which are likely to show linear polarisation signals of about 1% due to scattering of their own infrared emission by their atmospheres, assuming they exhibit inhomogeneities such as bands or spots. In addition, we present a new approach to the polarimetric calibration of NACO data based on measurements of unpolarised and polarised standard stars using the pupil-stabilised mode. We obtain no statistically significant detection of linear polarisation, and our data reduction method yields 1σ upper limits for the degree of polarisation of $[14.8, 11.2]\%$ for planet b and $[4.7, 5.9]\%$ for planet c in the H and K_s bands, respectively. The PADI technique significantly improves the speckle suppression compared to conventional ADI techniques, improving the contrast by almost an order of magnitude at the position of planet c $(0.96'')$ for the shorter wavelengths (H-band). Based on this initial application of the PADI technique, we discuss the potential for future improvements.

2.1 Introduction

The young HR 8799 system (Marois et al. 2008, Marois et al. 2010) is probably the most frequently imaged planetary system. The $\sim 30\,\mathrm{Myr}$ A5V star is orbited by four giant planets (e,d,c,b) with masses between 5 and $13\,M_{\mathrm{Jup}}$ at distances of $\sim [15, 24, 38, 68]\,\mathrm{AU}$, respectively (Marois et al. 2008, Marois et al. 2010, Currie et al. 2011). These planets are still very hot ($\sim 1000\,\mathrm{K}$) as they are still releasing gravitational energy in the form of thermal emission and are therefore bright in the infrared. This, together with the large separations from the parent star, makes them exceptional targets for the study of exoplanets through direct imaging. In the past years several studies have been carried out obtaining near-infrared and infrared measurements of these planets revealing very interesting chemical characteristics of their atmospheres that suggest the presence of thick clouds (e.g. Janson et al. 2010, Bowler et al. 2010, Barman et al. 2011, Currie et al. 2011, Madhusudhan et al. 2011).

Interestingly, the clouds could cause the infrared emission from these planets to be polarised. de Kok et al. (2011) performed radiative transfer simulations showing that such hot, giant planets could indeed emit polarised radiation if they present inhomogeneities in their atmospheres such as bands, spots or even flattening of the planet due to fast rotation (Marley & Sengupta 2011). This process has already been proposed as the most likely scenario for the explanation of polarised emission from brown dwarfs (Ménard et al. 2002, Tata et al. 2009, Miles-Páez et al. 2013) and opens up a whole new avenue for exploring giant planets through polarimetry. Depending on the characteristics of the atmospheric inhomogeneities, the planets' polarised signals will be a few percent. Although it is extremely challenging to detect, the degree and angle of polarisation could reveal otherwise unobtainable information such as the morphology of the distribution of clouds in the atmospheres (e.g. presence of bands, patches, etc. . .) or the rotation axis of the planets (de Kok et al. 2011, Madhusudhan & Burrows 2012).

Images of these planets are typically obtained using Angular Differential Imaging (ADI) (Marois et al. 2006). This technique takes advantage of the rotation of the sky during observations to distinguish between the stellar point spread function (PSF) and the "companion" signal. In the past years, several techniques and algorithms have been developed to combine images in optimal ways (e.g. Lafrenière et al. 2007, Amara & Quanz 2012, Soummer et al. 2012, Meshkat et al. 2013) and to improve the contrast by reducing the "speckle" noise in regions close to the star where the PSF is not stable (Hinkley et al. 2009).

Polarimetric imaging techniques have also greatly improved over the past few years and are applied to observations of circumstellar environments and planet formation as polarimetry can directly disentangle the (polarised) scattered flux from circumstellar matter, in the form of of a disc or in the atmosphere of a planet, from the (unpolarised) flux of the star formation (e.g. Hinkley et al. 2009, Hashimoto et al. 2011, Jeffers et al. 2012, Dong et al. 2012, Thalmann et al. 2013, Quanz et al. 2013b, Canovas et al. 2013). Like any other differential technique, polarimetry requires large fluxes. Additionally, optical elements in the telescope and instrument can introduce polarisation and also modify the polarisation coming from the target. These effects have to be properly calibrated.

In preparation for the next generation of imaging polarimeters such as e.g. SPHERE-ZIMPOL/IRDIS (Beuzit et al. 2006, Gisler et al. 2004, Schmid et al. 2006a, Thalmann et al. 2008, Langlois et al. 2010, Schmid et al. 2010, 2012) we combine, ADI and polarimetric techniques in an attempt to measure the polarised signal of the planets in the HR 8799 system. We focus on the HR 8799 b and c planets that have the largest separations, which allows us to apply conservative ADI and thereby minimising the risk of removing actual signal from the planet. The power of ADI and polarimetry resides in fundamentally opposite approaches where ADI benefits from a rapid sky rotation while polarimetry requires frames within a polarimetric cycle to be as stable as possible with respect to sky rotation. The challenge is to find a compromise in both observations and data reduction where both techniques can be jointly optimized.

In Section 7.2 we present the details of our observations and data reduction approach. In Section 7.4 we present the first results obtained, and in Section 7.6 we discuss the results and the potential of future investigations. Finally, Section 6.5 presents our conclusions and the future avenues we plan to take in order to optimise the technique.

2.2   Observations and data reduction

The observations were taken on the second half of the nights of 20 and 21 July 2012 (089.C-0688A, PI: R. de Kok) with the Adaptive Optics (AO)-assisted high resolution near-infrared instrument VLT/NACO (Lenzen et al. 2003, Rousset et al. 2003) under average seeing conditions and nominal AO performance. To perform these PADI observations we introduce a new observing mode that combines pupil-stabilised (or pupil-tracking) and dual-beam polarimetric modes with an advanced calibration approach. Several previous polarimetric studies have used NACO in the field-stabilised mode where the instrument rotates with the parallactic angle as the sky rotates (e.g Quanz et al. 2011, Quanz et al. 2012, Quanz et al. 2013b, Canovas et al. 2013). In that configuration the polarisastion signal of the target in the sky stays constant, but the instrumental effects vary with the rotation. We use the same pupistabilised mode of NACO that is used in Sparse Aperture Masking (SAM)-pol observations (Tuthill et al. 2010, Norris et al. 2012) without introducing the SAM mask in the optical path. This fixes the instrumental polarisation effects while letting the polarisation in the sky rotate with the parallactic angle. The advanced calibration we introduce corrects for instrumental polarisation, efficiency as well as the rotation of the sky reference system with respect to the (fixed throughout the observations) instrument reference system.

For our observations we fix the position of the instrument such that the first mirror in the NAOS adaptive optics system is crossed with the telescope mirror that reflects the light to the Nasmyth focus of the telescope (M3). In this crossed configuration the instrumental polarisation effects are minimised (Witzel et al. 2011, see Section 2.2.3 below for details) and, thanks to the pupil-tracking, kept stable during the observations. During the first half-night we obtained approximately $1.4\,\mathrm{hours}$ of total exposure for HR 8799 in the H-band. During the second night we obtained $0.6\,\mathrm{hours}$ of K_s-band total integration. Both data sets were obtained using the `S27` detector with a pixel-scale of $27.15\,\mathrm{maspixel}^{-1}$ in `HighDynamic` and `cube`

modes with the read-out in `Double RdRstRd` mode. We also used a dithering technique consisting of performing sets of measurements with an offset in the x (horizontal) direction of the detector that can then be subtracted to effectively remove background emission and detector bias.

NACO is equipped with a focal-plane mask, a rotatable half-wave plate (HWP) and a Wollaston prism to image linear polarisation. The Wollaston prism splits the beam into the ordinary and extraordinary, orthogonally polarised beams ($I_\perp$ and $I_\parallel$) separated $3.5''$ in the y (vertical) direction of the detector. To avoid beam overlap on the detector the focal plane mask divides the field of view vertically into two areas of $27''$ in length (x-direction) and $3.5''$ in height (y-direction). By rotating the HWP to different position angles it is possible to select the direction of linear polarisation to be measured. Given the (fixed) position of the mirrors in our pupil-tracking set up, we define the polarimetric reference system with respect to the detector such that the eigen-vector of the optical path in the telescope corresponds to the linear Stokes component Q'. We denote components of the Stokes vector defined in the instrument reference frame with a prime (e.g. Q') to distinguish them from components in the sky coordinate system (e.g. Q).

The observations presented in this study were taken without the polarimetric mask due to the fact that HR 8799 b orbits at an angular separation of $1.7''$, which would cause it to fall outside of the field of view at certain parallactic angles. In the following, a *polarimetric cycle* is defined as a set of four measurements obtained with the HWP positioned in consecutive steps of $22.5°$ (e.g. $[0, 22.5, 45, 67.5]°$). To minimize overheads we continuously rotated the HWP in steps of $22.5°$ instead of repeating the polarimetric cycle mentioned above, obtaining a total of sixteen measurements per dithering position, called a *polarimetric block* hereafter. This also allows us to estimage errors such as the Fourier analysis described by Patat & Romaniello (2006) or the study of the *"Null frames"* as described in (Bagnulo et al. 2009). Each H-band cube is composed of 35 frames with an exposure time of 0.45 s, while K_s-band cubes contain 15 frames at 0.9 s exposure time. Finally, our measurements did not use a coronagraph mask.

The data reduction consists of four steps: (a) image preparation, (b) polarimetric double difference, (c) polarimetric calibration and (d) speckle suppression using optimised principal components analysis (OPCA), which we describe in the following subsections.

2.2.1   Image preparation

Each data cube is associated with a particular dithering position ("left" or "right") and HWP orientation ($0, 22.5, 45, \dots$). To maximize the signal from the planets, the images of HR 8799 are saturated in the central ~ 15 pixels. Each data cube is first inspected for frames that have a maximum lower than a certain threshold indicative of e.g. low AO system performance and/or drifting. This threshold is determined by a visual inspection of the raw data. The remaining *good* frames are then corrected for bad pixels seen in dark and flat mean images by substituting their values with the median of the surrounding pixels. They are then dark-subtracted, flat-fielded, converted into photo-electrons using the specified gain of the detector
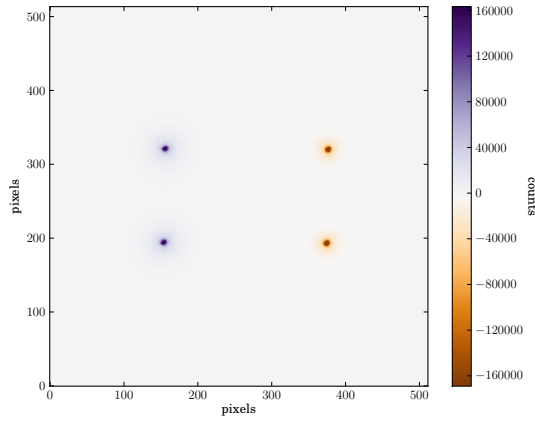
Figure 2.1: Example of resulting image when subtracting left and right dithered frames.

(1 count corresponds to 11 photo-electrons, as described in the NACO Period 89, Phase 2 user manual) and mean-combined into a single image. Each of these combined left or right images corresponds to one position of the HWP; sixteen images form a polarimetric block (see Table 2.1 below for details). Finally, dithered images of the same HWP angle in consecutive polarimetric blocks are subtracted to remove background and detector bias effects. An example of such subtracted image is shown in Figure 2.1.

The subtracted image is convolved with a Gaussian to detect the approximate location of the resulting four stellar image, and a box of $180{\times}180$ pixels is extracted around this position in the original (i.e. not-filtered) image. Unfortunately, due to the lack of the polarimetric mask, part of the PSF tail in the upper and lower beams overlap. The box size is therefore set to minimise the amount of overlapping area while assuring that the signal from planet b (with a separation of about ~ 74 pixels) is preserved. Each box is then registered by fitting a Moffat profile to the non-saturated pixels. The registration is carried out with an accuracy of an eighth of a pixel (i.e. ≈ 3.4 mas).

2.2.2 Polarimetric double difference

The signal in each box ($I_{\mathrm{UL,LL,UR,LR}}$) corresponds to a certain polarisation state, depending on the position of the HWP. Table 2.1 shows these correspondences according to our definitions of the Stokes Q' and U' components for the first (left-dithered) and second (right-dithered) polarimetric blocks. Subscripts UL, LL, UR and LR denote upper left, lower left, upper right and lower right corners of the left-right subtracted images. Adopting this notation, the *"double difference"* method recovers a Stokes component, e.g. Q', from left-dithered

frames via

$$Q'_i = 0.5 \cdot \left((I_{\mathrm{UL,1,i}} - I_{\mathrm{LL,1,i}}) - (I_{\mathrm{UL,2,i}} - I_{\mathrm{LL,2,i}}) \right), \tag{2.1}$$

where subscripts 1 and 2 denote the first and second positions of the HWP corresponding to the measured linear polarimetric component (Q or U), and i corresponds to the polarimetric cycle. As a result we obtain the $Q'_{1,i}$, $Q'_{2,i}$, $U'_{1,i}$ and $U'_{1,i}$ components (see *"Beam Subtr."* columns in Table 2.1). Note that left and right beams correspond to the same angle of the HWP but to a different data cube; thus left and right sides are measured at different times. This time difference corresponds to a complete polarimetric block, which corresponds to 4.2 minutes for the H-band data and to 3.6 minutes for the K_s-band data. The time separation between positions 1 and 2 of the HWP in each cycle is of about 31.5 s for the H-band and 27 s for the K_s-band.

TABLE 2.1: FIRST LEFT AND RIGHT DITHERED POLARIMETRIC BLOCKS

θ_{HWP} (°)	I_{UL}	-	I_{LL}	=	Beam subtr.	I_{UR}	-	I_{LR}	=	Beam subtr.
0	$I + Q'$	-	$I - Q'$	=	$Q'_{1,1}$	$I + Q'$	-	$I - Q'$	=	$Q'_{1,5}$
22.5	$I + U'$	-	$I - U'$	=	$U'_{1,1}$	$I + U'$	-	$I - U'$	=	$U'_{1,5}$
45	$I - Q'$	-	$I + Q'$	=	$Q'_{2,1}$	$I - Q'$	-	$I + Q'$	=	$Q'_{2,5}$
67.5	$I - U'$	-	$I + U'$	=	$U'_{2,1}$	$I - U'$	-	$I + U'$	=	$U'_{2,5}$
90	$I + Q'$	-	$I - Q'$	=	$Q'_{1,2}$	$I + Q'$	-	$I - Q'$	=	$Q'_{1,6}$
112.5	$I + U'$	-	$I - U'$	=	$U'_{1,2}$	$I + U'$	-	$I - U'$	=	$U'_{1,6}$
135	$I - Q'$	-	$I + Q'$	=	$Q'_{2,2}$	$I - Q'$	-	$I + Q'$	=	$Q'_{2,6}$
157.5	$I - U'$	-	$I + U'$	=	$U'_{2,2}$	$I - U'$	-	$I + U'$	=	$U'_{2,6}$
$\vdots$	$\vdots$	$\vdots$	$\vdots$	$\vdots$	$\vdots$	$\vdots$				
337.5	$I - U'$	-	$I + U'$	=	$U'_{2,4}$	$I - U'$	-	$I + U'$	=	$U'_{2,8}$

The double difference method requires that subtracted images are as similar as possible. In the beam subtraction, images are taken at the same time, but they differ in e.g. optical path and region of the detector. On the other hand, the subtraction of images taken at positions 1 and 2 of the HWP share the spatial characteristics but differ in time. For this study, the latter is of particular importance since the sky coordinate system rotates with respect to the detector during the observations. It is therefore key to assure that the signal of the planets stays as stable as possible between positions 1 and 2 of the HWP. Figure 2.2 shows the rotation rate in pixels of HR8799 b and c during the H-band measurements, the ones with the longest polarimetric cycle. Solid lines show the trajectories of planets b and c. Crosses and pluses correspond to b and c, respectively, and blue and red colors show $Q'_{1,i}$ and $Q'_{2,i}$, respectively.
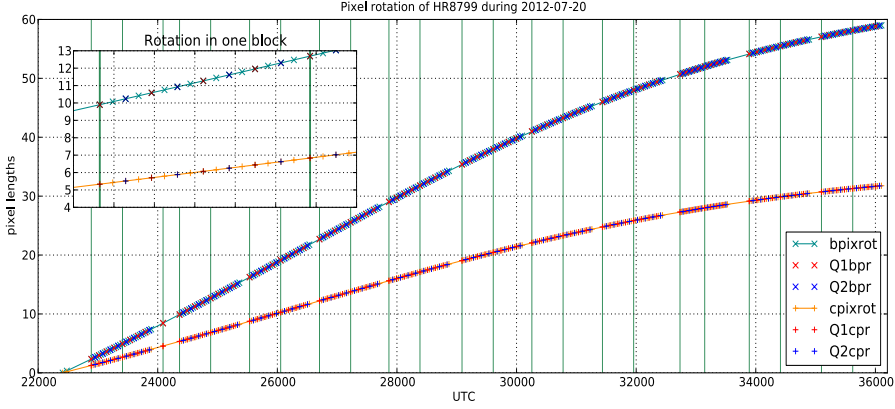
Figure 2.2: Rotation rate in pixels of planets HR8799 b and c during the first half night of our observations. Crosses and pluses mark the pixel rotation of planets b and c, respectively. Red and blue symbols show the positions of the planets (in pixels) at the UTC of the measurements of $Q_{1,i}$ and $Q_{2,i}$,respectively. Finally, vertical solid green lines indicate the start of each polarimetric block. The zoomed are shows that the rotation between $Q_{1,i}$ and $Q_{2,i}$ in a cycle is about 3/4 of a pixel.

The zoomed-in plot shows that the planets move about 3/4 of a pixel between these two measurements. Since the theoretical full-width-half-maximum (FWHM) of the PSF in H and K_s is of about ~ 2 and ~ 2.5 pixels, respectively, we can safely take the second step in the double difference method.

   Visual inspection of the $Q'_{1,i}$, $Q'_{2,i}$,$U'_{1,i}$ and $U'_{1,i}$ images revealed that the registration of the boxes was not accurate enough. To correct for these remaining misalignments the x and y gradients of the corresponding intensity image were fitted and subtracted form the $Q'_{1/2,i}$ and $U'_{1/2,i}$ images. The effects due to misalignment can be modeled using the gradient of the intensity image because the subtraction of two misaligned (similar) images can be approximated by the gradient. We fit the parameters c_x and c_y that minimise the expression:

$$\sum (Q' - c_x \nabla I_x - c_y \nabla I_y)^2 . \tag{2.2}$$

It is easy to show that the minimum, for e.g. Q', is found for

$$c_x, c_y = \frac{\sum (Q' \nabla I_{x,y})}{\sum (\nabla^2 I_{x,y})} . \tag{2.3}$$

   Figure 2.3 shows the result of such an operation (left panel) for a misaligned polarimetric image (right panel). Note that the correction in the central region generates an artificial structure due to the fact that this is the saturated region in the intensity images. The gradient
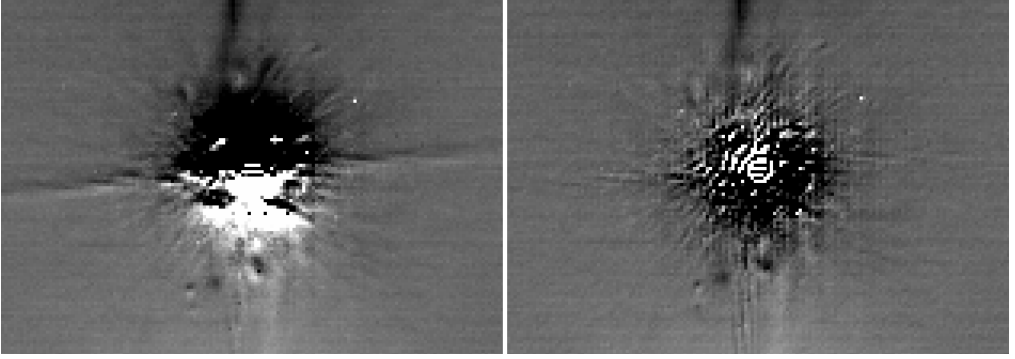
Figure 2.3: Correction of beam misalignment in a single-difference polarimetric frame by means of an intensity gradient subtraction. The left panel shows the original (misaligned) image, while the right panel shows the same frame after the correction. The structure present in the central region is likely an artifact since this region is saturated in the intensity image.

subtraction is applied when the sky-rotated frames have not yet been combined. The signal of the planets at this point is likely to be buried in the noise and, since the operation is averaged over all pixels, the likelihood of subtracting signal from the planets is low. However, we cannot assume that the planet signal is completely unaffected by the gradient subtraction. The method has previously been successfully applied in the first detection of the debris disc around HIP 79977 (Thalmann et al. 2013). To our knowledge, no study has been carried out to analyze the detailed impact of the gradient subtraction on the polarimetric results.

Finally, some of the beam-subtracted polarimetric images also showed single-pixels artifacts. They are the results of a large difference in the pixel values between the two beams. We identify pixels that deviate $> 3\sigma$ from their neighbours and substitute their value with the median of the neighbourhood.

Once the $Q'_{1,i}$, $Q'_{2,i}$, $U'_{1,i}$ and $U'_{2,i}$ images are corrected, Q'_i and U'_i Stokes components are then obtained (for each cycle) from

$$Q'_i = 0.5 \cdot (Q'_{1,i} - Q'_{2,i}) \quad \text{and} \quad U'_i = 0.5 \cdot (U'_{1,i} - U'_{2,i}),\tag{2.4}$$

which completes the double difference calculation as described in Eq. 2.1. The corresponding intensity images are then obtained as

$$I_{Q',i} = 0.5 \cdot (Q'_{1,i} + Q'_{2,i}) \quad \text{and} \quad I_{U',i} = 0.5 \cdot (U'_{1,i} + U'_{2,i}).\tag{2.5}$$

2.2.3 Calibration

NACO is located at the Nasmyth focus of the VLT UT4 telescope. The main consequence of this, and the fact that it was not specifically designed for polarimetric purposes, is that instru-

mental polarisation effects are significant and variable with wavelength as well as pointing for field-stabilised polarimetry. Witzel et al. (2011) presented a model for the instrumental polarisation (IP) generated by the optics of NACO when observing in field-stabilised mode. The model was built for the K_s band and was shown to be reliable when compared with polarised standard star measurements. However, the model does not include the effects of the low-inclination mirrors of the NAOS adaptive optics system or of the various dichroic elements sending light to the wavefront sensor. It also does not include the aging of coatings and is not applicable to H-band observations.

Instead of relying on a model, we directly measured the IP and cross-talk effects in the pupil-stabilised mode using unpolarised and polarised standard stars in the Gehrels (1974) and Whittet et al. (1992) catalogs. Since we keep the instrument fixed in the crossed configuration, the instrumental effects are minimized, which corresponds to the meridian crossing point in the Witzel et al. model (see Figure 6 of their paper). Our approach facilitates the correction of instrumental effects since they remain fixed throughout the observations, and the same calibration coefficients apply to all data recorded through the same filter. The only disadvantage is the required additional observing time, which is needed as the instrumental polarisation is expected to be larger ($IP \approx 2\%$) than the signal of the planet ($\sim 1.5\%$).

The linear Q and U Stokes components obtained by means of the double difference described above are defined with respect to the coordinate system within NACO. The goal of the calibration process is to obtain the elements of the response matrix of the telescope ($\mathbf{X}$, Ichimoto et al. 2008) that transforms the incoming Stokes vector $\mathbf{S_{in}}$ into the *measured* Stokes vector $\mathbf{S_{meas}}$ and that describe the instrumental impact on the polarimetric measurement. The process can be expressed as follows:

$$\begin{bmatrix} q'_{\text{meas}} \\ u'_{\text{meas}} \end{bmatrix} \mathbf{X M_{ROT}}(\alpha) \begin{bmatrix} q'_{\text{in}} \\ u'_{\text{in}} \end{bmatrix} \tag{2.6}$$

where $\mathbf{M_{ROT}}(\alpha)$ is the Mueller matrix for sky rotation with parallactic angle (α) and lower case q and u are fractional polarisation Stokes components ($q = Q/I$ and $u = (U/I)$. Note that, throughout the process, we neglect the circular polarisation (Stokes component V) as it is not measured and is not expected to be present in our target. The elements of the (normalised with the measured intensity, I_{meas}) response matrix $\mathbf{X}$ are,

$$\mathbf{X} = \begin{pmatrix} 1 & Q'_{\text{in}} \to I_{\text{meas}} & U'_{\text{in}} \to I_{\text{meas}} \\ I_{\text{in}} \to Q'_{\text{meas}} & Q'_{\text{in}} \to Q'_{\text{meas}} & U'_{\text{in}} \to Q'_{\text{meas}} \\ I_{\text{in}} \to U'_{\text{meas}} & Q'_{\text{in}} \to U'_{\text{meas}} & U'_{\text{in}} \to U'_{\text{meas}} \end{pmatrix}, \tag{2.7}$$

considering only linear polarisation Stokes components. Elements $X_{2,1}$ and $X_{3,1}$ describe the amount of IP generated by the system, which bias the measurements of Q' and U'. Elements $X_{2,2}$, $X_{2,3}$, $X_{3,2}$ and $X_{3,3}$ describe the efficiency with which the linear polarisation components are measured and the rotation taking place between Q' and U'. Elements $X_{2,1}$ and $X_{3,1}$ are not relevant since $Q', U' << I$. Because of our crossed configuration and the

definition of the reference system in the instrument (with Q' as the eigen-vector) we know that (ideally) elements $X_{3,1}$, $X_{2,3}$ and $X_{3,2}$ should be zero while element $X_{2,2}$ should be unity (i.e. transmission of Q' throughout the system should be perfect).

The fractional linear polarimetric components q'_{meas} and u'_{meas} can therefore be described as:

$$q'_{\mathrm{meas}} = a_{\mathrm{q}} + b_{\mathrm{q}}q'_{\mathrm{in}} + c_{\mathrm{q}}u'_{\mathrm{in}} \,, \tag{2.8}$$

and

$$u'_{\mathrm{meas}} = a_{\mathrm{u}} + c_{\mathrm{u}}q'_{\mathrm{in}} + b_{\mathrm{u}}u'_{\mathrm{in}} \,, \tag{2.9}$$

where $a_{\mathrm{q,u}}$ correspond to the bias IP elements in $\mathbf{X}$ and $b_{\mathrm{q,u}}$ and $c_{\mathrm{q,u}}$ are the coefficients for transmission and rotation of the linear components of the Stokes vector, respectively. Based on the fact that Q' is the eigen-vector of the system we can assume that $c_{\mathrm{q,u}}$ are negligible (i.e. there is no rotation between linear Stokes Q' and U') Then $b_{\mathrm{q,u}}$ can be considered as a coefficient for the efficiency of the measurement of a Stokes component.

The $a_{q,u}$ coefficients are directly obtained by measuring the fractional polarisation of unpolarised standard (US) stars:

$$\begin{bmatrix} q'_{\mathrm{US,meas}} \\ u'_{\mathrm{US,meas}} \end{bmatrix} = \begin{bmatrix} a_{\mathrm{q}} \\ a_{\mathrm{u}} \end{bmatrix} \,, \tag{2.10}$$

To obtain the $b_{\mathrm{q,u}}$ coefficients, we use a polarised standard (PS) star. These stars have tabulated values of degree and angle of polarisation (P, θ) for different wavelengths (Whittet et al. 1992). The fractional linear polarisation components q_{PS} and u_{PS} are obtained from

$$P = \sqrt{q_{\mathrm{PS}}^2 + u_{\mathrm{PS}}^2} \quad \text{and} \quad \theta = 0.5 \cdot arctan(u_{\mathrm{PS}}/q_{\mathrm{PS}}) \,. \tag{2.11}$$

Note that these components are defined in sky coordinates and, therefore, the measured components would rotate with parallactic angle (equivalent to placing a rotating polariser in front of the telescope. Thus,

$$\begin{bmatrix} q'_{\mathrm{PS,meas}} - a_{\mathrm{q}} \\ u'_{\mathrm{PS,meas}} - a_{\mathrm{u}} \end{bmatrix} = b_{\mathrm{q,u}} \mathbf{M_{ROT}}(\alpha) \begin{bmatrix} q_{\mathrm{PS}} \\ u_{\mathrm{PS}} \end{bmatrix} = b_{\mathrm{q,u}} \begin{pmatrix} cos(2\alpha) & sin(2\alpha) \\ -sin(2\alpha) & cos(2\alpha) \end{pmatrix} \begin{bmatrix} q_{\mathrm{PS}} \\ u_{\mathrm{PS}} \end{bmatrix} \,. \tag{2.12}$$

Measuring the polarisation of such a star (including the correction for the $a_{\mathrm{q,u}}$ bias) at two or more parallactic angles that differ by more than $45°$ allows us to accurately fit the sinusoidal variation of the polarisation, yielding the coefficients $b_{\mathrm{q,u}}$.

We obtain the fractional linear polarizations q'_{meas} and u'_{meas} for the unpolarised standard star HD 202573 (Gehrels 1974) and the polarised standard RCra 88 using the double

TABLE 2.2: RCRA 88 TABULATED DEGREE AND ANGLE OF POLARISATION

Band	$P\,(\%)$	$\theta\,(°)$
H	2.73 ± 0.07	92 ± 1
K	1.84 ± 0.09	95 ± 1

TABLE 2.3: CALIBRATION PARAMETERS

Band	a_{q}	b_{q}	a_{u}	b_{u}
H	-0.024	1.017	-0.005	0.569
K_{s}	-0.012	0.801	-0.002	0.469

difference method. The tabulated degrees and angles of polarisation of RCra 88 in both H and K bands are shown in Table 2.2 (Whittet et al. 1992). Both targets were observed during the same night as the science observations. The calibration observations do not suffer from saturation in the central region of the image. Except for not carrying out the OPCA, we followed the same data reduction steps that were also applied to the science data. We adjust the various threshold values defined for the data reduction when needed through visual inspection of the raw data. We note that the tabulated values are given for K-band instead of K_{s}. For the smaller average wavelength of our observations in the K_{s} band we expect (according to the Serkowski law for interstellar polarization, Serkowski 1971, 1973) a slightly larger polarization of the standard star as compared with the tabulated value for K band, but for the small degrees of polarization that we aim to measure, this difference is not significant.

Figure 2.4 shows the values of q' and u' measured for HD 202573 (upper panels) and RCra 88 (lower panels) in both H and K_{s} filters. Solid lines in all panels show the best fit to the data (assuming the rotation between Q' and U' is negligible), while dashed lines in the lower panels show the rotation of RCra 88's q_{PS} and u_{PS} obtained from the tabulated P and θ. The calibration coefficients found are $a_{\mathrm{q}}, b_{\mathrm{q}} = -0.024, 1.017$ and $a_{\mathrm{u}}, b_{\mathrm{u}} = -0.005, 0.569$ for H-band and $a_{\mathrm{q}}, b_{\mathrm{q}} = -0.012, 0.801$ and $a_{\mathrm{u}}, b_{\mathrm{u}} = -0.002, 0.469$ for K_{s}-band. Values of q and u of HD 202573 systematically yield an angle of polarisation θ of about $\sim 5°$. The random error (i.e. photon noise) in these measurements is of the order of $10^{-5}\%$ (i.e. $1/\sqrt{N_{\mathrm{phot}}}$ where N_{phot} is the total number of photons in all combined images). It is interesting to note that the value of the instrumental polarisation ($a_{\mathrm{q,u}}$) in our K_{s} measurements differ considerably from those obtained by Witzel et al. (2011) based on their model. With our crossed configuration and according to that study, we should obtain values of about $\sim 1\%$ in the K_{s} filter for both Q and U, which agrees with our results only for the case of a_{u}. To check the consistency of our measurements, we obtained the same coefficients $a_{\mathrm{q,u}}$ using data of HR 8799 taken with H and ND_short filters obtaining the same values for the best fit of the data. These discrepancies can be caused by the fact that the Witzel et al. model may not be fully realistic anymore due to e.g. ageing effects on the mirrors. Additionally, K_{s} measurements for RCra 88 at parallactic angles of about $100\,[\mathrm{deg}]$ of, in particular, q show rather systematic variations that are obviously larger than the error bars that represent the photon noise. The causes of these variations are yet unknown. Further analysis based on the Fourier and Null frames techniques (Patat & Romaniello 2006, Bagnulo et al. 2009) will be carried out to explore this issue.

The science data is then corrected as follows[1]. First, the fractional polarisations q'_{meas}

---

[1]We describe the process for q but the exact same steps are taken for the correction of u, applying the corre-
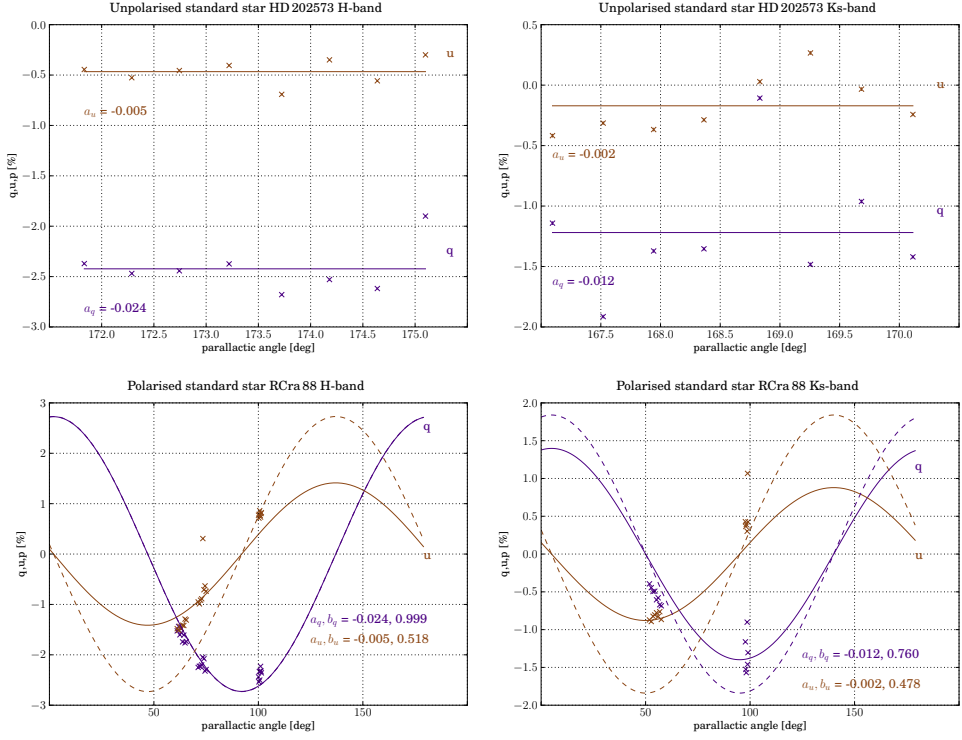
Figure 2.4: *Upper row:* Unpolarised standard star HD 202573 values for the fractional linear polarisation components q' and u' as a function of parallactic angle for H (left) and K$_s$ (right) bands. Cross markers show the data points while the solid line is the best fit to the data, providing the bias $a_{q,u}$. *Lower row:* RCra 88 Polarised standard values for fractional q' and u' components also in the H and K$_s$ bands. Cross markers denote data points while solid and dashed lines show the best fit (assuming the rotation between Q' and U' is negligible) and theoretical values, respectively. The coefficients obtained from these fits are annotated in each plot.

and u'_{meas} are obtained from Eq. 2.5, normalised to the corresponding intensities, i.e.

$$q'_{\mathrm{meas,i}} = 0.5 \cdot \left(\frac{Q'_{1,i}}{I_{Q',1,i}} - \frac{Q'_{2,i}}{I_{Q',2,i}} \right) \, . \tag{2.13}$$

These values are corrected for the IP bias via

$$q'_{\mathrm{biascorr,i}} = q'_{\mathrm{meas,i}} - a_q \, , \tag{2.14}$$

sponding coefficients.

and for the efficiency factor via

$$q'_{\text{biascorr+eff.corr,i}} = \frac{q'_{\text{biascorr,i}}}{b_q} \,. \tag{2.15}$$

To recover the absolute Stokes components, bias and efficiency corrected $q'_{\text{biascorr+eff.corr,i}}$ are multiplied by the total intensity in the Q' images,

$$Q'_i = q'_{\text{biascorr+eff.corr,i}} \cdot 0.5 \cdot (I_{Q',1,\text{i}} + I_{Q',2,\text{i}}) = q'_{\text{biascorr+eff.corr,i}} \cdot 0.5 \cdot I_{Q',\text{i}} \,. \tag{2.16}$$

Finally, Q'_i and U'_i images are derotated to the sky coordinate system using $\mathbf{M_{ROT}}(-\alpha)$,

$$Q_i = Q'_i cos(-2\alpha) + U'_i sin(-2\alpha)$$
$$U_i = -Q'_i sin(-2\alpha) + U'_i cos(-2\alpha) \tag{2.17}$$

These Q_i and U_i polarimetric images are now ready for the principal component analysis.

2.2.4 Optimised principal components analysis (OPCA)

We use the Optimised Principal Components Analysis (OPCA) code written by Meshkat et al. (2013). The PCA algorithm (see e.g. Amara & Quanz 2012) operates over the set of (sky rotated) images finding a number of basis functions describing the common features of the PSF by means of the singular value decomposition (SVD) of the data-set. Since the sky rotates with respect to the detector, this process is building a model library of the PSF and its typical variations. The projection of the individual PSFs onto a number of principal components is then subtracted from each frame, yielding the PSF-corrected image.

The OPCA code expands the capabilities of the regular PCA to maximise the S/N of the planet by specifying the inner and outer radii of the annular area to be optimised and by varying the number of co-added frames to avoid self-subtraction of a signal at a certain angular distance from the central star, which is achieved by rejecting frames with insufficient rotation in the SVD computation. This approach yields an improvement of the sensitivity of about $0.5\,\mathrm{mag}$ with respect to regular PCA and of $0.5\,\mathrm{mag}$ with respect to Locally Optimised Combination of Images (LOCI,Lafrenière et al. 2007) (Meshkat et al. 2013).

PCA methods are now extensively used in high-resolution imaging of exoplanets (e.g Amara & Quanz 2012, Meshkat et al. 2013, Quanz et al. 2013a, Thalmann et al. 2013) but they have never been, to our knowledge, applied to polarimetric data. The main complication is that we now have a minimum of four (I_i, Q_i and U_i) and up to six (I_i, Q_i, U_i, $I_{Q,i}$, $I_{U,i}$ and P_i) data sets with potentially different PSF and noise characteristics. We therefore optimise the OPCA parameters for each data set separately. In the end we want fractional polarimetric images (Q/I and U/I) and degrees and angles of polarisation where Q_i, U_i and
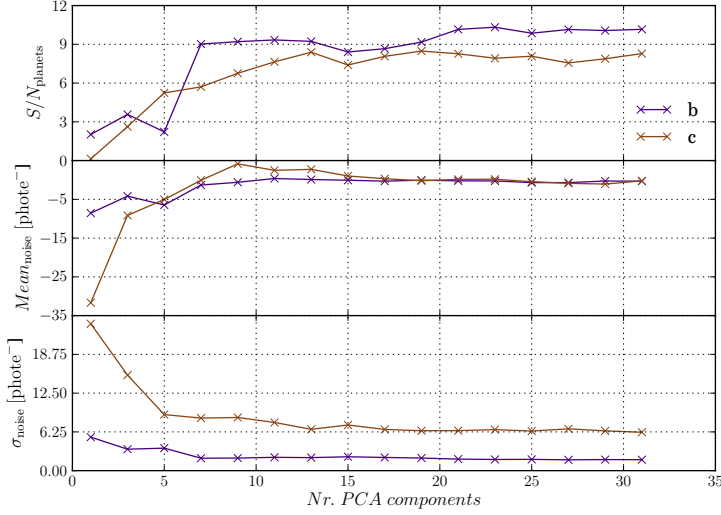
Figure 2.5: Signal-to-noise (S/N) and mean and standard deviation of the local noise curves used to find the optimal number of principal components to be subtracted from the b-optimised I data set in H-band.

I_i datasets need to be combined. These OPCA-corrected final images have very different background properties, and it is not clear what the impact of this is on detection and upper limit determinations. Fractional polarimetric images cannot be simply added because they are not linearly related, so applying OPCI to q_i and u_i datasets is not an option.

In any case, using the OPCA components optimised for the intensity to improve the Q_i and U_i data is not justified considering that the basis functions may be fundamentally different for intensity and polarization. In this first application of OPCA to polarimetric data, we independently optimise the OPCA components for I_i, Q_i and U_i. A detailed analysis of the impact of this approach on the final results is outside of the scope of the present effort.

The I_i and Q_i (and U_i) data sets have a total of 312 and 78 frames, respectively, in the H-band; in the K_s-band these numbers are lower, 156 and 39, respectively. Since we are interested in optimising the data at the radial position of the planets b and c, which are 35 and 65 pixels, we define the area to be optimised by OPCA as all pixels situated at radii between 20 and 80 pixels. For the optimisation of each frame, we reject neighbouring frames in which the sky rotation at the radius of the planets is less than one FWHM of the PSF. This rejection parameter is set for one radius at a time in OPCA, therefore we run OPCA on five datasets (I_i, Q_i, U_i, $Qcal_i$ and $Ucal_i$) for the two filters and twice again, one time for each planet radius.

To find the optimal number of principal components for each data set, we run OPCA with

TABLE 2.4: OPTIMAL NUMBER OF OPTIMISED PRINCIPAL COMPONENTS
SUBTRACTED FOR EACH DATA SET

Band	I_i		$Qcal_i$		$Ucal_i$		Q_i		U_i	
	b	c	b	c	b	c	b	c	b	c
H-band	23	25	6	11	3	6	10	3	9	4
K_s-band	11	27	11	8	4	9	10	8	10	7

a range of components for all twenty sets and record the statistics, e.g. maximum, sum, mean, median and standard deviation of four regions in the final mean-combined image of each data set. These four regions contain the signal in the pixels occupied by the planets, and the signal in a ring six pixels wide centered on their respective positions in the Intensity images, to evaluate the local background. We determine the optimal number of components for the intensity images, where the planets are detected, based on the best S/N defined as:

$$(S/N)_{\mathrm{planet}} = \frac{I_{\mathrm{max,planet}}}{\sigma_{\mathrm{loc.noise}}} , \tag{2.18}$$

where $I_{\mathrm{max,planet}}$ is the maximum intensity value in the region occupied by the planet signal and $\sigma_{\mathrm{loc.noise}}$ is the standard deviation of the pixels in the local noise region. Since this value is not representative of a detection in our polarimetric images, we choose the number of components for the Q_i and U_i data sets that minimises the standard deviation in the local background regions.

Figure 2.5 shows the I_i H-band b-optimised result. Note that the optimal parameters for c and b in H and K_s in I_i and Q_i and U_i only differ in the number of principal components subtracted from the frames (see Table 2.4) and the radius at which the rejection parameter is set. We optimise Q_i and U_i with both calibrated and uncalibrated data to monitor the impact of the calibration procedure on the final results.

2.3   Results

Figure 2.6 shows the signal to noise (S/N) maps of the mean-combined intensity images obtained after the optimal number of PCA components have been subtracted in H and K_s bands (upper and lower panels, respectively). These maps are obtained by convolving the image with the resolution element (depends on the filter) and then dividing the value in each pixel by the standard deviation of the pixels in a one-pixel-wide ring, centered on the star, at the radial position that contains that particular pixel. In this way an image of the estimated S/N in every pixel of the image can be obtained. However, to determine the actual S/N at the position of the planets, we apply Equation 2.18, which considers the local noise.

The left and right maps in Fig. 2.6 show the S/N maps for OPCA optimisation radii of 35 and 63 pixels, i.e. the approximate separation of c and b planets, respectively. The S/N ratio, as defined in Eq. 2.18 of planet b in H and K_s bands is 10.36 and 13.6, respectively. Planet c has lower S/N ratios, 8.95 and 6.62, mainly due to the fact that the region is dominated by speckle noise. The radial structure present in these intensity S/N maps seems to be dominant in the region of planet b, which could indicate that a more aggressive OPCA (i.e. that subtracts more principal components) may be a way of improving the results at this separation.

Figure 2.7 shows the same maps for calibrated Q and U images, where no statistically significant detection has been obtained.

However, a considerable improvement is achieved in terms of speckle and background
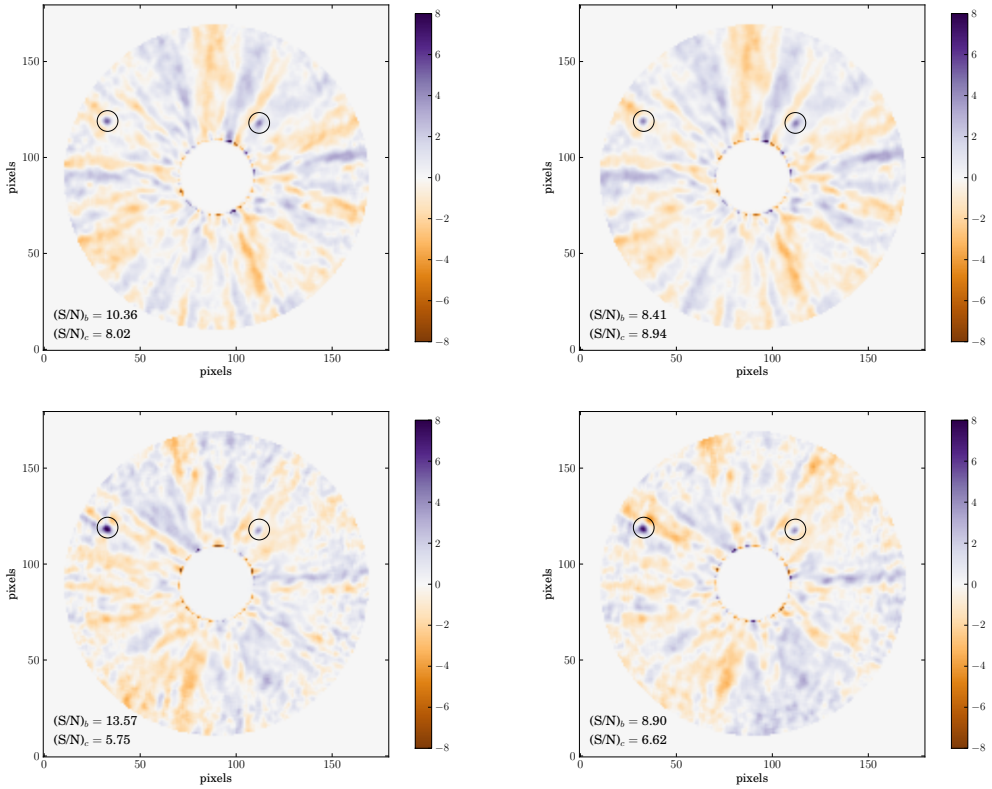

Figure 2.6: Signal-to-noise maps of the intensity images after subtraction of the optimal number of principal components. *Upper panels:* S/N maps in H-band for b (left) and c (right)-optimised OPCA reduction. *Lower panels:* The equivalent in the K_s-band. The black circles mark the positions of the planets.
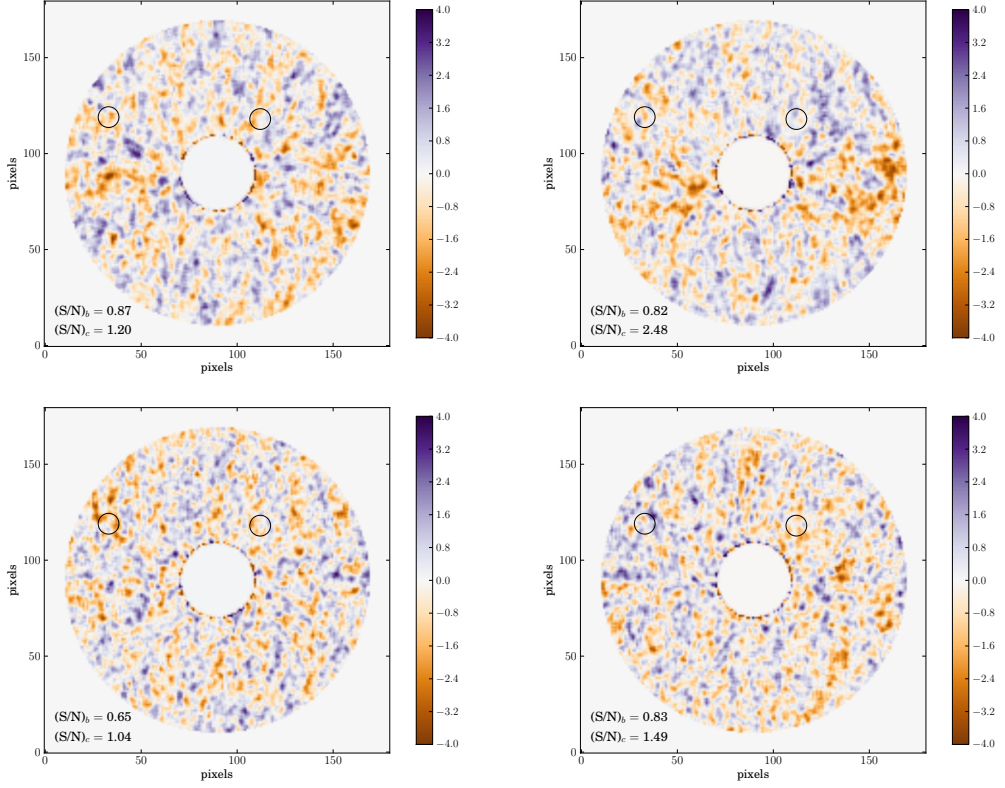
Figure 2.7: Signal-to-noise maps of the mean-combined, calibrated Q (left) and U (right) images after subtraction of the optimal number of principal components found for planet b in the case of the H-band data (upper panels) and the K_s-band data (lower panels). Black circles mark again the position of the planets.

noise reduction at the position of planet c. Figures 2.8 and 2.9 show the contrast curves obtained for both Q (upper panels) and U (lower panels) images obtained for the calibrated (left) and uncalibrated (right) data sets. Solid purple and brown lines show the radial profiles of the total intensity of the star and the 1σ standard deviation of this profile in the planet regions after OPCA. The dashed brown line shows the 1σ radial profile of the Stokes $Qcal, Q$ and $Ucal, U$ images, respectively. All curves are normalised to the flux of the star. For comparative evaluation of the curves, we show simulated profiles of the planets (stellar PSF scaled to the maximum value found for the planets in the intensity images $I_{\mathrm{max,planet}}$). The dashed lines show the maximum degree of polarisation expected for the planets due to the inhomogeneous atmospheres of 1% (de Kok et al. 2011).

Comparison of the purple and brown solid lines shows that our optimised PCA improves
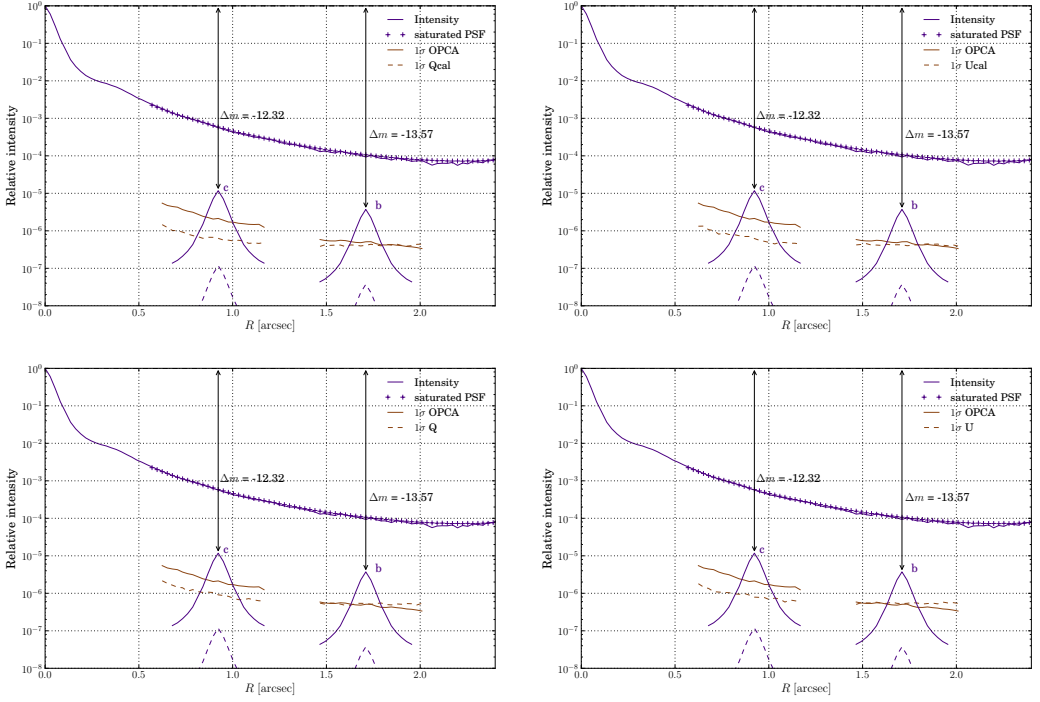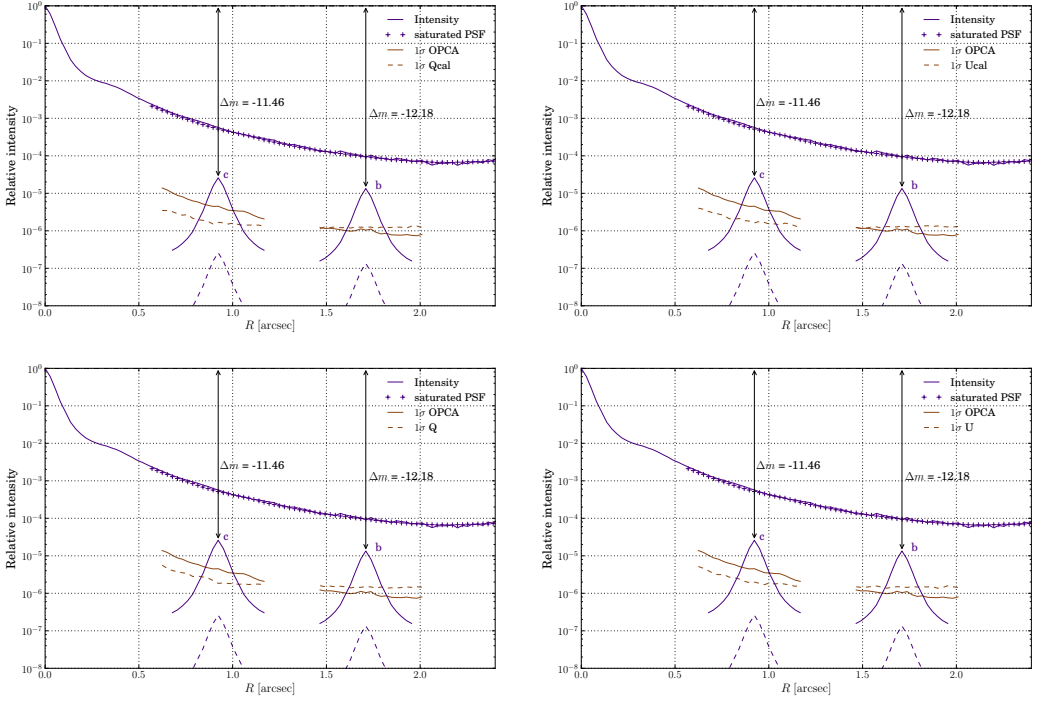
Figure 2.8: Contrast curves for H-band

the contrast by ~ 2 orders of magnitude in both filters at the position of the planets, although the improvement at the position of b in the H-band seems to be higher (~ 2.5 orders of magnitude). At the position of planet c our polarimetric results (brown dashed lines) show an additional improvement by a factor of ~ 8 and ~ 4 in the H and K_s bands, respectively, in both Q and U, while the improvement in the region occupied by planet b is insignificant. This suggests that the region, in the Q and U images, is dominated by photon noise and background subtraction. In the former case, the limitations of the polarimetry at this position could be improved by observing for longer time.

Upper (calibrated) and lower (uncalibrated) panels in these figures show that our calibration procedure yields better contrast improvement by a factor of ~ 4 in the H-band and ~ 2 in K_s band, at the position of planet c.

The upper limit for a 1σ detection on the linear polarisation of the planets can be obtained as

$$(q/u)_{\mathrm{max,planet}} = \frac{\sigma_{\mathrm{Q/U,planet}}}{I_{\mathrm{max,planet}}}, \tag{2.19}$$

Figure 2.9: Contrast curves for K$_s$-band

where $\sigma_{Q/U,\text{planet}}$ is the standard deviation of pixels at the position of the planet in the polarised images. According to this equation and the data reduction process described above, the upper limits for both the fractional q and u polarisation of planet b are $\approx 10\%$ in the H-band and $\approx 8\%$ in the K-s band, which give an upper limit for the degree of linear polarisation ($p = \sqrt{q^2 + u^2}$) of $p_{\text{max}} \approx 15$ and 11% for the H and K$_s$ bands, respectively. For planet c these values are considerably lower, $p_{\text{max}} \approx 4$ and 6% for the H and K$_s$ bands, respectively. All values are computed with calibrated data. Table 2.5 details these upper limits for the degree of fractional polarisation (p) and fractional q and u for each planet and filter.

2.4   Discussion

The S/N values and the upper limits obtained here are not yet sufficient to detect the expected polarisation signal of about a 1.5%. However, based on the analysis of the contrast curves of Figures 2.8 and 2.9, we conclude that PADI offers promising avenues for the improvement of the speckle noise suppression with respect to ADI techniques alone. Indeed, our results show that at the separation of planet c ($0.96''$), a region still dominated by speckle noise,

TABLE 2.5: SIGNAL TO NOISE VALUES AND UPPER LIMITS

Band	S/N		q_{max}		u_{max}		p_{max}	
	b	c	b	c	b	c	b	c
H-band	10.4	8.9	10.4%	2.6%	10.5%	3.9%	14.8%	4.7%
K_s-band	13.6	6.6	7.7%	3%	8%	5%	11%	6%

the improvement in contrast is almost an order of magnitude (in H-band) compared to using OPCA alone (almost 6 orders of magnitude in total with respect to the central star). Circumstellar regions not dominated by speckle noise are not benefitting nearly as much from this technique, although some improvement may be achieved by observing for longer times. When compared to polarimetry alone, PADI also proves superior in terms of speckle suppression. Comparing our contrast curves and previous observational studies such as Hinkley et al. (2009) (their Figure 2) show that PADI increases the contrast by about an order of magnitude at all angular separations.

The combination of polarimetric and angular differential imaging techniques is not straightforward and involves some trade-offs. Many different ways of combining the ADI and polarimetry still need to be investigated, which may lead to further improvements. In the following paragraphs we take a critical look at our procedures and discuss potential future improvements.

- *Combination of frames for polarimetry and OPCA:*
  As explained in Section 7.2 we carry out the double difference on the data before applying OPCA. At first sight, this may be reasonable since each double difference frame is obtained from frames in one polarimetric cycle, i.e. as close in time as possible. This ideally removes systematic differences between different beams and parts of the detector, leaving a set of rather *"clean"* frames for OPCA to work on. The modest sky rotation rate in our data (see Figure 2.2) makes it possible to take the double difference, but there is still some sky rotation and applying OPCA on beam-subtracted (i.e. single difference) frames instead of the double difference frames would have the advantage of OPCA working with differences that have been obtained from simultaneous images. Moreover, applying OPCA over, for example, sub-sets of all beam-subtracted frames of the same angle of the HWP could also improve its efficiency since the amount of sky rotation in between them is larger and the remaining systematic errors after the beam subtraction are more similar since the optical path is the same. This could reduce the number of components that have to be removed from the image, thereby minimising the risk of subtracting part of the planet signal. Another issue to take into account is the observing site. Since the rotation rate of a certain target in the sky differs from one site to another, the approach to this optimisation will most likely be different. As the sky rotation for HR8799 much larger when observed from e.g. Mauna Kea we can expect better ADI performance while the polarimetric performance may be diminished

in comparison with the site of the observations we present here (Paranal).

At an early stage of the study, we performed some tests in order to compare two combination methods: *beam subtraction, then double difference and then OPCA* and *beam subtraction, then OPCA and then double difference*. In those experiments we found no significant differences between the two approaches, but the data reduction process has since evolved and these results should not be considered as being conclusive. Moreover, the resulting Q' and U' still need to be derotated to the sky coordinate system according to the parallactic angle, which psoes the question of how to do this if OPCA is performed before the double difference.

Our approach is conservative since both double difference and OPCA methods are combined relatively independently and performed *as usual*. Polarimetric data sets can, however, be combined in many different ways, and it may indeed pay off to depart from the conservative view and explore completely new combinations, which will be considered in future efforts.

- *Gradient subtraction correction of bad centering in polarimetric frames:*
  The approach to correcting remaining centering imperfections in beam-subtracted images was introduced by (Snik et al. 2010) for solar polarimetric measurements and applied for the first time to the polarimetric measurements of a circumstellar disc by Thalmann et al. (2013). In the framework of our study it seems to be, as Figure 2.3 suggests, very successful. As explained in Section 7.2, the subtraction of the directional gradients of the intensity image is optimised by finding the c_x and c_y coefficients by means of Equation 2.3, but the impact of this gradient subtraction on the planet signal has not been quantified. Since the operation is applied to the data at a very early stage and the signal of the planets is likely to be within the noise, it seems safe to assume that the effect on the planet's combined signal after OPCA is minimal. Still, this needs to be confirmed.

- *Flux sensitivity:*
  We find values for the difference in magnitudes (Δm) between the star and the planets of $[-13.57, -12.32]\,\mathrm{mag}$ in the H-band and $[-12.18, -11.46]\,\mathrm{mag}$ in the K_s-band for b and c, respectively. These values differ by less than a magnitude from those measured in dedicated photometric studies (i.e. $[-12.6, -11.6]\,\mathrm{mag}$ for the H-band and $[-11.77, -10.85]\,\mathrm{mag}$ for the K_s band, Marois et al. 2008, Currie et al. 2011). This suggests that our sensitivity in flux is reasonably good. However, looking at the S/N maps of Figure 2.6 it is clear that some radial structure is still present, and we think that the values for the S/N found for the planets can still be improved by increasing the number of principal components subtracted from the intensity images.

While beam-subtracted polarimetric frames are corrected for centering errors through the gradient subtraction technique, the intensity frames remain as they are after the Moffat-fitting-based centering. This implies that some poorly centered frames may remain in the data set before the OPCA and will therefore be included in the SVD

computation. In principle this is taken care of by the SVD operation but it may make it less effective, meaning that for the same amount of principal components subtracted, a better-centered data set could have yielded higher fluxes in the planets.

Our centering approach based on the Moffat profile fitting to the (masked) saturated frames is a widely used technique applied to both polarimetric and angular differential imaging studies. Historically, maybe the cross-correlation between frames has been more frequently applied to polarimetric data although its application to saturated images is far from trivial. To our knowledge no comparative study has been published on this issue, which may be crucial for the success of PADI.

- *"a-posteriori" noise-reduction techniques:*
  To reduce the noise several techniques can been applied to the final intensity and po-
  larimetric images. As a first attempt at noise filtering, we applied a *matched filter* by
  convolving the images with the PSF of the star obtained from the non-saturated data.
  The aim is to *"smooth out"* signals that do not correlate with the PSF.

Figure 2.10 shows the same contrast curves as presented before for the calibrated H-band data set along with the curves of the 1σ value of the intensity image after OPCA and matched filter and of the same filter applied to the polarimetric images (yellow solid and dashed lines, respectively). The application of the filter yields a considerable improvement in the achievable contrast, particularly in the polarimetric images.

The 1σ upper limits for the fractional degree of polarisation we obtain at the position of the planets b and c are now of $[6, 2]\%$ for the H-band and $[6, 3]\%$ for the K_s-band. However, we note that these are preliminary results and further investigations are needed to fully understand the effect of the filter on the polarimetric data, particularly at the position of planet c. For example, in the case of the u fractional polarisation at the position of planet c, a bump is visible. Inspection of the filtered polarimetric image shows that the structure in that region is likely to be affected by the surrounding (noise) structure.
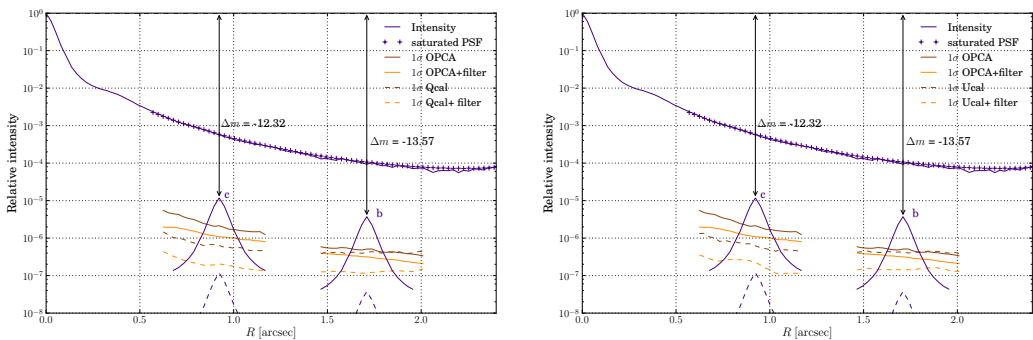

Figure 2.10: Contrast curves for H-band with resolution element filter included

If the application of this filter to the polarimetric images proves to be reliable, the values we obtain start to approach the maximum values of the expected polarisation. This is, without any doubt, one of our main avenues for future investigations.

2.5 Conclusions and outlook

We presented VLT/NACO combined polarimetric and angular differential imaging (PADI) measurements of the exoplanetary system HR 8799 in H and K_s bands. The goal of the study is to measure the polarisation of the planets b and c, which are likely to be about 1% polarised in the infrared as a consequence of scattering of their own infrared emission by their inhomogeneous atmospheres. Such a detection would directly confirm the presence of clouds in the atmospheres of these hot, giant planets. Once detected, the degree and the angle of polarisation can constrain morphological features of the atmosphere and physical characteristics such as the spin rotation axis of the planets.

Our study shows no detection of a significant, linearly polarised signal in the two planets. Our 1σ levels for a detection in the degree of polarisation at the position of the planets are $\sim [15, 11]\%$ for planet b and $[5, 6]\%$ for planet c in H and K_s bands, respectively. These 1σ upper limits are too large to draw scientific conclusions about particular characteristics of these planets. However far from optimal, our results do show the potential of the PADI technique for the improvement of speckle suppression in regions dominated by speckle noise; at short wavelengths and small separations the improvement in contrast is at least an order of magnitude as compared to conventional ADI approaches.

We introduce a new calibration method based on directly measuring the components of the telescope's Mueller matrix from measurements of unpolarised and polarised standard stars in pupil-stabilised mode. This approach has the advantage of providing instrumental polarisation and efficiency factors directly applicable to the science data at all wavelengths and pointing angles of interest, provided that the standard stars are measured in all filters needed and the polarised stars, in particular, at two parallactic angles separated by at least by $45°$.

Based on the points discussed in Section 7.6, it is clear that further investigations are needed to optimise this technique. Our main interest for the near future is to understand the sources of the limitation of our polarimetric sensitivity and to sort out the best way of combining the double difference and OPCA methods other than the conservative approach used here. As we pointed out in the discussion, the application of the matched filter to the polarimetric images appears to be promising and will be explored in the future. Another important focus of interest for the future is to explore the contrast improvements PADI yields at angular separations smaller than that of planet c, which we expect to be larger than an order of magnitude based on the performance we currently obtain.

With the upcoming commissioning and start of operations of VLT/SPHERE and the high-resolution and powerful polarimetric capabilities of its polarimeters (ZIMPOL and IRDIS), it seems imperative to explore the promising avenues for the characterisation of exoplanets that PADI offers.

Acknowledgements

Chapter 3

Imaging diagnostics for transitional discs

M. de Juan Ovelar, M. Min, C. Dominik, C. Thalmann, P. Pinilla, M. Benisty and T. Birnstiel.

> *One of the best prizes life has to offer is the*
> *chance to work hard at work worth doing.*
> – adapted from T. Roosvelt

Abstract

Transitional discs are a special type of protoplanetary discs where planet formation is thought to be taking place. These objects feature characteristic inner cavities and/or gaps of a few tens of AUs in the sub-millimetre images of the disc. This signature suggests a localised depletion of matter in the disc that could be caused by planet formation processes. However, recent observations have revealed differences in the structures imaged at different wavelengths in some of these discs. In this paper, we aim to explain these observational differences using self-consistent physical 2-D hydrodynamical and dust evolution models of such objects, assuming their morphology is indeed generated by the presence of a planet. We use these models to derive the distribution of gas and dust in a theoretical planet-hosting disc, for various planet masses and orbital separations. We then simulate observations of the emitted and scattered light from these models with VLT/SPHERE ZIMPOL, Subaru/HiCIAO, VLT/VISIR and ALMA. We do this by first computing the full resolution images of the models at different wavelengths, and then simulating the observations accounting for the characteristics of each particular instrument. The presence of the planet generates pressure bumps in the gas distribution of the disc whose characteristics strongly depend on the planet mass and position. These bumps cause large grains to accumulate while small grains are allowed into inner regions. This spatial differentiation of the grain sizes explains the differences in the observations since different wavelengths and observing techniques trace different parts of the dust size distribution. Based on this effect, we conclude that the combination of visible/near-infrared polarimetric and sub-mm images is the best strategy to constrain the properties of the unseen planet responsible for the disc structure.

3.1   Introduction

Transitional discs are generally believed to be the result of a planet forming stage in a circumstellar disc. As such, their study provides with important information that can help us to constrain the physics of the planet formation process. Therefore, a considerable amount of effort is currently being invested to understand these objects better, both theoretically and observationally. In general, the spectral energy distribution (SED) of these sources as well as interferometric measurements at sub-millimitre wavelengths show evidence for inner cavities and/or gaps (e.g. Strom et al. 1989, Espaillat et al. 2010, Andrews et al. 2011). One of the interpretations of these observations is that a fraction of the material in the disc is depleted by a forming planet (see the review of Williams & Cieza 2011, for an extensive view).

Recently observational work has called this conclusion into question based on e.g. measurements of the accretion rate (e.g. Calvet et al. 2005, Espaillat et al. 2007) and polarimetric observations of the inner regions of the disc (Dong et al. 2012). The latter one, of particular interest since it involves direct imaging of the disc structure, was carried out as a part of the near infrared (NIR) Strategic Explorations of Exoplanets and Disks with Subaru survey (SEEDS, Tamura 2009). The results of the survey were surprising regarding a number of transition discs classified as such based on sub-mm emission observations. The polarimetric images of these discs did not show the expected gap (Dong et al. 2012). A parametric model of the disc with a continuous radial distribution of small grains $\sim 1\,\mu$m and a significant depletion of big grains $\sim 1\,$mm in the inner regions of the disc was found to reproduce such observational discrepancies. These regions would appear empty in the sub-mm images whereas the presence of small grains, scattering light very efficiently in the NIR wavelengths, would explain the polarimetric measurements. However, due to the parametric nature of the model, the Dong et al. (2012) study could not provide an explanation of the physical mechanisms causing this differentiation of big and small dust grain distributions across the radial extent of the disc, but merely suggested that some filtering mechanism must be active.

Theoretical studies such as Rice et al. (2006), Zhu et al. (2011, 2012), Pinilla et al. (2012a) provide a potential physical explanation. The main drive for these studies is to explain how particles of dust in a disc can grow up to large sizes ($\sim 1\,$m) without being dragged towards the star by the radial drift mechanism. This constitutes one of the long standing problems in planets formation, the *"1-m barrier"* problem (Weidenschilling 1977, Brauer et al. 2008). In particular, one of the latest studies (Pinilla et al. 2012a), explored the influence the presence of a planet has on the distribution of gas and dust in the disc. In this study, the authors combine 2-D hydrodynamical simulations of the evolution of the gas distribution in a disc that hosts a planet with state of the art dust evolution models. These models include, for the first time, self-consistent calculations of the radial drift, coagulation and fragmentation mechanisms undergone by the dust (Birnstiel et al. 2010). They showed that the presence of a planet generates pressure gradients in the gas distribution that cause the velocity of the gas to increase to near-Keplerian values at specific radial positions. This reduces the differential velocity between dust and gas particles and, therefore, the drag force exerted on the dust. As a consequence, large particles ($\sim 1\,$mm), which are less affected by the gas drag, accumulate

in those radial locations where the pressure reaches a maximum, which allows them to grow "protected" from the radial drift. Smaller grains, still coupled to the gas, follow the accretion flow into the inner regions of the disc. The trapping and filtering characteristics and the radial position of these bumps are highly dependent on the mass and position of the planet.

If these models indeed reproduce the physical processes taking place in a transitional disc, measuring the characteristics of this size-differentiated dust distribution should allow to constrain characteristics of the planet that causes it. The observational differences found between sub-mm emission and NIR scattered images become then a powerful diagnostic tool for transitional discs and the planets they host. In this work, we perform a theoretical study simulating observations of hydrodynamical and dust evolution models, similar to those presented in Pinilla et al. (2012a), with SPHERE ZIMPOL, HiCIAO, VISIR and ALMA. Our aim is to 1) test whether these models can reproduce the general characteristic features found in observations, 2) analyse what different imaging techniques can tell us about the dust distribution and 3) detect the best imaging strategy to constrain characteristics of the planet such as mass and position from dust measurements. We would like to clarify that we do not aim to explain detailed characteristics revealed by particular observations of transitional discs.

The study is organised as follows: In Section 7.2, we describe the methodology used to obtain the disc models and the simulated observations. In Section 7.4 we present images and radial profiles obtained for the different cases and instruments considered and in Section 7.6 the discussion of those results. Finally, in Section 6.5 we provide a short summary of the study and list our conclusions.

3.2   Method

In order to generate images of a transitional disc, we base our study in the disc-planet inter-action models presented in Pinilla et al. (2012a). These models combine two dimensional hydrodynamical and dust evolution simulations including radial drift, coagulation and frag-mentation, to self-consistently reproduce the evolution of the gas and dust in the disc. We consider the cases of a disc with a planet of masses $M_{\mathrm{p}} = [1, 9, 15] \, M_{\mathrm{Jup}}$ at radial posi-tions $R_{\mathrm{p}} = [20, 40, 60]$ AU. We take the resulting distribution of dust and gas for these three cases after $3 \, \mathrm{Myr}$ of evolution and input them in the Monte-Carlo radiative transfer code MCMax, to produce full resolution intensity and polarised intensity images of the emitted and scattered flux. Finally, we simulate realistic observations with VLT/SPHERE ZIMPOL, Subaru/HiCIAO, VLT/VISIR and ALMA either using specific instrument simulators or con-volving the full resolution images with the characteristic point spread function (PSF) and adding realistic effects such as noise, and decrease in resolution due to seeing. In the follow-ing subsections we present the details of the steps followed.
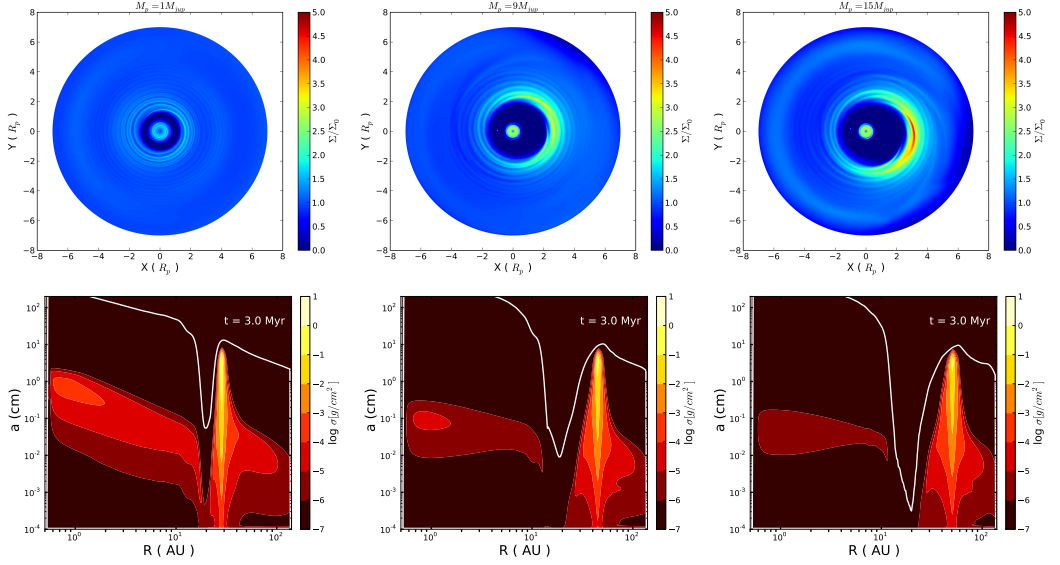
Figure 3.1: *Top panels:* 2D gas surface density for $[1, 9, 15]\,\mathrm{M_{jup}}$ after 1000 orbits of evolution. *Bottom panels:* Vertically integrated dust density distribution for each planet mass and for the case of R_p=20 AU. The white line corresponds to the size of particles that feel the highest radial drift and it is proportional to the gas surface density.

TABLE 3.1: DISC-PLANET SIMULATION
INPUT PARAMETERS FROM PINILLA ET AL. 2012

Temperature of the star (T_star)	$4730\,\mathrm{K}$
Radius of the star (R_star)	$1.7\,M_\odot$
Mass of the star (M_star)	$1\,M_\odot$
Mass of the disc (M_disc)	$0.0525\,M_\odot$
Position of the planet (R_p)	$[20, 40, 60]\,\mathrm{AU}$
Fragmentation velocity (v_f)	$10\,\mathrm{m/s}$
Inner disc radius ($R_\mathrm{disc,inn}$)	$0.025\,R_\mathrm{p}$
Outer disc radius ($R_\mathrm{disc,out}$)	$7.0\,R_\mathrm{p}$
Solid density of dust particles (ρ_dust)	$1.2\,\mathrm{g/cm^3}$
Alpha viscosity (α)	10^{-3}

3.2.1   Disc-planet interaction models

To obtain the gas and dust distribution of our transitional discs we follow the same simulation procedure used in Pinilla et al. (2012a). The results are obtained by first solving the equations for the hydrodynamical interactions between the gas in the disc and the planet, and then computing the evolution of the dust in a disc with the obtained gas surface distribution. The first computation is done by means of the two-dimensional hydrodynamical code FARGO (Masset 2000), which uses finite differences to solve the Navier-Stokes and continuity equations in a grid of annular cells that define the disc. The simulations were computed selecting open boundary conditions to allow the material to leave the grid. The logarithmically extended radial grid is taken for each case from $R_{\mathrm{disc,inn}} = 0.025$ to $R_{\mathrm{disc,out}} = 7.0$, using normalized units, such that the planet is located at $R_{\mathrm{p}} = 1.0$. Table 3.1 lists the input parameters used in these simulations. They are the same as in Pinilla et al. (2012a) but considering only $\Sigma \propto r^{-1}$, kinematic viscosity $\nu = \alpha c_s h$, with $\alpha = 10^{-3}$, and normalizing the mass of the disc to $M_{\mathrm{disc}} = 0.55\,M_{\odot}$. Stellar parameters are those typical of T-Tauri stars. Note that parameters defining the geometry of the disc, i.e. $R_{\mathrm{disc,inn}}$ and $R_{\mathrm{disc,out}}$ are defined with respect to the position of the planet such that they are always far enough from it allowing for a appropriate study of the effects it has in the inner and outer discs. Although this link may not be necessarily physical, it allows for comparison of the different planet separation cases without increasing the radial resolution of the simulations i.e. the required computational time.

The hydrodynamical simulations are done until the disc reaches a quasi-stable state after ~ 1000 planet orbits. The 2D gas surface density is then azimuthally averaged and used as the initial condition for the dust evolution modelling. Note that during the dust evolution modelling the gas surface density remains constant on timescales of millions of years, hence any mechanism that may disturb the gas density as, for instance, photoevaporation, is omitted. For the dust evolution simulations, we use the 1-D code described in Birnstiel et al. (2010), which computes the growth and fragmentation happening in the radial dust distribution due to radial drift, turbulent mixing and gas drag forces. The dust is initially distributed such that the dust-to-gas ratio is 1% and with an initial size of $1\,\mu$m. The dust distribution is evolved for $3\,\mathrm{Myr}$. We follow this process for all planet mass and radii cases, i.e., $M_{\mathrm{p}} = [1, 9, 15]\,M_{\mathrm{Jup}}$ and $R_{\mathrm{p}} = [20, 40, 60]\,\mathrm{AU}$.

Fig. 3.1 shows the results of these simulations for each planet mass studied and for the specific case of $R_{\mathrm{p}} = 20\,\mathrm{AU}$. Top panels show the 2D gas surface density after 1000 orbits of evolution. For each case, it is clear how the shape of the gap varies with the mass of the planet. For the case of $15\,\mathrm{M_{jup}}$, even a vortex appears at the outer edge of the gap due to the high mass of the planet (Ataiee et al. 2013).

Bottom panels of Fig. 3.1 show the vertically integrated dust density distribution (see Pinilla et al. 2012a, Eq. 5 and 6). The solid white line indicates the size of particles that feel the highest radial drift, which is directly proportional to the azimuthally averaged gas surface density (see Pinilla et al. 2012a, for details). The presence of the planet clearly perturbs the gas and dust density distributions, dividing the disc into inner and outer regions, where the distribution of dust particle sizes is clearly different. Note that, due to the 1-D nature of the

dust evolution code, the dust distribution cannot reproduce the asymmetries caused by the presence of e.g. vortices in the gas distribution. For the purposes of our study, where the aim is to analyse the radial morphology of the dust distribution, this approximation is sufficient.

3.2.2 Radiative Transfer simulations

To compute the emitted and scattered flux of the disc we use the Monte-Carlo radiative transfer code MCMax (Min et al. 2009). MCMax self-consistently solves the temperature and vertical structure of the distribution of gas and dust in the disc given the size and composition of the particles and the characteristics of the central star, including the effect of dust settling. It produces common observables for the study of the disc such as SED or emission and scattering images, at the desired wavelengths and inclination angles. MCMax is widely used to compare theoretical models of discs with observations (see Mulders et al. 2010, 2011, Mulders & Dominik 2012, de Vries et al. 2012, Canovas et al. 2012b, Jeffers et al. 2012, Lombaert et al. 2012, Honda et al. 2012, Min et al. 2012, Mulders et al. 2013, for some examples).

MCMax reads in the distribution of gas and dust obtained from the disc-planet models for all planet mass and separation cases as well as the central star and general disc parameters. It also requires a composition of the dust to compute the opacities and temperatures. We model this composition as a mixture of silicates ($\sim$58%), iron sulphide ($\sim$0.18%) and carbonaceous dust grains ($\sim$0.24%) with an average density of $\rho = 3.2\,\mathrm{g/cm^3}$ (Min et al. 2011). We set a porosity for the dust grains of $p = 0.625$ which corresponds to the $\rho = 1.2\,\mathrm{g/cm^3}$ used in the dust evolution simulations. The indexes of refraction needed to compute the opacities were obtained from Dorschner et al. (1995), Henning & Stognienko (1996) for the silicates, from Begemann et al. (1994) for the iron sulphide and from Preibisch et al. (1993) for the carbonaceous dust grains. MCMax self-consistently simulates the settling effect provided the viscous turbulence (α). We set this value to that of the disc-planet simulations (i.e. $\alpha = 10^{-3}$). The vertical structure of the gas in the disk is solved iteratively under the assumption of vertical hydrostatic equilibrium. The vertical structure of the dust is then computed using settling and vertical turbulent mixing.

With the resultant temperature and vertical structure, MCMax produces intensity and polarised intensity theoretical images of the disc at the desired wavelength. In this paper we will discuss the results obtained for wavelengths of $\lambda = [0.65, 1.6, 20, 850]\,\mu$m which are the most commonly used for imaging diagnostics of circumstellar matter.

3.2.3 Simulated observations

To simulate realistic observations of the modeled discs, we select a set of currently available (Subaru/HiCIAO and VLT/VISIR) and near future instruments (VLT/SPHERE-ZIMPOL and ALMA Complete Array) that are (or are likely to be) leading the field of imaging circumstellar environments. These instruments work in different regions of the electromagnetic spectrum, thus probing different features in the disc. We select a filter from the available ones in each instrument (RI, H, Q and $850\,\mu$m), and produce an MCMax full-resolution image for a particular wavelength in the filter range ($\lambda = [0.65, 1.6, 20, 850]\,\mu$m respectively). Then

TABLE 3.2: WAVELENGTH AND RESOLUTION OF THE
SIMULATED IMAGES

Instrument	$1.2\lambda/D$	final	$d = 140\,\mathrm{pc}$
SPHERE ZIMPOL	$0.02''$	$0.03''$	$\sim\ 4\,\mathrm{AU}$
Subaru HiCIAO	$0.04''$	$0.09''$	$\sim 13\,\mathrm{AU}$
VLT VISIR	$0.6''$	$0.62''$	$\sim 87\,\mathrm{AU}$
ALMA complete	$0.013''$	$0.015''$	$\sim\ 2\,\mathrm{AU}$

we either process these images using a specific instrument simulator, convolving it with a measured or simulated PSF of the instrument (depending on the case), and adding photon noise and loss of resolution accounting for realistic observational effects. We assume an exposure time of $t_{\mathrm{obs}} = 1200\,\mathrm{s}$ with all instruments. Table 3.2 shows the the theoretical and final resolution obtained for the simulated observation with each instrument. In the following paragraphs we explain the details of the image processing followed in each case.

- *R-band intensity and polarised intensity images with SPHERE ZIMPOL*:

  Intensity and polarised intensity observations with SPHERE in R-band are simulated with the SPHERE ZIMPOL simulator that comes as part of the SPHERE software package (Thalmann et al. 2008). SPHERE (Beuzit et al. 2006) is the planet finder designed for the Very Large Telescope, which is planned to see first light by the end of 2013. By means of its polarimeter ZIMPOL it provides linear polarimetric imaging capabilities for the characterisation of circumstellar environments and exoplanets (Gisler et al. 2004, Stuik et al. 2005, Thalmann et al. 2008, Roelfsema et al. 2010, Schmid et al. 2010). The simulator takes full resolution intensity and polarimetric images as the input, and generates the observed images simulating the artifacts and aberrations caused by the optical system. We choose the RI filter in the simulator and process the MCMax intensity, Stokes Q and U images. The final polarised intensity image was obtained as $PI = \sqrt{Q^2 + U^2}$.

- *H-band intensity and polarised intensity images with HiCIAO*:

  In the case of H-band images, we convolve the full resolution intensity and Stokes Q and U images with a measured HiCIAO H-band PSF. This PSF was obtained from the publicly available ACORNS-ADI data reduction pipeline (Brandt et al. 2013). We add photon noise to the convolved images as follows. First we add photon noise to the convolved intensity image. Then the previous noise-free intensity image is subtracted from this one to generate a photon noise map. We do this two consecutive times to generate different maps for the Q and U images. Each map is divided by two, assuming

that half of the observing time goes to each linear polarisation measurement (i.e. Q and U), and the result is added to the convolved Q and U images. The final polarised intensity image is then computed again as $PI = \sqrt{Q^2 + U^2}$. The final resolution obtained in this case is determined by the full width half maximum (FWHM) of the measured PSF.

- *Q-band intensity images with VISIR*:

  To simulate Q-band observations we use MCMax. Provided the dimensions of the primary and secondary mirrors and the exposure time, the code can generate a theoretical PSF to be convolved with the images and compute the corresponding photon noise. There is also the option to specify an angular width to be added to the simulated resolution determined by the PSF. This accounts for the effect of the observing conditions (i.e., seeing). We specify values for the primary and secondary mirrors of $D_1 = 8.4\,\mathrm{m}$ and $D_2 = 1\,\mathrm{m}$, an exposure time of $t_{\mathrm{obs}} = 12000\,\mathrm{s}$ and a seeing width of $w = 0.05''$.

- $850\,\mu\mathrm{m}$ *intensity images with ALMA*:

  The ALMA observations are simulated in a simplified way. The spatial resolution of ALMA can be estimated by calculating the resolution of a telescope with a primary mirror diameter as big as the baseline of the antenna array. For our study, we assume the maximum baseline provided by ALMA complete, which corresponds to $16\,\mathrm{km}$, and the diffraction-limited resolution at $850\,\mu\mathrm{m}$ is $13\,\mathrm{mas}$. The ALMA complete array was assembled and inaugurated in March 2013, although some antennas are still being tested. Observations for the next cycle (Early Science-Cycle 2), with still reduced capabilities, are expected to be performed in mid-2014. Full operations are expected to follow shortly after the end of Cycle 2 operations. To allow for slightly reduced performance, we use $15\,\mathrm{mas}$ as the FWHM of the PSF. We adjusted the exposure time to account for the fact that the actual collecting area of ALMA is less than that of a telescope with a mirror as big as the baseline. In the final configuration of ALMA complete (using only the $12\,\mathrm{m}$ antennas) the collecting area will be provided by 50 antennas of diameter $D = 12\,\mathrm{m}$. Therefore, we reduced the effective observing time ($t_{\mathrm{obs}} = 12000\,\mathrm{s}$) by a factor of $f_{\mathrm{corr.}} = (50 \cdot 6^2)/8000^2 = 2.81 \cdot 10^{-5}$. We then fold the theoretical image with the final PSF of $15\,\mathrm{mas}$ to produce the images presented here.

3.3 Results

Figure 3.2 shows a selection of the obtained simulated observations for all planet mass cases at $R_{\mathrm{p}} = 20\,\mathrm{AU}$ and after $3\,\mathrm{Myr}$ of evolution. Columns in the figure show, from left to right, polarised intensity (PI) for R-band with ZIMPOL, H-band PI with HiCIAO and intensity (I)
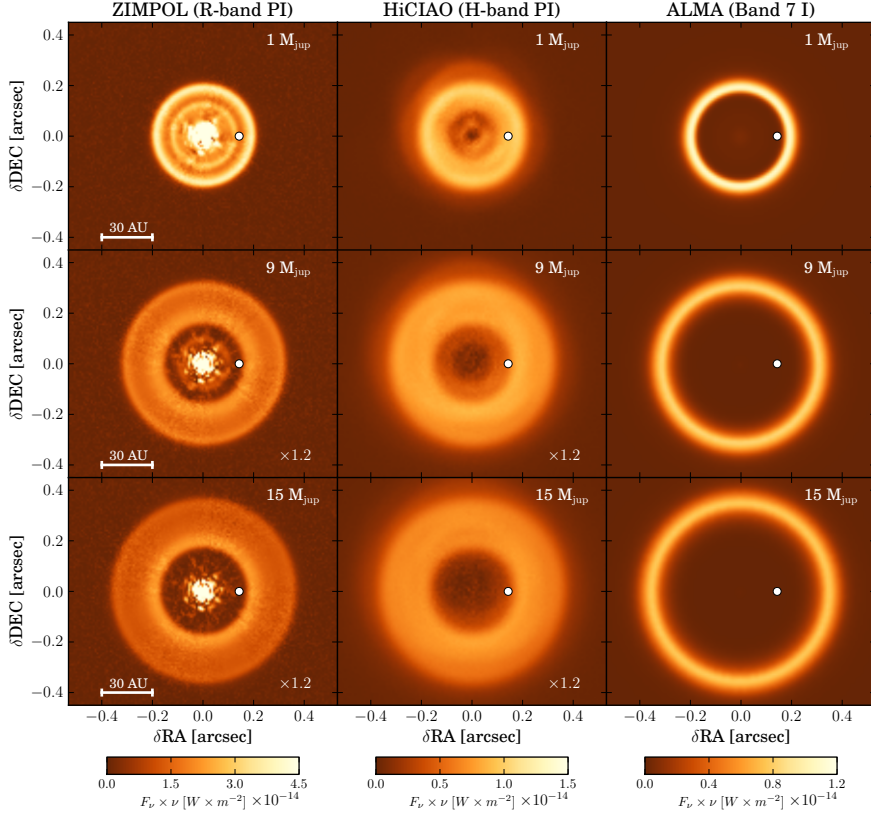
Figure 3.2: Simulated images of the disc-planet models used in this study for the case of an embedded planet orbiting at 20 AU (white dot). Left to right columns correspond to polarised intensity (PI) ZIMPOL images in the R-band ($0.65\,\mu$m), PI HiCIAO images in H-band ($1.6\,\mu$m) and intensity (I) ALMA images at $850\,\mu$m. Top, middle and bottom rows show images obtained for planet masses of $M_{\mathrm{p}} = [1, 9, 15]\,M_{\mathrm{Jup}}$ respectively. All images in the same band (column) share the colour scale, although the cases of 9 and $15\,M_{\mathrm{Jup}}$ in R and H polarised intensity have been multiplied by a small factor to enhance the contrast. See Section 7.2 for details on how the models/images were generated.

with ALMA at $850\,\mu$m, respectively. Rows show the different planet mass cases (i.e. $M_{\mathrm{p}} = [1, 9, 15]\,M_{\mathrm{Jup}}$ from top to bottom, respectively), and the white dot represents the position of the planet at 20 AU. Unless otherwise noted, radii lower than $R < R_{\mathrm{p}}$ or larger than $R > R_{\mathrm{p}}$ are referred to as *inner* and *outer* regions of the disc respectively.

The polarised intensity images obtained with the polarimetric capabilities of ZIMPOL (first column) reveal the structure of the disc remarkably well. In all planet mass cases, a
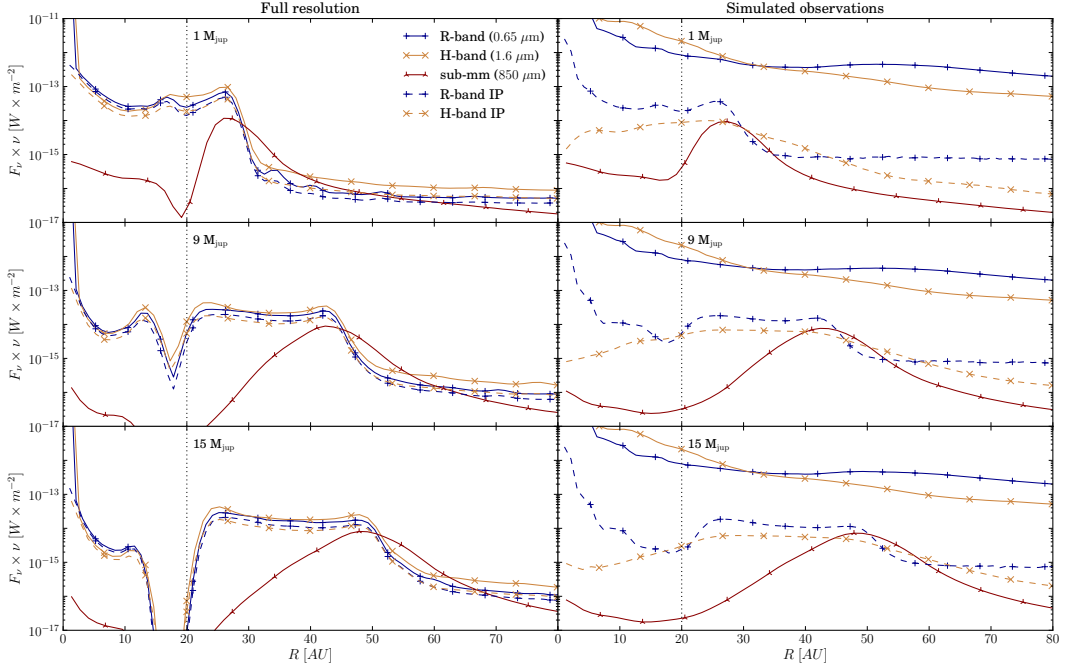
Figure 3.3: Radial profiles of the theoretical images (left panel) and simulated observations (right panel) of a 3 Myr disc with a planet of mass $M_{\mathrm{p}} = [1, 9, 15]\, M_{\mathrm{Jup}}$ from upper to lower panels, in the R (0.65 μm), H (1.6 μm) and 850 μm bands. Solid lines correspond to intensity (I) profiles while dashed lines correspond to polarised intensity (PI). The vertical dotted black line indicates the radial position of the planet at 20 AU.

gap at the position of the planet is detectable. Moreover, the three cases are different because the inner regions are actually resolved. In the case of polarimetric images obtained with HiCIAO and intensity images with ALMA, a gap of different sizes is also detected in all cases. However, these instruments do not detect any inner disc structure. Note that we did not use a coronagraph in our simulations in order to get to the smallest possible working angles. Published observations executed with HiCIAO often do use a coronagraph, masking what amounts to the inner disk in our simulations (see Sec. 7.6 below for details).

Figure 3.3 shows the computed intensity and polarised intensity radial profiles of the full resolution and (instrument) limited resolution images for all mass cases studied and a position of the planet of $R_{\mathrm{p}} = 20$ AU. We show profiles for intensity in R (0.65 μm), H (1.6 μm) and 850 μm bands (solid lines), together with polarimetric intensity in R (0.65 μm) and H (1.6 μm) bands (dashed lines). Top to bottom panels show the cases of a planet mass of $M_{\mathrm{p}} = [1, 9, 15]\, M_{\mathrm{Jup}}$, respectively. Full resolution panels on the left, therefore show the theoretical emission and scattering pattern of the disc for each planet mass case, while the

panels on the right (radial profiles of the simulated observations) show what would be imaged with the considered instruments (corresponding to the images in Figure 3.2).

3.3.1 Disc with a $1\,M_{\mathrm{Jup}}$ planet

The top row of Figure 3.2 shows the simulated observations with ZIMPOL, HiCIAO and ALMA for the $M_{\mathrm{p}} = 1\,M_{\mathrm{Jup}}$ case at $R_{\mathrm{p}} = 20\,\mathrm{AU}$. Both polarimetric images obtained with ZIMPOL in R-band and HiCIAO in H-band, detect scattered flux in the $R < 30\,\mathrm{AU}\,(\sim 0.2'')$ region that appears empty to ALMA at $850\,\mu\mathrm{m}$. However, the high spatial resolution delivered by ZIMPOL, allows to resolve a narrow and shallow gap at the position of the planet that is not detected by HiCIAO.

The top left panel in Figure 3.3 shows the radial profiles of the full resolution images for this planet mass case (i.e. before applying the instrument simulators). In all these wavelengths, the morphology of the profiles can be divided into inner, $r < 30\,\mathrm{AU}$, and outer, $r > 30\,\mathrm{AU}$, regions. Visible and NIR wavelengths show a sharp decrease in the scattered and emitted flux at this position ($r \sim 30\,\mathrm{AU}$) where the emission at $850\,\mu\mathrm{m}$ presents a narrow ($\sim 10\,\mathrm{AU}$) peak. In the inner 30 AU the scattered flux in both R and H bands and the emission in R show the narrow depletion of about a factor of ~ 4 at the position of the planet. The $850\,\mu\mathrm{m}$ emission profile is strongly depleted in this region.

The top right panel in Figure 3.3 shows the radial profiles of the simulated observations. Emission profiles at visible and NIR wavelengths (R and H bands) are completely dominated by the flux of the central star, thus the structure of the disc seen in the full resolution profiles is lost in the convolution with the PSF of the instrument. ALMA is immune to this effect because the star is too faint at these wavelengths. The high resolution of the instrument also allows for the detection of the ring at about 30 AU.

Polarimetric observations in R and H efficiently remove the stellar emission from the image and are able to show the inner edge of the outer disk. However, because of the high resolution of the instrument, only ZIMPOL images in R-band show the local depletion at the position of the planet.

These images and radial profiles are in agreement with what is expected from the results of Pinilla et al. (2012a). The presence of the planet triggers the spatial separation of the different dust grain sizes (see bottom panels of Fig. 3.1). Big grains ($\sim 1\,\mathrm{mm}$) are trapped in the pressure maximum at about $\sim 30\,\mathrm{AU}$, further out from the planet, and generate the emission detected by ALMA (i.e. ring at $\sim 30\,\mathrm{AU}$). Small ($\sim 1\,\mu\mathrm{m}$) grains are allowed in the radii closer to the star ($R < 30\,\mathrm{AU}$) and they are efficient scatterers at shorter wavelengths, which causes them to show up in the polarised intensity images.

3.3.2 Variation with planet mass

For higher planet masses, the spatial separation of dust grain sizes becomes stronger (see middle and right bottom panels of Fig. 3.1). The 9 and 15 M_{Jup} planet mass cases are shown in the middle and lower panels of Figures 3.2 and 3.3.

In both cases, the full resolution radial profiles show that both the outer sharp edge of the ring in visible and NIR wavelengths and the narrow emission ring at $850\,\mu$m are now located at $\sim$50 AU. The decrease in flux at the position of the planet becomes larger than one order of magnitude at all wavelengths. The gap becomes deeper and wider in all bands although for the sub-mm wavelengths this effect is stronger, indicating that indeed, big grains of dust are more subject to the depletion generated by the planet at these radii.

The loss of structure in R and H intensity images due to the convolution with the instrumental PSF is also present in these cases (blue and yellow solid lines in middle and lower right panels of Figure 3.3). Again, ALMA is able to detect the overall shape of the corresponding profile in the theoretical images, showing a ring at about $r \sim 50$ AU where the maximum of the theoretical profiles is placed.

The polarimetric images are also able to show structure in the $R < 50$ AU inner radii in these two planet mass cases. H-band PI images with HiCIAO, show an extended ring of scattered flux from $R \sim 10$ AU to $R \sim 50$ AU and from $R \sim 20$ AU to $R \sim 50$ AU for the intermediate and high planet mass cases respectively.

The ZIMPOL images in R-band are particularly interesting in this cases. For the $9\,M_{\rm Jup}$ planet case, the simulated observation profile (dashed blue line in middle-right panel of Figure 3.3) shows an inner ring that extends from $R \sim 5$ AU to $R \sim 15$ AU that is not present in the more massive $15\,M_{\rm Jup}$ case. The presence of this inner ring is a very interesting feature that differentiates between companion masses above or below the deuterium-burning limit of $\sim$13 $M_{\rm Jup}$[1], which is often used as a dividing line between planets and brown dwarf companions. The full resolution radial profiles of the H and R images in these two cases (blue and yellow lines in middle and bottom left panels of Fig. 3.3) show that the scattered flux from the inner ≤ 17 AU radii in the $9\,M_{\rm Jup}$ case is about an order of magnitude higher than that of the $15\,M_{\rm Jup}$ planet in that same region. Unfortunately, HiCIAO is not able to resolve it in the H-band, and in ZIMPOL images this radial region is dominated by speckles due to the proximity to the star. Therefore, although the feature is resolved, its detection is not reliable enough.

3.3.3   Effect of the disc inclination

So far, we have considered the case of a disc with a $i = 0°$ inclination (i.e. pole-on) but the emission and scattering images of inclined discs can differ considerably from this case. Figure 3.4 shows the same disc-planet cases presented in Figure 3.2 (i.e. $M_{\rm p} = [1, 9, 15]\,M_{\rm Jup}$ at $R_{\rm p} = 20$ AU) with an inclination of $i = 35°$ (angle measured from pole-on). In general, the structural features (i.e. gaps and rings) remain the same while the brightness patterns become asymmetrical. The polarised intensity images show clearly the effect of forward scattering, which makes the near side of the disc appear brighter than the far side. This effect is caused by the fact that dust particles, depending on their size with respect to the incoming wavelength, can scatter light differently in different directions. In particular, grains with sizes $2\pi a > \lambda$ are very strong forward scatterers which means that the population of $a > 1\,\mu$m dust grains

---

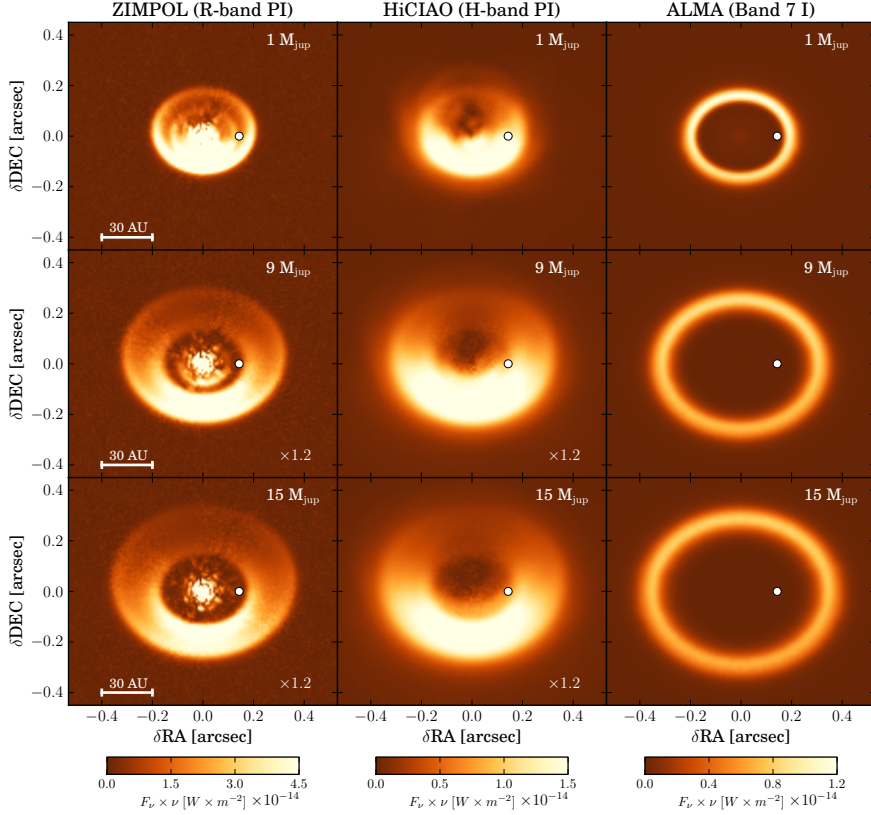[1]The deuterium-burning limit can range between 11–16 $M_{\rm Jup}$ depending on the metallicity (Spiegel et al. 2011)

Figure 3.4: Simulated images of the same discs as the ones shown in Figure 3.2, now with an inclination of $i = 35°$ (with respect to pole-on). Again columns, from left to right, show ZIMPOL polarised intensity in R-band ($0.65 \, \mu$m), HiCIAO polarised intensity in H-band ($1.6 \, \mu$m) and ALMA Band 7 ($850 \, \mu$m) intensity images, respectively. Near and far sides of the disc correspond to lower and upper parts of the images, respectively.

will show this effect in observations with ZIMPOL and HiCIAO PI at $\lambda \leq 1.6 \, \mu$m. The difference in brightness between both sides can be used as an estimator of the size of dust particles in the disc although one needs to be careful and appropriately account for the effects of dust particle shape and structure (Mulders et al. 2013).

In the transitional discs we model in this study, the effect of the forward scattering turns out to be even more useful since it makes possible to detect more clearly the dust particles in

the inner regions ($R < R_{\mathrm{p}}$) of the disc. Indeed, the ZIMPOL images of the $35°$ inclined discs for the $M_{\mathrm{p}} = 9, 15\, M_{\mathrm{Jup}}$ cases (middle and bottom images in the first column of Fig. 3.4) are now clearly distinguishable. The former shows scattering from the dust particles in the inner region of the disc while the latter does not, due to the fact that the depletion of particles is much higher in this case (see Section 7.6 below for details).

The ALMA simulations show the opposite behaviour in the brightness pattern, where the far side appears brighter than the near side. This is simply due to the fact that we are observing the emission of warmer dust in the far side and colder dust in the near side. In other words, we are looking directly at the wall of $1\,\mathrm{mm}$ particles illuminated by the star in the far side, while we are seeing the cold dust at the *"back"* of the disc in the near side.

3.3.4   Variation with planet position

As the planet orbits further away from the star, the basic inner disc–gap–outer disc morphology of the disc remains the same for all planet mass cases, all re-scaled to the position of the planet. Figure 3.5 shows ZIMPOL images in R-band ($0.65\,\mu\mathrm{m}$) for all three cases of planet mass studied before, now at planet orbit radii of $R_{\mathrm{p}} = [20, 40, 60]\,\mathrm{AU}$. The white dot indicates again the position of the planet. Overplotted, the contour black lines show the emission predicted for ALMA at $850\,\mu\mathrm{m}$.

The images show how the inner disc becomes more extended for larger orbit radii in all planet mass cases, although due to the larger distance between the dust and the star, the scattering weakens and the ZIMPOL images become fainter. This effect also increases with the mass of the planet in the outer part of the disc. The radius of the ring detectable by ALMA (black contour lines), which traces the particle trap, increases in general with planet mass and separation. It is important to note how for the case of $M_{\mathrm{p}} = 1\, M_{\mathrm{Jup}}$, the gap in the ZIMPOL images remains quite narrow, tracing, almost exactly, the orbit of the planet orbit radii of 20 and $40\,\mathrm{AU}$. In the case of $R_{\mathrm{p}} = 60\,\mathrm{AU}$ the inner disk becomes too faint to distinguish the outer edge.

3.3.5   Q-band ($20\,\mu\mathrm{m}$) measurements

Mid-infrared emission (MIR) measurements generally trace warm $\sim 10\,\mu\mathrm{m}$ dust emission. The presence of a circumstellar disc therefore broadens the footprint of the emission at these wavelengths and can cause the full width half maximum (FWHM) of the intensity profile to be larger than that of a point source. When a disc features an inner gap, the inner edge of the outer disc, i.e. the "wall", is exposed to the radiation from the central star and its temperature increases, which increase the MIR emission from that radial position. The PSF of imaging instruments observing at these wavelengths is too large to resolve inner gaps (see Table 3.2), but, if a wall is present, the FWHM of the intensity profile can be used, together with other diagnostics such as SED modeling, to estimate the position of the wall (Maaskant et al. 2013).

Figure 3.6 shows the variation of the intensity profile of our simulated observations at $20\,\mu\mathrm{m}$, for all masses and positions of the planets explored in this study. The upper-row panels show variation with position for a fixed mass while lower panels show variation with
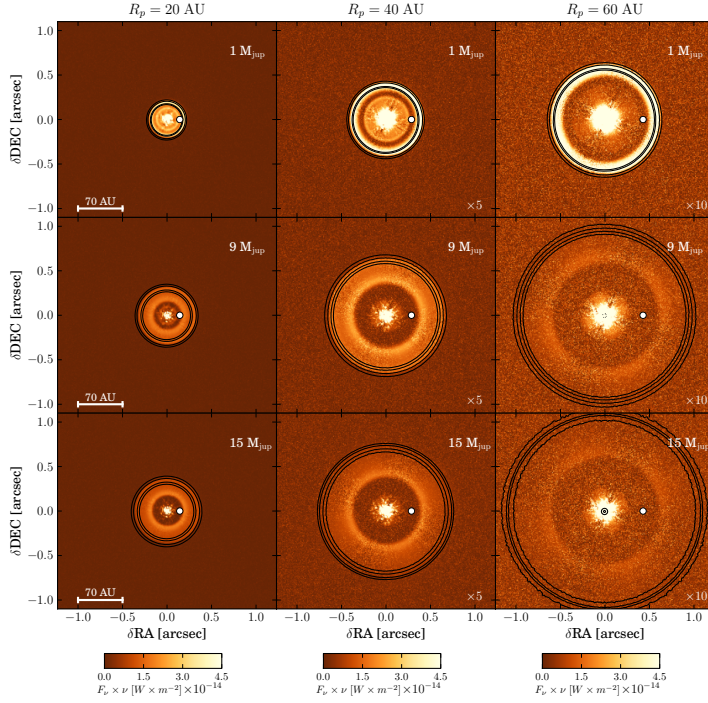
$R_p = 20$ AU $R_p = 40$ AU $R_p = 60$ AU

1 M$_{\rm jup}$ 1 M$_{\rm jup}$ 1 M$_{\rm jup}$

70 AU   ×5   ×10

9 M$_{\rm jup}$ 9 M$_{\rm jup}$ 9 M$_{\rm jup}$

70 AU   ×5   ×10

15 M$_{\rm jup}$ 15 M$_{\rm jup}$ 15 M$_{\rm jup}$

70 AU   ×5   ×10

δDEC [arcsec]

δRA [arcsec] δRA [arcsec] δRA [arcsec]

0.0   1.5   3.0   4.5   0.0   1.5   3.0   4.5   0.0   1.5   3.0   4.5
$F_\nu \times \nu \,[W \times m^{-2}] \times 10^{-14}$ $F_\nu \times \nu \,[W \times m^{-2}] \times 10^{-14}$ $F_\nu \times \nu \,[W \times m^{-2}] \times 10^{-14}$

Figure 3.5: Simulated ZIMPOL images of the different mass and orbit radius cases studied. Upper to bottom rows correspond to a $3\,\mathrm{Myr}$ disc model with a planet of masses $M_{\rm p} = [1, 9, 15]\,M_{\rm Jup}$, respectively. Columns show, from left to right, the different planet orbit cases, $R_{\rm p} = [20, 40, 60]$ AU, respectively. The white dot indicates the position of the planet in each image and the black contour lines correspond to the intensity ring detected by ALMA at $850\,\mu$m.

mass for a fixed position. In all panels, different colors correspond to different planet masses, different line styles to different planet positions and the profile of the calibrator star is shown as a striped black line for reference.

The generally accepted idea is that the more exposed and the closer to the star the wall is, the more emission we expect. In this sense, for a fixed mass of the planet, the larger the semi-major axis the lower values we can expect for the FWHM. On the other hand for a fixed planet separation, a heavier planet depleting more mass inside the gap leaves the wall more exposed to the radiation and should therefore correspond to a larger values of the FWHM. However, one should be careful when making these correlations, because the warm dust in the inner disc (if present) also has a contribution that is, in fact, dominant in some cases, as our results show.

Indeed, in Fig. 3.6 we see that when the position of the wall is relatively close to the star,
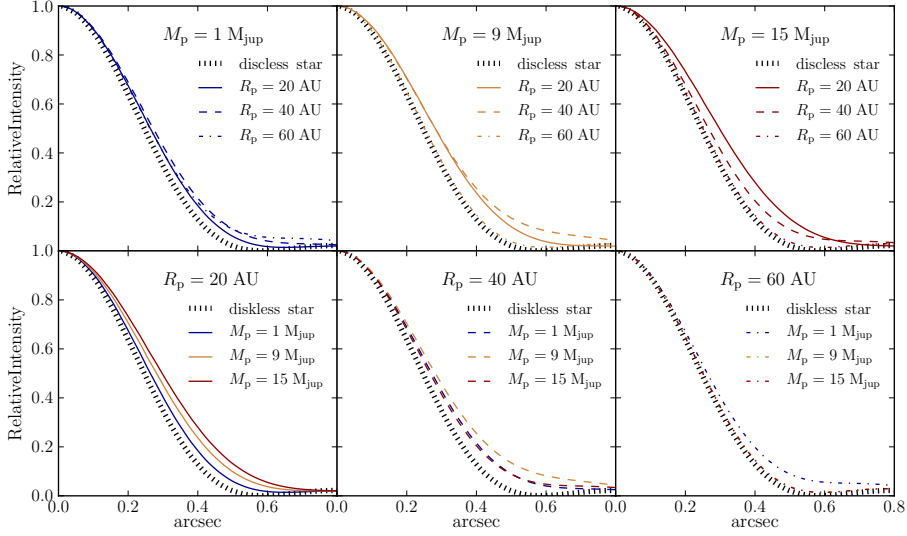
Figure 3.6: Synthetic $20\,\mu\mathrm{m}$ (Q-band) measurements for the different masses and planet positions considered. *Upper row:* variation of the PSF profile with planet position for fixed planet mass. *Lower row:* variation of the PSF profile with planet mass for a fixed planet position. In all panels, the different colors indicate different planet masses (blue, yellow and red for $M_{\mathrm{p}} = [1, 9, 15]\,M_{\mathrm{Jup}}$, respectively) while different line styles correspond to different planet positions (solid, dashed and dash-dotted for $R_{\mathrm{p}} = [20, 40, 60]$ AU, respectively). The black striped line shows the PSF corresponding to a diskless (calibrator) star for reference.

which holds for all planet mass cases with semi-major axis at 20 AU (lower left panel), the *"exposure"* effect dominates. More massive planets, which deplete more mass from the inner ($R \leq R_{\mathrm{p}}$) radii, yield broader intensity profiles. However, as the radial position of the planet increases the effect of the emission from the inner disc becomes increasingly important. At $R_{\mathrm{p}} = 40$ AU (lower middle panel), a $9\,M_{\mathrm{Jup}}$ planet will broaden the intensity profile more than a $15\,M_{\mathrm{Jup}}$. Since the wall is situated at roughly the same distance from the star (see images of Fig. 3.5), this can only be attributed to the emission of a more massive (i.e. less depleted) inner disc. We can see the effect as well in the upper panels of Fig. 3.6.

At $R_{\mathrm{p}} = 60$ AU (lower right panel) no measurable increase of the FWHM of the intensity profile is found for any planet mass. For all planet masses at this distance the inner disc is too depleted and the wall is too far away from the star (i.e. too cold) to contribute to the $20\,\mu\mathrm{m}$ emission.

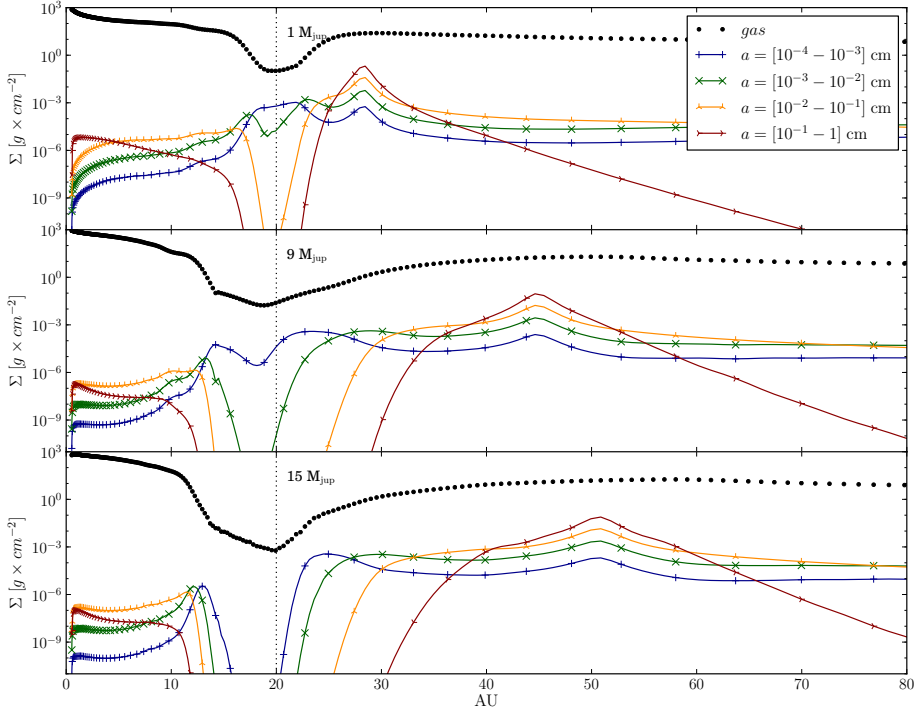Figure 3.9 of Appendix 3.6 shows, for completeness, the SEDs we obtained for all models presented in this study.

Figure 3.7: Surface density profiles for gas and different dust particle size ranges for the three planet mass cases, i.e. $M_p = [1, 9, 15]\, M_{\mathrm{Jup}}$. The vertical dotted line indicates the position of the planet at 20 AU.

3.4   Discussion

As explained in Pinilla et al. (2012a), the presence of a massive planet affects the gas in the disc generating pressure gradients in the pressure distribution, which would otherwise decrease monotonously with increasing separation. If the disc is not perturbed by a planet, the negative gradient of the radial gas pressure makes the gas rotate with sub-Keplerian velocities while the dust moves with near-Keplerian velocities. This difference generates a drag force that causes the dust to lose momentum and spiral inwards (Weidenschilling 1977, Brauer et al. 2008). However, if a perturbation is present in the gas, whenever the pressure gradient is positive the gas velocity grows until it becomes Keplerian in a pressure maximum, which counteracts this inward radial drift causing the dust particles to accumulate in that position (Klahr & Henning 1997, Fromang & Nelson 2005, Brauer et al. 2008, Johansen et al. 2009,

Pinilla et al. 2012b). What is interesting for our study is that the size of the particles that feel the trapping/filtering strongly depends on the strength of the pressure gradient (Pinilla et al. 2012a) which depends mainly on the characteristics of the planet (i.e. its mass) and the turbulence parameter α. In general, the bigger a particle, the less susceptible it is to drag force, and the more easily it is trapped in the pressure maximum. Small particles, on the other hand, are able to filter through the pressure maximum and populate the inner regions (Rice et al. 2006).

As a consequence of these physical processes, the dust in the disc under the presence of a planet behaves, in general, as follows. Driven by the depletion of gas in radii close to the planet's orbit, the dust distribution undergoes a depletion that affects different dust grain sizes in a different way. Big ($\sim$1 mm) dust grains are depleted more easily and "pushed" to radii where the pressure is maximum, further away form the planet. Small ($\sim$1 μm) grains are able to remain at radii close to the planet, "escape" the trap generated by the pressure bump, and flow into inner regions due to the radial drift. As the planet becomes more massive, the depletion becomes stronger for all grain sizes, although the radial separation of different grain sizes remains. Figure 3.7 shows the surface density profiles of gas and different particle size bins in the studied planet mass cases and planet orbit radius of $R_{\rm p} = 20$ AU. The solid blue line represents the surface density of very small particles ($a = [10^{-4}$–$10^{-3}]$ cm), while green, yellow and red represent particles of increasing size up to a maximum of $a = 1$ cm. Although the simulations consider particles sizes up to 2 m, the contribution of particles larger than 1 cm to the emitted and scattered light is negligible, so we did not include them in this plot for the sake of simplicity. According to the results presented in this study, the morphology of the dust distribution does not change with the planet's orbital radius but rather scales with it.

3.4.1 Visible and near-infrared polarimetric images vs. sub-mm observations

Since observations at different wavelengths trace (in general) different particle sizes, this spatial differentiation of the size distribution of dust in the disc opens the possibility to constrain planet parameters such as the mass and separation through multi-wavelength images of the emitted and/or scattered light from the disc. The images and radial profiles shown in Section 7.4 illustrate how the different observations trace different parts of this distribution. In general, ZIMPOL and HiCIAO polarised intensity images trace particles of about $1 \rightarrow 10\,\mu$m (blue solid line in Fig. 3.7), because these particles are very efficient scatterers at these wavelengths while bigger grains are not. ALMA Band 7 ($\lambda \sim 850\,\mu$m) is very sensitive to emission from grains of about 1 mm and it therefore highlights the ring of big particles trapped in the pressure maximum, while the inner regions, heavily depleted of these grains, appear empty.

ZIMPOL and HiCIAO images are different mainly because of resolution. Observing at shorter wavelengths, ZIMPOL is able to resolve the scattering due to the small grains in the inner region of the disc (down to the separation of the planet) while HiCIAO is only able to

detect the outer part. It is important to note that, in our simulations, HiCIAO images do not include the remnants of the star in the center of the image, visible in ZIMPOL images. This is due to the fact that HiCIAO observations are simulated convolving polarimetric full resolution images that come out of MCMax with the measured PSF of the instrument at H-band. Here we assume that the star is totally unpolarised and that polarimetry is perfectly done which suppresses the starlight completely. ZIMPOL images are simulated more realistically using the ZIMPOL simulator which includes the speckle pattern that would remain in the observation due to imperfect polarimetry.

The presence of an inner disc in ZIMPOL images could directly differentiate between a companion with mass below and above the deuterium-burning limit since in the latter the depletion of small grains is so strong in these regions that the scattered flux is not detected. Moreover, a close look at the images of Figure 3.5 suggests a relation between the radial positions of the wall detected in ZIMPOL polarimetric images and the ALMA sub-mm emission peak at $850\,\mu$m (black contours) that varies with planet mass but remains approximately constant with planet separation. In order to investigate this further, we computed the ratio of these features for each case of planet mass and separation studied.

Figure 3.8 shows the ratios versus planet mass for planet orbit radii of $R_{\mathrm{p}} = [20, 40, 60]$ AU. Using the radial profiles of the images, we define the position of the wall as the radial position of half the flux difference between the minimum flux at the bottom of the gap and the maximum flux at the wall (e.g. 23 and 27 AU for minimum and maximum flux positions in the case of $1\,M_{\mathrm{Jup}}$ at 20 AU, see the dashed blue line of upper right panel in Fig. 3.3). The upper and lower errors of the position are obtained by propagating the error on the determination of the mid-flux point and the peak of the emission in ZIMPOL and ALMA profiles respectively. Whenever those errors are lower than the corresponding resolution element (4 and 2 AU, for ZIMPOL and ALMA respectively), the resolution element was used instead. The position of the points of same planet mass in the figure are slightly offset to facilitate their distinction.

The ratios for each planet's orbit radius are best fitted with a power law,

$$f(M_{\mathrm{p}}) = c \cdot \left(\frac{M_{\mathrm{p}}}{M_{\mathrm{Jup}}} \right)^{\gamma} , \qquad (3.1)$$

with $c \sim 0.85$ and $\gamma \sim [-0.22, -0.18, -0.16]$ for $R_{\mathrm{p}} = [20, 40, 60]$ AU orbit radii, respectively.

Within the framework of our models, this figure serves as a mass estimator for the planet.

3.4.2 Mid-infrared vs. near-infrared polarimetric observations

Interestingly, recent observational work presented differences also between mid-infrared and polarimetric observations. In a recent paper, Maaskant et al. (2013) presented the case of HD 97048 (a Herbig Be/Ae star with a group I flared disc) where $24.5\,\mu$m T-ReCS (Gemini South) measurements agreed with a model of the disc that features a gap of ~ 30 AU (i.e. a wall positioned at 30 AU). The reason why this is interesting is that this was the first study
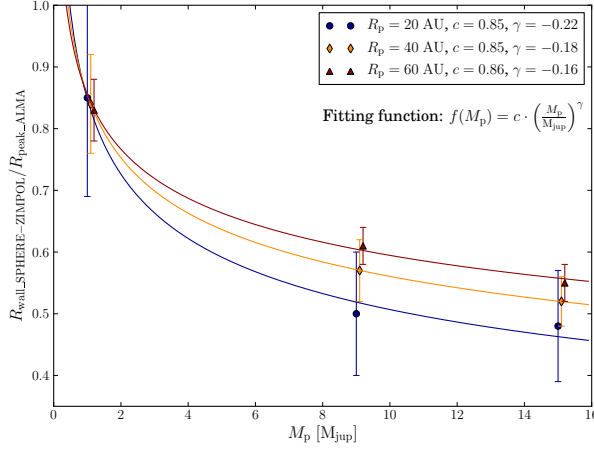
Figure 3.8: SPHERE ZIMPOL R-band outer gap edge to ALMA Band 7 peak ratio versus planet mass for the three planet orbit radii studied $R_{\mathrm{p}} = [20, 40, 60]$ AU.

that suggested the presence of a gap in this disc, despite the fact that this target has been observed in multiple occasions at different wavelengths (van Boekel et al. 2004, Lagage et al. 2006, Acke & van den Ancker 2006, Doucet et al. 2007, Doering et al. 2007, Martin-Zaïdi et al. 2007, van der Plas et al. 2009, Müller et al. 2011, Quanz et al. 2012). The closest-in observation, probing radial distances from $\sim$16–160 AU, was made by Quanz et al. (2012), who took VLT/NACO H- and K_{s}-band polarimetric images in which no gap was detected.

According to the results presented in this paper, these apparently discrepant observations would be consistent with the case of a disc hosting a planet of 1 or 9 M_{Jup} at 20 AU. Indeed the H-band Subaru/HiCIAO polarimetric images (similar to what would be observed with VLT/NACO) do not show a gap for these cases (second column upper panel in Fig. 3.2), other than the inner < 10 AU gap, which can be attributed to the fact that we assume a perfectly suppressed central source (see Sec. 3.4.3 below). The 9 M_{Jup} case, however, shows a depletion in the inner < 20 AU that would have been most likely detected by the Quanz et al. (2012) observations. If, based on this, we discard the larger planet mass case, the upper left panel of Figure 3.6 shows how the PSF measured at 20 μm would indeed appear broadened for the 1 M_{Jup} case. Here the cases of 1 M_{Jup} at 20 AU, 1 M_{Jup} at 40 AU and 15 M_{Jup} at 40 AU (lower central panel) would all be consistent with the same broadening but, again, the fact that the polarimetric H-band images do not show a gap or a depletion of dust in these regions discards the two latter options.

We note that the simulations presented here cannot be directly compared with either NACO or T-ReCS observations presented on those studies, nor used as predictions for future observations of this target, since the parameters of our star-disc system may differ considerably from those of HD 97048. Therefore we do not claim that a 1 M_{Jup} planet at 20 AU is

indeed responsible for the observational diagnostics presented in those papers. We simply use this observational case as a proof of concept of our diagnostic method where polarimetric imaging at short wavelengths can be used to disentangle otherwise degenerate cases that would agree with measurements at larger wavelengths.

3.4.3   Instrumental considerations

Regarding instrumental performance, and keeping in mind that the simulated images presented in this study for ZIMPOL and ALMA consider capabilities not available yet, it is clear that, whenever available, the upcoming ZIMPOL polarimeter will provide unprecedented spatial resolution for polarimetric images. This is a big advantage since currently available polarimeters such as Subaru/HiCIAO or VLT/NACO do not have the power to probe the innermost regions of the disc as well as to accurately resolve the outer edge of the gap. According to the results of this study, these features are of extreme importance to properly constrain the mass and position of the planet. Although we are aware that our simulations have limitations (e.g. accretion of dust from the inner disc onto the star is not taken into account and we only consider the presence of one planet) and cannot represent all possible disc-planet systems, they serve as a proof of concept for the power of using combined interferometric and polarimetric images to characterise these objects.

The results are in clear agreement with the differences observed between the SEEDS images obtained with HiCIAO and the interferometric results on the same targets. The gap shown by the ALMA images at $850\,\mu m$ is larger than the gap in HiCIAO polarised intensity images at $1.6\,\mu m$ by a factor of >2 in radial extent, for all planet mass cases. If the disc is one of the $1\,M_{\mathrm{Jup}}$ type simulated here (or a less massive single planet), the gap in polarised intensity could be too small to even be detected. Moreover, if the polarimetric images are taken using a coronagraph, as it is the case for most of the SEEDS observations, this can hide the gap. From the disc-planet systems considered in our simulations, observations with HiCIAO in H-band using the coronagraph ($d_{\mathrm{eff.coro.}} \sim 0.18''$, Dong et al. 2012) would have missed all gaps generated by planets lighter than (and including) $9\,M_{\mathrm{Jup}}$. Although the basic effect has been shown in parametric models before, this is the first time that self-consistent physical models have been used to explain these observational discrepancies.

3.5   Summary and conclusions

We present simulated imaging observations of a protoplanetary disc with a planet of masses $M_{\mathrm{p}} = [1, 9, 15]\,M_{\mathrm{Jup}}$ embedded in the disc and orbiting at $R_{\mathrm{p}} = [20, 40, 60]\,\mathrm{AU}$. We simulate intensity and polarised intensity images in the visible, near-infrared, mid-infrared and sub-mm wavelengths with current and near-future ground based imaging instruments with the aim of 1) test whether the proposed models explain observed differences between multi-wavelength observations recently presented, 2) study what different images can tell us about the dust distribution in the disc and 3) finding the best imaging strategy to infer planet mass and position. To simulate the disc-planet systems we use the models presented

in Pinilla et al. (2012a) that combine 2-D hydrodynamical and state of the art dust evolution simulations to self-consistently compute the evolution of the dust and the gas in the system including radial drift, fragmentation and coagulation processes (Masset 2000, Birnstiel et al. 2010).

To simulate the observations, we first obtain the theoretical emission and scattered light images running the Monte-Carlo radiative transfer code MCMax on the gas and dust radial surface density distribution obtained from the Pinilla et al. (2012a) models after $3\,\mathrm{Myr}$ of evolution, for the six planet masses and positions studied. We then process the theoretical images obtained in different ways to simulate observations with the upcoming SPHERE ZIMPOL polarimeter in the R-band ($0.65\,\mu\mathrm{m}$ intensity and polarised intensity images), HiCIAO in the H-band ($1.6\,\mu\mathrm{m}$ intensity and polarised intensity images), VLT-VISIR in the Q-band ($20\,\mu\mathrm{m}$) and ALMA ($850\,\mu\mathrm{m}$) with its future complete capabilities.

We find that:

1. The trapping and filtering mechanisms triggered by the presence of a $>1\,M_{\mathrm{Jup}}$ planet in the disc lead to different radial dust distributions for different grain sizes. This causes observations at different wavelengths to show different structures. Particles with large sizes ($\sim 1\,\mathrm{mm}$) are trapped in the pressure maximum outside the planet's orbit while smaller particles ($\sim 1\,\mu\mathrm{m}$) are allowed to drift to the inner radii. The former show up in sub-mm emission measurements as a ring at the radial position of the pressure maximum, while the latter are detected in polarised scattering flux at inner radii.

   The position of the pressure "trap", the amount of particles trapped and filtered, and the particle size threshold of the filtering process depend strongly on the mass of the planet. This effect allows to constrain planet mass and separation by combining multi-wavelength observations.

2. The Pinilla et al. (2012a) models are able to reproduce the "missing cavities" problem presented by the SEEDS survey (Dong et al. 2012; H-band images in this study), where no gaps were found in polarimetric H-band images for targets known to exhibit gaps at $850\,\mathrm{mm}$. Our simulated images with HiCIAO assume perfect polarimetry and a totally unpolarised star, which makes it just possible to detect a gap for all planet mass cases. In reality, speckle noise and, if used, the presence of a coronagraph would make the detection of the gap very unlikely.

3. Combination of sub-mm and polarimetric images in the visible wavelength range is the best imaging strategy to characterise the main features of the dust grain size distribution. An instrument like SPHERE ZIMPOL in the R-band ($\lambda = 0.65\,\mu\mathrm{m}$) could differentiate between the three planet mass cases studied in polarised intensity, particularly if the system is inclined. The high spatial resolution provided by the instrument allows to resolve the different structures in the inner region ($[10–20]\,\mathrm{AU}$), or lack thereof, that each mass generates, which is currently not possible using any other instruments.

4. Combination of near-infrared polarimetric images and mid-infrared measurements can also yield constraints on mass and planet position, although less accurately than the combination of diagnostics proposed as the best in this study (visible polarimetric and sub-mm images). This is due to the fact that the spatial resolution of polarimetric images at these wavelengths ($1.6\,\mu$m) is currently not enough to resolve the inner regions to the position of the planet. The warm dust in these regions also contributes to the FWHM measured at mid-infrared wavelengths. These causes some degeneracy in the models that would fit the measurements. Not having detailed spatial information in the polarimetric images for these regions (or even the gaps, which will be seen with SPHERE ZIMPOL) can make it difficult to disentangle the different planet mass and separation cases.

5. The results are also in agreement with the discrepancy between Q-band and near-infrared polarimetric observations of Maaskant et al. (2013) and Quanz et al. (2012) respectively, where a gap of $\sim$30 AU was found modeling the Q-band emission (at $24.5\,\mu$m) while NACO polarimetric images in H- and K_s-band did not show such a feature.

Acknowledgements
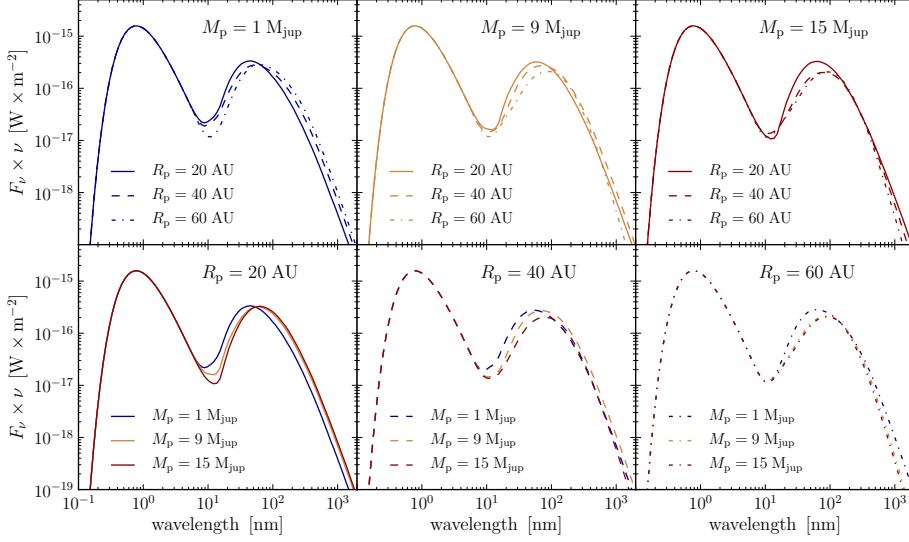
3.6   Appendix A: Spectral energy distributions

Figure 3.9: Synthetic Spectral Energy Distributions (SEDs) obtained for the different masses and planet positions studied. *Upper row:* variation of the SED with planet position for fixed planet mass. *Lower row:* variation of the SED with planet mass for a fixed planet position. In all panels, the different colors indicate different planet masses (blue, yellow and red for $M_{\mathrm{p}} = [1, 9, 15]\, M_{\mathrm{Jup}}$, respectively) while different line styles correspond to different planet positions (solid, dashed and dash-dotted for $R_{\mathrm{p}} = [20, 40, 60]$ AU, respectively)

Figure 3.9 shows the Spectral Energy Distributions (SEDs) of the models used in this study. The format is the same as that of Figure 3.6 where upper panels show SED variation with planet separation for a fixed planet mass, and lower panels show variation with planet mass for a fixed planet separation.

The depletion of the SED in the range $\lambda \approx [20$ - $100]\, \mu$m increases systematically with both planet mass and separation. For longer wavelengths, in the far infrared (FIR) to millimetre regime (i.e. $\lambda \approx [100$ - $1000]\, \mu$m), the flux increases with planet separation for the lowest planet mass case, whereas as the mass increases this relation seems to reverse. At the highest planet mass case, there is not significant variation with planet separation until $\lambda > 1\,$mm.

For fixed planet separations, the variation of the SED with mass in this region is only significant for the closest value, i.e $R_{\mathrm{p}} = 20\,$AU, although in the case of $R_{\mathrm{p}} = 60\,$AU the lightest planet shows an excess in flux with respect to the $M_{\mathrm{p}} = 9, 15\, M_{\mathrm{Jup}}$ cases at long wavelengths.

Chapter 4

Can habitable planets form in clustered environments?

M. de Juan Ovelar, J. M. D. Kruijssen, E. Bressert, L. Testi, N. Bastian and
H. Canovas.

> *Quality is not an act, it is a habit.*
> – Aristotle

Abstract

We present observational evidence of environmental effects on the formation and evolution of planetary systems. We combine catalogues of resolved protoplanetary discs (PPDs) and young stellar objects in the solar neighbourhood to analyse the PPD size distribution as a function of ambient stellar density. By running Kolmogorov-Smirnov tests between the PPD radii at different densities, we find empirical evidence, at the $> 97\%$ confidence level, for a change in the PPD radius distribution at ambient stellar densities $\Sigma \gtrsim 10^{3.5} \ \mathrm{pc}^{-2}$. This coincides with a simple theoretical estimate for the truncation of PPDs or planetary systems by dynamical encounters. If this agreement is causal, the ongoing disruption of PPDs and planetary systems limits the possible existence of planets in the habitable zone, with shorter lifetimes at higher host stellar masses and ambient densities. Therefore, habitable planets are not likely to be present in long-lived stellar clusters, and may have been ejected altogether to form a population of unbound, free-floating planets. We conclude that, while highly suggestive, our results should be verified through other methods. Our simple model shows that truncations should lead to a measurable depletion of the PPD mass function that can be detected with ALMA observations of the densest nearby and young clusters.

4.1 Introduction

For the past decade, exoplanetary systems are being discovered at a spectacular rate (e.g. Mayor et al. 2004, Borucki et al. 2011). Driven by these discoveries, there is an increasing interest in the global properties of planetary systems, from the epoch of their formation in protoplanetary discs (PPDs) to their long-term stability. While there is a natural focus on internal processes that govern the evolution of such systems (e.g. Lee & Peale 2003, Dullemond & Dominik 2005, Gorti et al. 2009b, Morbidelli et al. 2009, Brasser et al. 2009, Blum 2010, Williams & Cieza 2011), it is clear that not all planetary systems form in isolation and environmental effects should be considered as well. Particularly, theoretical studies show that external photoevaporation (Scally & Clarke 2001, Adams et al. 2004, 2006, Fatuzzo & Adams 2008) and dynamical interactions (Bonnell et al. 2001, Pfalzner et al. 2005, Olczak et al. 2006, 2010, Spurzem et al. 2009, Lestrade et al. 2011, Dukes & Krumholz 2012, Parker & Quanz 2012, Bate 2012) can lead to the truncation of PPDs and planetary systems.

While the external photoevaporation of PPDs has been studied observationally (O'dell et al. 1993, Robberto et al. 2008, Rigliaco et al. 2009, Mann & Williams 2010), there is no conclusive evidence of dynamical effects (Eisner & Carpenter 2006, Olczak et al. 2008, Reche et al. 2009). In part, this is likely due to the relatively short lifetimes of PPDs (up to ~ 8 Myr, e.g. Haisch et al. 2001, Hernández et al. 2008, Ercolano et al. 2011, Smith & Jeffries 2012) compared to the time it takes stellar encounters to have an observable effect on the disc population (~ 0.1–1 Gyr, e.g. Adams 2010). Previous observational studies on the Orion Nebula Cluster (ONC) (e.g. Eisner & Carpenter 2006, Olczak et al. 2008) did aim to find traces of dynamical interactions in the population of PPDs, but lacked a sufficient number of sources and/or suffered from uncertainties on the disc mass measurements.

We address the problem statistically by considering the sizes of PPDs as a function of their ambient stellar density, using samples of PPDs and young stellar objects (YSOs) from the latest infrared surveys. If stellar encounters truncate PPDs by tidally stripping the outskirts of the discs (e.g. Clarke & Pringle 1993, Heller 1995, Hall et al. 1996), this should be observable above some characteristic ambient stellar density ($\sim 10^3$ pc^{-3} Adams 2010), because the encounter rate increases with density (e.g. Binney & Tremaine 1987, Eq. 7-61). In this Letter, we find model-independent evidence of a change in the PPD size distribution for ambient stellar surface densities $\Sigma \gtrsim 10^{3.5}$ pc^{-2} at the $> 97\%$ confidence level.

4.2 Protoplanetary discs and their environment

4.2.1 Data selection

To verify whether a relationship exists between the sizes of PPDs and their ambient stellar surface density, Σ, we combine existing catalogues of PPDs and young stellar objects in star-forming regions (SFRs) of the solar neighbourhood.

The data for the PPDs is taken from circumstellardisks.org (Karl Stapelfeldt, NASA/JPL). This catalogue gathers resolved PPDs that have been confirmed and described in the litera-

ture. If a PPD is resolved in different wavelengths (probing different parts of the disc, see e.g. Lada et al. 2006), the catalogue lists the largest measured diameter, implying that the disc radii used in this work are lower limits. About 75% of the PPD radii in our final sample (see below) are measured at wavelengths around $1\ \mu$m, with only $\sim 25\%$ of the PPDs (all in low-density regions) being observed at mm wavelengths (see Appendix 4.5). The catalogue contains an estimate for how well-resolved each disc is by listing the number of diffraction-limited beams that fit within its diameter. We only consider the discs for which this value is greater than unity. This provides us with 133 PPD sources from which we exclude those whose host star is classified as a main sequence star, weak-line T-Tauri star, or Class 0 YSO. Sources at distances > 500 pc (which covers all our YSOs) are also excluded. These criteria reduce the sample to a total of 101 sources.

To estimate the local ambient surface density of each PPD source, we use publicly available near-infrared data of nearby SFRs (see Table 4.2 in Appendix 4.5). The ambient surface density of stars around each PPD is estimated as in Casertano & Hut (1985) – see Appendix 4.5 for a detailed explanation. The thus-obtained angular ambient surface densities are converted to physical ambient stellar surface densities, Σ, using the distances listed in Table 4.2. In cases where the listed PPD distance differs from the distance to the region that it is a member of, we adjust the PPD distance and size. Since a low surface density can be due to incomplete YSO coverage, any discs with $\Sigma < 0.1$ pc^{-2} are omitted from our analysis. Moreover, the minimum PPD radius that can be resolved increases with distance and hence introduces a distance-dependent selection bias. To avoid this, we exclude any PPDs smaller than the smallest radius (~ 50 AU) that is resolved in the most distant region of our sample, which is the Orion Nebula Cluster (ONC). The final sample thus contains 67 sources (see Table 4.1 in Appendix 4.5). Completeness does not affect the densities because the surveys of Table 4.2 are complete down to the hydrogen-burning limit.

4.2.2 A simple theoretical estimate for the truncation of discs

To interpret the data, we include a rough theoretical estimate for the expected truncation radii of PPDs as a function of Σ. This is obtained by combining the truncation induced by each particular encounter with the stellar encounter rate. The derivation is presented in detail in Appendix 4.6.

We use the numerical simulations of disc perturbations in clustered environments by Olczak et al. (2006) to obtain the disc radius as a function of the encounter parameters. We convert their expressions for the disc mass loss to a radial truncation assuming that it occurs by stripping the outer disc layers to the Lagrangian point between both stars, and adopting a PPD surface density profile $\Sigma_{\rm d} \propto r^{-1}$ (Olczak et al. 2006). Under these assumptions, we write for the upper limit to the disc radius

$$r_{\rm d}(r_{\rm p}, m_1, m_2) = \frac{r_{\rm p}}{\sqrt{m_2/m_1} + 1}, \tag{4.1}$$

where $r_{\rm p}$ is the pericentre radius at which the perturber passes, m_1 the mass of the perturbed system, and m_2 the mass of the perturber. This approximation is validated in Appendix 4.6.

The encounter radius r_{p} is obtained from the impact parameter b, encounter velocity v, and masses m_1 and m_2 by accounting for gravitational focussing (see Appendix 4.6). The masses are assumed to follow a Salpeter (1955) type initial mass function in the range 0.1–100 $M_\odot$, and the velocity distribution is taken to be Maxwellian with a velocity dispersion of $\sigma = 2$ km s^{-1}, as is typical for SFRs (Hillenbrand & Hartmann 1998, Covey et al. 2006). This enables the derivation of the encounter rate as a function of b and v (Binney & Tremaine 1987), which for a given age provides the total number of encounters n. Because encounters with pericentres at inclination angles $\theta \gtrsim 45°$ with respect to the disc plane affect the disc only mildly, about 30% of the n encounters lead to the disc truncation described by Eq. 4.1 (Pfalzner et al. 2005). We use the probability distribution functions (PDFs) for b, v, and m_2 to calculate the PDF of the 'most disruptive' encounter, i.e. the parameter set that gives the smallest disc size, according to Maschberger & Clarke (2008, Eq. A5). We then integrate the product of the disc radius r_{d}, the PDF of the 'most disruptive encounter', and the mass PDF of the perturbed object m_1 to obtain the expected disc truncation radius r_{tr}. To compare the theoretical estimate to the observations, we relate the stellar volume density ν to the surface density Σ as $\nu = \Sigma/2R$, where $R \approx 2$ pc is a typical radius for the SFRs in our sample (Hillenbrand & Hartmann 1998, Evans et al. 2009).

4.3 Results

4.3.1 Evidence for environmental effects

The upper panel of Fig. 4.1 shows the observed PPD radii versus Σ. The distribution is relatively insensitive to the ambient density until $\Sigma \sim 10^{3.5}$ pc^{-2}, where it appears truncated at large radii. This is consistent with the simple theoretical approximation from Sect. 4.2.2, which predicts a truncation at these densities for ages between 0.3 and 1 Myr (see Fig. 4.1). The affected PPDs are all in the ONC. If the truncation is interpreted as being due to dynamical interactions, the theoretical curves suggest that youngest sources in the ONC have ages of ~ 0.6 Myr, which is reasonably consistent with observations (Palla & Stahler 1999, Da Rio et al. 2010, Jeffries et al. 2011). However, this is not a unique explanation, since the truncation might also be due to external photoevaporation by nearby massive stars (e.g. Clarke 2007). It is also important to keep in mind that some fraction of the PPDs at this projected surface density will actually reside in a region of lower volume density, either behind or in front of the high-density core of the ONC. The distribution also shows some evidence of a density-independent upper limit to the PPD radius of $\sim 10^3$ AU, which could be related to binarity (Artymowicz & Lubow 1994, Kraus et al. 2012) or be intrinsic (Basu 1998).

To test the statistical significance of the change in the radius distribution, we perform a Kolmogrov-Smirnov (KS) test, which is theory-independent and thus insensitive to model assumptions. It gives the probability p_{KS} that two samples were drawn from the same parent distribution. Starting at the high-density end, we first divide the sample in density bins of $\{6, 7, 8\}$ objects per bin, which represents a balance between good statistics and enough bins to resolve the regime where the radius distribution changes. The KS test is then carried out
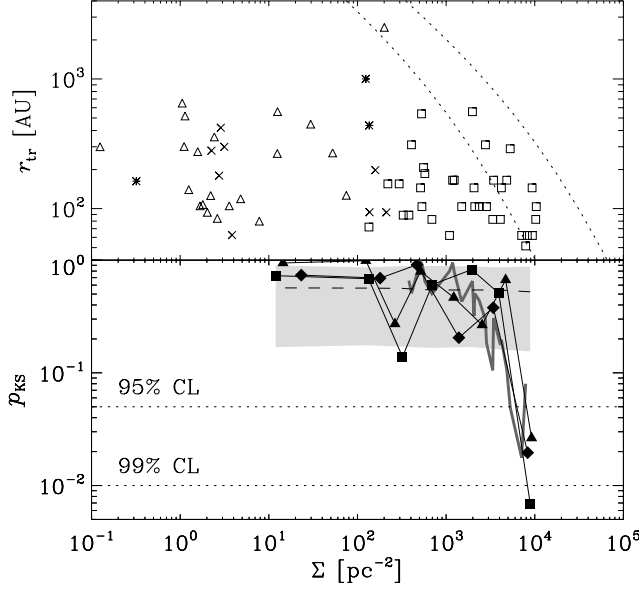
Figure 4.1: *Top panel*: Protoplanetary disc (PPD) radius distribution versus ambient stellar density. Squares, triangles, stars, and crosses correspond to ONC sources, T-Tauri stars, Herbig stars, and YSOs, respectively. Dotted lines represent the theoretical truncation for ages of 0.3 (top) and 1 Myr (bottom). *Bottom panel*: KS test p_{KS}-values for the PPD radii at that density to be consistent with the sample at lower densities, using $\{6, 7, 8\}$ (triangles, squares, diamonds) objects per density bin (see text). The grey thick line shows the p_{KS}-value for ONC PPDs only when dividing the subsample in two at the indicated density. The horizontal dashed line and grey area indicate the median p_{KS} and its 1σ dispersion retrieved from 30,000 Monte Carlo experiments to verify the significance of the results (see text). Dotted lines mark 95% (top) and 99% (bottom) confidence levels.

comparing radii in a bin at density Σ_{bin} with those at lower densities (i.e. 10^{-1} pc$^{-2} < \Sigma < \Sigma_{bin}$). We do not include bins at $\Sigma_{bin} < 10^1$ pc^{-2} to avoid low-number statistics in the reference sample. The bottom panel of Fig. 4.1 shows the results of the test. At intermediate densities, all KS tests give high p_{KS}-values, but for densities higher than $\Sigma \gtrsim 10^{3.5}$ pc^{-2} there is a pronounced drop. As such, the KS test yields a detection of a change in the PPD radius distribution at the $> 97\%$ confidence level. Note that this does not change when excluding the largest PPD in the sample (at $\Sigma \sim 200$ pc^{-2}). The result also holds within the ONC only (grey line in Fig. 4.1), when dividing the ONC subsample in two at each density and running a KS test for the radii at both sides of the separation. To check the result, we performed 30,000 Monte Carlo experiments in which the KS test was applied in the same way to distributions of randomly paired radii and surface densities, i.e. erasing any possible
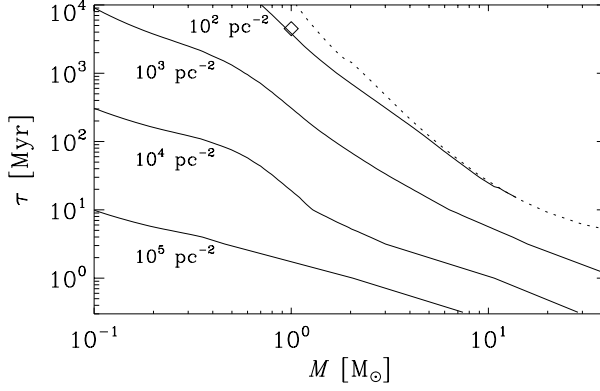
Figure 4.2: Habitable zone lifetime as a function of stellar mass for different ambient stellar densities. The dotted line indicates the total lifetime of the host star, and the diamond indicates Earth.

correlation. Figure 4.1 indicates the resulting median p_{KS} and its 1σ dispersion, showing that the results obtained for the original sample are unlikely to be due to the adopted statistical method.

4.3.2   Implications for habitable zone occupancy lifetimes

If the drop of the p_{KS}-value at high densities is indeed caused by dynamical truncation, then the model can be used to give the maximum time during which the habitable zone (HZ) can host a planet or a PPD ('HZ lifetime'). We calculate r_{tr} as a function of Σ and τ as in Fig. 4.1, but without averaging over the host stellar mass to retain the mass dependence. We then compare it to the inner radius of the HZ, $r_{\text{HZ}}^{\text{in}}$, and determine until which age they overlap, as a function of mass and ambient density. The radius $r_{\text{HZ}}^{\text{in}}$ depends on the required radiative equilibrium temperature T_{eq}, on the stellar luminosity L and on the properties of the planet (i.e. f, a proxy for atmospheric thermal circulation, and the Bond albedo A, see Kasting et al. 1993, Tarter et al. 2007):

$$r_{\text{HZ}}^{\text{in}} = \frac{1}{2}\sqrt{\frac{Lf(1-A)}{4\pi\sigma_{\text{T}}T_{\text{eq}}^4}}, \tag{4.2}$$

where σ_{T} is the Stefan-Boltzman constant. Following Borucki et al. (2011), we calculate $r_{\text{HZ}}^{\text{in}}$ for an Earth-like planet using $f = 1$, $A = 0.3$, and $T_{\text{eq}} = 307$ K, which is the maximum temperature that allows for the presence of liquid water when accounting for the greenhouse effect. The luminosity is taken from stellar evolution models at solar metallicity (Marigo et al. 2008). The results are shown in Figure 4.2 for ambient densities of $\Sigma = \{10^2, 10^3, 10^4, 10^5\}$ pc^{-2}. The HZ lifetime decreases with density and stellar mass,

due to the enhanced encounter rate and the large $r_{\mathrm{HZ}}^{\mathrm{in}}$, respectively. These estimates for the HZ lifetime hold both for PPDs and planetary systems, since dynamical interactions would have comparable effects in both cases (e.g. Olczak et al. 2006, Parker & Quanz 2012).

Figure 4.2 shows that, based on the Earth's existence alone, the solar system cannot have formed in a dense ($\Sigma > 10^3 \mathrm{~pc}^{-2}$) environment, unless the ambient density decreased on a short ($\tau \lesssim 100$ Myr) timescale. Conversely, meteoritic evidence indicates that the young solar system must have endured nearby supernovae (e.g. Cameron & Truran 1977), which provides a lower limit to the product $\Sigma\tau \gtrsim 10^{3.8} \mathrm{~Myr~pc}^{-2}$ (see the review by Adams 2010). A plausible scenario is thus that the solar system formed in a massive ($\sim 10^4 \mathrm{~M}_\odot$, $\Sigma \sim 10^3 \mathrm{~pc}^{-2}$), but unbound association, which dispersed on a short ($\tau \sim 10$ Myr) timescale (see e.g. Dukes & Krumholz 2012, although they refer to such a system as a 'cluster'). Our results seem to disagree with Eisner & Carpenter (2006) who derive the disc fraction in the ONC and find no evidence of disc truncations. However, their conclusion may result from low-number statistics, and PPD mass estimates are more uncertain than radius measurements. On the other hand, our results agree with the studies of Bonnell et al. (2001) and Spurzem et al. (2009), and would explain why no planets have been found in the globular clusters 47 Tuc and NGC 6397 (Gilliland et al. 2000, Nascimbeni et al. 2012), where $\tau\Sigma \sim 10^8 \mathrm{~Myr~pc}^{-2}$ within the half-mass radius. This implies such a high number of encounters that it is improbable that *any* bound planets survived, most of them likely to have escaped the cluster due to two-body relaxation (e.g. Kruijssen 2009).

We note that our theoretical estimates are conservative and provide upper limits to the disc sizes, because (1) we do not account for potentially higher ambient densities in the past (e.g. Bastian et al. 2008), (2) we neglect the presence of massive stars at earlier ages of the SFRs, (3) we only consider the most disruptive encounters and ignore the cumulative effect of weak perturbations. Figure 4.2 thus provides strict upper limits to the HZ lifetimes.

4.4 Further observational avenues

We present evidence for a change in the PPD radius distribution at ambient stellar densities of $\Sigma > 10^{3.5} \mathrm{~pc}^{-2}$ at the $> 97\%$ confidence level, in line with the expected range due to close encounters with other stars on a ~ 1 Myr timescale. These densities are only reached in the densest parts of the ONC, which is not only consistent with the detection of reduced PPD masses in the centre of the region (Mann & Williams 2010), but also with studies concluding that encounters are not important in the ONC as a whole (e.g. Scally & Clarke 2001). Our results demonstrate that the stellar environment can be an important factor in setting the habitability of planetary systems. For instance, the existence of unbound, free-floating planets (see e.g. Bihain et al. 2009, Sumi et al. 2011, Strigari et al. 2012) is a natural outcome of our results. However, a ubiquity of Earth-like planets in the HZ of stars remains likely because a large fraction ($\sim 90\%$) of stars forms in unbound associations (see Kruijssen 2012 for a recent review, and observational references therein), of which the density quickly decreases after their formation.

To verify our results, more observations of PPDs in clustered environments are desirable.
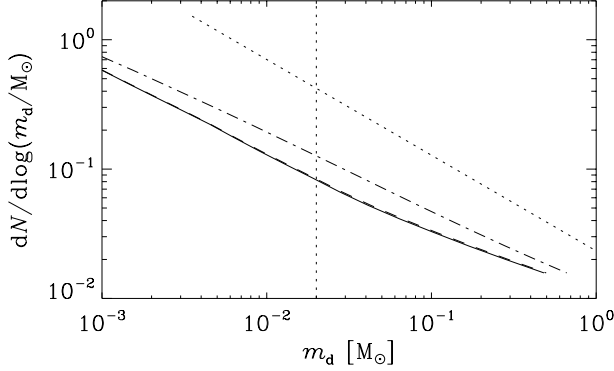
Figure 4.3: Evolution of the disc mass function (DMF) due to dynamical encounters at an age of 3 Myr for densities $\{2.25 \times 10^4, 2.5 \times 10^3, 5 \times 10^2\}$ pc^{-2} **(solid, dashed, dash-dotted)**, sampling NGC 3603 at **radius intervals of** $\{0" - 5", 16.5" - 43.5", 46.5" - 73.5"\}$**. The dotted curve** shows the initial DMF, and the vertical dotted line indicates the 4σ sensitivity limit of ALMA Cycle 1 (30 min at 1.3 mm) at the distance of NGC 3603.

A fruitful approach would be to probe PPD truncations using disc mass measurements, which would provide much larger samples of PPDs. Figure 4.3 shows the effect of (only) dynamical encounters on the disc mass function (DMF) using the disc mass loss description from Olczak et al. (2006) (see Appendix 4.7). This will be easily observable in dense and young stellar clusters with ALMA. While the full ALMA array will be able to directly measure disc sizes, we predict that, already from Early Science Cycle 1, the sensitivity will be sufficient to detect the variation of the DMF caused by the truncation (see Fig. 4.3), which would verify the result of Fig. 4.1.

Acknowledgments

Table 4.1: Distribution of PPD sources over the host star type. 'Unknown central star' indicates systems in which the central body has either not been detected or classified yet (mostly proplyd silhouettes in the ONC). Young stellar objects are classified as such if their enhanced envelope emission suggests a younger age than T-Tauri or Herbig Ae/Be. The 'KS' column shows the sample after applying density and radius cuts for the KS test of Fig. 4.1.

Type	Sources	KS
Herbig Ae or Be	15	3
T-Tauri	39	21
Unknown central star (ONC)	36	35
Young stellar object	11	8

Table 4.2: Star-forming regions used in this study, listing the names of the regions, their numbers of objects N_{obj}, and distances D. The fourth column shows the literature sources as (1) the Cores to Disks *Spitzer* survey (Evans et al. 2003), (2) the Taurus *Spitzer* survey (Rebull et al. 2010), (3) the Robberto et al. (2010) survey of the ONC.

Name	N_{obj}	D (pc)	Survey
Lupus I	20	150	1
Lupus III	79	150	1
Lupus IV	12	150	1
Ophiuchus	297	125	1
Orion Nebula Cluster	7759	414	3
Perseus	387	250	1
Serpens	262	415	1
Taurus	249	137	2

4.5 Appendix A: Properties of the sample

After the selection procedure detailed in Sect. 4.2.1, we list the final PPD sample in Table 4.1. To assess the heterogeneity of the sample, we show the wavelengths of the radius measurements as a function of ambient stellar density in Fig. 4.4. The vast majority of sources (75%) were measured in a narrow wavelength range below 3 μm (i.e near infrared wavelengths) with a spread of 0.25 dex and centred at 1.32 μm. The remaining sources were measured at millimetre wavelengths. For the ONC sample, 80% of all sources were measured at 0.66 μm with very little scatter overall. As shown in Fig. 4.4, the 16 sources of the total sample measured at millimetre wavelengths all have ambient surface stellar density < 200 pc^{-2}. Therefore the distribution at densities above this value can be considered to be homogeneous.
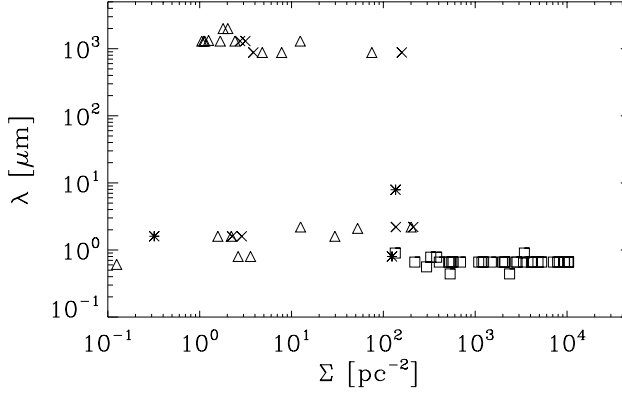
Figure 4.4: Wavelengths λ of the radius measurements for the final sample of protoplanetary discs versus ambient surface stellar density. Symbols have the same meaning as in the upper panel of Fig. 4.1.

The regions from which the YSOs are taken to estimate the ambient density are summarized in Table 4.2. Using these samples, the ambient surface density of stars around each PPD is estimated as (Casertano & Hut 1985):

$$\Sigma = \frac{N-1}{\pi d_N^2}, \tag{4.3}$$

where N is the rank of the Nth nearest neighbour, and d_N is the projected angular distance to that neighbour. We use $N = 20$, which is higher than the commonly-used value of $N = 7$ (cf. Bressert et al. 2010) and is chosen to improve the statistics of the density estimates. An additional effect of using a higher value of N is a slight decrease of the density estimates. This should be kept in mind when comparing our densities those in other work.

4.6 Appendix B: A simple model for PPD truncations

In this Appendix, we derive the upper limit to the radii of protoplanetary discs (PPDs) due to dynamical encounters. Where appropriate, we emphasize that the derivation is conservative, such that the obtained truncation radius is indeed an upper limit.

Olczak et al. (2006) performed numerical simulations of disc perturbations and provided an expression for the relative disc mass loss $\Delta M/M$ due to encounters with other stars (their Eq. 4). If we assume that the mass loss occurs by stripping the outer disc layers and adopt the disc surface density profile of $\Sigma_d \propto r^{-1}$ used in their work, then $\Delta r/r = \Delta M/M$. The expression for $\Delta r/r$ from Olczak et al. (2006) is consistent to within a factor of three with the scenario in which a disc is always truncated to the equipotential (Lagrangian) point between both stars. If the disc was already smaller than that radius, it is left relatively unperturbed.

For the rough estimate made here, it thus suffices to write for the upper limit to the disc radius

$$r_{\mathrm{d}}(r_{\mathrm{p}}, m_1, m_2) = \frac{r_{\mathrm{p}}}{\sqrt{m_2/m_1 + 1}}, \tag{4.4}$$

where r_{p} is the pericentre radius at which the perturber passes, m_1 is the mass of the perturbed system and m_2 is the mass of the perturber. The approximation of Eq. 4.4 follows Eq. 4 of Olczak et al. (2006) with reasonable accuracy for initial disc radii up to a few 10^3 AU (consistent with the parameter space in Fig. 4.1), encounter distances $r_{\mathrm{p}} > 0.002$ pc (i.e. $r_{\mathrm{p}}/r_{\mathrm{d}} > 0.2$) and mass ratios $m_2/m_1 > 1$. We have verified that these conditions are satisfied for the encounters that are expected to determine the disc truncation (see below). Following Binney & Tremaine (1987), the impact parameter b and the encounter radius due to gravitational focusing r_{p} are related as

$$b = r_{\mathrm{p}}\sqrt{1 + \frac{2G(m_1 + m_2)}{v^2 r_{\mathrm{p}}}}, \tag{4.5}$$

where v is the relative velocity of the encounter. This equation is inverted to derive r_{p} for each encounter.

The truncation radius r_{d} of Eq. 4.4 depends on the variable set $\{b, v, m_1, m_2\}$, for which we specify probability distribution functions (PDFs). For the masses, we use a Salpeter (1955) type initial mass function in the range 0.1 $M_\odot$–$m_{\max}$, where $m_{\max}$ depends on age due to stellar evolution. For ages $\tau < 4$ Myr we assume $m_{\max} = 100$ $M_\odot$, while at later ages it is set by the Marigo et al. (2008) stellar evolution models at solar metallicity. The mass function is:

$$\Phi_m \propto \frac{\mathrm{d}N}{\mathrm{d}m} \propto m^{-2.35}, \tag{4.6}$$

which is normalized such that $\int \Phi_m \mathrm{d}m = 1$. Assuming a Maxwellian velocity distribution, the total number of encounters per unit velocity $\mathrm{d}v$ and unit impact parameter $\mathrm{d}b$ follows from the encounter rate $\mathrm{d}^2N/\mathrm{d}b\mathrm{d}v$ as (Binney & Tremaine 1987)

$$\Phi_{\mathcal{N}} \propto \mathcal{N}(b, v) \equiv \tau \frac{\mathrm{d}^2 N}{\mathrm{d}b\mathrm{d}v} = \frac{8\pi^2 \nu \tau b}{(4\pi\sigma^2)^{3/2}} \exp\left(-\frac{v^2}{4\sigma^2}\right) v^3, \tag{4.7}$$

where ν is the local number density of stars, τ is the age of the region, and σ is the velocity dispersion. The relative velocity ranges from $v = 0$–∞ and the impact parameter from $b = 0$–b_{MAX} (see below). As in Eq. 4.6, we have normalized $\Phi_{\mathcal{N}}$ such that $\iint \Phi_{\mathcal{N}} \mathrm{d}b\mathrm{d}v = 1$, by writing $\Phi_{\mathcal{N}} = f_{\mathrm{dis}}\mathcal{N}(b, v)/n$ and defining $n \equiv \iint f_{\mathrm{dis}}\mathcal{N}(b, v)\mathrm{d}b\mathrm{d}v$ as the total number of encounters at age τ. The factor $f_{\mathrm{dis}} \approx 0.3$ represents the fraction of encounters that leads to disc mass loss according to Eq. 4.4. This accounts for the fact that encounters with pericentres at inclination angles $\theta > 45°$ with respect to the disc plane cause only weak mass loss and retrograde encounters leave the disc almost unperturbed (Pfalzner et al. 2005).

Given a sequence of encounters, the truncation of the PPD is set by the most disruptive encounter (Scally & Clarke 2001, although see Olczak et al. 2006), i.e. $r_{\rm p,min} = f(b_{\rm min}, v_{\rm min}, m_{\rm 2,max})$. If we assume that $\{b_{\rm min}, v_{\rm min}, m_{\rm 2,max}\}$ are uncorrelated, implying that the region is not mass-segregated, the PDF of the most disruptive encounter becomes

$$p(b_{\rm min}, v_{\rm min}, m_{\rm 2,max}) = p_b(b_{\rm min})p_v(v_{\rm min})p_m(m_{\rm 2,max}), \tag{4.8}$$

where $p_{\{b,v,m\}}$ represent the PDFs for the lowest b, lowest v and highest m_2, respectively. Following the method of Maschberger & Clarke (2008, Eq. A5), these three PDFs are defined as

$$
\begin{aligned}
p_b(b_{\rm min}) &= n\Phi_b(b_{\rm min})\left(\int_{b_{\rm min}}^{b_{\rm MAX}}\Phi_b(b')\mathrm{d}b'\right)^{n-1} \\
p_v(v_{\rm min}) &= n\Phi_v(v_{\rm min})\left(\int_{v_{\rm min}}^{\infty}\Phi_v(v')\mathrm{d}v'\right)^{n-1} \\
p_m(m_{\rm 2,max}) &= n\Phi_m(m_{\rm 2,max})\left(\int_{m_{\rm 2,MIN}}^{m_{\rm 2,max}}\Phi_m(m_2')\mathrm{d}m_2'\right)^{n-1}
\end{aligned}
\tag{4.9}
$$

where $\Phi_b(b)\Phi_v(v) \propto \Phi_{\mathcal{N}}(b,v)$ are the distribution functions for b and v, with $\Phi_b(b) \propto \nu\tau b$ and $\Phi_v(v) \propto \exp{(-v^2/4\sigma^2)}v^3/\sigma^3$, again normalized to unity in both cases. In Eqs. 4.9, $b_{\rm min}$, $v_{\rm min}$ and $m_{\rm 2,max}$ indicate variable limits, and $b_{\rm MAX}$ and $m_{\rm 2,MIN}$ indicate fixed limits. The fixed limit $b_{\rm MAX}$ represents the maximum impact parameter, which is given by the typical interstellar separation $b_{\rm MAX} = (48/\pi\nu)^{1/3}$ (the factor was chosen for consistency with Scally & Clarke 2001). It should be noted that while this is a physically motivated choice, it only weakly influences the result since the most likely most disruptive encounter will typically be at $b_{\rm min} \ll b_{\rm MAX}$. Assuming an age of $\tau = 1$ Myr, for surface densities of stars $\Sigma \leq 10^5$ pc^{-2} we find that p_b always peaks at impact parameters $b_{\rm min} > 0.002$ pc (i.e. $r_{\rm p}/r_{\rm d} \gtrsim 0.2$), whereas for $\Sigma \geq 10^0$ pc^{-2} the most likely most disruptive encounter always has $m_2 \geq 0.5$ M$_\odot$, which after averaging over the mass function to account for the distribution of m_1 gives $m_2/m_1 > 2$. This validates the use of the approximation in Eq. 4.4.

By combining the Eqs. 4.6 and 4.8, the total PDF is

$$\Phi_{\rm tot} = p_b(b_{\rm min})p_v(v_{\rm min})p_m(m_{\rm 2,max})\Phi_m(m_1). \tag{4.10}$$

It should be noted that we did not include the mass of the perturbed object m_1 in the PDF of the most likely most disruptive encounter (Eq. 4.8), but instead average over the mass PDF itself. The reason is that the stars in Fig. 4.1 span a range of masses, and a 'typical' relation between the truncation radius and ambient density is preferable.

Combining the previous equations gives a theoretical estimate for the typical truncation radius $r_{\rm tr}$ as a function of the ambient density, velocity dispersion and age:

$$r_{\rm tr} = \iiiint_V r_{\rm d}\Phi_{\rm tot}\mathrm{d}b_{\rm min}\mathrm{d}v_{\rm min}\mathrm{d}m_1\mathrm{d}m_{\rm 2,max}, \tag{4.11}$$

where V indicates the complete phase space, i.e. $0.1\,M_\odot$–m_{max} in mass, 0–∞ in velocity and 0–b_{MAX} in impact parameter. This expression provides the expected radius after the 'most likely most disruptive encounter', averaged over the stellar mass function to account for the unknown mass of the perturbed system.

4.7 Appendix C: Evolution of the disc mass function

To calculate the evolution of the disc mass function (DMF), we assume that the initial disc mass $m_{\mathrm{d,i}}$ is related to the host stellar mass m_1 as

$$m_{\mathrm{d,i}} = f_{\mathrm{d}} m_1, \tag{4.12}$$

where f_{d} is a constant. We adopt $f_{\mathrm{d}} = 0.03$, which is in good agreement with observations (Andrews & Williams 2005) and sufficiently accurate for the order-of-magnitude estimate made in Sect. 4.4. Using a Salpeter (1955) stellar initial mass function (cf. Eq. 4.6), the initial DMF is

$$\frac{\mathrm{d}N(m_{\mathrm{d,i}})}{\mathrm{d}m_{\mathrm{d,i}}} = \frac{1}{f_{\mathrm{d}}} \frac{\mathrm{d}N(m_1)}{\mathrm{d}m_1}, \tag{4.13}$$

For each host stellar mass, we calculate the characteristics of the most likely most disruptive encounter as in Appendix 4.6, using quantities that are appropriate for NGC 3603 (i.e. $\tau = 3$ Myr, $\sigma = 4.5$ km s^{-1}, and $R = 1.45$ pc). Given a certain encounter, the disc mass loss is calculated using the expression from Olczak et al. (2006, Eq. 4), which provides $\Delta \equiv \Delta m_{\mathrm{d}}/m_{\mathrm{d}}$ as a function of the host stellar mass m_1, the mass of the perturber m_2, the pericentre distance r_{p} and the disc radius r_{d}. To account for the dependence of Δ on the radius, it is calculated for all radii from the observed sample at ambient densities $10^{-1} < \Sigma/\mathrm{pc}^{-2} < 10^2$ (see Fig. 4.1), including those with $r_{\mathrm{d}} < 50$ AU since the corresponding regions are all nearby and hence the detection limit is less stringent. At these densities the encounter rate is so low that the observed disc radii can be interpreted as 'initial' radii. The obtained values of Δ are then averaged to remove the dependence on r_{d}, and integrated Φ_{tot} (see Eq. 4.10) in the same way as r_{tr} in Eq. 4.11. This provides the expected relative mass loss as a function of host stellar mass $\langle\Delta\rangle$,[1] and hence the final disc mass is approximately

$$m_{\mathrm{d}} = (1 - \langle\Delta\rangle)\, m_{\mathrm{d,i}}. \tag{4.14}$$

---

[1]Note that contrary to our Lagrangian approximation of Eq. 4.4, the disc mass loss of the Olczak et al. (2006) equation does not increase monotonically with decreasing pericentre distance – for very close encounters (typically $r_{\mathrm{p}}/r_{\mathrm{d}} < 0.2$) the disc mass loss is reduced. In such cases, the most disruptive encounter is not the closest encounter, and we account for this by adjusting r_{p} to the value where $\langle\Delta\rangle$ peaks.

The final DMF is then given by

$$
\begin{aligned}
\frac{\mathrm{d}N(m_\mathrm{d})}{\mathrm{d}m_\mathrm{d}} &= \left(\frac{\mathrm{d}m_\mathrm{d}}{\mathrm{d}m_\mathrm{d,i}}\right)^{-1} \frac{\mathrm{d}N(m_\mathrm{d,i})}{\mathrm{d}m_\mathrm{d,i}} \\
&= \frac{1}{(1 - \langle\Delta\rangle)} \frac{\mathrm{d}N(m_\mathrm{d,i})}{\mathrm{d}m_\mathrm{d,i}}.
\end{aligned}
\tag{4.15}
$$

Part II

Chapter **5**

M&m's:
An error budget and performance simulator code for polarimetric systems

M. de Juan Ovelar, F. Snik and C. U. Keller.

Abstract

Although different approaches to model a polarimeter's accuracy have been described before, a complete error budgeting tool for polarimetric systems has not been yet developed. Based on the framework introduced by Keller & Snik, in 2009, we have developed the M&m's code as a first attempt to obtain a generic tool to model the performance and accuracy of a given polarimeter, including all the potential error contributions and their dependencies on physical parameters. The main goal of the code is to provide insight on the combined influence of many polarization errors on the accuracy of any polarimetric instrument. In this work we present the mathematics and physics based on which the code is developed as well as its general structure and operational scheme. Discussion of the advantages of the M&m's approach to error budgeting and polarimetric performance simulation is carried out and a brief outlook of further development of the code is also given.

5.1   Introduction

Polarimetry is a very valuable remote-sensing technique that often yields information that is unobtainable through other techniques and is used in many different fields such as astronomy, Earth observation, biomedical diagnosis or land-mine and target detection, among others.

Nevertheless, the construction of such instruments has often relied on the knowledge obtained through experience than on a formal systems engineering approach, which is common practice when designing optical (imaging or spectroscopic) systems. Also, quite often, the polarimetry is implemented as an add on to an existing system which makes it sub-optimal by definition.It is only now, due to the increasing size and complexity of current instrumentation projects, that this is starting to be demanded. For this we need to be able to predict the behavior and accuracy of the polarimetric system in order to optimize the design process. Only with the implementation of polarimetric error budgeting can the polarimetric performance be fully traded off against optical performance and other merit functions (like cost).

In the systems engineering approach, the design process starts by setting the scientific requirements of the instrument which then must be translated into accuracy and sensitivity requirements. Polarimetric sensitivity is defined as the smallest signal that the instrument can detect above the noise and polarimetric accuracy is the uncertainty with which the instrument is able to measure a polarization signal after it has been detected with sufficient S/N (Snik & Keller 2013a). The former is limited by (photon) noise and spurious polarization effects that can be created by e.g. variable atmospheric properties or source variability. These effects are to a large extent decoupled from the polarimetric accuracy, and formalisms and codes exist to model them (Casini et al. 2012). The accuracy is limited by "real" polarization errors, which can be described by Mueller matrices. The goal of the design process then is to assure that the instrument will indeed meet the accuracy requirements when operating.

With this aim, one needs to simulate the performance of the different preliminary designs and make an estimation of the error budget throughout the system to detect which elements contribute, and in which way, to the final response of the instrument. This allows to deal with the limitations of the system in an early design stage. In optical systems dealing only with intensity it is common practice to make use of error budgeting and performance simulation tools that can carry out such an optimization process. Often this optical error budgeting involves adding wavefront errors (which are small, independent and scalar) in an RSS (root sum square) fashion, and force the total error to be smaller than a certain required value. The individual errors can then be distributed top-down, or added up bottom-up by adopting measured or modeled values, or a combination of both. So far, to our knowledge, a complete polarimetric error budgeting tool, working with a library of all possible error sources and their possible interactions has not yet been developed for polarimetric systems and this is mainly due to the complexity of the error propagation in these systems. Tyo (2002) and Boger et al. (2003) introduced polarimetric error budgeting with similar mathematical formalisms as presented in this paper, but their scopes focused on specific polarimetric elements.

Errors in polarimetry have to be expressed as vectors and their values are often larger than the measured signal itself, due to the fact that some elements, essential to perform polarime-

try, affect the polarization state of the incoming light in a major way. Often the degree of polarization of the signals to be measured is very low, and possibly much lower than the instrumental polarization. The main implication of this is that the common algorithms applied to optical systems for error propagation as RSS cannot be applied as such to polarimetric systems. In 2009 Keller & Snik analyzed this problem and developed a mathematical framework to transform the errors into additive ones to make them suitable for error budgeting and estimate the contribution of each physical parameter to the overall matrix.

Based on this framework we have developed the M&m's code that computes the error propagation through the polarimetric system of all the potential error contributions, e.g. misalignment and varying material properties, and their dependencies on (global) physical parameters, e.g. wavelength and temperature. The ultimate goal of the code is to provide insight of the contribution of error sources to the final polarimetric performance and estimate the polarimetric accuracy of a given design. The code only pertains to predicting the polarimetric accuracy of a certain instrument as it relates the incoming Stokes vector to the measurement result.

In Section 5.2 a description of the mathematical framework and the computational procedure is given. In Section 5.3 the physics for the modeling of error sources that M&m's uses in its library are explained. In Section 5.4 a description of the structure and operational modes of the code is given. Section 5.5 discusses the advantages and disadvantages of this approach for error budgeting of polarimetric systems and the next steps to be taken in the development of the simulator.

5.2   Error propagation in polarimetric systems: the math

5.2.1   Mathematical approach

In the Stokes formalism, every element in an optical system can be described as a 4×4 matrix called Mueller matrix ($\mathbf{M_{element}}$). The Stokes vector going out of each element $\mathbf{S_{out}} \equiv (I_{out}, Q_{out}, U_{out}, V_{out})^T$ is then obtained by multiplying this matrix by the incoming Stokes vector $\mathbf{S_{in}} \equiv (I_{in}, Q_{in}, U_{in}, V_{in})^T$, viz. :

$$\mathbf{S_{out}} = \mathbf{M_{element}} \mathbf{S_{in}} \,. \tag{5.1}$$

Each element of this matrix represents a relation between the components of $\mathbf{S_{in}}$ and $\mathbf{S_{out}}$:

$$\mathbf{M_{element}} = \begin{pmatrix} I_{in} \to I_{out} & Q_{in} \to I_{out} & U_{in} \to I_{out} & V_{in} \to I_{out} \\ I_{in} \to Q_{out} & Q_{in} \to Q_{out} & U_{in} \to Q_{out} & V_{in} \to Q_{out} \\ I_{in} \to U_{out} & Q_{in} \to U_{out} & U_{in} \to U_{out} & V_{in} \to U_{out} \\ I_{in} \to V_{out} & Q_{in} \to V_{out} & U_{in} \to V_{out} & V_{in} \to V_{out} \end{pmatrix} \,. \tag{5.2}$$

If we have a set of n elements forming an optical system we then have to multiply the respective element matrices from the last to the first optical element on the light path to get the total matrix for the system $\mathbf{M_{tot}}$.

$$\mathbf{M_{tot}} = \mathbf{M_n M_{n-1} \ldots M_2 M_1} \, . \tag{5.3}$$

Which obviously relates the incoming and outgoing Stokes vectors as follows:

$$\mathbf{S_{out}} = \mathbf{M_{tot} S_{in}} \, . \tag{5.4}$$

Each element's performance, and hence its corresponding Mueller matrix ($\mathbf{M_z}$ with $z = 1, 2, \ldots, n$), will depend on a certain number ($j_{max}(z)$) of physical parameters each of which will have a particular distribution of values, i.e. an uncertainty, or fixed offset. These uncertainties on each parameter's value will have an effect on the Mueller matrix of the element that can be expressed by the product of the error on the parameter ($\delta p_{j,z}$) and a matrix that tells us how this parameter affects each element of the main matrix, referred to as *"weight"* matrices ($\mathbf{m_{j,z}}$) in the following. In this way we can express the Mueller matrix of any element as the sum of a *"main"* matrix ($\mathbf{M}$) and $j_{max}(z)$ *"error"* matrices ($\delta p_j \cdot \mathbf{m_j}$):

$$\mathbf{M_z}\left(p_1 + \delta p_1, \ldots, p_j + \delta p_{j_{max}(z)}\right) = \mathbf{M}(p_1, \ldots, p_j) + \delta p_1 \cdot \mathbf{m_1} + \cdots + \delta p_j \cdot \mathbf{m_j} + \cdots + \delta p_{j_{max}(z)} \cdot \mathbf{m_{j_{max}(z)}} \, . \tag{5.5}$$

Now the error matrices, ($\delta p_{j,z} \cdot \mathbf{m_{j,z}}$), can be described by the first order of the Taylor approximation of $\mathbf{M}$ with respect to each parameter $p_{j,z}$ as showed by Keller & Snik (2009) and Tyo (2002). This is only valid if (1) the errors are small, compared to the value of the corresponding main matrix value, and (2) the errors are independent from each other. In some cases the error in certain parameters can be such that the first order of the Taylor expansion will not suffice to properly approximate the contribution to the main matrix and that higher orders have to be considered, but as a first step we will use the simplified expression.

Now, to find the total Mueller matrix of a particular system composed of n elements we would have to, following the Stokes formalism, multiply the corresponding Mueller matrices:

$$\mathbf{M_{tot}} = \prod_{z=n}^{1} \left[\mathbf{M_z}\left(p_{1,z}, \ldots, p_{j_{max}(z),z}\right) + \delta p_{1,z} \cdot \mathbf{m_{1,z}} + \cdots + \delta p_{j_{max}(z),z} \cdot \mathbf{m_{j_{max}(z),z}} \right] \, . \tag{5.6}$$

Taking into account the assumptions (1) and (2) made above, the resulting expression can be simplified as follows:

$$\mathbf{M_{tot}} \approx \prod_{z=n}^{1} \mathbf{M_z} + \sum_{z=n}^{1} \sum_{j=1}^{j_{max}(z)} \delta p_{j,z} \cdot \left(\prod_{k=1}^{z+1} \mathbf{M_k} \right) \mathbf{m_{j,z}} \left(\prod_{k=z-1}^{k=n} \mathbf{M_k} \right) \, . \tag{5.7}$$

5.2.2 Implementation of Polarimetric Modulation

The M&m's code is designed to simulate the polarimetric measurement process from calculating the Mueller matrix of a system to giving the final accuracy with which a certain Stokes parameter is measured. The procedure used to simulate the polarimetric measurement is schematically shown in Figure 5.1 and detailed below.
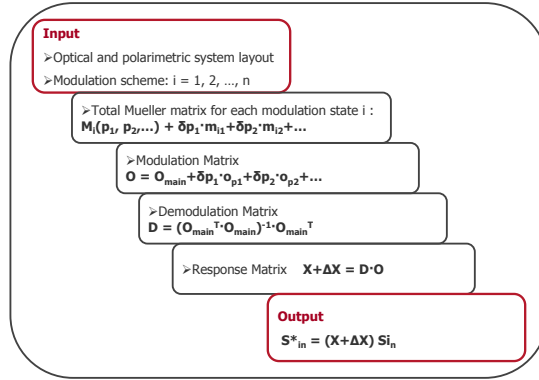

Figure 5.1: Schematic view of the M&m's computational procedure. The program starts with the input given in the master script. Then, making use of the M&m's library, it computes the Mueller matrices for the n elements and the final Mueller matrix of the system, for each modulation state i. Next step is to build the modulation matrix taking the first row of each main and weight matrices to propagate the error on each parameter into the modulation process. Then the modulation matrix $\mathbf{O}$ is split into a main matrix $\mathbf{O_{main}}$ and the corresponding matrices $\mathbf{o_{j,z}}$ for each parameter of the system. The demodulation matrix is either obtained computing the pseudo-inverse of $\mathbf{O_{main}}$ or specified by the user. The response matrix of the polarimeter $\mathbf{X}$ is then obtained as the product of the modulation and demodulation matrices and gives the relationship between the measured and the incoming Stokes vectors. The matrix $\mathbf{\Delta X}$ can then be used to perform the error budgeting (Ichimoto et al. 2008, Tyo 2002).

Once we have the expression describing how the errors $\delta p_{j,z}$ affect the main Mueller matrix of the system, we can calculate the total Mueller matrix for each modulation state (i). This enables us to build the modulation ($\mathbf{O}$) and demodulation ($\mathbf{D}$) matrices, including the error components, and eventually propagate the error to the final output of the polarimetric measurement process. The type of modulations implemented on the code are only spatial modulation, temporal modulation or a combination of both. Spectral modulation or channelled spectropolarimetry has a demodulation procedure based on Fourier transforms and therefore can't be represented by a linear operation.

Continuing with the nomenclature presented in Section 5.2.1, let us consider an optical system composed of n elements, each of which depends on a certain, and generally different, number of parameters ($p_{j,z}$, with $j = 1, 2, \ldots, j_{max}(z)$ and $z = 1, 2, \ldots, n$) and a modulation scheme composed of m modulation states. Note that we will then have an $h = \sum_{z=1}^{n} j_{max}(z)$ total number of parameters for the system, and $j = 1, 2, \ldots, j_{max}(z)$

inside each z optical element. Table 5.1 shows, for clarity, the definition and ranges of the indexes we will use in the following.

Table 5.1: Definition of indexes

Optical element	z	$z = 1, 2, \ldots, n$
Parameter in z	j	$j = 0, 1, \ldots, j_{max}(z)$
Modulation state	i	$i = 1, 2, \ldots, m$

For each modulation state i we would have a total Mueller matrix for the system:

$$i = 1, \quad \mathbf{M_{tot,1}} = \mathbf{M_1} + \delta p_{1,1} \cdot \mathbf{m_{1,1,1}} + \cdots + \delta p_{j,z} \cdot \mathbf{m_{j,z,1}} + \cdots + \delta p_{j_{max}(n),n} \cdot \mathbf{m_{j_{max}(n),n,1}}$$

$$i = 2, \quad \mathbf{M_{tot,2}} = \mathbf{M_2} + \delta p_{1,1} \cdot \mathbf{m_{1,1,2}} + \cdots + \delta p_{j,z} \cdot \mathbf{m_{j,z,2}} + \cdots + \delta p_{j_{max}(n),n} \cdot \mathbf{m_{j_{max}(n),n,2}}$$

$$\vdots$$

$$i = m, \quad \mathbf{M_{tot,m}} = \mathbf{M_m} + \delta p_{1,1} \cdot \mathbf{m_{1,1,m}} + \cdots + \delta p_{j,z} \cdot \mathbf{m_{j,z,m}} + \cdots + \delta p_{j_{max}(n),n} \cdot \mathbf{m_{j_{max}(n),n,m}}$$

.

Each $\mathbf{M_{tot,i}}$ represents the behavior of the instrument for each modulation state. There will be only a few Mueller matrices that will change with (i), since is only the modulator (spatial or temporal) that changes state. The code will be able to distinguish between those ones and the "static" ones so the calculation of the total Mueller matrix can be shortened.

Now if we have an incoming Stokes vector ($\mathbf{S_{in}}$) going through the system, for each modulation state we will get an intensity (I_i) measured at the detector. These intensities form a vector at the end of the modulation cycle, $\mathbf{I_{meas}} \equiv (I_1, I_2, \ldots, I_m)$. A linear combination of these m intensities will allow us to infer the state of polarization of the incoming light. This linear relation between the m intensities measured by the detector and the incoming stokes vector is given by the so-called modulation matrix ($\mathbf{O}$),

$$\mathbf{I_{meas}} = \mathbf{OS_{in}} \, . \tag{5.8}$$

The modulation matrix $\mathbf{O}$ is an $m \times 4$ matrix built by compiling the first row of every $\mathbf{M_{tot,i}}$ matrix. This can be understood remembering that it is in this row of the Mueller

matrix where we find how the components of the incoming Stokes vector get transformed into output intensity Eq. 5.2. Given the structure that these Mueller matrices now have, i.e. being split in a sum of matrices, we will obtain a modulation matrix that is also a sum of matrices. We will get a *main* modulation matrix ($\mathbf{O_{main}}$) obtained by compiling the first rows of main matrices $\mathbf{M_i}$ and h matrices $\mathbf{o_{j,z}}$, obtained by compiling the first rows of weight matrices $\mathbf{m_{j,z,i}}$, each one associated to one physical parameter of the system.

$$\mathbf{O} = \mathbf{O_{main}} + \delta p_{1,1} \cdot \mathbf{o_{1,1}} + \cdots + \delta p_{j,z} \cdot \mathbf{o_{j,z}} + \cdots + \delta p_{j_{max}(n),n} \cdot \mathbf{o_{j_{max}(n),n}} . \quad (5.9)$$

$\mathbf{O_{main}}$ tells us how the intensity is measured without taking into account the deviations of the parameters. The "separated" propagation of the errors to this point allows us to analyze how they affect the intensity measurement directly, so we can easily detect the elements and parameters that have more impact on the measurement before the demodulation process.

It is at this point of the process when we can implement detector errors such as bias drift and nonlinearities (see Section 5.3 for further description).

Once we have the measured intensity vector the demodulation process starts. The basic goal of this process is to infer $\mathbf{S_{in}}$ from the set of intensity measurements $\mathbf{I_{meas}}$. It is clear from Eq.7.3 that this can be done by the inverted matrix of $\mathbf{O}$, which we will refer to as $\mathbf{D}$, the *demodulation* matrix. This is a trivial mathematical problem only if $\mathbf{O}$ is a square matrix, which is the case for modulation schemes composed of four measurements. If the modulation scheme comprises a larger number of modulation states, i.e. $m > 4$, the solution for the inversion of $\mathbf{O}$ is no longer unique and we have an infinite number of *demodulation* matrices that fulfill the condition $\mathbf{DO} = \mathbf{1}$. Then the new problem is to find the demodulation matrix that optimizes the efficiencies of the system (del Toro Iniesta & Collados 2000, Tyo 2002). In 2000, del Toro Iniesta & Collados showed that the solution for this optimization problem is found by means of the Moore-Penrose pseudo-inverse matrix:

$$\mathbf{D} = (\mathbf{O^T O})^{-1} \mathbf{O^T} . \quad (5.10)$$

At this point we need to make some considerations. Given expressions (5.9) and (5.10) we would now have to calculate the Moore-Penrose pseudo-inverse matrix of a sum of a large number of matrices, depending on the total number of parameters in our system. Furthermore, we want to keep the errors $\delta p_{j,z}$ as unknown variables up to the end of the process so we can analyze the system in a generic way, without considering specific values for the errors. There are various mathematical formulae and theorems to obtain the inverse of a sum of matrices but , as far as we know, there is no way to obtain analytically the inverse of a structure like this particular one, specially with a variable number of matrices. The problem of how errors propagate through the non-linear process of matrix inversion has been analyzed by Ramos & Collados (2008) for gaussian errors but systematic errors have a complete different distribution which makes them unsuitable for this procedure. A simplified approach is to obtain $\mathbf{D}$ by means of an "ideal" or "best known" modulation matrix, which would be $\mathbf{O_{main}}$ in our case.

This can be justified arguing that during data reduction one has to choose a demodulation matrix. The best knowledge one has of the modulation matrix is obtained after modeling (or calibrating). This matrix would be $\mathbf{O_{main}}$ for us, since it represents de *"ideal"* behavior of the modulation matrix. In this way we can also propagate the error in the parameters as unknown variables through the demodulation process.

Therefore:

$$\mathbf{D}^* = (\mathbf{O_{main}^T O_{main}})^{-1} \mathbf{O_{main}^T} \,. \tag{5.11}$$

There is also the possibility of using a pre-defined demodulation matrix which, even though it may not be the optimal one, will be required in many practical situations. This can be easily implemented in the code by providing the demodulation matrix together with the input and not deriving it from the calculated modulation matrix. Also the code needs to be suitable for partial polarimeters, i.e. polarimeters only measuring a part of the Stokes vector, for which the modulation matrix when written as a $m \times 4$ matrix is singular and non-invertible. Therefore the code would have to be able to reduce the dimensionality.

Once we have the demodulation matrix we can finally find the vector that will represent the "measured" incoming Stokes vector, $\mathbf{S_{in}^*}$,

$$\mathbf{S_{in}^*} = \mathbf{D I_{meas}} \,. \tag{5.12}$$

Note that this vector is not a Stokes vector since is obtained through the matrices $\mathbf{O}$ and $\mathbf{D}$ which are not Mueller matrices.

Ideally this output will be exactly the Stokes vector that comes in the polarimeter so that:

$$\mathbf{S_{in}^*} = \mathbb{1} \mathbf{S_{in}} \,. \tag{5.13}$$

Of course this is not the case since no instrument is exempt from creating some uncalibrated instrumental polarization and cross-talk along the measurement process. To take this into account it is useful to introduce the concept of a *response matrix* $\mathbf{X}$ (Ichimoto et al. 2008). This matrix, which is not a Mueller matrix, has dimensions of 4×4 and can be defined as the one representing the measurement process i.e. it relates the incoming Stokes vector ($\mathbf{S_{in}}$) with the vector $\mathbf{S_{in}^*}$ that we obtain in the end as the "measured" Stokes vector

$$\mathbf{S_{in}^*} = \mathbf{X S_{in}} \,. \tag{5.14}$$

Again, in ideal conditions $\mathbf{X}$ would be the identity matrix, but since we have errors in the process it will have values different from unity. In the end, what we aim to do with the M&m's code is to model this response matrix, so find the range of values its elements can take on, and this is done by propagating our error-dependent matrices $\mathbf{o_{j,n}}$ up to the end of

the inversion process. Considering equations 7.3, 7.4 and 6.2 it is obvious that we can obtain $\mathbf{X}$ by means of $\mathbf{D}$ and $\mathbf{O}$ as follows:

$$\mathbf{X} = \mathbf{DO} \, . \tag{5.15}$$

If we now introduce the expression for $\mathbf{O}$, Eq. 5.15 becomes:

$$\mathbf{X} = \mathbf{D}[\mathbf{O_{main}} + \delta p_{1,1} \cdot \mathbf{o_{1,1}} + \cdots + \delta p_{j,z} \cdot \mathbf{o_{j,z}} + \cdots + \delta p_{j_{max}(n),n} \cdot \mathbf{o_{j_{max}(n),n}}] \, . \tag{5.16}$$

which applying the distributive property gives:

$$\mathbf{X} = \mathbf{DO_{main}} + \delta p_{1,1} \cdot (\mathbf{Do_{1,1}}) + \cdots + \delta p_{j,z} \cdot (\mathbf{Do_{j,z}}) + \cdots + \delta p_{j_{max}(n),n} \cdot (\mathbf{Do_{j_{max}(n),n}}) \, . \tag{5.17}$$

If the demodulation matrix is the pseudo-inverse of the main modulation matrix, i.e. we have computed $\mathbf{D}$ instead of using a pre-defined one, the first term of the right side of the equation is the identity matrix and each $(\mathbf{Do_{j,z}})$ term represents a variation of the response matrix depending on the corresponding $p_{j,z}$.

$$\mathbf{X} = \mathbb{1} + \delta p_{1,1} \cdot \mathbf{\Delta X_{1,1}} + \cdots + \delta p_{j,z} \cdot \mathbf{\Delta X_{j,z}} + \cdots + \delta p_{j_{max}(n),n} \cdot \mathbf{\Delta X_{j_{max}(n),n}} = \mathbb{1} + \mathbf{\Delta X} \tag{5.18}$$

In this way, we have propagated the errors up to the final matrix that models the complete measurement process.

5.2.3   Error budgeting

The matrices $\mathbf{\Delta X_{j,z}}$ and $\mathbf{\Delta X}$, from Equation 5.18, can be seen as *"accuracy matrices"* to be directly used for error budgeting by comparing them with the requirements set for the polarimeter.

This can be done in different ways such as comparing the complete accuracy matrix ($\mathbf{\Delta X}$) with a "requirements matrix" that one builds from the scientific requirements (Eq. 5.19, Ichimoto et al. 2008):

$$\mathbf{\Delta X} \leq \mathbf{\Delta X_{req}} \, . \tag{5.19}$$

To simplify the process only the most stringent components of the $\mathbf{\Delta X_{req}}$ can be considered.

Another approach is to assume an input Stokes vector ($\mathbf{S_{in,def}}$) and compute the difference or vector norm between the this input and the measured Stokes vectors ($\mathbf{S_{in}^*}$) obtained by multiplying with $\mathbf{\Delta X}$ (Eq. 5.20, Tyo 2002) :

$$\sum_{k=1}^{4} \left(\mathbf{\Delta X} \cdot \mathbf{S_{in,def}} \right)_k^2 \leq ||\epsilon||^2 \, . \tag{5.20}$$

The requirement on polarimetric accuracy is then described by the vector norm $||\epsilon||$, and should be fulfilled for all possible input Stokes vector.

5.2.4   Implementation of Calibration

The code can be set up such that it describes the full procedure of calibration, after the Mueller matrices for the calibration optics including error terms have been introduced. These results should then be fed back into the code to describe the calibrated polarimetric measurements. However, the error propagation from the calibration to the measurement is not straightforward and has only be mathematically described in the case of Gaussian errors (Ramos & Collados 2008). Possibly a complete Monte Carlo simulation has to be performed to fully model this process.

In any case, real calibration results and the estimated errors thereupon can be implemented directly by replacing the pertinent part of the modeled Mueller matrix train.

5.3   Overview of polarimetric errors: the physics

Now that we have defined the mathematical procedure we need to introduce the physics behind the error modeling, i.e. determine $\mathbf{m_{j,z}}$. An error budgeting code like M&m's is only useful once it is able to consider almost any kind of error to any kind of optical element. Based on the current literature, an extensive library is therefore created out of which most relevant Mueller matrices and error matrices can be taken or computed.

Errors affecting polarimetric measurements can be widely ranging in both type and scale and can arise from many different sources like missalignments, manufacturing errors or variations of the working temperature. In polarimetry, every element before the polarimeter, even a simple glass plate, can affect the measurement. Therefore a careful analysis of each element must be done in order to model its behavior as accurately as possible.

There are two main ways in which this can be done. One way is based on the direct characterization of the elements in the lab, or what could be seen as the empirical approach. This method, of course, provides a quite complete knowledge of the particular element one is considering but lacks of potential for generalization and it is limited by the accuracy of the measuring system. Another approach is to start from the general analytical expression of the element's Mueller matrix depending on various physical parameters and derive the error matrices as a first order Taylor expansion to each parameter. In our case we consider

both possibilities, so the code can estimate an approximation of the *weight matrices* for each parameter and it can also include error matrices that are already determined.

5.3.1   Parameters

Parameters can be separated in two groups, the ones affecting the Mueller matrix of only one particular element, e.g. the birefringence of the material of a retarder or the extinction ratio of a polarizer, and those which are common for all the system, e.g. wavelength and temperature. The latter will be represented in the code by global parameters. This means that all Mueller matrices inasmuch they depend on wavelength and temperature will automatically have error matrices associated to them that scale with wavelength or temperature. Thus the variation of system performance with wavelength and temperature can be estimated from the code's output. It is clear that with only a first-order approximation of Mueller matrix variation with wavelength, only relatively narrow band-widths can be considered. If one element has a different temperature than the others, its Mueller matrix at that temperature and corresponding error matrix for temperature changes can be also inserted separately.

5.3.2   Library of Mueller Matrices and Error Matrices

The following describes the implementation of Mueller matrices of common optical elements. It also describes which error sources can be used in the code and under which assumptions.

Rotations

This is a special case because it is not an element per se. A single rotation Mueller matrix describes the rotation of the $[Q, U]$ coordinate system. The only error in this process is an offset to this rotation (or a certain distribution of offsets). For the case of a freely rotating element, two rotation matrices need to be inserted, one before and one after the element (which can be a compound of several Mueller and error matrices). The amount of rotation and the error thereof is identical, but have an opposite handedness, unless the elements in between modify Stokes coordinate system like an odd number of mirrors do.

Rotation is often used in temporal modulation, so the variation of the Mueller matrix with modulation state is generically implemented in this function.

Linear Polarizers

The ideal Mueller matrix of a linear polarizer assumes that linear polarization in the $+Q$ direction gets transmitted. In the case of spatial modulation by using a polarizing beam-splitter, this direction can be switched to $-Q$ in the input script that handles the modulation sequence.

The following error terms are implemented:

- Limited extinction ratio. The extinction ratio is here defined such that its value is <1. The error matrix for limited extinction ratio is described by Snik (2006). This error necessarily has a first and second order.

- Depolarization cf. Nee et al. (1998).

- Field-of-view effects. This is described with the 3D geometry of the polarizers axes compared to the input polarization.

Retarders

The most frequently used retarders are based on birefringent (liquid) crystals. The retardance can be computed once the material's birefringence and the plate's thickness is known:

$$\delta = 2\pi \frac{(n_e - n_o) \cdot d}{\lambda} \, . \tag{5.21}$$

The refractive indices for many crystals are listed by Ghosh (1998).
Various error sources are readily derived from this:

- Variation with wavelength.

- Variation of the thickness.

- Offset of the birefringence.

- The variation of the birefringence with temperature can be computed from thermo-optic coefficients listed by Ghosh (1998). See Hale & Day (1988). Also the thermal expansion of the plate is taken into account.

- The variation of retardance upon a change of incidence angle and azimuth, as described by the equations in Evans (1949).

- Dichroism, as determined by the Fresnel equations for the two polarization directions along the two crystal axes.

- Polarized fringes due to multiple reflections within the birefringent plate manifest themselves as a sinusoidal partial polarization pattern as a function of wavelength, as well as a wavelength-dependent modification of the retardance. These effects are calculated by using the Berreman calculus as described by (Weenink et al. 2013). The mitigation of these effects by using AR coatings can be implemented ad-hoc.

Since most wave-plates used for instrumentation are actually compounds of two or more layers of different materials, it makes sense then to consider compound wave plates as unit elements in the system. Several frequently used wave plates will be predefined in the M&m's library: achromatic and superachromatic wave plates and liquid crystals like Liquid Crystal

Variable Retarders (LCVRs) en Ferroelectric Liquid Crystals (FLCs). For the first cases, the alignment between the two plates becomes an important error parameter. For the liquid crystals, the switching angles (that often drive the modulation sequence) will be subject to errors.

Also a standard Fresnel rhomb will be implemented. The main error sources there will be:

- Variation of retardance with incidence angle and azimuth.

- Stress birefringence.

Mirrors

The Mueller matrix of a mirror is based on the models applied to accurate ellipsometry performed by van Harten et al. (2009). According to it, a mirror can be characterized knowing the following parameters: the incidence angle (α) and wavelength (λ) of the incoming light, the complex index of refraction of the metal, and, if present, the thickness and index of refraction of the dielectric film layer on top of the mirror's surface. This layer can be an artificial overcoating or can occur naturally due to the growth of the aluminum oxide layer (van Harten et al. 2009). The equations that lead to a mirrors Mueller matrix are numerous and complex and directly describe the dependence of the Mueller matrix on various physical parameters:

- Variation with wavelength due to the variation of the refractive indices.

- Variation with incidence angle and azimuth.

- Aging which involves a growth of the layer of dielectric material on the mirror. Also a dust layer can be described with an effective growth of this layer (Snik et al. 2013).

Glass Components

It is often assumed that glass components like lenses do not modify or create polarization, and therefore the ideal Mueller matrix is the unit matrix. Various error sources can however exist:

- Glass components can introduce linear polarization if a ray of light hits it at a non-normal incidence. This is fully determined by the Fresnel equations, after linearizing those for the incidence angle. It needs to be computed at every glass-air interface.

- Stress birefringence occurs in every piece of glass. A certain direction (or distribution) of the stress tensor needs to be assumed.

Detectors

Although the action of a detector cannot be described by a Mueller matrix, its non-ideal properties can adversely affect the polarimetric accuracy. Fortunately, these error terms can easily be implemented using a similar formalism.

It is assumed that an ideal detector linearly converts the intensity to a data number. This corresponds with a fully multiplicative term comparable with a diagonal Mueller matrix. Two important error terms are:

- Bias drift or uncorrected stray light.

- Detector non-linearity. This obviously needs to be described with a second order (or higher) error term.

Keller (1996) has shown that such errors can couple with instrumental polarization to create spurious signals.

5.4   Overview of the code

The M&m's is a code written in Python which makes it accessible to a broad audience cost-free. The name arises from the basic structure of the Mueller matrices (Eq. 5.5) that is propagated all along: the "main" matrix ($\mathbf{M}$) and the "weight" matrices ($\mathbf{m}$).It is structured in two main parts, the *"input/master script"* and the *"M&m's library"*.

The *input/master script* represents the input to the program. In it, the user has to specify all the information about the set up to be simulated, e.g. type and order of the optical elements on the light path, modulation states, global parameters, rotations and misalignments between them, etc.... In this input one can also provide particular matrices to be used instead of those from the library such as specific calibrated error matrices for a certain element or demodulation matrices. The user also needs to specify the mode in which the code should operate.

The *M&m's library* is a compilation of functions that can be separated in two groups according to their functionality.

The first group is composed of *"element functions"* computing the Mueller matrix of typical optical elements in terms of the physical parameters in which the element depends on and deriving the corresponding weight matrices. The library contains functions to model mirrors, glass elements, waveplates and polarizers among others.

The second group is formed by the *"mode functions"* which, depending on the mode selected, operate with the Mueller matrices obtained for the elements in order to get the desired output. Figure 5.2 shows a flow diagram of the information through the different elements and stages of the code.

With the aim of making it suitable for different types of analysis it operates in three modes:
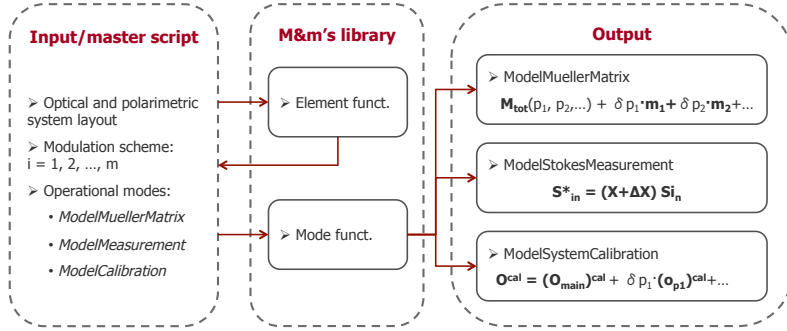
Figure 5.2: Flow diagram of the M&m's operation. The master script sends the input information to the library's selected element functions to be used. The output of this operation is sent to the master script which then sends the matrices to the selected mode function producing the final required output.

- *ModelMuellerMatrix*

- *ModelStokesMeasurement*

- *ModelSystemCalibration*

The first mode, *ModelMuellerMatrix*, computes the total Mueller matrix of a given system. It takes the matrix for each element that come as the output of the *element functions* and then multiplies the matrices following the formalism explained above. It gives the total Mueller matrix for the system as an output with the structure shown in Eq. 5.7. This is useful to analyze how the different element/parameters will affect the final behavior of the polarimetric set up but also to estimate the Mueller matrix of optical systems upstream, i.e. the telescope in front of the polarimeter.

The second mode, *ModelStokesMeasurement*, computes the vector that it is measured at the end of the process (S_{out}^*), i.e. it propagates the error matrices through the modulation and demodulation operations. In the end we get the correspondence between the incoming and the measured Stokes vector by means of the response matrix X which contains the effect of the physical parameters of the system on the measurement, represented by the propagated *weight matrices* (ΔX).

The third mode, *ModelSystemCalibration* computes the polarimetric modulation matrix as obtained after calibration and the errors pertaining to these results. This mode has not yet been implemented since, as we pointed out before, the error propagation through this operation to a calibrated measurement model needs to be investigated.

5.5   Discussion and outlook

In this manuscript we have presented the mathematical, physical and operational basis of the M&m's code for simulating the performance of a given polarimetric system. The mathemat-

ical framework developed by Keller & Snik allows us to propagate the contribution of the different errors separately up to the end of the measurement process. The main advantage of this approach is that it allows us to, at any point of the measurement process, identify the critical sources of deviation in the measurement without having to specify any particular error for the parameters. Furthermore the matrix ($\mathbf{\Delta X}$), which is dependent on the δp_j scalar errors, can be directly compared to the accuracy matrix required for the system to set the tolerances on the parameters, because we have propagated δp_j as unknown variables through the process.

The main disadvantage is that it relies on assumptions (1) and (2) presented in Sec. 5.2.1 (errors are small and independent) when aproximating the weight matrices by the first term of the Taylor expansion of the Mueller matrix. Higher order terms may therefore need to be implemented.

The code will be verified by comparing its results with those from a full Monte Carlo simulation (which can be done by using the same library of Mueller matrices), and with the results of a dedicated lab set up. At the end only a Monte Carlo simulation or lab measurements can fully characterize the system, but the M&m's approach provides a better insight on the system's dependencies. This allows us to easily detect, early in the design process, which ones will be the limiting elements/parameters when analyzing the accuracy that different designs, considered for a polarimetric system, can provide. It also can easily estimate the instrumental polarization introduced by optical systems, keeping also track of which elements have more impact.

The code aims to be open, so it can be used by anyone, general, so it can be applied to any polarimetric design, and complete in terms of error modeling. In this sense, we will keep the library open so it can be easily updated with new matrices for elements and errors.

The code is still in an early stage of development and it will be made accessible to the public as soon as it has been verified, and most relevant errors have been implemented.

The following upgrades to the code are still under consideration:

- A complete description of a distribution (random or systematic) of the physical parameters that drive the errors. This way, after propagation, the error contributions can be added in an RSS fashion, see citetkeller09.

- Adding the possibility of introducing higher-order error terms.

- Full implementation of the simulation of the calibration process and the calibrated measurement process. It may be necessary to implement a Monte Carlo simulation of the calibration process to fully propagate the systematic errors, as currently only Gaussian errors can be propagated (Ramos & Collados 2008) .

- Integration with the optical design, such that all Mueller matrices are explicitly dependent on the local incidence angles and azimuths. For converging beams, an average Mueller matrix plus a distribution of values around that can thus be obtained. A link with ZEMAX would be a logical choice for this. A simple simple solution would be to parameterize the distance to the pupil plane for each element and supply a range of incidence angle and azimuths.

Abstract

Polarimetry is a particularly powerful technique when imaging circumstellar environments. Currently most telescopes include more or less advanced polarimetric facilities and large telescopes count on it for their planet-finder instruments like SPHERE-ZIMPOL on the VLT or EPICS on the future E-ELT. One of the biggest limitations of this technique is the instrumental polarization (IP) generated in the telescope optical path, which can often be larger than the signal to be measured. In most cases this instrumental polarization changes over time and is dependent on the errors affecting the optical elements of the system. We have modeled the VLT and E-ELT telescope layouts to characterize the instrumental polarization generated on their optical paths using the M&m's code, an error budget and performance simulator for polarimetric systems. In this study we present the realistic Mueller matrices calculated with M&m's for both systems, with and without the setups to correct for the IP, showing that correction can be achieved, allowing for an accurate polarimetric performance.

6.1   Introduction

Polarimetry is becoming increasingly popular in the field of the direct imaging of circumstellar environments. Since light scattered by the material surrounding a star becomes linearly polarized having an instrument that is able to disentangle polarized from unpolarized light it is, in principle, possible to suppress the light coming from the start to observe just the surroundings (Snik & Keller 2013b). Its use can improve the contrast between the star and the surroundings by more than four orders of magnitude, a power that is getting the attention of the astronomical community, highly interested these days on the detection and characterization of exoplanets.

A big limitation of the technique is the instrumental polarization introduced by the optical systems used to collect the light. This instrumental polarization varies with time and the pointing direction of the telescope. Since the polarization signal of light scattered by circumstellar matter is expected to be of the order of a few percent (Stam et al. 2004, Stam 2008), these variable instrumental effects can be crucial when performing accurate polarimetry of exoplanets and circumstellar environments.

6.1.1   Instrumental polarization at the Nasmyth focus

Polarization is created whenever there is a break in the symmetry of the system the light is going through. In this sense, telescopes should not, in principle, introduce any polarization as long as one measures along the optical axis. Unfortunately, most current and near-future telescopes take the polarimetry to the Nasmyth focus meaning that light has to be taken out of the optical axis of the telescope, normally going through a $45\deg$ reflection on a mirror. This process can generate up to 5% linear polarization signal in the visible wavelength range (Gehrels 1960, Cox 1976, Joos et al. 2008, van Harten et al. 2009, Perrin et al. 2010). Also, a fraction of the incoming linear polarization gets lost in the process due to a conversion into circular polarization, the so called "crosstalk". It is known that these instrumental effects can be corrected by further reflection on a second "twin" mirror positioned in what is called a "crossed" configuration(Cox 1976). The main problem when applying this solution to Nasmyth focus instruments is that the mirror used to deflect the light rotates together with the telescope and therefore this "crossed" configuration only occurs for certain positions of the system.

In this study we analyse two solutions proposed for two extremely advanced linear polarimeters located at the Nasmyth focus of their respective telescopes: SPHERE-ZIMPOL at the Very Large Telescope (VLT) and EPICS-EPOL at the European Extremely Large Telescope (E-ELT). In both cases the reduction of instrumental polarization to values of less than 1% is crucial for the required performance of the instruments. Using the M&m's code we simulate both optical systems to calculate the instrumental polarization generated in their paths, and the solutions applied in both designs to correct for it.

6.2 M&m's SIMULATIONS

The M&m's code is an error budgeting and performance simulator for polarimetric systems (de Juan Ovelar et al. 2011). It makes use of the Mueller matrix formalism to simulate the response of a polarimetric system and the effect that potential errors, in the parameters of each individual optical element, have on it. It is conceived in principle as a systems engineering tool to help in the design process of polarimeters by accurately simulating the performance of different designs and detecting the problematic elements/parameters of the optical system.

In the Mueller formalism the polarization state of light is described by a 1x4 vector known as the Stokes vector, $\mathbf{S} = (I, Q, U, V)^T$, where I is the intensity, $\pm Q$ and $\pm U$ are linear polarizations in the $0/90°$ and $45°$ directions and V is circular polarization. The effect that an optical system has on the polarization state of light passing through it, can be described as the product between the incoming Stokes vector ($\mathbf{S_{in}}$) and a 4x4 matrix that accounts for the properties of the system, i.e the Mueller matrix ($\mathbf{M}$). However the process of measuring the polarization state of light involves modulation/demodulation steps to first encode the polarization state in different intensities that can be measured by the detector, and second recover the polarization state from the acquired intensity measurements. This process can be also modeled using a 4x4 matrix (i.e. the response matrix, $\mathbf{X}$), and can also account for calibration processes. The M&m's code is able to calculate both $\mathbf{M}$ and $\mathbf{X}$, and the dependencies of the various optical elements on physical parameters like temperature, wavelength, misalignment, ageing, etc.. While the former relates the incoming Stokes vector with the Stokes vector coming out of the system,

$$\mathbf{S_{out}} = \mathbf{M_{element}} \mathbf{S_{in}} \,, \tag{6.1}$$

the latter relates the incoming Stokes vector with the measured Stokes vector,

$$\mathbf{S_{meas}} = \mathbf{X} \mathbf{S_{in}} \,. \tag{6.2}$$

Techniques to reduce the instrumental polarization can be based on modifying the system or the modulation/demodulation process. In this sense, the two systems analysed in this study are perfect examples of the two different approaches. While SPHERE-ZIMPOL corrects most of the instrumental polarization modifying the setup, EPICS-EPOL makes use of a polarization "switch" that eliminates the instrumental effects after the modulation/demodulation process.

6.2.1 General considerations

The M&m's code is currently in the development/validation phase. The code aims to be general and realistic and it has implemented most of the dependencies for the parameters of the different optical elements. Nevertheless, there are some general considerations that should be taken into account when analysing the simulations performed for this study.

- Chromaticity of metallic materials is not implemented yet. This implementation is complicated since the values of the real and imaginary parts of the index of refraction for each wavelength have to be interpolated from tables of materials and this complicates the computation. This is an issue that will be corrected in the near future. However we have verified that the effect is negligible for the cases analysed in this study.

- Chromaticity of dielectric and birefringent materials is implemented. This holds also for the dielectric protective coatings of mirrors.

- Mirrors in the same system have all the same characteristics and no differential effects between them are taken into account. This effect will be covered in future simulations.

- Temperature dependencies are implemented whenever realistic characterization of the elements in terms of temperature behaviour is available.

- Whenever real optical elements are used, real characteristics and design parameters are implemented to define the element on the simulation.

- The Mueller matrices have only been established for the chief ray. The effects of the converging beams are still to be implemented.

- For the case of SPHERE-ZIMPOL the efficiency of the detector was taken into account.

6.3   SPHERE-ZIMPOL at the VLT

One of the most important upcoming instruments counting on polarimetry for the detection of exoplanets is the SPHERE planet finder at the VLT. The imaging polarimeter designed for this instrument is ZIMPOL, a single-beam polarimeter that makes use of a fast modulation-demodulation technique to achieve very high polarimetric sensitivity (Gisler et al. 2004, Beuzit et al. 2006, Thalmann et al. 2008, Roelfsema et al. 2010). As we noted before, the SPHERE instrument is placed in a VLT Nasmyth focus and therefore directly suffers from the instrumental polarization problem discussed above.

The solution for the correction of the IP proposed in this case is a setup, located between M3 and the instrument itself, designed to drastically reduce the effect of the reflection on M3. This setup consists of a half-wave plate (HWP), HWP1, that rotates at half the zenith angle to stabilise the direction of the polarization introduced by M3, and a second mirror, M4, to compensate for this polarization (Stuik et al. 2005). The configuration is such that M3 and M4 are "crossed" when the telescope is pointing to zenith. As the telescope moves from zenith, M3 rotates as well and the direction of the polarization generated when light gets reflected on it moves accordingly. The role of HWP1 is then to "derotate" this polarization such that it always comes back to the direction for which M4 can compensate (Tinbergen 2007). M4 is designed to have the same characteristics of M3 such that the differences between them are minimized and therefore the compensation is optimal. HWP1 needs to be an achromatic

retarder such that this compensation is achieved over the $500 - 900$ nm wavelength range SPHERE was designed for. Accounting for non ideal elements used in the instrument, a tolerance for the instrumental polarization in Q of 10^{-2} is set. The correction was shown to work theoretically during the design phase using the Mueller Matrix formalism with standard Mueller matrices for the components available at the moment (Joos 2007). At the end of 2010 ZIMPOL had successfully passed the subsystem testing and is currently being integrated and tested together with the rest of the SPHERE subsystems. With the information we have now about the definitive components of ZIMPOL we have performed new simulations of the optical system with the Mnms's code including wavelength, temperature and zenith angle dependencies to have a more realistic view of the M3-HWP1-M4 performance.

The components of the simulated setup and its main characteristics are listed in Table 6.1. It is important to remark that the ZIMPOL components have been simulated with the real specifications, chromatic and temperature dependent behaviour as well as properties obtained after characterization.

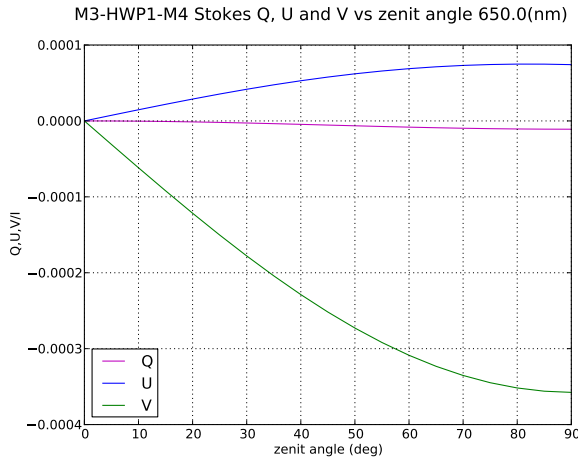| M3	Silver coated mirror	$45°$ incidence angle
	150 nm SiO$_2$ protective layer	rotating with the zenith angle
HWP1	MgF$_2$/Quartz achromatic retarder	Fast axis at zenith/2
	wavelength range: $500 - 900$ nm	
M4	Silver coated mirror	$45°$ incidence angle
	150 nm SiO$_2$ protective layer	fixed

Table 6.1: M3-HWP1-M4 System components

The simulation is carried out for two setups. The first one corresponds to the situation where we have M3, rotating from zenith to horizon ($z = [0 - 90]°$) and M4 fixed in the Nasmyth focus. This configuration compensates the instrumental polarization only when $z = 0°$. The second one corresponds to the actual design where HWP1 is in between the mirrors, rotating at half the speed of the telescope, i.e. $\theta_{HWP1} = z/2$ at all times. The simulation is carried out for ranges of zenith angle of $0 - 90$ deg and wavelengths of $500 - 900$ nm. The resultant Mueller matrices of both systems are shown for the range of zenith angles considered in Fig. 6.5 in the Appendix. When applying this matrix to an incoming ray of unpolarized light (i.e. $\mathbf{S_{in}} = (1, 0, 0, 0)^T$) the resultant Stokes vector coming out of the system has the normalized components Q/I, U/I and V/I shown in Fig. 6.1.

Figure 6.1 shows that the the instrumental polarization in Stokes Q, when HWP1 is included, gets stabilized with a value of 10^{-5} , well within the specifications for SPHERE-ZIMPOL. A maximum value of less than $4 \cdot 10^{-4}$ is introduced in the worst case, which is given for $z = 90$deg in the normalized Stokes V component. Stokes U stays below the 10^{-4} level for the whole range of telescope positions. The residual effects after the correction (6.1) are mainly due to the realistic modeling of the HWP, which is not a perfect achromatic HWP.

M3-M4 Stokes Q, U and V vs zenit angle 650.0(nm)

(a)

M3-HWP1-M4 Stokes Q, U and V vs zenit angle 650.0(nm)
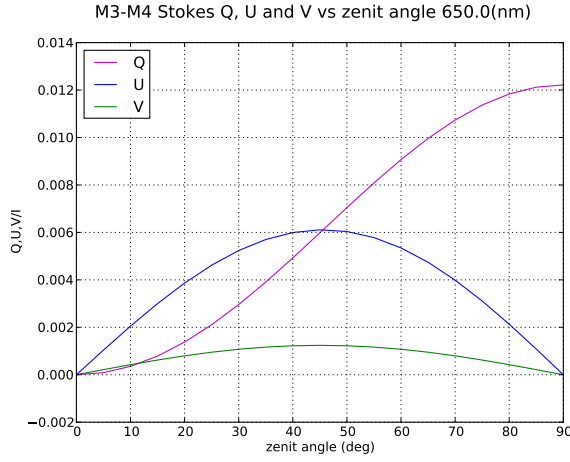
(b)

Figure 6.1: Results for the simulations of the VLT's M3-HWP1-M4 setup with the M&m's code. Stokes components Q, U and V normalized to the intensity are shown for different zenith angles in the case of having only M3-M4 (a) or M3-HWP1-M4 (b) before the instrument. The instrumental polarization gets drastically reduced with the stabilization performed by HWP1.

The solution applied in this case is therefore shown to be extremely effective. On top of this reduction of the instrumental polarization generated by M3, the real ZIMPOL setup counts

λ_{cent}/FWHM	550/80	655/60	717/20	750/150	770/20	820/20	820/80	870/60
Stdv(Q/I)	$\sim 10^{-3}$	$3 \cdot 10^{-4}$	$\sim 10^{-3}$	$3 \cdot 10^{-4}$	$9 \cdot 10^{-4}$	$2 \cdot 10^{-3}$	$6 \cdot 10^{-4}$	10^{-3}
Stdv(U/I)	$9 \cdot 10^{-4}$	$3 \cdot 10^{-4}$	$\sim 10^{-3}$	$5 \cdot 10^{-4}$	$\sim 10^{-3}$	$2 \cdot 10^{-3}$	$9 \cdot 10^{-4}$	$3 \cdot 10^{-3}$
Stdv(V/I)	$4 \cdot 10^{-4}$	$4 \cdot 10^{-4}$	$2 \cdot 10^{-3}$	$4 \cdot 10^{-4}$	$3 \cdot 10^{-3}$	$2 \cdot 10^{-3}$	$2 \cdot 10^{-3}$	

Table 6.2: Standard deviation of the measurements performed with ZIMPOL of the M3-HWP1-M4 laboratory setup for different filters.

with a polarization compensator (a tiltable and rotatable glass plate) before the detector to remove any instrumental polarization generated by the elements in the SPHERE-ZIMPOL optical path itself, i.e. after M4.

6.3.1 ZIMPOL laboratory measurements of the M3-HWP1-M4 instrumental polarization

During the testing phase of ZIMPOL, a set of measurements was taken with a simulator for the M3-HWP1-M4 setup. For these measurements, the polarization compensator was taken out to allow a clear measurement of the instrumental polarization generated. Figure 6.2 shows the results of these measurements for normalized Q, U and V Stokes components. The measurements were taken with eight different filters covering the wavelength range of the instrument (see Table 6.2). Zenith angles range from 0 to $90°$ in steps of $10°$. The estimated photon noise for this measurements is $5.77 \cdot 10^{-4}$. Table 6.2 shows the standard deviation of these measurements for each Stokes component and filter. The largest value, $\sigma = 0.0028$, is given for the $870/60$ nm filter in U/I. This implies a largest variation of the instrumental polarization over the whole zenith angle range of less than 0.3% which confirms the success of this compensation system.

An unexpected wavelength-dependent bias is present in the measurements, which also varies from one Stokes component to another. This effect is likely to be compensated by the polarization compensator, which explains why it was not seen before. The proposed explanation for it is the generation of polarized fringes by one of the elements in the modulator system of ZIMPOL. This modulation system consists of three different retarders. The first one in the optical path is an achromatic quarter-wave plate (QVIS), only introduced when measuring Stokes V. The second one is an achromatic half-wave plate (HWPZ), used to modulate between Stokes Q and U. And the third one is a ferro-electric liquid crystal (FLC), that switches very rapidly the position of its fast axis to modulate the sign of the polarization going through the analyzer. This FLC is composed of several plates of different materials containing a very thin layer of birefringent liquid crystal that changes the direction of its fast axis when a voltage is applied. This change can be done very rapidly (at the order of kHz) which is very useful in polarimetry since it allows to perform the modulation at high frequencies and therefore reduce the differences between consecutive intensity measurements, which reduces systematic errors.
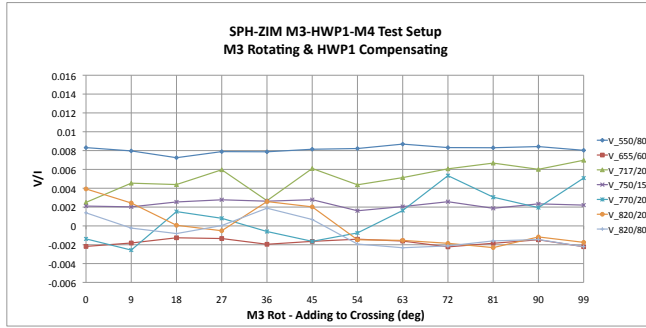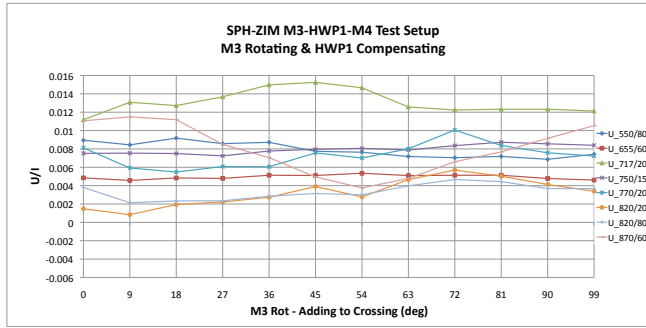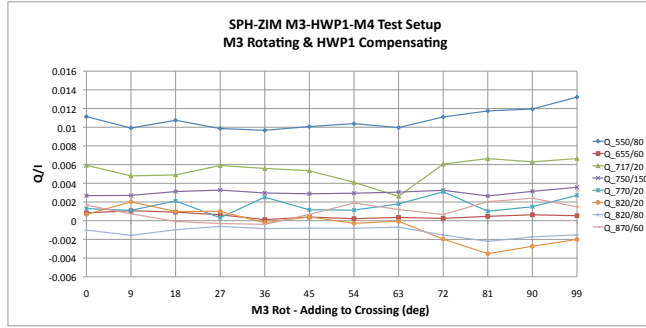
(a)

(b)

(c)

Figure 6.2: ZIMPOL laboratory measurements of the instrumental polarization generated by the M3-HWP1-M4 setup. The normalized Stokes components Q, U and V are shown separately for different filters covering the wavelength range of the instrument.

However, FLCs are known to generate wavelength-dependent polarization effects such as the ones observed with ZIMPOL and presented in this study (Gisler et al. 2003). An attempt to build a physical model, in the context of the M&m's code, to reproduce ZIMPOL's FLC behaviour was done. The model is briefly explained in the following lines and the results are shown in Fig.6.3. To simulate the measurements, the complete modulation scheme was modeled as well as the components of the ZIMPOL modulation system. These components and their main characteristics are shown in Table 6.3. An efficiency of 0.855 for the ZIMPOL detector was also taken into account (Schmid et al. 2012).

QVIS	MgF$_2$/Quartz achromatic QWP	Fast axis at $45°$
	$\lambda_{\mathrm{range}} = [500 - 900]$ nm	for Stokes V meas.
HWPZ	MgF$_2$/Quartz achromatic HWP	Fast axis at $0°$ for Q meas.
	$\lambda_{\mathrm{range}} = [500 - 900]$ nm	and at $22.5°$ for U meas.
FLC	HWP	Fast axis at $-24.4°$
	$\lambda_{\mathrm{design}} = 665$ nm	temperature variations incl.
	Weak polarizer	chromatism of brifringence incl.
HWP0	Quartz chromatic HWP	Fast axis at $64.4°$ for Q meas.
	$\lambda_{\mathrm{range}} = [500 - 900]$ nm	at $22.5°$ for U meas.

Table 6.3: ZIMPOL modulation system components

The FLC was modeled as an element with retarding and a weak polarizing properties. The latter component describes the polarized fringes generated by multiple internal reflections in a birefringent medium. One of the main limitations when modeling FLCs is that most of the details of the materials and layout are not provided by the manufacturer. In particular the birefringence and thickness of the liquid crystal are unknown, among the exact materials used for the plates containing it. The approach to simulate the FLC characteristics was to calculate the thickness of the retarding layer based on a birefringence obtained with a typical dispersion law for liquid crystals (Xu et al. 2006) at the FLC design wavelength (665nm). At this particular wavelength the FLC acts as a perfect half-wave plate. To make it achromatic a chromatic half-wave plate is added after the exit surface (HWP0) of the FLC to compensate the dispersion. This achromatizing HWP was also simulated in the code with the realistic characteristics provided by the manufacturer. The model for the weak polarizing component was developed following Aitken & Hough (2001) but leaving two parameters free, one defining its effective polarizing thickness by multiplying the calculated thickness for the retarding component, p_{thick}, which ranges from 0 to 1, and another one accounting for the fact that the liquid crystal is surrounded by a medium different than air, p_{n}. A fitting process to the ZIMPOL data for the measured polarization in different filters at $z = 0$ deg was carried out giving a best fit for $p_{thick} = 0.325$ and $p_n = 1.396$. The results of this fitting process are shown in Fig. 6.3. The effect of temperature on the switching angle of the FLC is also included in

the model based on actual measurements performed at ASTRON for the characterization of the FLC used in the setup. The results are obtained for a specific wavelength, therefore we convolved them with the profiles of the filters used for the measurements (dashed magenta lines in Fig. fig:ZIMPOLMnms).
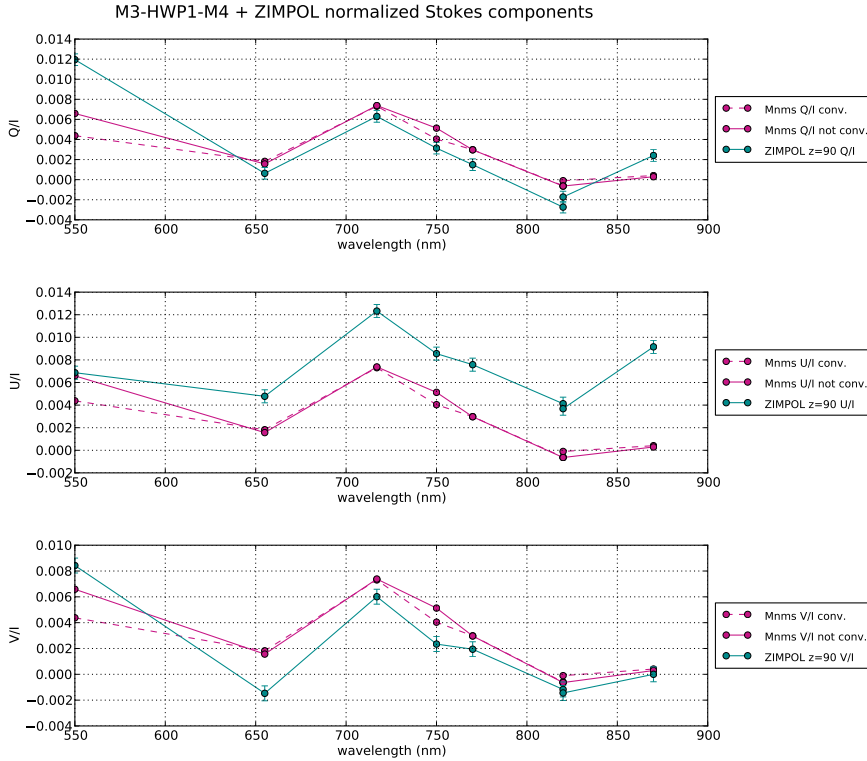

Figure 6.3: Results for the fitted M&m's model of the M3-HWP1-M4 setup plus ZIMPOL modulation system. Magenta lines correspond to the M&m's results using $p_{thick} = 0.325$ and $p_n = 1.396$ (see text) with solid and dashed lines denoting monochromatic and convolved results using rectangular profiles with the FWHM of each filter (see Table 6.2). Turquoise lines show the ZIMPOL measurements with the different filters for rotation of M3 in the laboratory simulator of $z = 90\,\mathrm{deg}$, which corresponds with a zenith angle of $0\,\mathrm{deg}$ in the M&m's simulation.

To include the effects of the FLC to the final measured values of Q/I, U/I and V/I, we simulate the measurements with the M&m's code by implementing the modulation and

demodulation process. This means that various realizations of the complete Mueller matrix train are constructed for the different switching angles of the FLC, the rotation of the HWPZ and the insertion of the QVIS. The modulation matrix is constructed from the first rows of these (six) total Mueller matrices. The demodulation matrix is identical to that used in the ZIMPOL measurements.

The results clearly show a good correspondence with the data. The deviation between the M&m's simulation and the ZIMPOL measurement is of almost a constant 0.15% in Stokes Q, for all wavelengths excluding $550\,\mathrm{nm}$, a maximum of 0.4% for Stokes U and a maximum of 0.35% for Stokes V. The overall shape of the measured polarized fringes is well reproduced. Through this modeling process we could confirm that the polarization features seen in the measurements indeed follow a sine curve for all three Stokes Q, U and V with similar characteristics in the three cases, which again points to the FLC as the origin of the effect. However, there is still a systematic residual to these fits. This implies that there is still an unknown contribution to the instrumental polarization. This source may be identified once all error terms to the Mueller matrices are analyzed using the M&m's code.

6.4   EPICS-EPOL at the E-ELT

EPOL is the imaging polarimeter designed for the EPICS (Exoplanet Imaging Camara and Spectrograph) instrument on the future $39\,\mathrm{m}$ E-ELT (Keller et al. 2010). This advanced polarimeter aims to not only detect but also characterize the atmospheres of exoplanets which raises the level of the requirements on polarimetric accuracy and therefore restricts the tolerances for instrumental linear polarization much more (i.e. $< 10^{-3}$) (Keller et al. 2010). EPICS will be also located in the Nasmyth focus of the E-ELT and in this case the telescope will deal with as much as six mirrors before the polarimeter. This number of mirrors is still not fixed in the design and there is the option of having EPICS located after mirror 5 directly. In this study we simulated the case for which EPICS is located after six mirrors. It is important to notice that the instrumental polarization will be even more stabilized if EPICS will be located at a straight-through Nasmyth port, i.e. without M6. This will be analyzed futher in future work.

The first three mirrors are aligned and rotationally symmetric but M4, M5 and M6 are positioned in a non symmetric configuration with M4 and M5 rotating together with the telescope and M6 fixed in the Nasmyth focus. Due to the large diameter of the beam reaching the Nasmyth port a solution like the one applied to the SPHERE-ZIMPOL case has to be ruled out because there is currently no HWP with the large clear aperture needed. Instead, the proposed solution is to install a HWP at the intermediate focus (IF) of the telescope, located at the optically uncorrected focus within M4. Light passes through this focus on its way from M2 to M3 and therefore, before hitting M4. The HWP placed here rotates the direction of the polarization coming from the sky and the telescope up to this point (i.e. sky-M1-M2-M3) to the orthogonal direction and thus changing its sign. The polarization generated along the optical path of the telescope below (i.e. M4-M5-M6) remains unrotated. By taking two sets of measurements with the HWP in the "neutral" and "rotated" positions and subtracting them,

one can suppress the instrumental polarization in the demodulation process.

To show how the instrumental polarization issues of the E-ELT can be mitigated, we implement a rotatable HWP in the intermediate focus of the E-ELT, identical to the one used in SPHERE-ZIMPOL. Behind M6, the linear polarization direction selected by the HWP in the IF is measured using an FLC, and circular polarization is measured with the addition of a QWP before the FLC. Again, two different setups where modeled. The first one simulates the M4-M5-M6 system and the second one the system including the intermediate focus HWP. The characteristics and positions of the components are listed in Table 6.4. The simulations were carried out for the same ranges of zenith angle and wavelength as in the SPHERE-ZIMPOL case (i.e. $z = [0 - 90]$ deg and $w = [500 - 900]$ nm).

IFHWP	MgF$_2$/Quartz achromatic HWP	Fast axis at $0°$ for 1st mod. scheme
	wave. range: $500 - 900$ nm	and at $45°$ for for 2nd mod. scheme
M4	Aluminum coated mirror	$8.5°$ inc. angle
	no protective layer	rotating with zenith angle
M5	Aluminum coated mirror	$36.5°$ incidence angle
	no protective layer	rotating with zenith angle
M6	Aluminum coated mirror	$45°$ incidence angle
	no protective layer	fixed
	Modulation system inside EPOL	
QWP	MgF$_2$/Quartz achromatic QWP	Fast axis at $45°$
	in only for Stokes V measurement	
	wave. range: $500 - 900$ nm	
FLC	ideal HWP	Fast axis at $0/45°$ for Q meas.
	design wavelength: 510 nm	Fast axis at $22.5/67.5°$ for U meas.
	birefringence $= 0.15$	

Table 6.4: EELT components.

The results of the E-ELT simulations are shown in Fig. 6.4 where the normalized Stokes Q, U and V are plotted for the complete range of zenith angles in the two configurations described above. The complete response matrix is again shown in Fig. 6.6 (Appendix A). The instrumental polarization generated by the E-ELT optical configuration is of the order of a few percent, while the compensation by the IFHWP completely suppresses it for the Stokes Q and U components and in the case of Stokes V it reduces it to less than 0.4% in the worst case. It is important to remark again that neither of these two polarimeters are aimed to measure circular polarization, and therefore the compensation of the circular instrumental polarization generated is not a priority. Nevertheless, the simulation was carried out to be as complete as possible and therefore we included all the calculations for Stokes V.
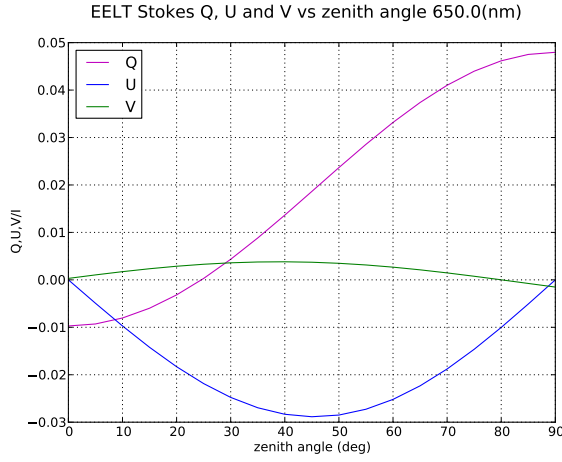
(a)
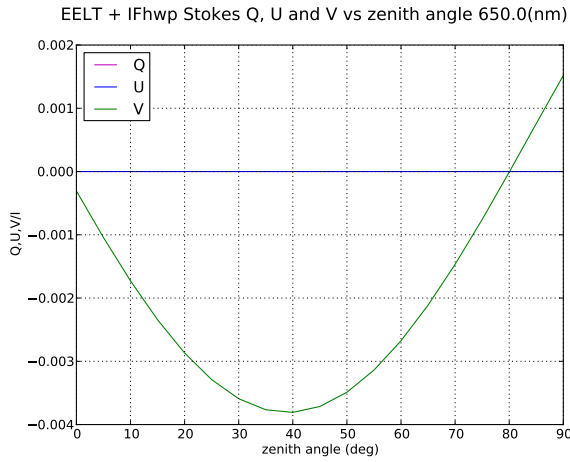
(b)

Figure 6.4: Normalized Stokes components for the M4-M5-M6 (a) and IFHWP-M4-M5-M6 (b) systems.

6.5 Conclusions

Using the M&m's code, we have performed simulations of the polarimetric behaviour of the VLT and E-ELT telescopes up to their Nasmyth focus, where the corresponding planet finder

instruments, SPHERE and EPICS, are located. We have shown that the linear instrumental polarization generated in the optical path of the telescopes is of the order of 1% for the VLT case, and of 5% for the E-ELT case. These values severely limit the accuracy with which polarimeters can measure. However, very effective compensation and correction techniques have been developed in both cases and were also simulated. The results of these simulations show that the compensation achieved is indeed effective in both reducing and stabilising the instrumental polarization. In the case of the VLT, the SPHERE instrument has a dedicated setup at the entrance of the Nasmyth port, to compensate the polarization generated by the tertiary mirror (M3). This solution reduces the linear instrumental polarization from 1% to $10^{-3}\%$, keeping it stable for the complete range of rotation angles of the telescope, with respect to zenith. For the E-ELT, the solution consists on including a HWP before the non symmetric reflections on mirrors M4, M5 and M6, i.e. at the optically uncorrected intermediate focus of the telescope, that rotates the polarization coming from the sky while the polarization generated downstream (by M4, M5 and M6) remains unrotated. By subtracting two set of measurements with the HWP in the "neutral" and "rotated" positions the instrumental linear polarization, reaching values of 5%, is supressed, assuming that the time variations of the setup between these two set of measurements are negligible. Variations of several per cents in instrumental polarization during tracking will completely confound the polarimetric characterization of exoplanets, even after calibration at the $\sim 10\%$ relative level. Hence, minimization and stabilization of this instrumental polarization will be crucial to meet the science goals of EPICS. We will address the issues of calibratability in future work.

These two simulations show that, although instrumental polarization at the Nasmyth focus of telescopes can be a very important limitation when doing accurate polarimetry, it can be stabilised and reduced to levels completely within the required tolerances.

We also show ZIMPOL measurements of a laboratory setup simulating the M3-HWP1-M4 system. The measurements, taken with the polarization compensator out of the setup, showed a wavelength dependent polarization feature. The proposed explanation is the generation of polarized fringes by the FLC component on the modulation system of ZIMPOL. To test it, M&m's simulations of the system, including a weakly polarizing component as part of the FLC, were performed. The overall behaviour is well reproduced for all three Q, U and V Stokes components although the values are not exact. This is expectable since the details of the material and thickness of the different layers that compose the FLC are unknown. The values obtained by the simulation are the result of a fitting process of two parameters in the weakly polarizing matrix included in the FLC. The simulation differs from the measurements in less than $4 \cdot 10^{-3}$ for all Stokes Q, U and V with a particularly good agreement of an almost constant $2 \cdot 10^{-3}$ difference for Stokes Q.

Although further validation has to be carried out, the M&m's has been proven to be capable of performing realistic simulations of polarimetric systems and a useful tool for diagnosing and analyzing potential problems in the system. In further work, we will use the M&m's code to its full extent by adding error terms pertaining to all physical parameters in the VLT/SPHERE-ZIMPOL and E-ELT/EPICS-EPOL systems that may vary between calibration measurements and observations. Using such polarimetric error budgeting, we will be
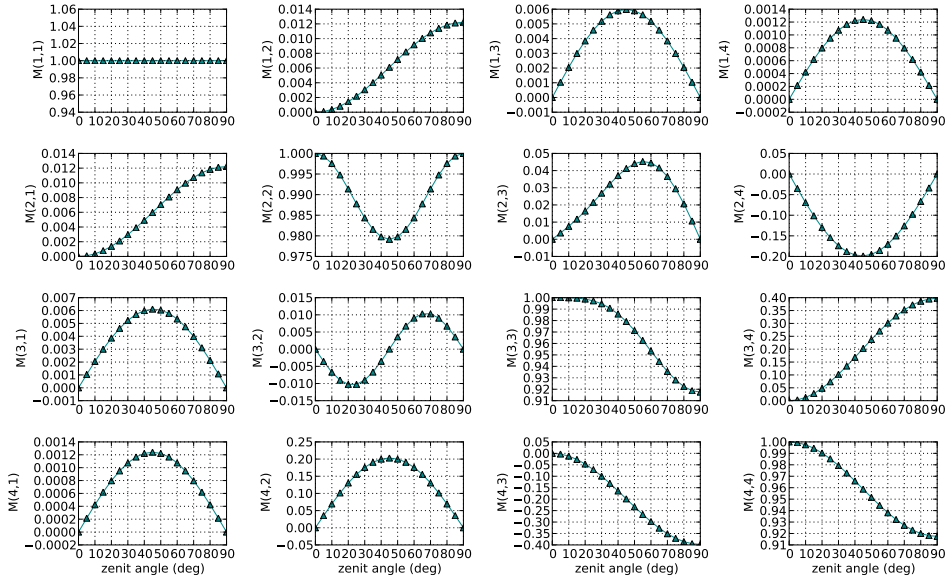
able to predict the limits of the instruments (in their various proposed configurations) to carry out spectropolarimetric characterization of exoplanets.
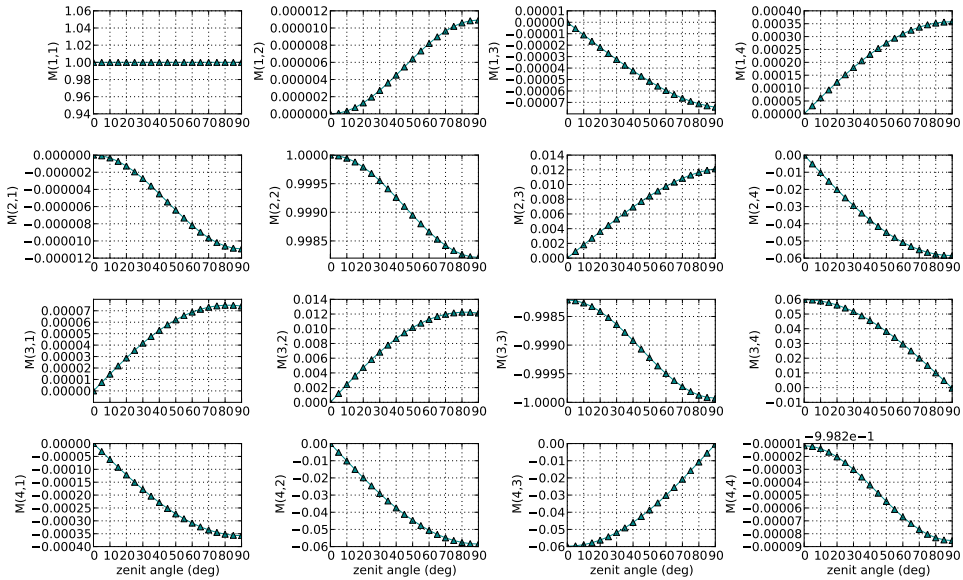
Aknowledgments

6.6   Appendix A: System matrices

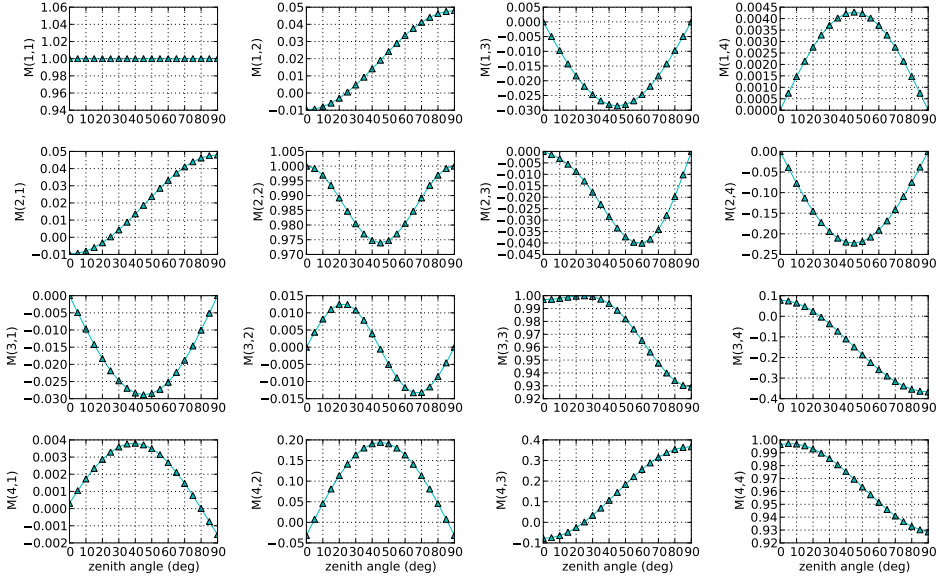M3-M4 matrix elements vs zenit angle for 650.0(nm)

(a)

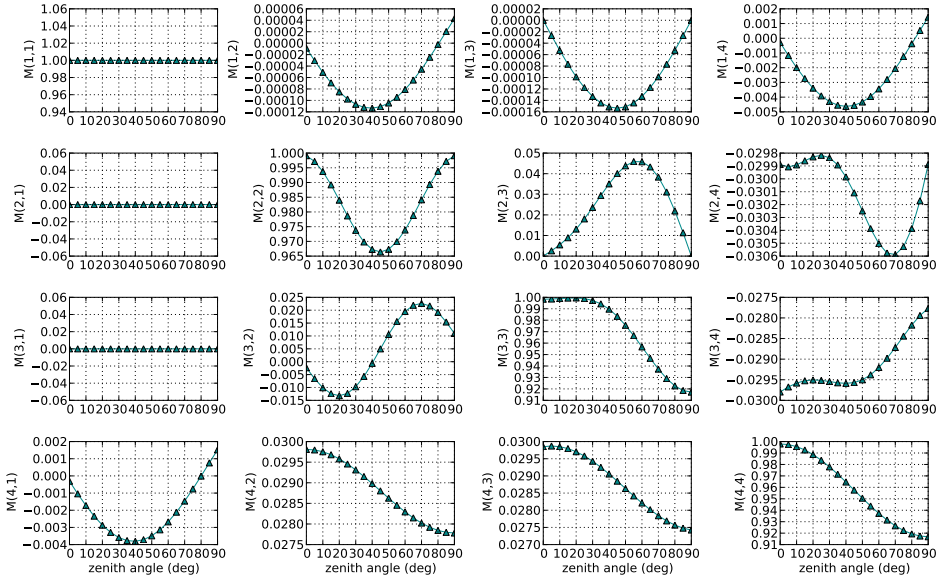M3-HWP1-M4 matrix elements vs zenit angle for 650.0(nm)

(b)

Figure 6.5: Resulting total Mueller matrix of the VLT system for the case of having M3 and M4 (a) and the compensating M3-HWP1-M4 setup (b).

EELT response matrix elements vs zenith angle for 650.0(nm)

(a)

EELT+IFhwp response matrix elements vs zenith angle for 650.0(nm)

(b)

Figure 6.6: Resulting response matrix of the E-ELT system for the case of having M4, M5 and M6 only (a) and the same system including a half-wave plate at the intermediate focus of the telescope (b).

Chapter 7

Instrumental Polarisation at the Nasmyth focus of the E-ELT

M. de Juan Ovelar, F. Snik, C. U. Keller and L. Venema.
Submitted to Astronomy & Astrophysics (2013)

Abstract

The ∼39-m European Extremely Large Telescope (E-ELT) will be the largest telescope ever built. This makes it particularly suitable for sensitive polarimetric observations, as polarimetry is a photon-starved technique. However, the telescope mirrors may severely limit the polarimetric accuracy of instruments on the Nasmyth platforms by creating instrumental polarisation and/or modifying the polarisation signal of the object. In this paper we characterise the polarisation effects of the two currently considered designs for the E-ELT Nasmyth ports as well as the effect of ageing of the mirrors. By means of the Mueller matrix formalism, we compute the response matrices of each mirror arrangement for a range of zenith angles and wavelengths. We then present two techniques to correct for these effects that require the addition of a modulating device at the "polarisation-free" intermediate focus that acts either as a switch or as a part of a two-stage modulator. We find that the values of instrumental polarisation, Stokes transmission reduction and cross-talk vary significantly with wavelength, and with pointing, for the lateral Nasmyth case, often exceeding the accuracy requirements for proposed polarimetric instruments. Realistic ageing effects of the mirrors after perfect calibration of these effects may cause polarimetric errors beyond the requirements. We show that the modulation approach with a polarimetric element located in the intermediate focus reduces the instrumental polarisation effects down to tolerable values, or even removes them altogether. The E-ELT will be suitable for sensitive and accurate polarimetry, provided frequent calibrations are carried out, or a dedicated polarimetric element is installed at the intermediate focus.

7.1   Introduction

The European Extremely Large Telescope (E-ELT) is a ~ 39-m optical/infrared telescope that will take ground-based astronomy to the next level (Delabre 2008, McPherson et al. 2012). Its more than $970\,\mathrm{m}^2$ of collecting area and unprecedented spatial resolving power will allow for revolutionary astronomical observations. Amongst the science goals of the E-ELT are the study of exoplanets and protoplanetary systems, high redshift galaxies and star formation processes (Hook et al. 2009, Liske et al. 2012). These fields are particularly demanding, observationally speaking, and will therefore benefit directly from the technological leap the E-ELT represents. However, photometry, spectrometry and imaging techniques will not be able to assess the complete spectrum of open questions without the help of polarimetry (see, e.g., Strassmeier & Others 2009).

The polarisation state of light retains information about the physical processes by which it is produced (e.g. magnetic fields, reflection and scattering, inherent asymmetries, etc, Tinbergen 1996, Clarke 2010, Snik & Keller 2013b). In addition, polarimetry boosts high contrast imaging techniques by suppressing the flux from the unpolarised central star while keeping the signal from the (polarised) scattering circumstellar matter. This makes it particularly suited for direct imaging and characterisation of exoplanets and the circumstellar discs in which they are born (see Seager et al. 2000, Stam et al. 2004, Stam 2008, de Kok et al. 2011, Hashimoto et al. 2011, Quanz et al. 2011, Quanz et al. 2012, Quanz et al. 2013b, Dong et al. 2012, Thalmann et al. 2013, Canovas et al. 2013, de Juan Ovelar et al. 2013, for some theoretical and observational examples).

Provided a proper instrument design, polarimetry and spectropolarimetry are techniques mainly limited in *sensitivity* (i.e., the noise level for the polarisation measurement, Snik & Keller 2013b) by the amount of photons collected. However, each element in the optical path can affect the polarisation state of the light coming from the astronomical source limiting the polarimetric *accuracy* (Snik & Keller 2013b). In terms of photon collecting power the E-ELT will be ideal for polarimetry. However, the configuration of the mirrors designed for the Nasmyth focus of this telescope is of particular complexity posing a challenge to perform accurate polarimetry at this location

The folding of light to the Nasmyth focus of telescopes is usually achieved by a $90°$ reflection on a mirror which generates linear (instrumental) polarisation (IP) signals of a few percent (e.g. up to a 5% at visible wavelengths Gehrels 1960, Cox 1976, Joos et al. 2008, van Harten et al. 2009, Perrin et al. 2010). Additionally, a fraction of the incoming linear polarisation is lost in the process due to conversion into circular polarisation, which is known as the "cross-talk" (CT) between linear and circular Stokes parameters. It is known that these instrumental effects can be corrected by further reflection on a second "twin" mirror positioned in a "crossed" configuration (Cox 1976). In the case of Nasmyth focus instruments, however, the mirror used to deflect the light rotates together with the telescope while the "crossed twin" usually remains fixed at the Nasmyth port causing this "crossed" configuration to only occur for certain positions of the telescope.

A retarding element positioned at the entrance of the Nasmyth port can be used to de-

rotate the polarisation such that it is always compensated by the "twin" mirror (Sanchez Almeida et al. 1995, Tinbergen 2007). This solution has been successfully applied to the design of ZIMPOL (see de Juan Ovelar et al. 2012a), the polarimeter of the VLT's planet finder SPHERE (Gisler et al. 2004, Stuik et al. 2005, Beuzit et al. 2006, Thalmann et al. 2008, Roelfsema et al. 2010, Schmid et al. 2010). In the particular case of the E-ELT, this solution is not applicable since the size of the light beam at this location is too large for the currently available high-quality retarders. Additionally, in the E-ELT the Nasmyth folding is achieved through consecutive reflection on a minimum of two and a maximum of three mirrors instead of one depending on the finally chosen design. To perform accurate polarimetry with the E-ELT it is therefore crucial to analyse the polarisation properties of the optical design and either correct for or calibrate any instrumental polarisation effects.

In this paper, we quantitatively characterise the polarisation properties of the two currently proposed Nasmyth optical designs of the E-ELT and analyse two techniques to reduce the instrumental effects. The study is organised as follows. In Section 7.2 we briefly describe the basics of our modeling approach while in Section 7.3 we describe the details of the simulations performed. Section 7.4 describes the results obtained and discusses an example of ageing effects on the mirrors after calibration and Section 7.5 describes the solutions proposed to correct for the instrumental effects found. Finally Section 7.6 presents a discussion of the results obtained and the conclusions of our study.

7.2   Modeling approach

We use the performance simulator for polarimetric systems code **M&m's** (de Juan Ovelar et al. 2011) to compute the instrumental polarisation effects generated in the optical path of the E-ELT telescope up to the Nasmyth focus. By means of the Mueller matrix formalism, the code calculates the polarisation properties of a given optical system as well as the effects of the measurement process followed.

In the this formalism the polarisation state of light is described by a 1×4 vector known as the Stokes vector, $\mathbf{S} = (I, Q, U, V)^T$, where I is the intensity, Q and U are linear polarisations in the $0/90°$ and $\pm 45°$ directions and V is circular polarisation (symbols in boldface denote matrices or vectors). The effect that an optical element has on the polarisation state of light passing through it, can be described as the product between the incoming Stokes vector ($\mathbf{S_{in}}$) and a 4×4 matrix that accounts for the polarisation properties of the element (i.e. a Mueller matrix $\mathbf{M}$),

$$\mathbf{S_{out}} = \mathbf{M_{element}}\mathbf{S_{in}} \,. \tag{7.1}$$

The same holds for an optical system composed of several elements,

$$\mathbf{S_{out}} = \mathbf{M_n} \cdot ...\mathbf{M_2} \cdot \mathbf{M_1} \cdot \mathbf{S}_{in} = \mathbf{M}_{total} \cdot \mathbf{S}_{in} \,, \tag{7.2}$$

where $\mathbf{M_n}...\mathbf{M_1}$ represent the Mueller matrices of the n elements of the optical system with 1 being the first element in the optical path and n being the last.

In order to measure the Stokes components the modulation and demodulation steps need to be included in the process. The first one consists of "encoding" the polarisation state of the incoming light in a set of intensity measurements that can be registered by the detector and is usually performed by two elements in the polarimeter: the modulator and the analyser. The former modifies the state of the incoming polarisation, while the latter acts as a polarisation *"filter"*. By changing the position of the modulator in particular steps (i.e. *modulation scheme*), one can control which polarisation (Q, U or V, or a linear combination thereof) passes through the analyser and is contained in the measured intensity ($I_{\mathrm{meas,i}}$, with i ranging from 1 to m and m being the total number of intensity measurements performed, as well as the positions/states of the modulator). This process can be described by the *"modulation matrix"* ($\mathbf{O}$) which then relates the incoming Stokes vector to the $1 \times m$ measured intensity vector ($\mathbf{I}_{\mathrm{meas}} = (I_1, I_2, \ldots, I_m)^{\mathrm{T}}$),

$$\mathbf{I}_{\mathrm{meas}} = \mathbf{O}\mathbf{S}_{\mathrm{in}} , \tag{7.3}$$

where each row in $\mathbf{O}$ is the first row of the $\mathbf{M}_{\mathrm{total}}$ matrix of the system at each modulation state m. Each component of the incoming Stokes vector can then be obtained from a linear combination of these m intensity measurements, a process that is known as demodulation,

$$\mathbf{S}_{\mathrm{meas}} = \mathbf{D}\mathbf{I}_{\mathrm{meas}} , \tag{7.4}$$

which yields the "measured" Stokes vector ($\mathbf{S}_{\mathrm{meas}}$).

The complete polarimetric measurement process (i.e. including optical system properties, modulation and demodulation steps) can then be represented by a matrix that is often known as the *"response matrix"* ($\mathbf{X}$, Ichimoto et al. 2008) which relates the incoming Stokes vector with the measured Stokes vector,

$$\mathbf{S_{meas}} = \mathbf{X}\mathbf{S_{in}} , \tag{7.5}$$

where $\mathbf{X} = \mathbf{D}\mathbf{O}$.

The response matrix is a 4×4 matrix that therefore includes the effect of both the optical system and the defined modulation/demodulation schemes. This makes it a powerful tool for diagnosing the impact of systematic effects on the polarimetric capabilities of any optical system accounting for the modulation/demodulation processes.

The results obtained in this study are presented in terms of the response matrix and to facilitate their analysis Eq. 7.6 shows the relation each of its element represents,

$$\mathbf{X} =$$

$$\begin{pmatrix}
I_{in} \to I_{\text{meas}} & Q_{in} \to I_{\text{meas}} & U_{in} \to I_{\text{meas}} & V_{in} \to I_{\text{meas}} \\
I_{in} \to Q_{\text{meas}} & Q_{in} \to Q_{\text{meas}} & U_{in} \to Q_{\text{meas}} & V_{in} \to Q_{\text{meas}} \\
I_{in} \to U_{\text{meas}} & Q_{in} \to U_{\text{meas}} & U_{in} \to U_{\text{meas}} & V_{in} \to U_{\text{meas}} \\
I_{in} \to V_{\text{meas}} & Q_{in} \to V_{\text{meas}} & U_{in} \to V_{\text{meas}} & V_{in} \to V_{\text{meas}}
\end{pmatrix}. \quad (7.6)$$

Diagonal elements represent the fractional transmission of a Stokes component throughout the measurement process. Elements in the first column ($I_{in} \to Q, U, V_{\text{meas}}$) give the polarisation that is generated by the system (IP). Elements relating $Q_{\text{in,meas}}$ and $U_{\text{in,meas}}$ are known as rotation while the ones relating $Q_{\text{in,meas}}$ or $U_{\text{in,meas}}$ with $V_{\text{in,meas}}$ give the crosstalk (CT). In presenting our results, we analyse the CT focusing on elements $X_{3,2}$, $X_{4,2}$ and $X_{4,3}$.

Provided a set of optical elements and the modulation/demodulation schemes, the **M&m's** code computes all Mueller matrices of the elements and generates the $\mathbf{M}_{\text{total}}$, $\mathbf{O}$, $\mathbf{D}$ and $\mathbf{X}$ of the system. In obtaining $\mathbf{X}$ the code either computes $\mathbf{D}$ as the inverse or pseudo-inverse of $\mathbf{O}$, depending on the particular case (del Toro Iniesta & Collados 2000), or requires the user to specify it. In the simulations presented in this study we define the demodulation matrix such that it corresponds to an ideal polarimeter. The reason for this is that our aim is to model the behaviour inherent to the optical arrangement and the impact the modulation has on it and not the behaviour of the polarimeter. In this way, the matrix $\mathbf{O}$ includes the realistic behaviour of the elements in the optical system while $\mathbf{D}$ is only computed for the ideal polarimeter. This will cause the response matrix to show the behaviour of the optical system including the modulation scheme but not any effects from the polarimeter.

Some other considerations regarding our simulations are

1. The dispersion of the index of refraction with wavelength is included for all materials used. However, for the thin amorphous alumina layer on top of the mirrors a constant value of n=1.6 was assumed, which is an approximation of the value in the studied region ($[500 - 900]$ nm, Eriksson et al. 1981).

2. Unless explicitly noted, all mirrors have the same characteristics, i.e. no differential effects are included.

3. Whenever available, real material characteristics and design parameters are used to describe optical elements.

4. The Mueller matrices have only been established for the chief ray and therefore the center of the field of view.

5. Only ideal Mueller matrices are taken into account, i.e. deviations from the characteristic values of the parameters of optical elements are not included.
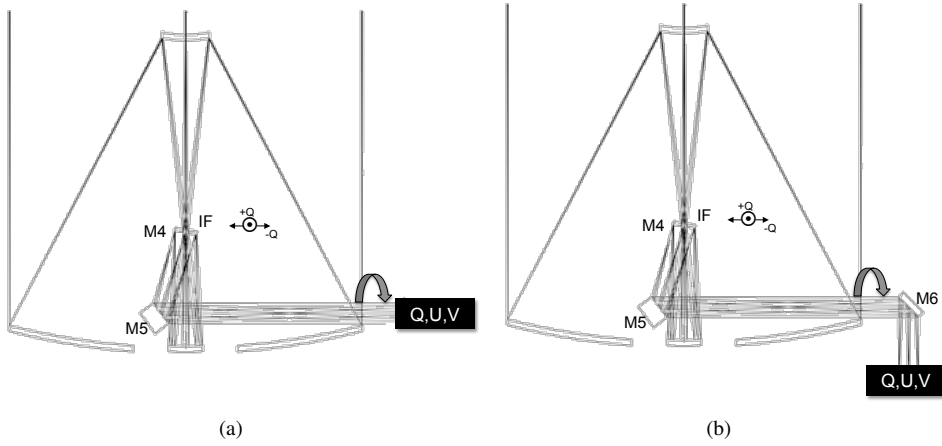
Figure 7.1: Mirror arrangements considered for the E-ELT Nasmyth configuration with mirrors and intermediate focus (IF) of the telescope marked. (a) *Straight-through* configuration, with the Nasmyth focus directly after the fifth reflection. (b) *Lateral* configuration, with a sixth mirror fixed in the Nasmyth port. The Q, U, V box represents a perfect full-Stokes polarimeter at the corresponding Nasmyth focus. The rotation axis of the telescope and the $\pm Q$ directions at the intermediate focus position are indicated. Adapted from Delabre (2008).

6. The efficiency of the detector is assumed to be perfect.

7. We quantify polarisation effects that can be described with Mueller matrices. We therefore disregard polarisation effects that may be brought about by, e.g., (residual) seeing, differential aberrations, or diffraction effects. As such, the results presented here are for the average of the point spread function (PSF) of the telescope (Sanchez Almeida & Martinez Pillet 1992)

7.3   E-ELT Nasmyth configurations.

Figure 7.1 shows the positions of the E-ELT mirrors in the two Nasmyth configurations considered by the current optical design. In the first one (Fig. 7.1(a)), *straight-through* hereafter, the light is sent to the Nasmyth focus after reflection on the five mirrors fixed to the telescope. These mirrors, therefore, rotate with the zenith angle around the Nasmyth ports as the telescope tracks. The second set up considered, *lateral* hereafter, adds a sixth mirror fixed at the Nasmyth port (Fig. 7.1(b)). The first three mirrors (M1, M2 and M3) are rotationally symmetric, which makes their contribution to the instrumental polarisation effects negligible (Sanchez Almeida & Martinez Pillet 1992). Moreover, we computed the average polarised point spread function (PSF) of the combination of M1, M2 and M3, including the effect of

TABLE 7.1: MODULATION SCHEME FOR E-ELT *straight-through* AND *lateral* CONFIGURATIONS

Modulation state	QWP[1]	HWP[1]	Measured Stokes component	
m	(°)	(°)	*straight-through*	*lateral*
1	out	0	Q	Q
2	out	45	$-Q$	$-Q$
3	out	22.5	$-U$	$-U$
4	out	67.5	U	U
5	45	0	$-V$	V
6	45	45	V	$-V$

[1] QWP and HWP columns show the angle between the fast axis of the wave-plates and the axis of the analyser.

the segments of M1, and found that even if one of the 798 segments is missing in the outer ring, the IP due to M1 is smaller than $\sim 0.003/798 \approx 10^{-6}$. Therefore, we only consider the effect of mirrors [M4,M5] or [M4, M5, M6] when simulating the *straight-through* and *lateral* arrangements respectively. All mirrors are made out of aluminum (index of refraction obtained from Rakic 1995) and have a $4\,\mathrm{nm}$ Al_2O_3 layer adopted from the measurements of van Harten et al. (2009). Mirrors M4, M5 and M6 have incidence angles of $8.5°$, $36.5°$ and $45°$ respectively. We consider a range of telescope zenith angles of $z = [0\text{ - }90]\,\mathrm{deg}$ and wavelengths of $\lambda = [500\text{ - }900]\,\mathrm{nm}$, and a temperature of $T = 10°C$.

We define the reference system to be fixed to the telescope which is equivalent to having the instrument physically co-rotating at the Nasmyth port (e.g. pupil tracking), implementing a half-wave plate in the instrument that converts the coordinate system of the telescope to the local one, or de-rotating the data obtained during the data reduction. The $+Q$ direction is defined as being aligned with the $s-$ direction of mirror M4, see Fig. 7.2. With the $+Q$ direction as a reference, the Stokes $+U$ direction is defined to be rotated clockwise by $45°$ and Stokes $+V$ is defined to be rotating counterclockwise[1], as we look into the direction of propagation of the light.

The total Mueller matrices of both optical arrangements are then computed by the code as:

$$\mathbf{M}_{straight\text{-}through} = \mathbf{M_{M5}}\mathbf{M_{M4}}\,, \tag{7.7}$$

---

[1] We determine the rotation of V by following the rotation of the electric field vector in a plane fixed at a position (Hecht 2001)

and

$$\mathbf{M}_{lateral} = \mathbf{R(z)M_{M6}R(z)M_{M5}M_{M4}} \,, \tag{7.8}$$

where $\mathbf{M}$ stands for Mueller matrices of mirrors and $\mathbf{R}$ for Mueller matrices of rotations.

To simulate the ideal polarimeter we implement a perfect modulator using perfect half-wave and quarter-wave plates (HWP and QWP) to measure Stokes Q, U and V, respectively. The HWP rotates the direction of the incoming linear polarisation with respect to its *fast axis*. The QWP transforms circular polarisation into linear polarisation depending also on the orientation of its fast axis. The QWP is therefore included in our simulations only for the modulation states where we want to measure V. The analyser is a perfect polariser aligned with the $+Q$ direction of the (rotating) reference system.

We then specify a six-step modulation scheme to encode the Q, U and V Stokes components and an (ideal) demodulation matrix that recovers them. While the modulation scheme can be used for both configurations of the E-ELT considered here, the demodulation matrix has to be designed specifically for each case since the additional mirror has an effect on how the Stokes components are encoded. Table 7.1 shows the modulation scheme used and the Stokes component that each modulation state encodes for the two setups simulated.

Finally, we consider the following requirements for each element of the response matrix, based on those set for the high-contrast imaging polarimeter E-ELT/EPICS-EPOL (Keller et al. 2010):

- linear IP (i.e. $I \rightarrow Q, U$) $< 0.1\%$;

- transmission of linear polarisation (i.e. $Q \rightarrow Q$ and $U \rightarrow U$) $> 95\%$;

and high-resolution spectropolarimeters such as ESPaDOns and HARPSpol (Barrick et al. 2010, Snik et al. 2011)

- cross-talk ($Q, U \leftrightarrow V$) $< 1\%$.

7.4 Response matrices of the E-ELT Nasmyth configurations and effect of mirror ageing

7.4.1 Response matrices

Figure 7.2 shows the response matrix for the two arrangements studied, normalised to the measured intensity (i.e. element $X_{1,1}$), as a function of the zenith angle of the telescope. Solid and dashed lines correspond to the *lateral* and *straight-through* configurations, respectively, while plus and cross markers denote wavelengths of $\lambda = [550, 850]$ nm, the approximated limits of the wavelength range studied. The light-green areas represent the range of values of each element that falls inside the requirements defined above. Note that, in this particular cases, the modulation scheme is such that, when using the ideal demodulation matrix, the response matrix $\mathbf{X}$ coincides with the Mueller matrix of the systems.
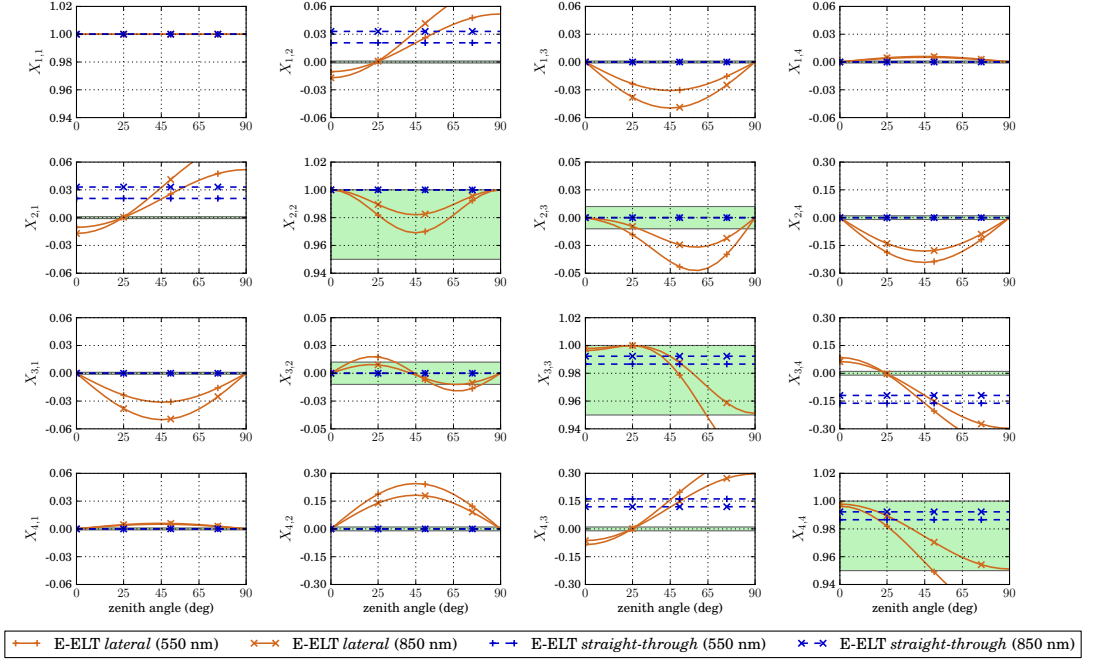
Figure 7.2: Normalised response matrices (**X**) versus zenith angle (z) obtained for the E-ELT's two Nasmyth configurations considered and for the approximated limits of the wavelength range studied ($\lambda = [550, 850]$ nm). Solid and dashed lines correspond to the *lateral* and *straight-through* configurations, respectively. Plus and cross markers denote wavelengths of $\lambda = [550, 850]$ nm, respectively. The light-green area represent the range of values inside the requirements adopted in this study (see Section 7.3)

1. *Straight-through* Nasmyth configuration:
   M4-M5-Nasmyth focus

   Dashed blue lines in Fig. 7.2 show the values of the elements of the response matrix in this configuration. Here, the reference system is fixed to the telescope because mirrors M4 and M5 rotate together with it. This causes the response matrix to be independent of the zenith angle. This reference system can easily be implemented in any instrument by e.g. making the instrument co-rotate with the telescope, placing a retarding element before the instrument capable to de-rotate de polarization, or de-rotating via the data reduction.

   In terms of instrumental polarisation (elements $X_{1,2}$, $X_{1,3}$, $X_{1,4}$) only Stokes Q is generated by this system (element $X_{1,2}$) with values in the range of $\sim [2-3.4]\%$ depending

on the wavelength. These values fall well out of the requirements (light-green area).

Because the polarimeter is aligned with the Q direction of the system and it rotates together with the telescope, Stokes Q is transmitted without loss throughout the measurements process (element $X_{2,2}$). The transmission of Stokes U and V ($X_{3,3}$ and $X_{4,4}$) varies depending on the wavelength well within the requirements defined for these elements.

Cross-talk here only occurs between linearly polarised light in the U direction and circularly polarised light V ($X_{4,3}$), with values in the range of $\sim [12-16]\%$, outside of the 1% required.

2. *Lateral* configuration:
   M4-M5-M6-Nasmyth focus

   Solid yellow lines in Fig. 7.2 show now the values of the elements of the response matrix in the *lateral* configuration, again with plus and cross markers denoting values for wavelengths of $\lambda = [550, 850]$ nm, respectively. The configuration includes now one more mirror (M6) fixed in the Nasmyth platform. Since the reference system is fixed with respect to the telescope (i.e. moves together with M4 and M5), the system behaves *"as if"* M6 would be rotating with the zenith angle, which introduces a dependency of the response matrix with the zenith angle.

   Both linear and circular instrumental polarisation are now generated and vary with the zenith angle. Stokes Q remains outside the specifications for all zenith angles other than $z = 25°$ (element $X_{1,2}$). Whereas in the case of Stokes U and V, the requirements are only met at angles of $z = [0, 90]°$ (elements $X_{1,3}$ and $X_{1,4}$).

   Transmission of all Stokes components (diagonal elements) remains within the requirements except for the case of U and V at long wavelengths and for zenith angles larger than $z > 65°$ (elements $X_{3,3}$, $X_{4,4}$).

   Here, the cross-talk takes place between both Stokes Q and U and Stokes V, and it varies with the zenith angle. In the first case(element $X_{4,2}$) the values fall only inside the requirements for zenith angles of $z = [0, 90]°$. In the case of cross-talk between U and V ($X_{4,3}$) that only happens for $z = 25°$.

7.4.2   Effect of ageing of mirrors after calibration

It is clear that the E-ELT mirrors produce instrumental polarisation effects that are in many cases considerably outside of the requirements set. The first question to answer is whether these effects can be calibrated to the required accuracy. A comprehensive simulation of calibration procedures is beyond the scope of this paper. However, for a first estimate of the calibrability, we can compute the impact that variation on mirror properties have on the response matrix.
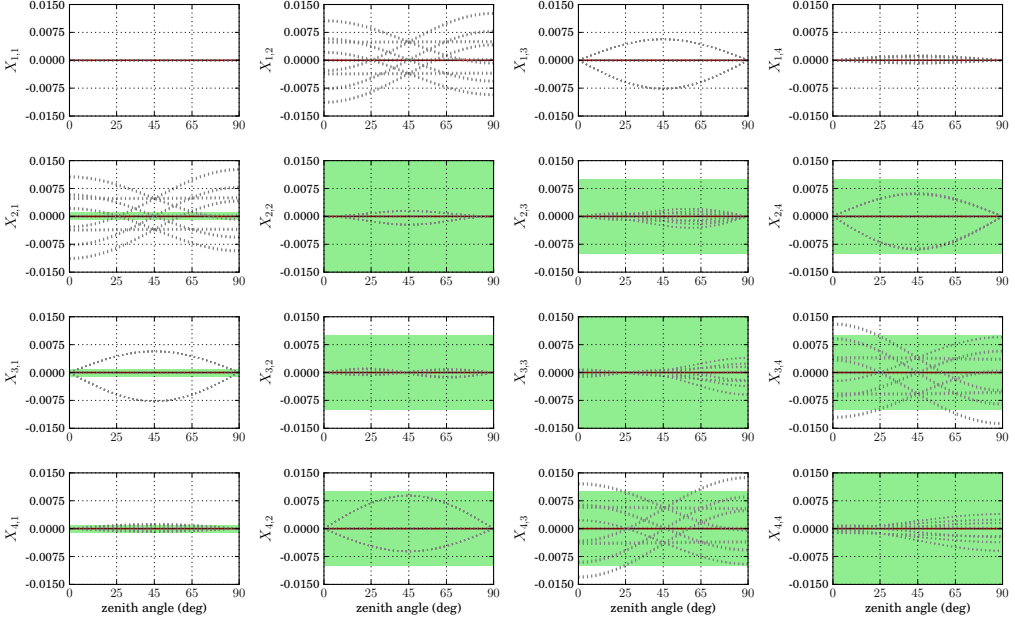
Figure 7.3: Variations of the response matrix of the lateral Nasmyth case due to uncalibrated variations of mirror properties. Solid red line shows the values for the elements after calibration at $\lambda = 650$ nm, and dotted grey lines the deviations caused by the ageing. The areas shaded in green represent the requirements for polarimetric accuracy (See Section 7.1).

For this exercise, we use the *lateral* Nasmyth configuration and assume a perfect calibration of the instrumental effects found. We then vary the properties of M4, M5 and M6 such that it mimics the effects of ageing and mirror pollution, which are the major contributors to the variation of the polarisation properties of telescope mirrors. To this aim we 1) vary the effective thickness of the dielectric layer on the mirror (d_f) by $1\,\mathrm{nm}$, corresponding to a decrease in mirror reflectivity of $\sim 10\%$ due to the build-up of dust and grime on top of the mirrors, and 2) we vary the absorption term for the mirrors ($\mathrm{Im}(n_m)$) by 10%, to represent ageing effects (Joos et al. 2008). The variation of these two parameters are positively correlated (Snik & Keller 2013a). We assume that these variations are independent for M4, M5 and M6, and can go in both directions as mirror cleaning or recoating can take place before or after the calibration.

Fig. 7.3 presents the deviations upon the $\mathbf{X}$ matrix in the lateral Nasmyth case for all cases of variations of mirror properties after perfect calibration has taken place. These uncalibrated effects alone make system fall out of the requirements in the case of linear IP and CT between U and V. As these results show, frequent calibrations need to take place for polarimetric E-

ELT instruments to operate within requirements and even in this case, current state of the art calibration methods are still far from the perfect calibration assumotion we have used here (Skumanich et al. 1997, Beck et al. 2005, Ichimoto et al. 2008, Selbing 2010, Socas-Navarro et al. 2011, Harrington et al. 2011, Schou et al. 2012).

7.5   Correction of the instrumental effects: *switch* and *two-stage modulation* techniques

A method for correcting the instrumental effects has to modify the response matrix of the system which, as explained in Section 7.2, depends on the Mueller matrix of the optical system and on the modulation/demodulation process. The correction, therefore, can be achieved either modifying the instrument, e.g. adding elements in the light path that compensate the polarisation effects or adapting the polarisation modulation, or any combination of both.

The first approach is, mathematically speaking, equivalent to intrinsically modifying the Mueller matrix of the optical system. In the second one, additional modulation steps are introduced to separate the instrumental polarisation effects from the source polarisation, and consecutively be minimized with an additional, differential measurement.

In this section we present two techniques of the second type, the *switch* and *2-stage modulation* techniques. We apply them to the correction of the instrumental effects generated on the E-ELT *lateral* configuration, found to be the least optimal for performing accurate polarimetry. In both cases, retarding elements are placed in the intermediate focus of the telescope (see below) to modify the modulation scheme. To fully characterize the effect of these elements in the measurement process, they are always simulated as realistic wave-plates, while the retarders used for the polarimeter are still simulated as ideal elements. The **D** matrix is still computed for an ideal polarimeter.

7.5.1   The *switch* technique

The *switch* technique is a simple modulation-related technique to apply (Tinbergen 1996, Stuik et al. 2005). The idea is to implement a rotatable wave-plate as early in the light path as possible to "switch" the sign of the incoming polarisation while keeping the instrumental effects, generated downstream, fixed. In the case of the E-ELT, this element could be installed in the intermediate focus (IF) of the telescope (see Figure 7.1). Light passes through this IF on its way from M2 to M3 and therefore, before reaching M4, which makes this focus "polarisation-free". This wave-plate, the *switch* hereafter, rotates the direction of the either linear or circular polarisation coming from the sky and the telescope up to this point (i.e. sky-M1-M2-M3), alternatively between two orthogonal positions, thus changing its sign. However, the polarisation generated along the optical path of the telescope below (i.e. M4-M5-M6) remains unrotated. By taking two sets of measurements with the *switch* in these two positions and subtracting them, one can ideally suppress most of the instrumental polarisation generated in the Q and U directions.

TABLE 7.2: MODULATION SCHEME FOR E-ELT *lateral* CONFIGURATION (M4-M5-M6) +
IF-SWITCH

Modulation state	HWPif[1]	QWP[1]	HWP[1]	Measured Stokes component
m	(°)	(°)	(°)	
1	0	out	0	Q
2	0	out	45	-Q
3	0	out	22.5	-U
4	0	out	67.5	U
5	0	45	0	-V
6	0	45	45	V
7	45	out	0	-Q
8	45	out	45	Q
9	45	out	22.5	U
10	45	out	67.5	-U
11	45	45	0	-V
12	45	45	45	V

[1], HWPif, QWP and HWP columns show the angle between the fast axis of the wave-plates and the defined $+Q$ axis.

A potential disadvantage of this technique comes from the fact that the two measurements are taken with a delay in time. If the measurements are separated in time they might end up being slightly different and the subtraction is not perfect anymore. Therefore, the technique benefits from a rapid switching/modulation duty cycle.

To show how this arrangement would correct the linear IP in the *lateral* case, we simulate the *IFswitch* with a HWP at the intermediate focus (HWPif) rotating between $0/45°$ and therefore correcting the instrumental polarisation generated in the Q direction. Table 7.2 shows the resulting modulation scheme. This element is simulated using realistic specifications of an achromatic HWP. The element is composed of two crossed birefringent plates made of quartz and magnesium fluoride (MgF_2) with thicknesses $t_{quartz} = 841.2\,\mu m$ and $t_{MgF_2} = 674.8\,\mu m$. These two plates together comprise an achromatic HWP with a working range of $\lambda = 500 - 900\,nm$ centered at $\lambda = 650\,nm$. Refractive indices for quartz and magnesium fluoride were obtained from Ghosh (1999) and Bass et al. (2009), respectively.

The wavelength range of the HWP is the limiting factor of this solution since, any deviation from a perfect half-wave plate will affect the switching performance. Table 7.2, shows the positions of all elements involved in the modulation.

TABLE 7.3: MODULATION SCHEME FOR E-ELT *lateral* CONFIGURATION (M4-M5-M6) + 2-STAGE MODULATION

Modulation state m	HWPif[1] (°)	QWPif[1] (°)	HWP[1] (°)	Measured Stokes component
1	0	out	0	Q
2	0	out	45	-Q
3	22.5	out	0	U
4	22.5	out	45	-U
5	45	out	0	-Q
6	45	out	45	Q
7	67.5	out	0	-U
8	67.5	out	45	U
9	out	45	0	V
10	out	45	45	-V
11	out	-45	0	-V
12	out	-45	45	V

[1] HWPif, QWPif and HWP columns show the angle between the fast axis of the wave-plates and the defined $+Q$ axis.

7.5.2   The *2-stage modulation* technique

The *switch* technique solves the issue of the polarisation generated in the system for either linear or circular polarisation (not both). However, the same principle can be taken further to develop a *2-stage modulation* technique. In this case, a full-blown polarisation modulator is located in a "polarisation-free" location upstream (in this case, again, the IF of the E-ELT). This modulator converts the measureable polarisation into a polarisation state that is mostly or fully transmitted by the optical system behind it, known as the "eigen-vector" of the system (Lopez Ariste & Semel 2011, Snik & Keller 2013b). For relatively simple cases, this eigen-vector is linear polarisation, e.g. $+Q$ for the straight-through Nasmyth port case. In general, this eigen-vector is elliptical, and varies with the instrument configuration, e.g. the pointing in the lateral Nasmyth case.

We apply such a two-stage modulator for the E-ELTe placing a modulator in the IF that consists of two achromatic wave plates: HWPif and QWPif. The QWPif is implemented in the same way as the HWPif of subsection 7.5.1 by modifying the thicknesses of the two layers, $t_{quartz} = 421.1\,\mu$m and $t_{MgF_2} = 337.8\,\mu$m, to make it a quarter-wave plate. These plates (HWPif and QWPif) are used to modulate Q, U and V in a classical way by sequen-
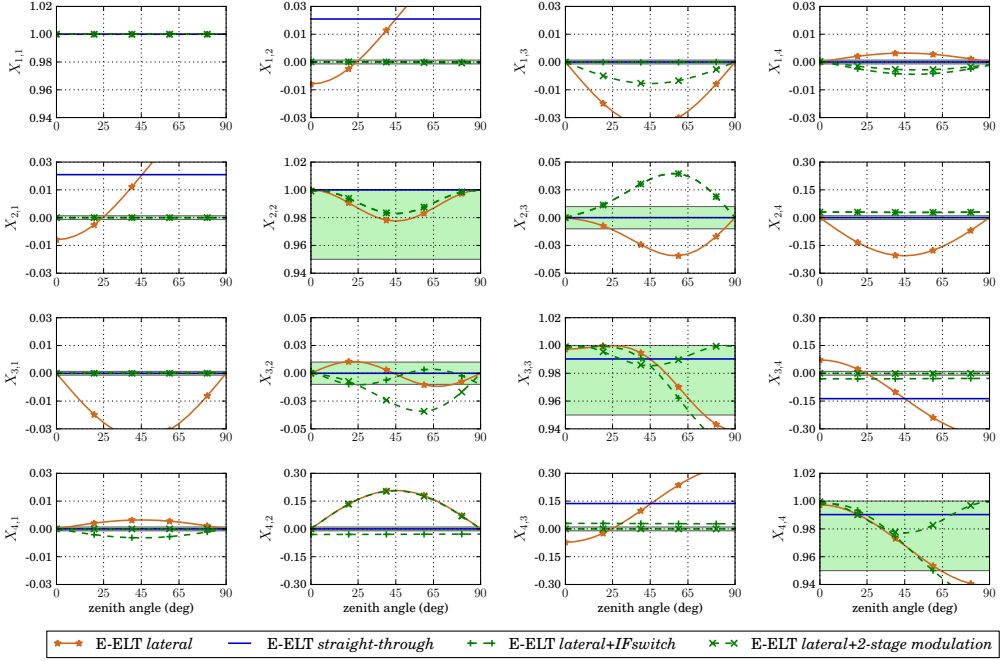
Figure 7.4: Normalised response matrices ($\mathbf{X}$) versus zenith angle (z) obtained for the four configurations simulated at $\lambda = 650$ nm. Solid, dotted-dashed, dotted and dasehd lines correspond to the *lateral*, *straight-through*, *straight-through+IFswitch* and *lateral+IFswitch* configurations.

tially converting those polarisation states into Q. This direction is not an eigen-vector for the lateral Nasmyth case, but it comes sufficiently close. The polarimeter on the Nasmyth platform now only measures Stokes Q, which allows for a much faster duty cycle than the first modulator in the IF. Table 7.3 shows the position of the elements for this modulation scheme.

7.5.3 Corrected response matrix

Figure 7.4 shows a comparison of the four configurations analysed in this study, i.e. E-ELT *lateral*, E-ELT *straight-through*, E-ELT *lateral+IFswitch* and E-ELT *lateral+2-stage modulation*. The elements of the four response matrices are shown for a fixed wavelength of $\lambda = 650$ nm, which is the centre of the wavelength range studied. Solid lines correspond to the original *straight-through* and *lateral* matrices (blue unmarked and yellow star-marked, respectively) while dashed green lines correspond to the corrected ones, with plus and cross markers denoting values for *lateral+IFswitch* and *lateral+2-stage modulation*, respectively.

Linear IP is completely suppressed by the two methods (elements $X_{1,2}$, and $X_{1,3}$) while circular IP is only compensated for in the *lateral+2-stage modulation* case. The CT between Q and V is improved only in the *lateral+IFswitch* solution while that taking place between U and V is significantly improved in this same case and completely corrected for in the *lateral+2-stage modulation* arrangement. This technique also improves considerably the transmission of all Stokes vectors while the *lateral+IFswitch* only meet the requirements for zenith angles of $z \leq 65$. The rotation element, $X_{3,2}$, presents, however, a much worse behaviour for the *lateral+2-stage modulation* case.

7.6   Discussion and conclusions

The results shown in Fig. 7.2 show that, according to the requirements set, none of the two Nasmyth configurations being considered for the E-ELT are suitable for performing accurate polarimetry. However, the instrumental effects generated in the *straight-through* configuration, i.e. IP in the Q direction and CT between U and V, are at least independent of the pointing of the telescope when adopting a coordinate system that co-rotates with the telescope which makes it relatively easy to correct for (e.g., using a tilted glass plate to compensate the IP).

Depending on the science requirements, calibration can be a good enough solution to the problem. However, the time required to perform calibration measurements for polarimetry is considerably long due to the fact that photometric and polarimetric measurements are needed as well as a similar signal to noise ratio in both the science and calibration observations. As an example, in current polarimetric observations of circumstellar environments, up to a 50% of the observing time can be lost between calibration with polarimetric standard stars and overheads.

The frequency with which calibration measurements have to be performed is also an important parameter to account for since, as shown in Section 7.4.2, small variations of parameters of the optical elements can quickly impact the quality of the measurements.

It is in the light of this conclusion that we propose alternative solutions based on extended modulation approaches to correct for the instrumental effects. The *switch* and *two-stage* modulation techniques are applied to the *lateral* Nasmyth configuration and their response matrices computed for the same range of zenith angles and wavelengths considered before. Figure 7.4 shows how most of the instrumental effects are stabilised and/or corrected for. In general, the *switch* technique works very well for systems that are focused on the measurement of linear polarisation while the *2-stage modulation* has the potential of taking care of circular polarisation issues as well. An additional advantage of the latter implementation is the better response of the system to the measurement of U (see element $X_{3,3}$ of Fig. 7.4) In short, the *2-stage modulation* improves the efficiency of the polarimeter by tuning the eigenvector of the system to the Stokes component that is being measured. This, in the framework of our simulations, comes at the price of increasing the rotation between Q and U and the CT between Q and V. However, it is important to remark that our modulation scheme is just an example and that different modulation schemes can be optimised to compensate for the

particular instrumental effects a given observation has to deal with.

These effective and versatile techniques require the addition of retarding elements to the optical path of the telescope which, considering the already complex optical design of the E-ELT, may be a disadvantage. However they also have the advantage of decreasing the calibration time required. The retarding elements used in the cases presented in this study also introduce a higher dependency of the values of the response matrix with wavelength, although this depends strongly on the design of the retarder/s and, in principle, it is feasible to taylor them to suit the requirements of a particular case.

In summary, the E-ELT poses considerable challenges to performing accurate polarimetry, but with the current state of polarimetric techniques it is definitely possible to achieve this goal.

Acknowledgements

Bibliography

Acke, B. & van den Ancker, M. E. 2006, Astron. Astrophys., 449, 267 (cited on page 72)

Adams, F. C. 2010, Annu. Rev. Astron. Astrophys., 48, 47 (cited on pages 78 and 83)

Adams, F. C., Hollenbach, D., Laughlin, G., & Gorti, U. 2004, Astrophys. J., 611, 360 (cited on pages 13 and 78)

Adams, F. C., Proszkow, E. M., Fatuzzo, M., & Myers, P. C. 2006, Astrophys. J., 641, 504 (cited on pages 13 and 78)

Aitken, D. K. & Hough, J. H. 2001, Pub. Astron. Soc. Pacific, 113, 1300 (cited on page 117)

Alexander, R. 2013, ArXiv e-prints (cited on pages 10 and 12)

Alexander, R. D. & Armitage, P. J. 2007, MNRAS, 375, 500 (cited on page 11)

Alexander, R. D., Clarke, C. J., & Pringle, J. E. 2006, MNRAS, 369, 216 (cited on page 12)

Amara, A. & Quanz, S. P. 2012, MNRAS, 427, 948 (cited on pages 30 and 41)

Andrews, S. M. & Williams, J. P. 2005, Astrophys. J., 631, 1134 (cited on page 89)

Andrews, S. M., Wilner, D. J., Espaillat, C., et al. 2011, Astrophys. J., 732, 42 (cited on pages 12 and 54)

Artymowicz, P. & Lubow, S. H. 1994, Astrophys. J., 421, 651 (cited on page 80)

Ataiee, S., Pinilla, P., Zsom, A., et al. 2013, Astron. Astrophys., 553, L3 (cited on page 57)

Baglin, A., Auvergne, M., Barge, P., et al. 2006, in ESA Special Publication, Vol. 1306, ESA Special Publication, ed. M. Fridlund, A. Baglin, J. Lochard, & L. Conroy, 33 (cited on page 1)

Bagnulo, S., Landolfi, M., Landstreet, J. D., et al. 2009, PASP, 121, 993 (cited on pages 8, 32, and 39)

Barman, T. S., Macintosh, B., Konopacky, Q. M., & Marois, C. 2011, Astrophys. J., 733, 65 (cited on pages 2, 15, and 30)

Barrick, G., Benedict, T., & Sabin, D. 2010, in Society of Photo-Optical Instrumentation Engineers (SPIE) Conference Series, Vol. 7735 (cited on page 134)

Baruteau, C. & Masset, F. 2013, in Lecture Notes in Physics, Berlin Springer Verlag, ed. J. Souchay, S. Mathis, & T. Tokieda, Vol. 861, 201 (cited on page 10)

Baruteau, C., Meru, F., & Paardekooper, S. J. 2011, MNRAS, 416, 1971 (cited on page 10)

Bass, M., DeCusatis, C., Enoch, J., et al. 2009, Handbook of Optics, Third Edition Volume IV: Optical Properties of Materials, Nonlinear Optics, Quantum Optics (set), Handbook of Optics (McGraw-Hill Education) (cited on page 139)

Bastian, N., Gieles, M., Goodwin, S. P., et al. 2008, MNRAS, 389, 223 (cited on page 83)

Basu, S. 1998, Astrophys. J., 509, 229 (cited on page 80)

Bate, M. R. 2012, MNRAS, 419, 3115 (cited on page 78)

Beck, C., Schlichenmaier, R., Collados, M., Rubio, L. B., & Kentischer, T. 2005, Astron. Astrophys., 443, 1047 (cited on page 138)

Begemann, B., Dorschner, J., Henning, T., Mutschke, H., & Thamm, E. 1994, Astrophys. J. Lett., 423, L71 (cited on page 58)

Bell, C. P. M., Naylor, T., Mayne, N. J., Jeffries, R. D., & Littlefair, S. P. 2013, MNRAS, 434, 806 (cited on page 12)

Beuzit, J.-L., Feldt, M., Dohlen, K., et al. 2006, The Messenger, 125, 29 (cited on pages 21, 31, 59, 112, and 129)

Bihain, G., Rebolo, R., Zapatero Osorio, M. R., et al. 2009, Astron. Astrophys., 506, 1169 (cited on page 83)

Binney, J. & Tremaine, S. 1987, Galactic dynamics (Princeton, NJ, Princeton University Press, 1987, 747 pp.) (cited on pages 78, 80, and 87)

Birnstiel, T., Dullemond, C. P., & Brauer, F. 2010, Astron. Astrophys., 513, A79 (cited on pages 12, 17, 54, 57, and 74)

Birnstiel, T., Dullemond, C. P., & Pinilla, P. 2013, Astron. Astrophys., 550 (cited on page 11)

Blum, J. 2010, Research in Astronomy and Astrophysics, 10, 1199 (cited on page 78)

Boger, J. K., Stokes, S. D., Bowers, D. L., Ratliff, B. M., & Fetrow, M. P. 2003, Proc. SPIE, 5158, 113 (cited on page 94)

Bohren, C. F. & Huffman, D. R. 1983, Absorption and scattering of light by small particles (Wiley) (cited on pages 4 and 5)

Bonnell, I. A., Smith, K. W., Davies, M. B., & Horne, K. 2001, MNRAS, 322, 859 (cited on pages 13, 78, and 83)

Borucki, W. J., Koch, D. G., Basri, G., et al. 2011, Astrophys. J., 736, 19 (cited on pages 15, 78, and 82)

Boss, A. P. 1997, Science, 276, 1836 (cited on page 10)

Bowler, B. P., Liu, M. C., Dupuy, T. J., & Cushing, M. C. 2010, Astrophys. J., 723, 850 (cited on pages 2, 15, and 30)

Brandt, T. D., McElwain, M. W., Turner, E. L., et al. 2013, Astrophys. J., 764, 183 (cited on page 59)

Brasser, R., Morbidelli, A., Gomes, R., Tsiganis, K., & Levison, H. F. 2009, Astron. Astrophys., 507, 1053 (cited on pages 12 and 78)

Brauer, F., Dullemond, C. P., & Henning, T. 2008, Astron. Astrophys., 480, 859 (cited on pages 10 and 11)

Brauer, F., Dullemond, C. P., & Henning, T. 2008, Astron. Astrophys., 480, 859 (cited on pages 12, 54, and 69)

Bressert, E., Bastian, N., Gutermuth, R., et al. 2010, MNRAS, 409, L54 (cited on page 86)

Calvet, N., D'Alessio, P., Hartmann, L., et al. 2002, Astrophys. J., 568, 1008 (cited on page 12)

Calvet, N., D'Alessio, P., Watson, D. M., et al. 2005, Astrophys. J. Lett., 630, L185 (cited on pages 12 and 54)

Cameron, A. G. W. 1978, Moon and Planets, 18, 5 (cited on page 10)

Cameron, A. G. W. & Truran, J. W. 1977, icarus, 30, 447 (cited on page 83)

Canovas, H., Ménard, F., Hales, A., et al. 2013, Astron. Astrophys., 556, A123 (cited on pages 15, 16, 30, 31, and 128)

Canovas, H., Min, M., Jeffers, S. V., Rodenhuis, M., & Keller, C. U. 2012a, Astron. Astrophys., 543, A70 (cited on page 8)

Canovas, H., Min, M., Jeffers, S. V., Rodenhuis, M., & Keller, C. U. 2012b, Astron. Astrophys., 543, A70 (cited on pages 15 and 58)

Carson, J., Thalmann, C., Janson, M., et al. 2013, Astrophys. J. Lett., 763, L32 (cited on page 3)

Casassus, S., van der Plas, G., M, S. P., et al. 2013, nat, 493, 191 (cited on pages 11, 13, and 16)

Casertano, S. & Hut, P. 1985, Astrophys. J., 298, 80 (cited on pages 79 and 86)

Casini, R., de Wijn, A. G., & Judge, P. G. 2012, Astrophys. J., 757, 45 (cited on page 94)

Chauvin, G., Lagrange, A. M., Dumas, C., et al. 2004, Astron. Astrophys., 425, L29 (cited on page 15)

Clarke, C. J. 2007, MNRAS, 376, 1350 (cited on page 80)

Clarke, C. J., Gendrin, A., & Sotomayor, M. 2001, MNRAS, 328, 485 (cited on page 12)

Clarke, C. J. & Pringle, J. E. 1993, MNRAS, 261, 190 (cited on page 78)

Clarke, D. 2010, Stellar Polarimetry (Wiley) (cited on page 128)

Close, L. M., Roddier, F., Hora, J. L., et al. 1997, Astrophys. J., 489, 210 (cited on page 15)

Covey, K. R., Greene, T. P., Doppmann, G. W., & Lada, C. J. 2006, aj, 131, 512 (cited on page 80)

Cox, L. J. 1976, MNRAS, 176, 525 (cited on pages 20, 110, and 128)

Currie, T., Burrows, A., Itoh, Y., et al. 2011, Astrophys. J., 729, 128 (cited on pages 30 and 49)

Da Rio, N., Robberto, M., Soderblom, D. R., et al. 2010, Astrophys. J., 722, 1092 (cited on page 80)

de Juan Ovelar, Diamantopoulou, S., Roelfsema, R., et al. 2012a, Proc. SPIE, 8449 (cited on page 129)

de Juan Ovelar, Snik, F., & Keller, C. U. 2011, in Society of Photo-Optical Instrumentation Engineers (SPIE) Conference Series, Vol. 8160 (cited on pages 111 and 129)

de Juan Ovelar, M., Kruijssen, J. M. D., Bressert, E., et al. 2012b, Astron. Astrophys., 546, L1 (cited on page 14)

de Juan Ovelar, M., Min, M., Dominik, C., et al. 2013, ArXiv e-prints (cited on pages 13 and 128)

de Kok, R. J., Stam, D. M., & Karalidi, T. 2011, Astrophys. J., 741, 59 (cited on pages 17, 18, 30, 45, and 128)

de Vries, B. L., Acke, B., Blommaert, J. A. D. L., et al. 2012, Nature, 490, 74 (cited on page 58)

del Toro Iniesta & Collados, M. 2000, Appl. Opt., 39, 1637 (cited on pages 9, 99, and 131)

del Toro Iniesta, J. C. 2003, Introduction to Spectropolarimetry (Cambridge University Press) (cited on pages 7 and 9)

Delabre, B. 2008, Astron. Astrophys., 487, 389 (cited on pages 4, 128, and 132)

Doering, R. L., Meixner, M., Holfeltz, S. T., et al. 2007, Astron. J., 133, 2122 (cited on page 72)

Dong, R., Rafikov, R., Zhu, Z., et al. 2012, Astrophys. J., 750, 161 (cited on pages 13, 15, 30, 54, 73, 74, and 128)

Dorschner, J., Begemann, B., Henning, T., Jaeger, C., & Mutschke, H. 1995, Astron. Astrophys., 300, 503 (cited on page 58)

Doucet, C., Habart, E., Pantin, E., et al. 2007, Astron. Astrophys., 470, 625 (cited on page 72)

Dukes, D. & Krumholz, M. R. 2012, Astrophys. J., 754, 56 (cited on pages 13, 78, and 83)

Dullemond, C. P., Brauer, F., Henning, T., & Natta, A. 2008, Physica Scripta Volume T, 130, 014015 (cited on page 12)

Dullemond, C. P. & Dominik, C. 2004, Astron. Astrophys., 421, 1075 (cited on page 12)

Dullemond, C. P. & Dominik, C. 2005, Astron. Astrophys., 434, 971 (cited on pages 12 and 78)

Eisner, J. A. & Carpenter, J. M. 2006, Astrophys. J., 641, 1162 (cited on pages 13, 78, and 83)

Ercolano, B., Bastian, N., Spezzi, L., & Owen, J. 2011, MNRAS, 416, 439 (cited on pages 12 and 78)

Eriksson, T. S., Hjortsberg, A., Niklasson, G. A., & Granqvist, C. G. 1981, Appl. Opt., 20, 2742 (cited on page 131)

Espaillat, C., Calvet, N., D'Alessio, P., et al. 2007, Astrophys. J. Lett., 670, L135 (cited on pages 12 and 54)

Espaillat, C., D'Alessio, P., Hernández, J., et al. 2010, Astrophys. J., 717, 441 (cited on page 54)

Evans, J. W. 1949, Journal of the Optical Society of America (1917-1983), 39, 229 (cited on page 104)

Evans, N. J., Allen, L. E., Blake, G. A., et al. 2003, pasp, 115, 965 (cited on page 85)

Evans, N. J., Dunham, M. M., Jørgensen, J. K., et al. 2009, Astrophys. J. Suppl., 181, 321 (cited on page 80)

Fatuzzo, M. & Adams, F. C. 2008, Astrophys. J., 675, 1361 (cited on pages 13 and 78)

Fromang, S. & Nelson, R. P. 2005, MNRAS, 364, L81 (cited on page 69)

Furlan, E., Luhman, K. L., Espaillat, C., et al. 2011, Astrophys. J. Suppl., 195, 3 (cited on page 13)

Gehrels, T. 1960, Astron. J., 65, 466 (cited on pages 20, 110, and 128)

Gehrels, T. 1974, Planets, Stars and Nebulae Studied with Photopolarimetry (University of Arizona Press) (cited on pages 37 and 38)

Ghosh, G. 1998, Handbook of thermo-optic coefficients of optical materials with applications (Academic Press, Palik, Edward D.), 115 (cited on page 104)

Ghosh, G. 1999, Optics Communications, 163, 95 (cited on page 139)

Gilliland, R. L., Brown, T. M., Guhathakurta, P., et al. 2000, Astrophys. J. Lett., 545, L47 (cited on pages 14 and 83)

Gisler, D., Feller, A., & Gandorfer, A. M. 2003, in Society of Photo-Optical Instrumentation Engineers (SPIE) Conference Series, ed. S. Fineschi, Vol. 4843, 45–54 (cited on page 117)

Gisler, D., Schmid, H. M., Thalmann, C., et al. 2004, Proc. SPIE, 5492, 463 (cited on pages 21, 31, 59, 112, and 129)

Gorti, U., Dullemond, C. P., & Hollenbach, D. 2009a, Astrophys. J., 705, 1237 (cited on page 12)

Gorti, U., Dullemond, C. P., & Hollenbach, D. 2009b, Astrophys. J., 705, 1237 (cited on page 78)

Haisch, K. E., Lada, E. A., & Lada, C. J. 2001, Astrophys. J. Lett., 553, L153 (cited on page 78)

Hale, P. D. & Day, G. W. 1988, Appl. Opt., 27, 5146 (cited on page 104)

Hall, S. M., Clarke, C. J., & Pringle, J. E. 1996, MNRAS, 278, 303 (cited on page 78)

Harrington, D. M., Kuhn, J. R., & Hall, S. 2011, Pub. Astron. Soc. Pacific, 123, 799 (cited on page 138)

Hartmann, L., Calvet, N., Gullbring, E., & D'Alessio, P. 1998, Astrophys. J., 495, 385 (cited on page 12)

Hashimoto, J., Tamura, M., Muto, T., et al. 2011, Astrophys. J. Lett., 729, L17 (cited on pages 15, 30, and 128)

Hecht, E. 1987, Optics 2nd edition

Hecht, E. 2001, Optics 4th edition (cited on page 133)

Heller, C. H. 1995, Astrophys. J., 455, 252 (cited on page 78)

Henning, T. & Stognienko, R. 1996, Astron. Astrophys., 311, 291 (cited on page 58)

Hernández, J., Hartmann, L., Calvet, N., et al. 2008, Astrophys. J., 686, 1195 (cited on page 78)

Hillenbrand, L. A. & Hartmann, L. W. 1998, Astrophys. J., 492 (cited on page 80)

Hinkley, S., Oppenheimer, B. R., Soummer, R., et al. 2009, Astrophys. J., 701, 804 (cited on pages 8, 30, and 48)

Hodapp, K. W., Suzuki, R., Tamura, M., et al. 2008, Proc. SPIE, 7014 (cited on page 16)

Honda, M., Maaskant, K., Okamoto, Y. K., et al. 2012, Astrophys. J., 752, 143 (cited on page 58)

Hook, I., Liske, J., Villegas, D., & Kissler-Patig, M. 2009, The Messenger, 137, 51 (cited on page 128)

Huitson, C. M., Sing, D. K., Vidal-Madjar, A., et al. 2012, MNRAS, 422, 2477 (cited on page 15)

Ichimoto, K., Lites, B., Elmore, D., et al. 2008, Sol. Phys., 249, 233 (cited on pages 9, 37, 97, 100, 101, 130, and 138)

Ida, S. & Lin, D. N. C. 2004, Astrophys. J., 604, 388 (cited on page 10)

Janson, M., Bergfors, C., Goto, M., Brandner, W., & Lafrenière, D. 2010, Astrophys. J. Lett., 710, L35 (cited on page 30)

Jeffers, S. V., Min, M., Waters, L. B. F. M., et al. 2012, Astron. Astrophys., 539, A56 (cited on pages 15, 30, and 58)

Jeffries, R. D., Littlefair, S. P., Naylor, T., & Mayne, N. J. 2011, MNRAS, 418, 1948 (cited on page 80)

Johansen, A., Youdin, A., & Klahr, H. 2009, Astrophys. J., 697, 1269 (cited on page 69)

Joos, F. 2007, PhD thesis, ETH (cited on page 113)

Joos, F., Buenzli, E., Schmid, H. M., & Thalmann, C. 2008, in Society of Photo-Optical Instrumentation Engineers (SPIE) Conference Series, Vol. 7016 (cited on pages 20, 110, 128, and 137)

Kalas, P., Graham, J. R., Chiang, E., et al. 2008, Science, 322, 1345 (cited on pages 2, 3, 161, and 169)

Karalidi, T. & Stam, D. M. 2012, Astron. Astrophys., 546, A56 (cited on page 18)

Karalidi, T., Stam, D. M., & Guirado, D. 2013, Astron. Astrophys., 555, A127 (cited on page 18)

Karalidi, T., Stam, D. M., & Hovenier, J. W. 2011, Astron. Astrophys., 530, A69 (cited on page 18)

Karalidi, T., Stam, D. M., & Hovenier, J. W. 2012, Astron. Astrophys., 548, A90 (cited on page 18)

Kasper, M., Beuzit, J.-L., Verinaud, C., et al. 2010, Proc. SPIE, 7735 (cited on page 21)

Kasting, J. F., Whitmire, D. P., & Reynolds, R. T. 1993, icarus, 101, 108 (cited on page 82)

Keller, C. U. 1996, Sol. Phys., 164, 243 (cited on page 106)

Keller, C. U., Schmid, H. M., Venema, L. B., et al. 2010, in Society of Photo-Optical Instrumentation Engineers (SPIE) Conference Series, Vol. 7735 (cited on pages 4, 15, 21, 119, and 134)

Keller, C. U. & Snik, F. 2009, in Astronomical Society of the Pacific Conference Series, Vol. 405, Solar Polarization 5: In Honor of Jan Stenflo, ed. S. V. Berdyugina, K. N. Nagendra, & R. Ramelli, 371 (cited on pages 19, 95, and 96)

Kemp, J. C., Henson, G. D., Steiner, C. T., & Powell, E. R. 1987, nat, 326, 270 (cited on page 3)

Klahr, H. H. & Henning, T. 1997, Icarus, 128, 213 (cited on page 69)

Koch, D. G., Borucki, W., Webster, L., et al. 1998, Proc. SPIE, 3356, 599 (cited on pages 1 and 15)

Kraus, A. L., Ireland, M. J., Hillenbrand, L. A., & Martinache, F. 2012, Astrophys. J., 745, 19 (cited on page 80)

Kruijssen, J. M. D. 2009, Astron. Astrophys., 507, 1409 (cited on page 83)

Kruijssen, J. M. D. 2012, MNRAS~in~press, arXiv:1208.2963 (cited on pages 13 and 83)

Lada, C. J. & Lada, E. A. 2003, Annu. Rev. Astron. Astrophys., 41, 57 (cited on page 13)

Lada, C. J., Muench, A. A., Luhman, K. L., et al. 2006, aj, 131, 1574 (cited on page 79)

Lafrenière, D., Marois, C., Doyon, R., Nadeau, D., & Artigau, É. 2007, Astrophys. J., 660, 770 (cited on pages 30 and 41)

Lagage, P. O., Doucet, C., Pantin, E., et al. 2006, Science, 314, 621 (cited on page 72)

Lagrange, A. M., Bonnefoy, M., Chauvin, G., et al. 2010, Science, 329 (cited on pages 2 and 3)

Langlois, M., Dohlen, K., Augereau, J.-C., et al. 2010, Proc. SPIE, 7735 (cited on page 31)

Lee, M. H. & Peale, S. J. 2003, Astrophys. J., 592, 1201 (cited on page 78)

Lenzen, R., Hartung, M., Brandner, W., et al. 2003, Proc. SPIE, 4841, 944 (cited on pages 16 and 31)

Lestrade, J. F., Morey, E., Lassus, A., & Phou, N. 2011, Astron. Astrophys., 532 (cited on page 78)

Liske, J., Padovani, P., & Kissler-Patig, M. 2012, Proc. SPIE, 8444 (cited on page 128)

Lombaert, R., de Vries, B. L., de Koter, A., et al. 2012, Astron. Astrophys., 544, L18 (cited on page 58)

Lopez Ariste, A. & Semel, M. 2011, in Astronomical Society of the Pacific Conference Series, Vol. 437, Solar Polarization 6, ed. J. R. Kuhn, D. M. Harrington, H. Lin, S. V. Berdyugina, J. Trujillo-Bueno, S. L. Keil, & T. Rimmele, 403 (cited on page 140)

Luhman, K. L., Allen, P. R., Espaillat, C., Hartmann, L., & Calvet, N. 2010, Astrophys. J. Suppl., 186, 111 (cited on page 11)

Luhman, K. L. & Mamajek, E. E. 2012, Astrophys. J., 758, 31 (cited on page 13)

Maaskant, K. M., Honda, M., Waters, L. B. F. M., et al. 2013, Astron. Astrophys., 555, A64 (cited on pages 13, 66, 71, and 75)

Madhusudhan, N. & Burrows, A. 2012, Astrophys. J., 747, 25 (cited on page 30)

Madhusudhan, N., Burrows, A., & Currie, T. 2011, Astrophys. J., 737, 34 (cited on page 30)

Mamajek, E. E. 2009, in American Institute of Physics Conference Series, ed. T. Usuda, M. Tamura, & M. Ishii, Vol. 1158, 3–10 (cited on page 11)

Mann, R. K. & Williams, J. P. 2010, Astrophys. J., 725, 430 (cited on pages 13, 78, and 83)

Marigo, P., Girardi, L., Bressan, A., et al. 2008, Astron. Astrophys., 482, 883 (cited on pages 82 and 87)

Marley, M. S. & Sengupta, S. 2011, MNRAS, 417, 2874 (cited on page 30)

Marois, C., Lafrenière, D., Doyon, R., Macintosh, B., & Nadeau, D. 2006, Astrophys. J., 641, 556 (cited on pages 17 and 30)

Marois, C., Macintosh, B., Barman, T., et al. 2008, Science, 322 (cited on pages 2, 3, 30, 49, 161, and 169)

Marois, C., Zuckerman, B., Konopacky, Q. M., Macintosh, B., & Barman, T. 2010, nat, 468, 1080 (cited on pages 2, 3, 30, 161, and 169)

Martin-Zaïdi, C., Lagage, P. O., Pantin, E., & Habart, E. 2007, Astrophys. J. Lett., 666, L117 (cited on page 72)

Maschberger, T. & Clarke, C. J. 2008, MNRAS, 391, 711 (cited on pages 80 and 88)

Masset, F. 2000, A&A Suppl., 141, 165 (cited on pages 17, 57, and 74)

Matzner, C. D. & Levin, Y. 2005, Astrophys. J., 628, 817 (cited on page 10)

Mayama, S., Hashimoto, J., Muto, T., et al. 2012, Astrophys. J. Lett., 760 (cited on page 11)

Mayor, M., Pepe, F., Queloz, D., et al. 2003, The Messenger, 114, 20 (cited on page 1)

Mayor, M. & Queloz, D. 1995, nat, 378, 355 (cited on page 1)

Mayor, M., Udry, S., Naef, D., et al. 2004, Astron. Astrophys., 415, 391 (cited on page 78)

McPherson, A., Gilmozzi, R., Spyromilio, J., Kissler-Patig, M., & Ramsay, S. 2012, The Messenger, 148, 2 (cited on pages 4 and 128)

Ménard, F., Delfosse, X., & Monin, J.-L. 2002, Astron. Astrophys., 396, L35 (cited on pages 17 and 30)

Meshkat, T., Kenworthy, M., Quanz, S. P., & Amara, A. 2013, submitted to ApJ (cited on pages 30 and 41)

Miles-Páez, P. A., Zapatero Osorio, M. R., Pallé, E., & Peña Ramírez, K. 2013, Astron. Astrophys., 556, A125 (cited on page 30)

Milli, J., Mouillet, D., Mawet, D., et al. 2013, Astron. Astrophys., 556, A64 (cited on pages 4 and 17)

Min, M., Canovas, H., Mulders, G. D., & Keller, C. U. 2012, Astron. Astrophys., 537, A75 (cited on pages 15 and 58)

Min, M., Dullemond, C. P., Dominik, C., Koter, A. D., & Hovenier, J. W. 2009, Astron. Astrophys., 497, 155 (cited on pages 17 and 58)

Min, M., Dullemond, C. P., Kama, M., & Dominik, C. 2011, Icarus, 212, 416 (cited on page 58)

Mohanty, S., Jayawardhana, R., Huélamo, N., & Mamajek, E. 2007, Astrophys. J., 657, 1064 (cited on page 15)

Morbidelli, A., Brasser, R., Tsiganis, K., Gomes, R., & Levison, H. F. 2009, Astron. Astrophys., 507, 1041 (cited on pages 12 and 78)

Mordasini, C., Alibert, Y., Benz, W., & Naef, D. 2009, Astron. Astrophys., 501, 1161 (cited on page 10)

Mueller, H. 1948, J. Opt. Soc. Am., 38, 661 (cited on page 6)

Mulders, G. D. & Dominik, C. 2012, Astron. Astrophys., 539, A9 (cited on page 58)

Mulders, G. D., Dominik, C., & Min, M. 2010, Astron. Astrophys., 512, A11 (cited on page 58)

Mulders, G. D., Min, M., Dominik, C., Debes, J. H., & Schneider, G. 2013, Astron. Astrophys., 549, A112 (cited on pages 58 and 65)

Mulders, G. D., Waters, L. B. F. M., Dominik, C., et al. 2011, Astron. Astrophys., 531, A93 (cited on page 58)

Müller, A., Carmona, A., van den Ancker, M. E., et al. 2011, Astron. Astrophys., 535 (cited on page 72)

Muto, T., Grady, C. A., Hashimoto, J., et al. 2012, Astrophys. J., 748, L22 (cited on page 16)

Muzerolle, J., Calvet, N., & Hartmann, L. 1998, Astrophys. J., 492, 743 (cited on page 12)

Najita, J. R., Strom, S. E., & Muzerolle, J. 2007, MNRAS, 378, 369 (cited on page 12)

Nascimbeni, V., Bedin, L. R., Piotto, G., De Marchi, F., & Rich, R. M. 2012, Astron. Astrophys., 541 (cited on pages 14 and 83)

Nee, S. M. F., Yoo, C., Cole, T., & Burge, D. 1998, Appl. Opt., 37, 54 (cited on page 104)

Nordsieck, K. H. 1974, Publ. Astron. Soc. Pac., 86, 324 (cited on page 8)

Norris, B. R. M., Tuthill, P. G., Ireland, M. J., et al. 2012, Nature, 484, 220 (cited on page 31)

O'dell, C. R., Wen, Z., & Hu, X. 1993, Astrophys. J., 410, 696 (cited on page 78)

Ohashi, N. 2008, Astrophys. Space Sci., 313, 101 (cited on page 11)

Okuzumi, S. 2009, Astrophys. J., 698, 1122 (cited on page 10)

Olczak, C., Pfalzner, S., & Eckart, A. 2008, Astron. Astrophys., 488, 191 (cited on page 78)

Olczak, C., Pfalzner, S., & Eckart, A. 2010, Astron. Astrophys., 509 (cited on pages 13 and 78)

Olczak, C., Pfalzner, S., & Spurzem, R. 2006, Astrophys. J., 642, 1140 (cited on pages 13, 78, 79, 83, 84, 86, 87, 88, and 89)

Oppenheimer, B. R., Baranec, C., Beichman, C., et al. 2013, Astrophys. J., 768, 24 (cited on page 15)

Palla, F. & Stahler, S. W. 1999, Astrophys. J., 525, 772 (cited on page 80)

Parker, R. J. & Quanz, S. P. 2012, MNRAS, 419, 2448 (cited on pages 13, 78, and 83)

Patat, F. & Romaniello, M. 2006, Publ. Astron. Soc. Pac., 118, 146 (cited on pages 32 and 39)

Patience, J., King, R. R., de Rosa, R. J., & Marois, C. 2010, Astron. Astrophys., 517 (cited on page 15)

Perrin, M. D., Graham, J. R., Larkin, J. E., et al. 2010, in Society of Photo-Optical Instrumentation Engineers (SPIE) Conference Series, Vol. 7736 (cited on pages 20, 110, and 128)

Pfalzner, S., Vogel, P., Scharwächter, J., & Olczak, C. 2005, Astron. Astrophys., 437, 967 (cited on pages 78, 80, and 87)

Pinilla, P., Benisty, M., & Birnstiel, T. 2012a, Astron. Astrophys., 545, A81 (cited on pages 11, 17, 54, 55, 57, 63, 69, 70, and 74)

Pinilla, P., Birnstiel, T., Ricci, L., et al. 2012b, Astron. Astrophys., 538, A114 (cited on page 70)

Pollack, J. B., Hubickyj, O., Bodenheimer, P., et al. 1996, icarus, 124, 62 (cited on page 10)

Preibisch, T., Ossenkopf, V., Yorke, H. W., & Henning, T. 1993, Astron. Astrophys., 279, 577 (cited on page 58)

Quanz, S. P., Amara, A., Meyer, M. R., et al. 2013a, Astrophys. J. Lett., 766 (cited on pages 13 and 41)

Quanz, S. P., Avenhaus, H., Buenzli, E., et al. 2013b, Astrophys. J. Lett., 766, L2 (cited on pages 15, 30, 31, and 128)

Quanz, S. P., Birkmann, S. M., Apai, D., Wolf, S., & Henning, T. 2012, Astron. Astrophys., 538, A92 (cited on pages 15, 31, 72, 75, and 128)

Quanz, S. P., Schmid, H. M., Geissler, K., et al. 2011, Astrophys. J., 738, 23 (cited on pages 15, 31, and 128)

Rafikov, R. R. 2005, Astrophys. J. Lett., 621, L69 (cited on page 10)

Rakic, A. D. 1995, Appl. Opt., 34, 4755 (cited on page 133)

Ramos, A. A. & Collados, M. 2008, Appl. Opt., 47, 2541 (cited on pages 99, 102, and 108)

Rebull, L. M., Padgett, D. L., McCabe, C. E., et al. 2010, Astrophys. J. Suppl., 186, 259 (cited on page 85)

Reche, R., Beust, H., & Augereau, J. C. 2009, Astron. Astrophys., 493, 661 (cited on page 78)

Regály, Z., Juhász, A., Sándor, Z., & Dullemond, C. P. 2012, MNRAS, 419, 1701 (cited on page 11)

Rice, W. K. M., Armitage, P. J., Wood, K., & Lodato, G. 2006, MNRAS, 373, 1619 (cited on pages 11, 54, and 70)

Rigliaco, E., Natta, A., Randich, S., & Sacco, G. 2009, Astron. Astrophys., 495, L13 (cited on page 78)

Robberto, M., Ricci, L., Da Rio, N., & Soderblom, D. R. 2008, Astrophys. J. Lett., 687, L83 (cited on page 78)

Robberto, M., Soderblom, D. R., Scandariato, G., et al. 2010, aj, 139, 950 (cited on page 85)

Rodenhuis, M., Canovas, H., Jeffers, S. V., et al. 2012, Proc. SPIE, 8446 (cited on pages 4, 8, and 16)

Roelfsema, R., Schmid, H. M., Pragt, J., et al. 2010, Proc. SPIE, 7735 (cited on pages 21, 59, 112, and 129)

Rosotti, G. P., Ercolano, B., Owen, J. E., & Armitage, P. J. 2013, MNRAS, 430, 1392 (cited on page 12)

Rousset, G., Lacombe, F., Puget, P., et al. 2003, Proc. SPIE, 4839, 140 (cited on pages 16 and 31)

Safronov, V. S. 1969, Evoliutsiia doplanetnogo oblaka. (cited on page 10)

Salpeter, E. E. 1955, Astrophys. J., 121 (cited on pages 80, 87, and 89)

Sanchez Almeida, J. & Martinez Pillet, V. 1992, Astron. Astrophys., 260, 543 (cited on page 132)

Sanchez Almeida, J., Martinez Pillet, V., & Kneer, F. 1995, A&A Suppl., 113, 359 (cited on page 129)

Scally, A. & Clarke, C. 2001, MNRAS, 325, 449 (cited on pages 13, 78, 83, and 88)

Schmid, H. M., Beuzit, J.-L., Feldt, M., et al. 2006a, in IAU Colloq. 200: Direct Imaging of Exoplanets: Science & Techniques, ed. C. Aime & F. Vakili, 165–170 (cited on pages 21 and 31)

Schmid, H. M., Beuzit, J. L., Mouillet, D., et al. 2010, in In the Spirit of Lyot 2010 (cited on pages 21, 31, 59, and 129)

Schmid, H.-M., Downing, M., Roelfsema, R., et al. 2012, in Society of Photo-Optical Instrumentation Engineers (SPIE) Conference Series, Vol. 8446 (cited on pages 21, 31, and 117)

Schmid, H. M., Joos, F., & Tschan, D. 2006b, Astron. Astrophys., 452, 657 (cited on page 8)

Schou, J., Borrero, J. M., Norton, A. A., et al. 2012, Sol. Phys., 275, 327 (cited on page 138)

Seager, S. & Deming, D. 2010, Annu. Rev. Astron. Astrophys., 48, 631 (cited on page 15)

Seager, S., Whitney, B. A., & Sasselov, D. D. 2000, Astrophys. J., 540, 504 (cited on page 128)

Selbing, J. 2010, ArXiv e-prints (cited on page 138)

Semel, M., Donati, J.-F., & Rees, D. E. 1993, Astron. Astrophys., 278, 231 (cited on page 8)

Serkowski, K. 1971, in IAU Colloq. 15: New Directions and New Frontiers in Variable Star Research, ed. W. Strohmeier, 11 (cited on page 39)

Serkowski, K. 1973, in IAU Symposium, Vol. 52, Interstellar Dust and Related Topics, ed. J. M. Greenberg & H. C. van de Hulst, 145 (cited on page 39)

Sicilia-Aguilar, A., Henning, T., Juhász, A., et al. 2008, Astrophys. J., 687, 1145 (cited on page 11)

Skumanich, A., Lites, B. W., Pillet, V. M., & Seagraves, P. 1997, Astrophys. J. Suppl., 110, 357 (cited on page 138)

Smith, R. & Jeffries, R. D. 2012, MNRAS, 420, 2884 (cited on page 78)

Snellen, I. A. G., de Kok, R. J., de Mooij, E. J. W., & Albrecht, S. 2010, Nature, 465, 1049 (cited on page 15)

Snik, F. 2006, in Society of Photo-Optical Instrumentation Engineers (SPIE) Conference Series, Vol. 6269 (cited on page 104)

Snik, F., de Wijn, A. G., Ichimoto, K., et al. 2010, Astron. Astrophys., 519, A18 (cited on page 49)

Snik, F., Karalidi, T., & Keller, C. U. 2009, Appl. Opt., 48, 1337 (cited on page 8)

Snik, F. & Keller, C. U. 2013a, in 'Planets, Stars & Stellar Systems', ed. T. D. Oswalt, H. Bond, & Others (Springer) (cited on pages 94 and 137)

Snik, F. & Keller, C. U. 2013b, in Planets, Stars & Stellar Systems, ed. T. D. Oswalt, H. Bond, & Others (Springer) (cited on pages 110, 128, and 140)

Snik, F., Kochukhov, O., Piskunov, N., et al. 2011, in Astronomical Society of the Pacific Conference Series, Vol. 437, Solar Polarization 6, ed. J. R. Kuhn, D. M. Harrington, H. Lin, S. V. Berdyugina, J. Trujillo-Bueno, S. L. Keil, & T. Rimmele, 237 (cited on page 134)

Snik, F., van Harten, G., & Keller, C. U. 2013, to be submitted (cited on page 105)

Socas-Navarro, H., Elmore, D., Ramos, A. A., & Harrington, D. M. 2011, Astron. Astrophys., 531, A2 (cited on page 138)

Soummer, R., Pueyo, L., & Larkin, J. 2012, Astrophys. J. Lett., 755, L28 (cited on page 30)

Spiegel, D. S., Burrows, A., & Milsom, J. A. 2011, Astrophys. J., 727, 57 (cited on page 64)

Spurzem, R., Giersz, M., Heggie, D. C., & Lin, D. N. C. 2009, Astrophys. J., 697, 458 (cited on pages 13, 78, and 83)

Stam, D. M. 2008, Astron. Astrophys., 482, 989 (cited on pages 110 and 128)

Stam, D. M. & Hovenier, J. W. 2005, Astron. Astrophys., 444, 275 (cited on page 18)

Stam, D. M., Hovenier, J. W., & Waters, L. B. F. M. 2004, Astron. Astrophys., 428, 663 (cited on pages 110 and 128)

Stamatellos, D. & Whitworth, A. P. 2008, Astron. Astrophys., 480, 879 (cited on page 10)

Stokes, G. G. 1852, Trans. Cambridge Phil. Soc., 9, 399 (cited on page 6)

Strassmeier, K. G. & Others. 2009, E-ELT Spectropolarimetry: The Science Case (cited on pages 4 and 128)

Strigari, L. E., Barnabè, M., Marshall, P. J., & Blandford, R. D. 2012, MNRAS, 423, 1856 (cited on page 83)

Strom, K. M., Strom, S. E., Edwards, S., Cabrit, S., & Skrutskie, M. F. 1989, Astron. J., 97, 1451 (cited on pages 12 and 54)

Stuik, R., Tinbergen, J., Joos, F., & Schmid, H. M. 2005, Proc. SPIE, 343, 94 (cited on pages 21, 22, 59, 112, 129, and 138)

Sumi, T., Kamiya, K., Bennett, D. P., et al. 2011, nat, 473, 349 (cited on page 83)

Tamura, M. 2009, in American Institute of Physics Conference Series, ed. T. Usuda, M. Tamura, & M. Ishii, Vol. 1158, 11–16 (cited on page 54)

Tarter, J. C., Backus, P. R., Mancinelli, R. L., et al. 2007, Astrobiology, 7, 30 (cited on page 82)

Tata, R., Mart'ın, E. L., Sengupta, S., et al. 2009, Astron. Astrophys., 508, 1423 (cited on pages 17 and 30)

Thalmann, C., Janson, M., Buenzli, E., et al. 2013, Astrophys. J. Lett., 763, L29 (cited on pages 15, 30, 36, 41, 49, and 128)

Thalmann, C., Schmid, H. M., Boccaletti, A., et al. 2008, Proc. SPIE, 7014 (cited on pages 21, 31, 59, 112, and 129)

Tinbergen, J. 1996, Astronomical Polarimetry (Astronomical Polarimetry, by Jaap Tinbergen, pp.˜174.˜ISBN 0521475317.˜Cambridge, UK: Cambridge University Press, September 1996.) (cited on pages 8, 128, and 138)

Tinbergen, J. 2007, Publications of the Astronomical Society of the Pacific, 119, 1371 (cited on pages 112 and 129)

Tinetti, G., Vidal-Madjar, A., Liang, M.-C., et al. 2007, Nature, 448, 169 (cited on page 15)

Tuthill, P., Lacour, S., Amico, P., et al. 2010, Proc. SPIE, 7735 (cited on page 31)

Tyo, J. S. 2002, Appl. Opt., 41, 619 (cited on pages 94, 96, 97, 99, and 102)

van Boekel, R., Min, M., Leinert, C., et al. 2004, Nature, 432, 479 (cited on page 72)

van der Marel, N., van Dishoeck, E. F., Bruderer, S., et al. 2013, Science, 340, 1199 (cited on pages 11 and 13)

van der Plas, G., van den Ancker, M. E., Acke, B., et al. 2009, Astron. Astrophys., 500, 1137 (cited on page 72)

van Harten, G., Snik, F., & Keller, C. U. 2009, Publ. Astron. Soc. Pac., 121, 377 (cited on pages 20, 105, 110, 128, and 133)

Weenink, J., Snik, F., Keller, C. U., van Harten, G., & Hendrix, P. C. J. 2013, submitted to A&A (cited on page 104)

Weidenschilling, S. J. 1977, MNRAS, 180, 57 (cited on pages 10, 11, 54, and 69)

Weidenschilling, S. J. 2008, Physica Scripta Volume T, 130, 014021 (cited on page 12)

Whittet, D. C. B., Martin, P. G., Hough, J. H., et al. 1992, Astrophys. J., 386, 562 (cited on pages 37, 38, and 39)

Williams, J. P. & Cieza, L. A. 2011, Annu. Rev. Astron. Astrophys., 49, 67 (cited on pages 12, 54, and 78)

Witzel, G., Eckart, A., Buchholz, R. M., et al. 2011, Astron. Astrophys., 525, A130 (cited on pages 31, 37, and 39)

Wolszczan, A. & Frail, D. A. 1992, nat, 355, 145 (cited on page 1)

Xu, P., Li, X., Muravski, A., Chigrinov, V., & Valyukh, S. 2006 (SID) (cited on page 117)

Zhu, Z., Nelson, R. P., Dong, R., Espaillat, C., & Hartmann, L. 2012, Astrophys. J., 755, 6 (cited on pages 10, 11, and 54)

Zhu, Z., Nelson, R. P., Hartmann, L., Espaillat, C., & Calvet, N. 2011, Astrophys. J., 729, 47 (cited on pages 11 and 54)

Zsom, A., Ormel, C. W., Güttler, C., Blum, J., & Dullemond, C. P. 2010, Astron. Astrophys., 513 (cited on page 10)

Nederlandse Samenvatting

Beeldvorming van exoplaneten en protoplanetaire schijven

Het onderzoek naar exoplaneten is een relatief jong en extreem spannend veld in de sterren-kunde. Tot op de dag van vandaag zijn meer dan 700 exoplaneten ontdekt, en er wachten meer dan 3000 kandidaten om bevestigd te worden. De reden waarom we "kandidaat" exo-planeten hebben is dat een aantal van de meest succesvolle technieken die we gebruiken om exoplaneten te detecteren "indirect" zijn, wat betekent dat ze informatie geven waaruit we de aanwezigheid van een exoplaneet kunnen afleiden, zonder een directe detectie. Figure A toont de bevestigde exoplaneten tot op de dag van vandaag, met de direct waargenomene als rode ruiten, de met indirecte methodes gedetecteerde als blauwe stippen en de planeten in ons zonnestelsel als gele vierkanten. Dit figuur illustreert het feit dat het aanzienlijk moeilijker is om een beeld van een exoplaneet te verkrijgen dan om zijn aanwezigheid af te leiden uit indirecte informatie.

Het probleem met het direct detecteren van exoplaneten is tweeledig. Ten eerste is het verschil in helderheid tussen de ster en de planeet groot (ongeveer 9 ordes van grootte voor een planeet als Jupiter en een ster als de Zon, en tot 11 ordes voor een planeet als onze Aarde), wat het extreem moeilijk maakt om het licht van de planeet te onderscheiden van de gloed van het sterlicht. Ten tweede spreiden de optische elementen van de telescopen die we gebruiken om afbeeldingen mee te vormen het licht van de ster (en de planeet) uit in een diffractie patroon, wat onze mogelijkheid om dichtbij de centrale ster te kijken beperkt[1]. Bovenop deze beperkingen komt het feit dat wanneer we sterren waarnemen met telescopen op de grond, het licht van de sterren en de planeten die daaromheen draaien door onze atmosfeer moet, welke niet stationair is. Dit zorgt ervoor dat het lichtpatroon dat we waarnemen continu verandert (dit is de reden waarom sterren fonkelen aan de hemel als we naar ze kijken vanaf de grond). De uiteindelijke afbeeldingen van de ster zien er wazig uit, wat het moeilijker maakt om de kleine en zwakke planeet te onderscheiden van zijn ster.

Om deze problemen te overwinnen hebben astronomen en ingenieurs behoorlijk succes-volle waarneem- en datareductietechnieken ontwikkeld, maar zelfs daarmee staat het bereik
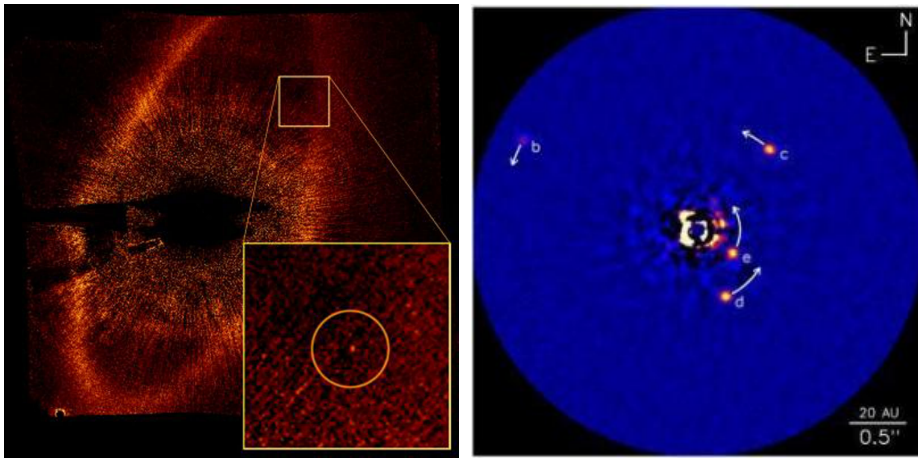
---

[1]Dit limiet staat bekend als de "diffractie limiet"van de telescoop en hangt af van de golflengte van de waarneming en de diameter van de primaire spiegel van de telescoop, zo dat je bij gelijke golflengte dingen dichterbij de ster kunt zien met grotere spiegels
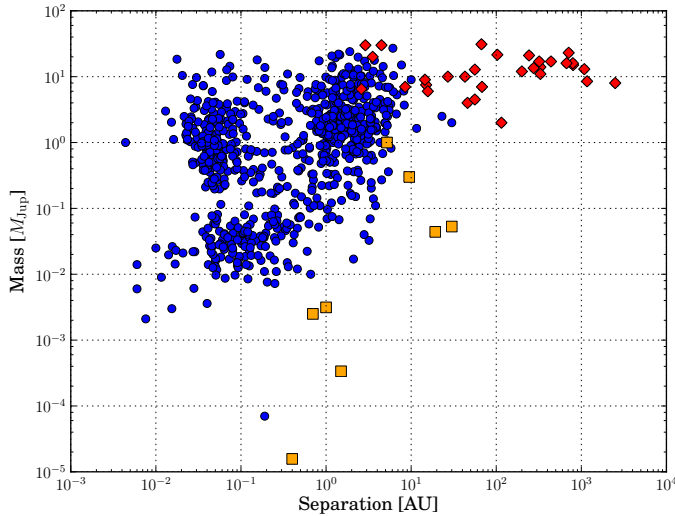
Figuur A: Massa vs. afstand grafiek van momenteel bevestigde exoplaneten. De rode ruiten zijn degene die gedetecteerd zijn door directe beeldvorming en de gele vierkanten zijn de planeten in ons zonnestelsel. *Bron:* exoplanet.eu.

aan planeetmassa's en afstanden tot de ster die waarneembaar zijn met directe beeldvormende methodes op dit moment ver van wat nodig is om een planeet als de Aarde waar te nemen (zie in Figuur A dat de rode ruiten corresponderen met planeten die zwaarder zijn dan Jupiter en op relatief grote afstand om hun ster draaien). Om Figuur A in perspectief te plaatsen: bedenk dat onze zwaarste planeet, Jupiter, zich zou bevinden op coordinaten (5 AU, 1 M_{Jup}), waarbij AU staat voor astronomische eenheden (1 astronomische eenheid correspondeert met de afstand tussen de Zon en de Aarde). De buitenste planeet in ons zonnestelsel, Neptunus, zal punt (30 AU, 0.05 M_{Jup}) innemen, terwijl de Aarde zou staan op positie (1 AU, 0.003 M_{Jup}). Daarom is het duidelijk dat we onze beeldvormende mogelijkheden moeten verbeteren als ons doel is om planeten waar te nemen die vergelijkbaar zijn met die in ons zonnestelsel.

De reden waarom het direct waarnemen van planeten zo belangrijk is omdat we ze dan veel beter kunnen karakteriseren. Uiteraard is onze menselijke nieuwsgierigheid niet bevredigd als we alleen weten dat er een exoplaneet is; we willen weten hoe deze eruit ziet, of het oceanen en continenten heeft zoals de Aarde, dat het meer lijkt op het droge oppervlak van Mars, of dat het klimaat gedomineerd wordt door sterke stormen zoals het geval is bij bijvoorbeeld Jupiter. We willen weten of leven zoals wij het kennen op die planeet kan bestaan, of er begroeiing is, water, of dat de atmosfeer is gevuld met zwavel in plaats van stikstof en zuurstof. Al deze vragen kunnen veel beter beantwoord worden als we direct het licht kunnen

Figuur B: Afbeeldingen van twee direct waargenomen exoplaneten. *Links:* Fomalhaut b (Kalas et al. 2008). *Rechts:* HR8799 b,c,d en e (Marois et al. 2008, Marois et al. 2010). *Bron:* (van links naar rechts) Paul Kalas/UC Berkeley, NASA, ESA; NRC-HIA, C. Marois, and Keck Observatory

registreren dat van de planeet komt, omdat dit licht informatie bevat over zijn samenstelling en structuur. Als voorbeeld van direct waargenomen exoplaneten waarop karakterisatie is toegepast laat Figuur B twee afbeeldingen zien van de exoplaneten die cirkelen om de sterren die bekend staan als Fomalhaut en HR 8799.

Een ander belangrijk veld waarin directe beeldvorming cruciaal wordt is dat van protoplanetaire schijven, de kraamkamers van de planeten. Planeetvorming is een natuurlijk gevolg van stervorming. Een ster vormt uit een wolk van gas en stof die instort onder zijn eigen zwaartekracht. Maar niet al het gas en stof dat aanwezig is in de wolk belandt in de ster. De overgebleven materie vormt een roterende circumstellaire schijf die de ster blijft voeden met materiaal, en waarin ook planeet formatie kan plaatsvinden. Deze planeten vegen het stof en gas in hun baan op, waardoor gaten in de protoplanetaire schijf onstaan Figuur C illustreert dit proces. Het precieze proces waardoor planeten vormen is niet volledig begrepen, en het is hoogstwaarschijnlijk niet uniek, omdat de exoplaneten die wij kennen allemaal erg verschillend zijn. Daarom is het enorm belangrijk om de ontwikkeling van deze protoplanetaire schijven waarin planeetvorming plaatsvindt te bestuderen. Het afbeelden van deze schijven, met name de regionen het dichtst bij de ster, levert op zichtbare en nabij-infrarode golflengtes problemen op vergelijkbaar met exoplaneten, omdat het materiaal rond de ster ook erg zwak straalt.
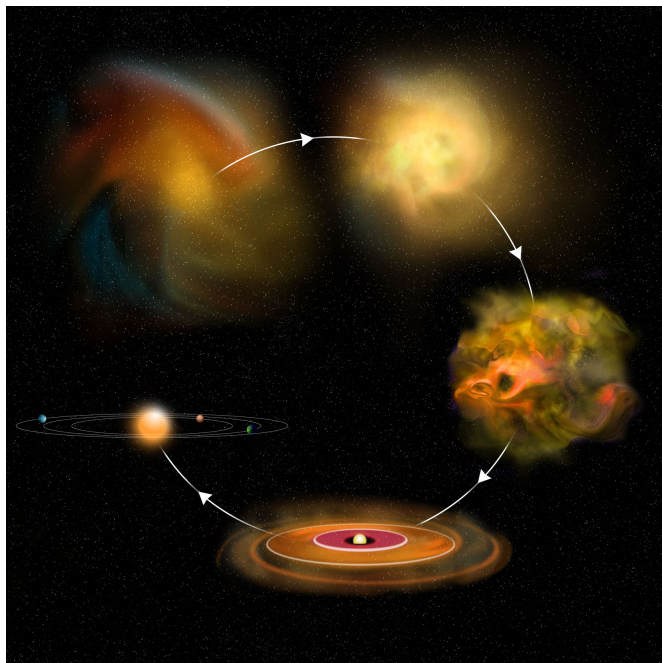
Figuur C: Illustratie van het ster- (en planeet-) vormingsproces. *Bron:* Bill Saxton, NRAO/AUI/NSF

Polarimetrie ter verbetering van ons begrip van planeten en protoplanetaire schijven

Een belangrijke techniek die gebruikt kan worden ter verbetering van onze beeldvorming en karakterisatie van circumstellaire omgevingen is polarimetrie. Licht is opgebouwd uit elektrische en magnetische golven die trillen in richtingen loodrecht op elkaar als het licht voortbeweegt. Als de componenten van het elektrische veld een vast fase- en amplitudeverschil hebben zeggen we dat het licht gepolariseerd is. Afhankelijk van de precieze waardes van deze verschillen kan licht lineair, circulair en elliptisch gepolariseerd zijn. Licht dat van sterren komt is voornamelijk ongepolariseerd, omdat het bestaat uit meerdere golven, die elk op een andere manier gepolariseerd zijn. Het netto resultaat is dat het elektrische veld niet beschikt over een vaste ratio van fase en/of amplitude, en dus heeft het licht geen voorkeurs polarisatie richting. Echter, processen zoals reflectie en verstrooiing kunnen licht dat oorspronkelijk ongepolariseerd is polariseren, en dit is het effect waarvan astronomische polarimetrie gebruik maakt. Wanneer het licht van een ster de atmosfeer van een planeet bereikt, of de materie in een protoplanetaire schijf, dan wordt een deel ervan verstrooid door kleine deeltjes. Deze verstrooide straling wordt lineair gepolariseerd tijdens het verstrooiingsproces,
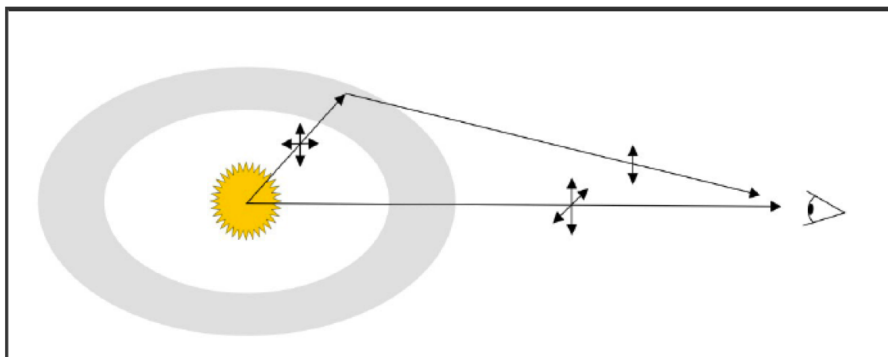
Figuur D: Schematische weergave van de lineaire polarisatie van licht als gevolg van verstrooiing van sterlicht op de stofdeeltjes in een circumstellaire schijf. *Bron:* M. Rodenhuis

wat het mogelijk maakt om het te onderscheiden van het licht van de centrale ster, waarmee het verschil in helderheid tussen de ster en de omliggende materie afneemt met wel 6 ordes van grootte (niveau behaald met huidige technieken en instrumenten). Figuur D illustreert dit idee.

Naast het helpen oplossen van het contrast probleem hangt de resulterende polarisatie toestand van het verstrooide licht sterk af van de eigenschappen van de deeltjes die het licht verstrooien, zoals grootte, samenstelling en vorm. Daarom kan analyse van het gepolariseerde signaal, komend van de circumstellaire materie, informatie verschaffen die niet op andere manieren verkregen kan worden. Dit proefschrift is gewijd aan het verkennen van manieren waarop polarimetrie ons kan helpen om exoplaneten en hun vorming te begrijpen, en het ontwikkelen van nieuwe technieken om de bijbehorende wetenschappelijke en technische uitdagingen te overwinnen.

In Deel I van dit proefschrift presenteren we verschillende studies die als doel hebben een bijdrage te leveren aan de verbetering van de karakterisatie van planeten en de omgeving waarin zij vormen, door middel van directe beeldvorming en polarimetrie. In Hoofdstuk 2, presenteren we de eerste poging om een gepolariseerd signaal te verkrijgen van de exoplaneten die cirkelen om HR 8799 (rechter afbeelding in Figuur A). Deze opwindende studie, die nog niet voltooid is, is gebaseerd op het combineren van de modernste polarimetrische, observationele en dataverwerkingstechnieken om het gepolariseerde signaal te meten van deze zware planeten, hetgeen zeer belangrijke informatie bevat over de structuur van hun atmosfeer en een aantal fysische parameters zoals de oriëntatie van hun rotatie-as en de hoeveelheid afplatting van de bol als gevolg van deze rotatie. Tot dusver zijn we er niet in geslaagd het signaal te detecteren, maar onze resultaten tonen veelbelovende wegen voor de toepassing van deze combinatie van technieken, en we hopen de huidige resultaten te verbeteren op basis van verder onderzoek.

In Hoofdstuk 3 voeren we een studie uit waarin we waarnemingen op verschillende golf-

lengtes en met verschillende waarneemtechnieken combineren, om grenzen te stellen aan de eigenschappen van een planeet in wording die een gat creëert in de schijf. Dit soort schijven met gaten staat bekend als transitie schijven, omdat aangenomen wordt dat ze de overgangsfase zijn tussen een volledige schijf en een schijfloze ster, mogelijk omringd door een planetenstelsel. Hoewel andere theorieën geopperd zijn ter verklaring van de gaten is het mogelijk om deze gaten te creëren door vormende planeten in de schijf, en we laten zien dat als dat het geval is, de karakteristieken van de structuur die we zien in de schijf, gebruikmakend van verschillende waarneemtechnieken, de eigenschappen van de planeet helpen te bepalen zonder de planeet direct te zien. In het bijzonder, de combinatie van beeldvormende polarimetrie op visuele golflengtes en interferometrische waarnemingen op sub-millimeter golflengtes kan de bestaande onzekerheid in planeetmassa en afstand behoorlijk sterk inperken.

De studie gepresenteerd in Hoofdstuk 4 is de enige studie in dit proefschrift die niet (direct) gebruikmaakt van polarimetrie. De reden hiervoor is dat het een statistische studie is van de populatie van protoplanetaire schijven waarvan de grootte (dat wil zeggen de straal) al is gemeten door directe beeldvorming[2]. Deze schijven draaien soms om sterren die weer omgeven worden door andere sterren. In feite vormen de meeste sterren in groepen waarvan sommige gedurende lange tijd bij elkaar blijven, waardoor ze elkaars ontwikkeling beïnvloeden. Daarom is het interessant de vraag te stellen of de omgeving waarin een ster zich ontwikkelt invloed heeft op zijn vermogen om planeten te vormen, omdat een protoplanetaire schijf verstoord kan worden door interacties met omliggende sterren. Dit is precies het doel van de studie. Helaas hebben we geen afbeeldingen van schijven in gebieden met veel sterren, maar het gebied met de hoogste dichtheid van sterren waarin schijven afgebeeld zijn (het Orion Nebula Cluster) lijkt kleinere schijven te bevatten, wat erop wijst dat de omgeving een afkappend effect heeft. Om deze relatie tussen de omgeving en de schijf eigenschappen te bewijzen moeten we gebieden met hogere ster dichtheden verkennen. We hebben daarom voorstellen ingediend om nieuwe waarnemingen uit te voeren met de splinternieuwe Atacama Large Millimeter/submillimeter Array (ALMA).

Een belangrijke beperking voor het uitvoeren van polarimetrische beeldvorming is de hoeveelheid fotonen die een telescoop kan verzamelen. Dit wordt voornamelijk bepaald door de diameter van de primaire spiegel van de telescoop. De grootste telescopen die momenteel operationeel zijn hebben primaire spiegel diameters van ongeveer 8-10 meter. Gelukkig kunnen astronomen in het volgende decennium beginnen te observeren met veel grotere telescopen, zodat de hoeveelheid licht die we kunnen verzamelen van zwakke objecten zoals exoplaneten en protoplanetaire schijven, evenals de resolutie waarmee we kunnen observeren, enorm zal toenemen. Een van deze opkomende faciliteiten is de European Southern Observatory's (ESO's) European Extremely Large Telescope (E-ELT) welke een primaire spiegel zal hebben met een diameter van 39 meter. De bouw en werking van zo'n telescoop is een extreem uitdagende taak door de complexiteit van de systemen die nodig zijn om de positionering en de juiste werking te controleren van alle optische elementen, welke groter zullen zijn dan ooit tevoren.

---

[2]Stralen van sommige van de gebruikte schijven zijn gemeten, voor het eerst of ter bevestiging, met behulp van polarimetrische beeldvorming.

Deel II van dit proefschrift is erop gericht om de instrumentele effecten te bestuderen die aangemaakt worden door de verschillende optische elementen van de E-ELT telescoop. Zoals hiervoor genoemd wordt de polarisatie toestand van licht beïnvloed door processen als reflectie en verstrooiing. Dit is een voordeel voor het afbeelden van exoplaneten en circumstellaire schijven, maar het is ook een nadeel, want de belangrijkste elementen van een telescoop zijn spiegels. Elke reflectie aan een spiegel maakt polarisatie aan, en verandert de polarisatie die het licht al had, wat het moeilijk maakt om uit elkaar te rafelen welk gepolariseerde signaal van het astronomische object komt en wat door de telescoop is veroorzaakt. Daarom is het erg belangrijk om een grondige studie te verrichten naar de telescoop, deze effecten te karakteriseren, en te komen met technieken om ervoor te corrigeren. Dit is precies wat we doen in Hoofdstukken 5 to 7, waar we vinden dat, hoewel de polarimetrische effecten in deze telescoop groot zijn, het mogelijk is om hiervoor te corrigeren (en ze soms compleet op te heffen), waarmee we de condities scheppen die gevoelige en nauwkeurige polarimetrie mogelijk maken.

English Summary

Imaging exoplanets and protoplanetary discs

The field of exoplanets is a relatively young and extremely exciting one in Astronomy. Up to this date, more than 700 exoplanets have been discovered and there are more than 3000 candidates waiting to be confirmed. The reason why we have *"candidate"* exoplanets is that some of the most successful techniques we use to detect exoplanets are *"indirect"*, meaning that they provide information with which we can infer the presence of a planet rather than directly detect it. Figure A shows the confirmed exoplanets known up to date with those detected through direct imaging marked as red diamonds, those detected through indirect methods marked as blue dots and the planets in our Solar System marked in yellow squares. This figure illustrates the fact that it is considerably more difficult to get an image of an exoplanet than to infer its presence form indirect information.

The trouble with directly detecting exoplanets comes mainly from two facts. First the difference in brightness between the star and the planet is large (about 9 orders of magnitude for a planet like Jupiter and a star like the Sun, and up to 11 for a planet like our Earth), which makes it extremely difficult to distinguish the light of the planet from the halo of the central star-light. Second, the optical elements of the telescopes we use to get images spread the light from the star (and the planet) into a diffraction pattern that limits our capability to look close in to the central star[1]. On top of these limitations, when we observe stars from ground-based telescopes, the light from the stars and the planets that orbit them has to go through the atmosphere which is not stationary. This causes the light pattern to look different as time goes on (this is the reason why stars *twinkle* in the sky when we look at them from the ground) and the final images of the stars to look blurry, which complicates the task of distinguishing the small and faint planet from its parent star.

To overcome these problems, astronomers and engineers have developed quite successful observing and data reduction techniques, but even with their help, the range of planet masses and separations from the star that are detectable through direct imaging methods are far from allowing the detection of a planet like the Earth (note that the red diamonds in Figure A

---

[1]This limit is known as the "diffraction limit" of the telescope and depends on the wavelength of observation and the diameter of the primary mirror of the telescope, such that, for the same wavelength, one can see things closer to the star when using bigger mirrors
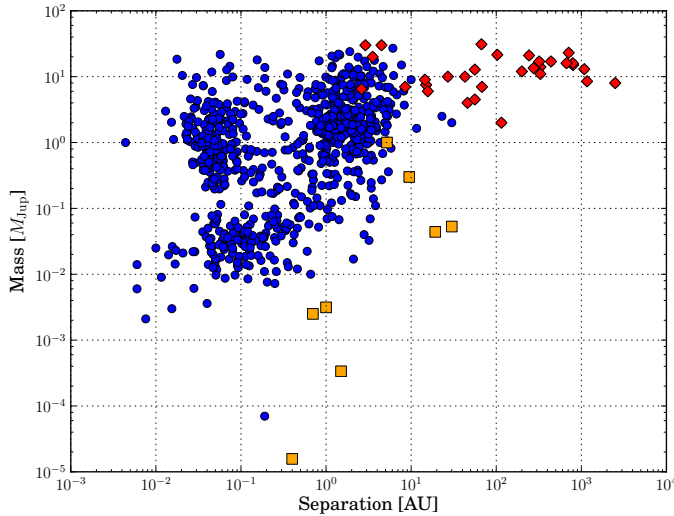
Figure A: Mass vs. separation plot of currently confirmed exoplanets. The red diamonds are the ones that have been detected by direct imaging and the yellow squares are the planets in our Solar System. *Source:* exoplanet.eu.

correspond to planets that are more massive than Jupiter and orbit the star relatively far away from their parent star). To put Figure A into perspective consider that our most massive planet, Jupiter, will be placed at coordinates (5 AU, 1 M_{Jup}), where AU stands for astronomical units (one astronomical unit corresponds to the distance between the Sun and the Earth). The outermost planet in our Solar System, Neptune, will occupy point (30 AU, 0.05 M_{Jup}), while the Earth would stand at position (1 AU, 0.003 M_{Jup}). It is therefore clear that we need to improve our imaging capabilities if we aim to detect planets similar to the ones that form our Solar System.

The reason why detecting planets directly is so important is because we can perform much better characterisation. Of course our curiosity as human beings is not content with just knowing an exoplanet is there; we want to know what the exoplanet looks like, if it features oceans and continents like the Earth, if it looks more like the dry surface of Mars or if its climate is governed by strong storms as it is the case of, for example, Jupiter. We want to know if life as we know it can be hosted by that planet, if there is vegetation, water, or if the atmosphere is filled with sulfur instead of nitrogen and oxygen. All these questions can be much better addressed if we can directly register the light coming from the planet, which contains information about its composition and structure. As an example of directly imaged exoplanets where characterisation has been performed on, Figure B shows two images of the
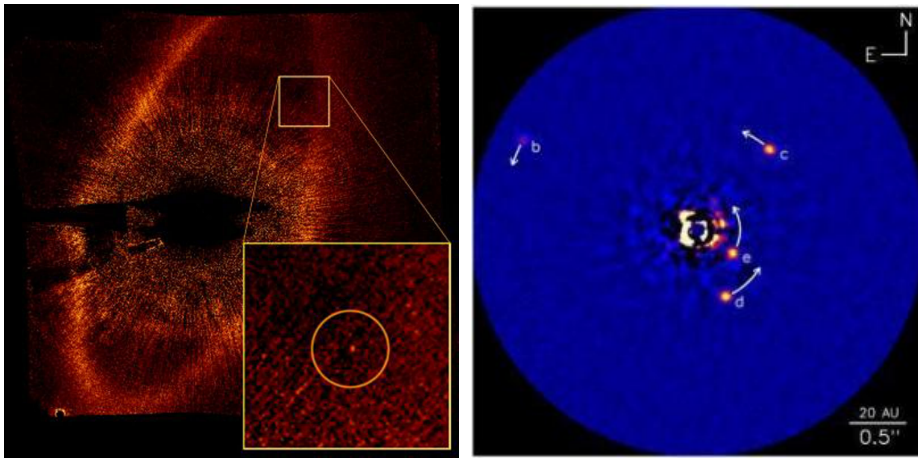
Figure B: Images of two directly detected exoplanets. *Left:* Fomalhaut b (Kalas et al. 2008). *Right:* HR8799 b,c,d and e (Marois et al. 2008, Marois et al. 2010). *Images credit*: (from left to right) Paul Kalas/UC Berkeley, NASA, ESA; NRC-HIA, C. Marois, and Keck Observatory

exoplanets orbiting around the stars known as Fomalhaut and HR 8799.

Another important field where direct imaging becomes crucial is that of protoplanetary discs, which are the cradles of planets. Planet formation is a natural outcome of star formation itself. A star forms out of a cloud of gas and dust that collapses under its own gravitational potential. But not all the gas and dust present in the original cloud ends up in the star. The remaining matter ends up forming a rotating circumstellar disc that keeps on feeding the star with material and also, we believe, undergoes planet formation processes which can create gaps and holes in the disc. Figure C shows an illustration of this process. The exact process by which planets form is not completely understood, and it is most likely not unique since the characteristics of the exoplanets we know are very different from one another. It is therefore extremely important to investigate the evolution of these protoplanetary discs in which planet formation takes place. Imaging these discs at visible and near-infrared wavelengths and, in particular, the closest regions to the star, poses similar challenges as exoplanet imaging, since the material surrounding the star is also very faint.

Polarimetry to improve our understanding of planets and protoplanetary discs

An important technique that can be used to improve our imaging and characterisation capabilities of circumstellar environments is polarimetry. Light is composed of electric and magnetic waves that vibrate in directions perpendicular to each other as the light propagates.
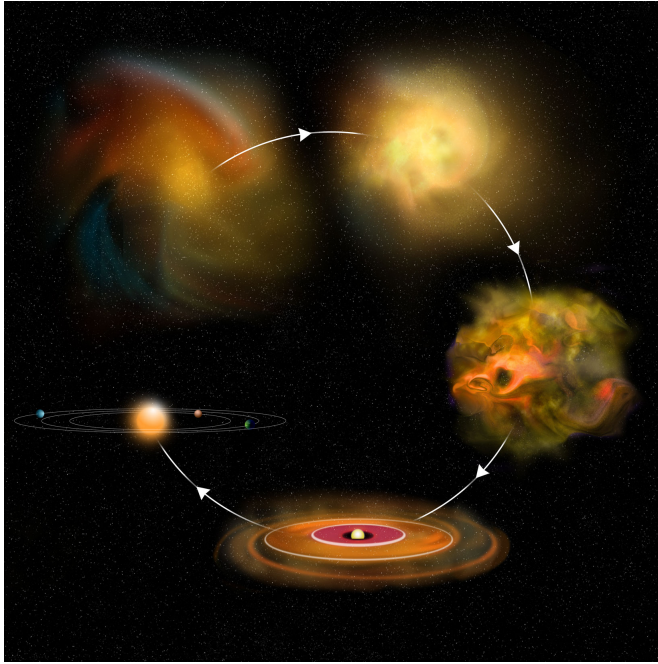
Figure C: Illustration of the star (and planet) formation process. *Image credit:* Bill Saxton, NRAO/AUI/NSF

If the components of the electric field propagate maintaining a fixed difference in phase and amplitude we say that light is polarised. Depending on the particular values of these differences light can be linearly, circularly and elliptically polarised. Light coming from the stars is mainly unpolarised because it is composed of multiple waves, each one polarised in a different way. The net result is that the electric field does not feature fixed ratios of phase and/or amplitude and therefore the light has no preferential polarisation state. However, processes such as reflection and scattering can polarise light that is originally unpolarised and this is the effect astronomical polarimetry exploits. When the light of a star reaches the atmosphere of a planet or the material in a protoplanetary disc a fraction of it gets scattered by the small particles that compose the medium. These scattered radiation becomes linearly polarised in the scattering process which makes it possible to distinguish it from the light of the central star, reducing the difference in brightness between the star and the surrounding matter by up to 6 orders of magnitude (level achieved with current techniques and instruments). Figure D illustrates this idea.

In addition to helping overcome the contrast problem, the resulting polarisation state of the scattered light depends strongly on characteristics of the particles that scatter the radiation
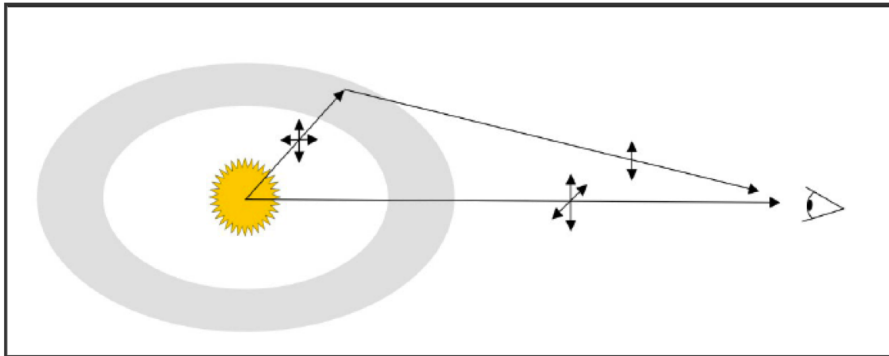
Figure D: Schematic view of the linear polarisation of light that results from the scattering of star-light on the dust particles present in a circumstellar disc. *Image credit:* M. Rodenhuis

such as, for example, size, composition, and shape. Therefore the analysis of the polarised signal coming from the circumstellar matter can yield information that is not obtainable by other means. This thesis is dedicated to explore the ways in which polarimetry can help us to understand exoplanets and their formation, and to develop new techniques to overcome the scientific and technical challenges its use poses.

In Part I of this thesis, we present several studies that aim to contribute to the improvement of characterization of planets and the environment in which they form through direct imaging and polarimetry. In Chapter 2, we present the first attempt to obtain polarisation signal from the exoplanets orbiting HR 8799 (right image in Figure A). This exciting study, which is not yet finished, is based on combining current state-of-the-art polarimetric, observing and data reduction techniques to measure the polarised signal of these massive planets which contains very important information about the structure of their atmosphere and some physical parameters such as the orientation of their spin axis and the amount of flattening their rotation around this axis causes to the globe. So far, we have not been able to detect the signal, but our results show promising avenues for the application of this combination of techniques and we still hope to improve the current results upon further investigation.

In Chapter 3 we perform a study in which we combine observations at different wavelengths and with different observing techniques to constraint properties of a planet that creates a gap/hole in a disc as it forms. These type of disc, featuring holes and/or gaps are known as *transition discs* because they are believed to be the transition phase between a full disc and a discless star possibly orbited by a planetary system. Although other theories have been proposed to explain the gaps/holes, it is possible to create these features by forming planets in the disc, and we show that, if this is the case, the characteristics of the structure we see in the disc using different observing techniques can help us constraining characteristics of the planet without directly seeing it. In particular, the combination of imaging polarimetry at visible wavelengths and interferometric observations at sub-mm wavelengths can quite tightly

constrain the planet's mass and separation.

The study presented in Chapter 4 is the only study in this thesis that does not (directly) include the use of polarimetry. The reason for this is that it is a statistical study on the population of protoplanetary discs of which the size (i.e. the radius) has been already measured through direct imaging[2]. These discs are sometimes orbiting stars that are surrounded by others. Indeed, most stars form in groups of stars of which some will remain close to each other for a long time affecting the evolution of one another. It is therefore interesting to ask oneself the question wether the environment in which a star evolves has any impact on its potential to form planets, since a protoplanetary disc can be perturbed by interactions with surrounding stars. This is precisely the goal of the study. Unfortunately, we do not have images of discs in regions very populated by stars, but the region of highest density of stars in which discs have been imaged (the Orion Nebula Cluster) seems to feature smaller discs, suggesting that the environment does have a truncation effect. To finally prove this relation between the environment and the disc properties we need to explore regions of higher density of stars for what we propose to perform new observations with the brand new Atacama Large Millimetre/sub-millimetre Array (ALMA).

An important limitation for performing polarimetric imaging is the amount of photons a telescope is able to collect. These light collecting capabilities are mainly determined by the diameter of the telescope's primary mirror. The largest telescopes currently operational have primary mirror diameters of about 8-10 metres. Fortunately, in the next decade astronomers will be able to start observing with telescopes much bigger than these and the amount of light we can collect from faint objects like exoplanets and protoplanetary discs will increase greatly, as well as the resolution with which we will be able to observe. One of these upcoming facilities is the European Southern Observatory's (ESO's) European Extremely Large Telescope (E-ELT) which will have a primary mirror of 39 metres in diameter. The construction and operation of such telescope is an extremely challenging task due to the complexity of the systems that are needed to control the positioning and good functioning of all optical elements, which will feature sizes never considered before.

The second part of this thesis (Part II) is oriented to study the instrumental effects generated by the different optical elements of the E-ELT telescope. As we have mentioned before, the polarisation state of light gets affected by processes like reflection and scattering. This is an advantage for imaging exoplanets and circumstellar discs, but it also is a disadvantage since the main elements of a telescope are mirrors. Every reflection on a mirror creates polarisation, and also modifies the polarisation that light already had, making difficult to disentangle what polarised signal came from the astronomical object and what was created by the telescope. For this reason, it is very important to make a thorough study of the telescope, characterise these effects and come up with techniques to correct for them. And this is precisely what we do in Chapters 5 to 7, finding that, although the polarimetric effects in this complex telescope are large, it is possible to correct them and sometimes completely cancel them, assuring the conditions to perform very sensitive and accurate polarimetry.

---

[2]Some of the disc radii used in the study have been measured, for the first time or confirmed, using polarimetric imaging.

Curriculum vitae

I was born in Madrid, Spain, on the 27th of July of 1981. After obtaining a high school degree in science I obtained a bachelor's degree in Aerospace Engineering at the Technical University of Madrid, in Spain. During my last year here I obtained a studentship to work at the Airbus factory in Madrid, where I spent almost a year in the Procurement Quality department. Here I assisted with the supervision of Airbus contractors responsible for the development of new production techniques for Airbus airplane's parts, getting very interested in the production and treatment of materials. After this experience and finishing a course on numerical analysis of aerospace structures, I got a job at the aerospace technology company SENER. At this stage, however, it was clear to me that my passion was closer to the scientific rather than the practical side of engineering so I decided to start combining the job with a master's degree in materials science. Shortly after starting these studies I obtained a Rafael Calvo Rodes fellowship to work for two years at the National Institute of Aerospace Technology (INTA), at the Space Programs department, and left my job at SENER. In 2008, I obtained a studentship at the European Space & Technology Centre (ESTEC) of the European Space Agency (ESA) in Noordwijk, The Netherlands. The position, at the Advanced Concepts Team (ACT), was to develop a short study on the "Transport of nanoparticles in the interplanetary medium", which then turned into my master's thesis. To perform this study, I had to learn a lot about the dynamical behaviour of interstellar dust grains and its relation to radiation forces. This amazing experience gave me the final push I needed to reaffirm my intention of pursuing a scientific career instead of an engineering one. At my return to Spain, I got a studentship to work at ESA's European Space & Astronomy Centre (ESAC), to work on the calibration of the EPIC cameras onboard the XMM-Newton satellite based on spectroscopy of the Cassiopea A and SNR N132D supernovae. In February 2010, I started my PhD research at the Astronomical Institute of Utrecht, Utrecht University, in the group of prof. C. U. Keller which was transferred to the Sterrewacht Leiden when the directive board of the Utrecht University closed our institute. During the past four years I have participated in different international schools such as the Saas-Fee Course in Switzerland, meetings in San Francisco and San Diego (USA), Munich and Heidelberg (Germany), Yibin (China), Victoria (Canada), Amsterdam and Noordwijk (The Netherlands), and observing runs at the Roque de los muchachos and Paranal observatories in Spain and Chile, respectively.

Acknowledgments

I would like to start by thanking my promotor prof. C. U. Keller and co-promotor dr. ir. F. Snik for giving me the opportunity of starting this PhD. This time has been the most important and challenging of my life so far and I am very thankful for all I learned through it.

In the following pages, I would like to thank the wonderful people I found on the way and to whom I owe a great deal of this achievement.

I feel like it would be unfair to not mention some of the people from my pre-PhD times that contributed significantly to my decision of starting this career. So thanks to Ana Llavona for teaching me how to *"think properly"* and how rewarding it can be to challenge yourself and to my fellow students, friends and staff at the Aerospace and Materials Engineering schools, for all I learned and got done with their help. Thanks also to the groups I worked in at both Airbus and INTA; excellent examples of professionalism, honesty and supportive work environment that I found greatly inspiring. My time at ESTEC was, without a doubt, a turning point for me and I have to thank the ACT group for making me love every day I spent there. A particular mention has to go to Kevin for being my saviour when I first arrived in Leiden and a great friend ever since, and to my project (later MSc. thesis) supervisor Jose Llorens ("the solver"). He was a true inspiration for me and I will always be grateful for all the effort he put on the thesis and for all he taught me about programming and python...this is just priceless!! Thanks also to my supervisors at ESAC, Matteo Guainazzi and Andy Pollock, and the staff and students I met there whom with I shared great times.

Out of all the scientific experiences I had during the past four years, the collaborations carried out in Munich and Amsterdam have been the most inspiring and motivating ones. I would like to thank Eli Bressert, Leonardo Testi, Giovanni Rosotti, Christian Thalmann, Paola Pinilla, Gjis Mulders, Myriam Benisty and Til Birnstiel for being always so open and willing to help and explain things to me. I am indebted to you all for the time and effort you invested on our (beautiful) papers and proposals together. Dearest Carsten and Michiel, I cannot thank you enough for the amazing time I have had working with you at the API. Thanks so much for all you have taught me, for making me feel at home in the "cookie" family right from the first day, for all your patience, time, advice and support. Working with you was really inspiring and I hope we can keep the connection in the future. I would also like to take this opportunity to thank Xander Tielens for his advice and help through complicated times and for his share of responsibility in starting this collaboration. I am very grateful for

what you did.

I have a very special place in my heart for the ExPo project I had the pleasure to work in many times in the past years. The bulk of my optics and polarimetric knowledge has been gained working with this wonderful instrument and the members of the team. I would like to thank Michiel Rodenhuis for the large amount of time and effort he invested in teaching me the secrets of the instrument, particularly at the start when I was lost in books about polarimetry...it was like "seeing the light"!!! Thanks also to Hector (the master of the pipeline who taught me a great deal about data reduction), Michiel (Min), Sandra, Tim, Laurens and Jos for their work and dedication to ExPo. It is beautiful.

I would like to thank also the people I have met thanks to the HR 8799 project. Observing at Paranal is quite an experience and I have to thank Julien Girard and Dimitri Mawet, for the wonderful time I had there and for all the help and support they have given me ever since. I would like to thank Remco de Kok, for writing this awesome proposal and having such exciting scientific ideas. Thanks also to Tiffany Meshkat and Matt Kenworthy for their crucial contribution to the data reduction and analysis, and to Julien Milli for the enlightening discussions we had during the data reduction process.

Many thanks to Lars Venema for the wonderful chats we have had and for his valuable input to our E-ELT work. Thanks also to Ronald Roelfsema for his dedication and work, for replying to my emails no matter the time of the day (and the day of the weekend) and for working so hard to get the ZIMPOL data for our study.

I am confident I could not have been luckier with the group of friends I found in Utrecht. They made me feel at home in tough times and became friends for life. Thanks to Alito, my angel, who took care of me in countless occasions, makes the best home-made cocktails ever and has attended to all of my gatherings including the move to Leiden in which he performed exceedingly well (and which I am sure he regrets!!!). I will never forget how you beat my circumstellar disc costume in the battle for the "queen of the carnival" place...speechless. To Carlo ("boni") for the countless hours we have spent talking about music, science and life in general. No retreat my friend...no surrender. Ah!! and for that tiramisu of yours...it is real heaven. Thanks to el par de inappropriate *"viejas chismosas"* que son Esteban and Hector and the late addition of Daniel to the club. No matter how bad my day was, they would always make me laugh and remind me that things I worry about most of the time are not really that important. Thanks so much (also to Carlo) for that wonderful song (making-off video included) that I can always take with me so I don't forget how old and lame I am getting...this is what true friends are for. Aninha (my doll) and Angela, thanks a lot for all the scientific-shopping and chatting days. I am very happy that I met you and that we could team-up against the guys when it comes to the defense of clothing self-awareness for scientist. Sjors(iiiii), the *"golden one"*. Thanks so much for all the good times we shared (parties and photo-shoots included), for reviewing the dutch summary so quickly and for being the first (and only) person to recognise me for my contribution to the XMM-Newton report, that felt great!!. Thanks a lot also to Nikola and lovely Nada, for their great advices and the times I spent at their place. To Klara for being such a great *comrade* and also for her great advices, I wish we could have shared more time together! To Catherine, for being such a sweet person and

helping me so much with many issues in Utrecht. I loved our chats during our time sharing the office and I am really grateful for the support you always made me feel. Jos(iiiiiiiii) and Ge(eeee)rard...there is just no better company one could have when backpacking through China, and to discuss the nightmare that is the world of reference systems in polarimetry. I am very grateful for having had you by my side during this time, you have been excellent fellows in this challenge! Special thanks to Gerard, for always (ALWAYS!!) being willing to listen and help, for his vital work on the dutch summary and for being part of the group of "best officemates" of all times, together with Visa and Tim. I have loved being with you all in the office. Having the chance to chat, ask questions, learn from your work and discuss all sort of issues has definitely made this time much better. I also have to give Tim(iiii) a special mention for the countless times he helped me no matter what the issue was related to. LaTex, Python, optics, buying tickets for German football games...You are one of the smartest and most capable people I have met. I want to thank Steven for being sooo helpful and caring always about me. And (super) Renia...I have learnt so much from you...you wouldn't believe it!!! Thanks a lot for bearing me as a pseudo-boss and for becoming the good friend you are now. Joke, Stephanie, Thomas, Andrei, Elena, thanks for the good times we've shared.

I have to thank also the (many and) very nice students I have met in Leiden and Amsterdam. Koen, Lucas, Rik, Sebastian, Nicola, Irene (loca!!), Gilles, Marissa, Mattia, Silvia, Heather, Edith, Rob, Renske...I'm sure I am forgetting someone so please forgive me and know that I am very grateful for the times we have shared. The borrels, pizza talks, parties and breakfasts in the roof...it was awesome!!! Matteo and Tiffany, it was a pleasure to work with you!! Thank you so much for all the effort, the explanations and the great work you put in the projects we had. I hope we get to work more together in the future. And Tiff, thanks for accepting the tedious position of paranymph!!! I'm very happy you'll be by my side!

My girlfriends...mi Cheli!! mi más mejor! Gracias por acompañarme siempre. No importa cuanto tiempo pase sin vernos, yo se que estás ahí. Mi golfini...mi Naz. Gracias de corazón por hacerme sentir como en casa, por levantarme la moral siempre y mantenerme a raya. Thanks sooo much to Leah, for knowing how to handle my crises like a boss!!! and for being such an amazing woman. You are an inspiration my friend. Thanks sooo much to my crazy slovak Emili(iiiiiin)a for being such a great room-mate and friend. Thanks also to Margaret the most amazing friend + climbing + (trying to) working out partner. To Toni, Malte and Carolien for the great times we shared in Utrecht. Muchas gracias también a Ruth(ini) y Eva, por acogerme en su grupo (y bajo su techo) desde el primer día (allá por 2008). A Nita, Ale, Bea, Roci, Paula y Marian por hacerme sentir que no pasa el tiempo cada vez que nos vemos. A Gianni por los sabios consejos en momentos de crisis. Muchas gracias a Paco por creer siempre en mi y hacérmelo sentir. Y a los López-Ruiz por abrirme las puertas de su casa y su familia y por el apoyo que me han mostrado siempre.

Diederik, you have made all the difference. I will never forget all the effort and care you have put into this and the faith you had in me from the first moment. I just don't think I can thank you enough for all your support and teaching. You have become a mentor and a very dear friend for me and I am sorry to tell you that this is only the start...you (and amazing Sophie) will have to be there now for the rest haha!! And Steve...I am very thankful to you

for all the help and support you're giving me. It was an honour to have you onboard for the proposal, so thanks!! And thanks to Immi also for her support during this past months...I look forward to our future times in Liverpool!

I want to thank very specially Frank, Joe, Joanna, and Janet for all their support and patience during this time. I am very grateful for the wonderful times we have spent together in the past two years and I'm looking forward to all that's left!! as I said, I promise holidays will be holidays from now on!!

I can't be more grateful to have the family I have. Muchisimas gracias por el apoyo incondicional, los ánimos y el cariño que me habéis dado durante este tiempo. Por comprender que me haya perdido partes importantes de vuestras vidas y por hacerme sentir que siempre puedo volver a casa. Quiero agradecer a mi mami que esté siempre cerca, que me haga sentir siempre que me quiere tanto y que sea como es. Me siento muy orgullosa de ser tu hija. A mi gordi, mi sis, por hacerme reir siempre, por ser tan genial, tan artista y tan *apañá*. Eres estupenda y no sabes como agradezco haberte tenido a mi lado estos 23 años. A mi padre por la cantidad de cariño y cosas buenas que me ha dado, por la música y las batallitas!!. Y, por supuesto, a mis perritos, Duncan, Lilo, Rey, Rox y Railers por llenarme de alegría.

Finally, I would like to thank the person that has suffered the most for the completion of this thesis. Thank you Nate for all you have done to keep me sane. Thanks for going through each day with me. I simply can't imagine how would I have done it without your help, patience, support and love. You are the best thing that could happen to me and I hope you know how grateful I am to have you by my side. I can't wait to write our next chapter together.

I am very grateful to have had the chance to share this important time with you all.
I will never forget it.

Maria de Juan Ovelar
Liverpool, 28th of October, 2013